Bouncing and Walking Droplets: Towards a Hydrodynamic Pilot-Wave Theory

by

Jan Moláček

B.A., Mathematics, University of Cambridge (2007)

Submitted to the Department of Mathematics
in partial fulfillment of the requirements for the degree of

Doctor of Philosophy

at the

MASSACHUSETTS INSTITUTE OF TECHNOLOGY

June 2013

Author .....
Department of Mathematics
May 3, 2013

Certified by .....
John W. M. Bush
Professor of Applied Mathematics
Thesis Supervisor

Accepted by .....
Michel Goemans
Chairman, Department Committee on Graduate Theses

Bouncing and Walking Droplets:

Towards a Hydrodynamic Pilot-Wave Theory

by

Jan Moláček

Submitted to the Department of Mathematics
on May 3, 2013, in partial fulfillment of the
requirements for the degree of
Doctor of Philosophy

Abstract

Coalescence of a liquid drop with a liquid bath can be prevented by vibration of the bath. In a certain parameter regime, a purely vertical bouncing motion may ensue. In another, this bouncing state is destabilized by the droplet's wavefield, leading to drop motion with a horizontal component called walking. The walking drops are of particular scientific interest because Couder and coworkers have demonstrated that they exhibit many phenomena reminiscent of microscopic quantum particles. Nevertheless, prior to this work, no quantitative theoretical model had been developed to rationalize and inform the experiments before our work.

In this thesis, we develop a hierarchy of theoretical models of increasing complexity in order to describe the drop's vertical and horizontal motion in the relevant parameter range. Modeling the drop-bath interaction via a linear spring is found lacking; therefore, a logarithmic spring model is developed. We first introduce this model in the context of a drop impacting a rigid substrate, and demonstrate its accuracy by comparison with existing numerical and experimental data. We then extend the model to the case of impact on a liquid substrate, and apply it to rationalize the dependence of the bouncing droplet's behaviour on the system parameters. The theoretical developments have motivated further experiments, which have in turn lead to refinements of the theory.

We proceed by modeling the evolution of the standing waves created by impact on the bath, which enables us to predict the onset of walking and the dependence of the walking speed on the system parameters. New complex walking states are predicted, and subsequently validated by our detailed experimental study. A trajectory equation for the horizontal motion is obtained by averaging over the vertical bouncing.

Thesis Supervisor: John W. M. Bush
Title: Professor of Applied Mathematics

To my parents, Marie & Josef,
in loving memory.

Acknowledgments

I would like to thank first of all my advisor John Bush, for his continued support, encouragement, patience and guidance, and for providing interesting problems to work on. I have learned a lot from him, from scientific writing to good eating, and I am very grateful for his hospitality.

The experimental data published in this thesis could not have been obtained without Daniel Harris, who built the set-up and taught me how to operate it. I am grateful to Anand Oza for valuable discussions and helpful comments, and to Øistein Wind-Willassen for his help with the experiments. I wish to thank also my thesis committee, Professors Ruben Rosales and Gareth McKinley.

On a more personal note, I would like to thank my family and friends in Boston, who helped me retain, at least partly, my sanity: Qinwen Xiao, Jonathan and Ying Rameseder, Höskuldur Halldorsson, Anand Oza, Rosalie Belanger-Rioux, Tracy Washington, Eric Marberg, Mehdi Ben Abda, Alejandra Terminel, Alexandra van Geen and Renato Umeton. Special thanks go to Madeleine Patston for her patience and love, and for providing the light at the end of the tunnel.

Finally, I would like to mention my mathematics a physics teachers Iva Petrová and Přemysl Šedivý, who encouraged me to pursue my scientific interests, and Václav Cviček, without whom I would not have considered studying outside of my native country.

Contents

List of Figures

List of Tables

Chapter 1

Introduction

"Guttas in saxa cadentis umoris longo in spatio pertundere saxa."
"The drops of rain make a hole in the stone, not by violence, but by oft falling."

Lucretius, De Rerum Natura IV.

The impact of liquid drops upon liquid or solid boundaries has long been a source of fascination and inspiration. Scientific investigations of the interactions between drops, jets and liquid surfaces were initiated by Lord Rayleigh [104, 105] and Arthur M. Worthington [128, 129] in the 1870s. In order to study the dynamics of these processes, often happening over timescales too short for the human eye to perceive, they developed the technique of stroboscopy, invented by Joseph Plateau who himself was involved in the study of liquid films and droplets [92]. The stroboscope relies upon the production of a short intense burst of light, and the art of triggering and compacting the flash was perfected by Harold E. Edgerton, as evidenced by his photographs of nuclear explosions. His collection of high-speed photographs [34] included captivating images of energetic drop impacts with the subsequent formation of craters with crown-like rims, and undoubtedly spurred a renewed interest in the subject.

The development and wide adoption of high-speed imaging has revealed the full range of phenomena associated with drop impact [120]. In the coalescence cascade [121, 5], a succession of progressively smaller drops is created during partial coalescence of the original drop with a liquid bath. Following vigorous drop impact on a bath, ejecta sheets may arise [119], evolving over timescales of mere microseconds. Experimental [111, 67, 15, 58, 10, 96], theoretical [20, 84, 1, 95, 62, 14] and numerical [115, 8, 9, 70, 85] works abound, revealing and rationalizing the vast array of possible behaviour and the rich physics involved. For an overview of the different impact phenomena, see Rein [106] or Yarin [131].

The impact of liquid droplets on solid and fluid surfaces is important in a variety of industrial and biological processes. Industrial applications include insecticide and pesticide design [36, 80, 127], inkjet printing [126] and fuel injection, as well as the design of airplane, ship and windmill blades [132]. For many plants and small creatures, the impact and adherence of a raindrop can lead to tissue damage or other deleterious consequences, such as compromised photosynthesis in the case of plants and respiration in the case of insects; thus, the integument of many plants and insects is hydrophobic [101, 7]. Understanding the dynamics of collisions between drops of different sizes in the atmosphere is a prerequisite to predicting the onset of rain, while raindrop impact on the sea or a puddle has major effect on the aeration of the surface layer and dispersal of spores and microorganisms. The motivation for this thesis is the hydrodynamic quantum analogue system recently discovered by Yves Couder.

In this thesis, we shall focus on drop impact on solids and fluids at relatively low impact speeds, in which both the droplet and the impactor are only weakly distorted. When the impactor is a rigid substrate, the droplet will come to rest on its surface after a series of rebounds during which its initial kinetic energy is dissipated. When the impactor is a liquid bath, the drop will eventually coalesce, after the intervening air layer separating it from the bath beneath it drains below a critical thickness [18]. However, when the bath is shaken vertically, the energy lost to dissipation and wave creation at each rebound can be offset by a transfer of kinetic energy from the bath. Thus the coalescence can be prevented, the drop being instead sustained in a bouncing motion, as was first discovered by Walker [124], since the intervening air layer does not have sufficient time to drain during impact.

As the amplitude of the bath oscillation is increased further, the drop may execute a period-doubling cascade, culminating in a chaotic vertical motion [98], a feature common to systems involving bouncing on a periodically oscillating platform [37, 73, 21]. For drops within a certain size range, the interplay between the drop and its own wave field causes the vertical bouncing to become unstable: the drop begins to move horizontally, an effect first reported by Couder *et al.* [19]. Note that for sufficiently high bath acceleration, known as the Faraday threshold, the bath surface becomes unstable, and a standing wave pattern emerges [38, 4]. As the bath acceleration approaches the Faraday threshold from below, the decay rate of the surface waves created by the drop impacts is reduced and a particular wavelength is selected, corresponding to the least stable wavenumber.

Interaction of walking drops and the surface waves reflected from the boundaries [16, 30] or from other drops [100, 98, 97, 29, 28, 32, 43, 99] leads to a variety of

interesting phenomena reminiscent of quantum mechanics [6], such as tunneling across a sub-surface barrier [30], single-particle diffraction in both single- and double-slit geometries [16] or quantization of circular orbits [43]. Considering the drop motion from a statistical perspective, interesting patterns emerge in the probability density function of the drop's position. Harris *et al.* showed that inside a circular corral, the density function reflects the most unstable mode of the cavity. Investigation of the drop's statistical behaviour in more complex geometries is currently underway.

The discovery of the walking drop system by Couder provided the first experimental realization of a pilot-wave system, first theoretically proposed by de Broglie [22] as a realist, deterministic interpretation of quantum mechanics. This pilot-wave theory for the dynamics that would underly the statistical theory provided by the standard quantum mechanics would constitute a hidden variable theory. The two crucial components of de Broglie's theory, namely the resonance between the particle and its guiding wave, and the monochromatic nature of the guiding wavefield, are both present in Couder's system. Von Neumann produced a proof [123] that ostensibly ruled out all hidden-variable theories; however, the proof was later found to be flawed [2, 3]. Nevertheless, the prejudice against pilot-wave theory persists. It is hoped that with the insights gained from the walking drop system and the rational theory for it developed herein, this unfortunate historical legacy can be rectified.

Exploration of the possible analogies between the drop-bath system described above and quantum mechanics is a growing field of research [83, 55, 54, 56]. Compared to the amount of experimental work done, theoretical modeling has been lacking. While an early phenomenological model [100, 32] was capable of reproducing certain observed behaviours, it was unable to provide quantitative predictions of the system behaviour. The material in this thesis is intended to improve the situation by developing the first rational model of the interaction between the drop's vertical and horizontal motion, which is shown to be necessary to capture the full variety of the observed droplet behaviour. It should serve as a starting point for numerical simulations of the system [88, 75]. Moreover, it will guide the experimenters in their search for new phenomena, a goal first achieved in the results reported in chapter 4.

The work presented in this thesis was motivated by the following basic questions:

- Q1: When a drop is placed on a vibrating fluid bath, over what range of system parameters will it coalesce, bounce or walk?
- Q2: When it does walk, how quickly will it walk?
- Q3: What is the optimal drop size to prevent coalescence or to observe walking?

Chapters 3 through 5 provide the answers to these questions, while raising many new ones.

The need for predictive accuracy and numerical speed necessitated development of a new model for the drop-bath interaction, which we call the *logarithmic spring model*. It is developed in three stages in chapters 2-4. In chapter 2, we treat the normal impact of a drop on a rigid curved impactor. We there introduce our quasi-static model, which provides an adequate approximation to the drop dynamics in the limit of low impact speeds. Its application requires finding the static shape of a drop under the influence of gravity, which allows for the calculation of drop's surface and gravitational potential energy. Expressing the static shape in terms of spherical harmonics then enables us to find the kinetic energy and dissipation associated with the change of the shape within this drop shape family. Finally, the drop's equation of motion is derived and solved numerically, and its predictions are compared with the existing experimental results and numerical work. Our model captures both the effects of the substrate curvature and the drop's initial kinetic energy on the impact dynamics. Since the equations of motion show that the reaction force acting on the drop during impact is nearly linearly dependent on the deformation length, with a logarithmic correction, we dub this model the "logarithmic spring". Chapter 2 appears as published in Moláček, J. and Bush, J. W. M 2012: A Quasi-static Model of Drop Impact, *Physics of Fluids* 24 127103.

In chapter 3, we adapt the model in order to consider low energy drop impact on a liquid bath, as arises for walking droplets. This is achieved by extending the quasi-static approximation to the shape of the deformed bath. In order to achieve sufficient accuracy over the relatively large range of Weber numbers of interest, higher order terms are included in the equations that are fixed by matching the experimental data on the coefficient of restitution and contact time. The model is then applied to rationalize the regime diagrams describing the behaviour of drops bouncing on a vibrating bath, under the further assumption that the bath returns to its equilibrium shape between successive drop impacts. A dimensionless number defined as the ratio of the bath driving frequency to the drop natural oscillation frequency, which we dub the *vibration number*, is shown to collapse the experimental data for different values of driving frequency. We predict a number of new bouncing states, as well as the coexistence of multiple bouncing states with the same periodicity but different average mechanical energy. The coalescence threshold is shown to be well captured by the model, confirming that a detailed description of the intervening air layer dynamics is not necessary; rather, it serves only to transfer stress between droplet and

bath. Chapter 3 is currently under review at the *Journal of Fluid Mechanics*: Drops bouncing on a vibrating bath, Moláček, J. and Bush, J. W. M.

In chapter 4, we consider the spatio-temporal evolution of the bath surface after each drop impact, then the destabilizing influence of this wavefield on the bouncing states. For driving close to the Faraday threshold, the surface is found to be locally approximated by a standing wave with nearly exponential temporal decay and a radial form described by a Bessel function. By considering the horizontal force balance using a heuristic formula for the tangential drag on the drop during impact, we are able to rationalize the limited extent of the parameter range where walking occurs, as well as the speed of the walking drops. The location and extent of the walking region is found to be crucially dependent on the stability and existence of the various vertical bouncing modes. By integrating over one period of the vertical motion, the vertical dynamics can be filtered out, yielding a trajectory equation for the drop's horizontal motion. Chapter 4 is currently under review at the *Journal of Fluid Mechanics*: Drops walking on a vibrating bath: towards a hydrodynamic pilot-wave theory, Moláček, J. and Bush, J. W. M.

In chapter 5, we present the results of an integrated experimental and theoretical investigation of droplets bouncing on a vibrating fluid bath. A comprehensive series of experiments provides the most detailed characterisation to date of the system's dependence on fluid properties, droplet size and vibrational forcing. A number of new bouncing and walking states are reported, including complex periodic and aperiodic motions. Particular attention is given to the first characterisation of the different gaits arising within the walking regime. In addition to complex periodic walkers and limping droplets, we highlight a previously unreported mixed state, in which the droplet switches periodically between two distinct walking modes. Our experiments are complemented by a theoretical study based on our previous developments, which provides a basis for rationalising all observed bouncing and walking states. Chapter 5 is currently under review at the *Physics of Fluids*: Exotic states of bouncing and walking droplets, Wind-Willassen, Ø, Moláček, J., Harris, D. M. and Bush, J. W. M.

In chapter 6, we conclude our study of the bouncing and walking drops, discussing the strengths and weaknesses of our model, and proposing directions in which the theory might be extended.

Chapter 2

Drops Bouncing on a Rigid Substrate

2.1 Background

In this chapter we treat the impact of a liquid drop on rigid or weakly-deformable substrates. The nature of small droplet collision depends on the wettability of the impacted surface, which will in general depend in turn on its surface chemistry and texture [44]. If the droplet wets the substrate, the spreading and detachment of the droplet will depend critically on the contact line dynamics [131]. In this chapter, we consider the case of non-wetting impact, in which a thin air layer is maintained between the droplet and the surface, so that contact line dynamics need not be considered. Such is the case for relatively low-energy impact of drops on super-hydrophobic surfaces [125], a rigid surface coated with a liquid film [47] or a highly viscous liquid surface [25].

We further restrict our attention to low-energy impacts in which the droplet deformation remains small, allowing for an analytical treatment. Two key parameters that characterize the impact are the contact time T_C and the coefficient of restitution C_R. The contact time can be defined as the time over which the droplet experiences a reaction force from the impacted object; the coefficient of restitution as the ratio of the normal components of outgoing to incoming velocity: $C_R = \frac{(V_{out})_n}{(V_{in})_n}$. While, strictly speaking, these definitions can only be approximate due to the interaction between drop and impactor via viscous forces in the intervening gas, for the class of problems to be considered, the resulting ambiguity is negligible.

Six physical variables affect the normal impact of a nonwetting drop on a flat rigid

surface: the droplet radius R_0 and impact speed V_{in}, the liquid density ρ, dynamic viscosity μ and surface tension σ and the gravitational acceleration g (see Table 2.1). These give rise to three nondimensional groups. The Weber number $\mathcal{W}e = \rho R_0 V_{in}^2/\sigma$, Bond number $\mathcal{B}o = \rho g R_0^2/\sigma$ and Ohnesorge number $\mathcal{O}h = \mu\left(\sigma\rho R_0\right)^{-1/2}$ prescribe the relative magnitudes of, respectively, inertia, gravity and viscosity to surface tension. Considering the effects of the surrounding gas on the drop dynamics requires the inclusion of two more physical variables - the gas density ρ_g and gas viscosity μ_g - giving rise to two more nondimensional groups, ρ_g/ρ and $\mathcal{O}h_g = \mu_g\left(\sigma\rho R_0\right)^{-1/2}$. For the parameter range of interest, $\rho_g/\rho \ll 1$ and $\mathcal{O}h_g \ll \mathcal{O}h$, the influence of these two parameters is negligible. To incorporate the influence of substrate curvature, we consider the impacted solid to have a uniform radius of curvature R_2 and introduce the nondimensional group $\mathcal{R} = 1 - R_0/R_2$ (see Fig. 2-1). Defining the curvature of a concave substrate to be negative, we note that $\mathcal{R} = 1$ for a flat surface, $\mathcal{R} \to \infty$ for a sharp pin-shaped surface and $\mathcal{R} = 0$ for a surface whose curvature matches that of the drop.

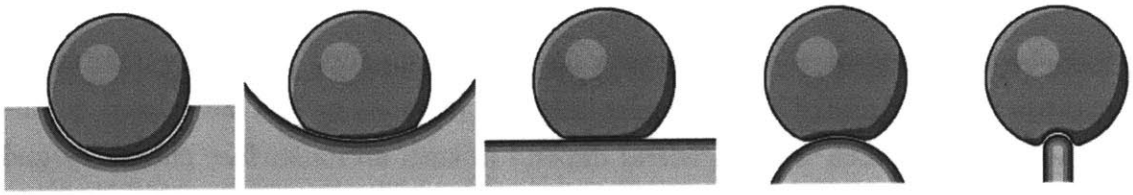

Figure 2-1: A drop of radius R_0 impacts a rigid surface with radius of curvature R_2 (see Figure 2b). Several values of the curvature parameter $\mathcal{R} = 1 - R_0/R_2$ are shown: from left to right, $\mathcal{R} = 0$, $\mathcal{R} = 0.5$, $\mathcal{R} = 1$, $\mathcal{R} = 2$ and $\mathcal{R} \gg 1$.

Studies of liquid drop impact at small and moderate Weber numbers ($\mathcal{W}e < 30$) are scarce in comparison with their high Weber number counterparts. Foote [42] was the first to model numerically the dynamics of a nearly inviscid drop impacting a solid wall, his computations providing estimates for the contact time, contact area and pressure distribution inside the drop. Gopinath & Koch [53] modeled the collision of two identical water drops at low Weber numbers by decomposing their deformation into spherical harmonic modes. In the limit $\ln\left(1/\mathcal{W}e\right) \gg 1$, they were able to use approximations of the behaviour of the Legendre polynomials $P_m(x)$ to show that the contact time increases logarithmically with decreasing $\mathcal{W}e$. The inherent symmetry of the collision of two *identical* drops means that it is in many ways equivalent to the rebound of a single drop from a flat rigid boundary and allows us to implement their results in the present work.

Richard & Quéré [109] measured the coefficient of restitution C_R of small water

drops (0.4mm$\leq R_0 \leq$ 0.5mm) bouncing on a super-hydrophobic surface for $0.02 \leq We \leq 2$. They reported C_R as large as 0.94, noting that it remains relatively constant above a critical impact velocity below which it sharply drops to zero, presumably because the contact angle hysteresis becomes important for sufficiently low Weber numbers. Richard *et al.* [108] measured the contact time T_C in the same configuration for $0.3 \leq We \leq 37$ and found it to be nearly independent of the Weber number in this range, with a slight increase at the lower end of the We spectrum. Okumura *et al.* [84] measured the contact time in the same configuration for $0.003 \leq We \leq 1$ and two drop radii $R_0 = 0.4$mm and $R_0 = 0.6$mm, and noted an increase of T_C with decreasing We, which they attributed to the influence of gravity. They also presented a simple model for the drop dynamics, using a linear spring approximation to the reaction force obtained by approximating the drop distortion as a superposition of pure translation and vibration in the second fundamental harmonic mode.

Simple scaling suggests that the contact time scales as $T_C \approx A\left(\frac{\rho R_0^3}{\sigma}\right)^{1/2}$, as does the period of free oscillations of a drop [103]. The coefficient $A = A(Bo, We, Oh)$ is in general a function of the three nondimensional groups. However, when $We \gg Bo^2$, the effects of gravity can be neglected (Okumura *et al.* [84]); similarly when $Oh \ll 1$ the effects of viscosity can be neglected. When these two conditions are met, we expect $A \approx A(We)$. Richard *et al.* [108] found experimentally that $A \approx 2.6$ for $1 < We < 30$, while the numerical models of Foote [42] and Gopinath & Koch [53] indicate that for $We < 1$, $A(We) \sim \ln \frac{1}{We}$. The linear spring model of Okumura *et al.* [84] predicts $A = 2.31$ independent of We, and thus must become invalid for sufficiently low We. We expect the coefficient of restitution C_R to depend most strongly on Oh, with $C_R \to 0$ as $Oh \to \infty$ and $C_R \to 1$ as $Oh \to 0$. Interestingly, for sufficiently high We, $\lim_{Oh \to 0} C_R \approx 0.91 < 1$, because part of the initial translational energy is transferred to oscillations of the drop surface, as demonstrated by Richard & Quéré [109].

We here present a relatively simple model of non-wetting liquid drop impact valid in the limit of $We \ll 1$ that encorporates the influence of the curvature of the impacted surface. We approximate the drop shape at any instant by one from the quasi-static family of sessile shapes of a drop in a homogeneous gravitational field. The precise shape is thus prescribed by the effective Bond number, which will be the single independent variable in our model. We proceed by finding the first order approximation to the static drop shape in §2, which yields the change of the drop's surface and gravitational potential energies. In §3 we find the spherical harmonic decomposition of the static shape, from which we derive the kinetic energy and viscous

Symbol	Meaning	Typical value	
R_0	drop radius	$0.1 - 1$	mm
R_2	substrate radius of curvature	$-\infty - 0.1$	mm
ρ	drop density	10^3	kg/m^3
σ	drop surface tension	$10^{-2} - 10^{-1}$	N/m
g	gravitational acceleration	9.81	m/s^2
V_{in}	drop incoming speed	$0.1 - 1$	m/s
V_{out}	drop outgoing speed	$0.01 - 1$	m/s
μ	drop dynamic viscosity	$10^{-3} - 10^{-1}$	kg/(m·s)
μ_a	air dynamic viscosity	$2 \cdot 10^{-5}$	kg/(m·s)
T_C	contact time	$3 \cdot 10^{-4} - 2 \cdot 10^{-2}$	s
C_R	$= V_{in}/V_{out}$ coefficient of restitution	$0.18 - 1$	
l_C	$= (\sigma/\rho g)^{1/2}$ capillary length	$1 - 3$	mm
$\mathcal{W}e$	$= \rho R_0 V_{in}^2/\sigma$ Weber number	$0.01 - 1$	
$\mathcal{B}o$	$= \rho g R_0^2/\sigma$ Bond number	$10^{-3} - 10^{-1}$	
$\mathcal{O}h$	$= \mu (\sigma \rho R_0)^{-1/2}$ drop Ohnesorge number	$0.004 - 2$	
$\mathcal{O}h_g$	$= \mu_a (\sigma \rho R_0)^{-1/2}$ gas Ohnesorge number	$10^{-4} - 10^{-3}$	
$\mathcal{R}$	$= 1 - \frac{R_0}{R_2}$ relative curvature parameter	$0 - \infty$	

Table 2.1: List of symbols used together with the typical values encountered in the experiments at low $\mathcal{W}e$ reported by Okumura [84], Richard & Quéré [109] and Terwagne [116].

damping associated with a change of drop shape within the static shape family. We then form the Lagrangian of the system and derive the equation of motion. In §4, we analyze the asymptotic behaviour of contact time in the limit $\ln 1/\mathcal{W}e \gg 1$, both with and without the influence of gravity. We develop a simple numerical model to which we compare the predictions of the quasi-static model in cases where there are no existing data. We investigate the role of the substrate curvature on drop dynamics and show that to leading order the combined effects of curvature and impact speed can be described by a single nondimensional parameter.

2.2 The shape of a static drop

The leading order deformation to a static drop caused by a weak uniform gravitational field was deduced by Chesters [13], and subsequently considered by Smith & van De Ven [114], Shanahan [112] and Rienstra [110]. It will be briefly rederived here, in part to introduce the notation adopted in this chapter. Consider a liquid drop with density ρ, surface tension σ and undeformed radius R_0, that sits on a solid substrate with constant radius of curvature R_2 (see Table 2.1 for the list of symbols). We set

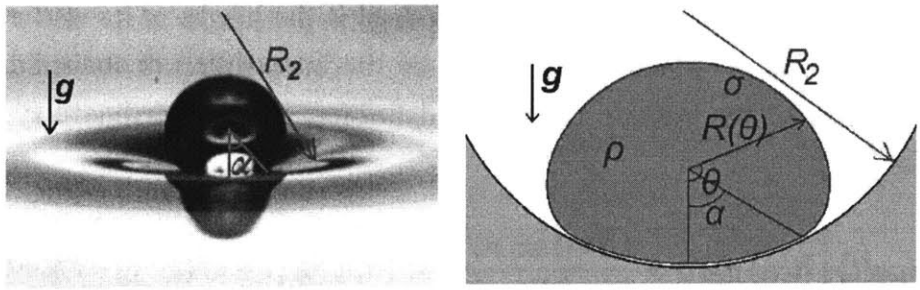

Figure 2-2: Axisymmetric sessile drop of density ρ and surface tension σ resting on a surface with radius of curvature R_2. Without gravity, the drop would be spherical with radius R_0, under gravitational force $\boldsymbol{g}$ it deforms to a shape given by $R = R(\theta)$ in spherical coordinates. The drop shape conforms to that of the substrate over the area $0 \leq \theta \leq \alpha$.

$R_2 > 0$ if the solid is concave (as in Fig. 2-2) and $R_2 < 0$ if it is convex. It will be useful to define the relative curvature parameter $\mathcal{R} = 1 - R_0/R_2$ (see Fig. 2-1). Under the influence of a weak gravitational acceleration g, the drop deforms to an axisymmetric shape given in spherical coordinates by

$$R(\theta) = R_0 \left(1 + \epsilon f(\cos\theta)\right) \quad , \tag{2.1}$$

where $\epsilon \ll 1$. We place the center of our coordinate system at the droplet's center of mass, and align the vector $\theta = 0$ with gravity. We will assume a contact angle close to π, as our goal is to model the impact of water drops on super-hydrophobic surfaces, or drops which remain separated from the solid by a thin gas film. The drop shape conforms to that of the underlying solid in the region $0 \leq \theta \leq \alpha$. We write $\cos\alpha = 1 - \delta$, with δ being the *relative contact area*, specifically, the ratio of the contact area to its maximum possible value $2\pi R_0^2$, and assume $\alpha = O\left(\epsilon^{1/2}\right)$, so that $\delta = O(\epsilon)$, as will be justified in what follows.

2.2.1 Drop energetics

The surface energy of the drop is given by

$$\begin{aligned} \mathcal{S}.\mathcal{E}. &= \sigma \int_0^{\pi} 2\pi R\sqrt{R^2 + R'^2}\sin\theta \mathrm{d}\theta = \\ &= 2\pi\sigma R_0^2 \int_{-1}^{1} 1 + 2\epsilon f + \epsilon^2\left(f^2 + \tfrac{1}{2}f'^2(1-x^2)\right) + O\left(\epsilon^3\right)\mathrm{d}x \ , \end{aligned} \tag{2.2}$$

where $x = \cos\theta$. The potential energy of the drop is the height of its center of mass above a reference point, which we choose to be the intersection of the solid and the axis of symmetry of the system. Then, by definition of our coordinate system, we have, using (2.1):

$$\mathcal{P}.\mathcal{E}. = \tfrac{4}{3}\pi\rho g R_0^3 \left[R(\alpha)\cos\alpha + \frac{(R(\alpha)\sin\alpha)^2}{2R_2} \right] = \tfrac{4}{3}\pi\rho g R_0^4 \left[1 + \epsilon f(1-\delta) - \delta\mathcal{R} + O\left(\epsilon^2\right) \right] \quad . \tag{2.3}$$

The volume of the droplet must remain constant under any deformation. Expressing the volume as an integral of $R(\theta)$ and integrating by parts once, we obtain $\frac{4}{3}\pi R_0^3 = \frac{2\pi}{3}\int_0^\pi R^3(\theta)\sin\theta d\theta$. Substituting again for $R(\theta)$ from (2.1) and using $x = \cos\theta$ yields

$$\int_{-1}^{1} f + \epsilon f^2 \mathrm{d}x = O\left(\epsilon^2\right) \quad . \tag{2.4}$$

The condition that the center of mass is located at the origin is equivalent to $0 = \frac{\pi}{2}\int_0^\pi R^4(\theta)\sin\theta\cos\theta d\theta$. Once again, substituting from (2.1) yields

$$\int_{-1}^{1} f x \mathrm{d}x = O\left(\epsilon\right) \quad . \tag{2.5}$$

In the contact region, the value of $f(x)$ is prescribed by the shape of the substrate:

$$f(x) = \mathcal{R}\frac{1-x}{\epsilon} + \left(f(1-\delta) - \mathcal{R}\frac{\delta}{\epsilon} \right) \quad 1-\delta \le x \le 1 \quad . \tag{2.6}$$

Substituting for $\int_{-1}^{1} f dx$ from (2.4) into (2.2) gives

$$\mathcal{S}.\mathcal{E}. = 2\pi\sigma R_0^2 \left[2 + \epsilon^2 \int_{-1}^{1} \left(\frac{1}{2} f'^2 (1-x^2) - f^2 \right) \mathrm{d}x + O\left(\epsilon^3\right) \right] \quad . \tag{2.7}$$

Minimizing the total energy of the drop $\mathcal{E}_{TOT} = \mathcal{P}.\mathcal{E}. + \mathcal{S}.\mathcal{E}.$, subject to the constraints (2.4) and (2.5), leads to minimizing the functional
$\int_{-1}^{1-\delta} \frac{1}{2} f'^2(1-x^2) - f^2 - \lambda_1 f - \lambda_2 f x \, \mathrm{d}x$, where λ_1, λ_2 are the Lagrange multipliers corresponding to the constraints (2.4) and (2.5), respectively. The Euler-Lagrange equation gives

$$\frac{\mathrm{d}}{\mathrm{d}x}\left[f'(1-x^2) \right] + 2f + \lambda_1 + \lambda_2 x = O\left(\epsilon\right) \quad . \tag{2.8}$$

The general solution of (2.8) (inhomogeneous Legendre's equation) which is well-

behaved at $x = -1$, i.e. at $\theta = \pi$, is given by

$$f(x) = \frac{\lambda_2}{3} x \ln(1-x) + \frac{2-\lambda_1}{2} + cx \quad . \tag{2.9}$$

We determine c and λ_1 from constraints (2.4) and (2.5). Absorbing λ_2 into ϵ finally gives

$$f(x) = \frac{x}{3} \ln\left(\frac{1-x}{2}\right) + \frac{1}{6} + \frac{4}{9}x + O(\epsilon) \quad , \tag{2.10}$$

which is equivalent to Eqn. (12) in Shanahan [112]. Combining expressions (2.6) and (2.7), and substituting for $f(x)$ from (2.10) yields

$$\mathcal{S.E.} = 2\pi\sigma R_0^2 \left[2 - \frac{\epsilon^2}{9}\left(\ln\frac{\delta}{2} + \frac{11}{6}\right) + \frac{1}{2}\mathcal{R}^2\delta^2 + O\left(\epsilon^3\right)\right] \quad . \tag{2.11}$$

Substituting for $f(x)$ from (2.10) into (2.3) and adding that to (2.11) yields an expression for the total energy

$$\frac{\mathcal{E}_{TOT}}{2\pi\sigma R_0^2} = 2 - \frac{\epsilon^2}{9}\left(\ln\frac{\delta}{2} + \frac{11}{6}\right) + \tfrac{1}{2}\mathcal{R}^2\delta^2 + \tfrac{2}{3}\mathcal{B}o\left[\epsilon\left(\frac{1}{3}\ln\frac{\delta}{2} + \frac{11}{18}\right) + \delta\mathcal{R}\right] + O\left(\epsilon^3\right) \quad . \tag{2.12}$$

Differentiating (2.12) with respect to ϵ gives $\epsilon = \mathcal{B}o$, differentiating with respect to δ then gives $\left(\delta\mathcal{R} - \frac{\mathcal{B}o}{3}\right)^2 = O\left(\mathcal{B}o^3\right)$, so

$$\delta = \frac{\mathcal{B}o}{3\mathcal{R}} + O\left(\mathcal{B}o^{3/2}\right) \quad . \tag{2.13}$$

We have thus determined the leading order change to the droplet shape due to gravity. The deformations are of order $\mathcal{B}o$ and so is the relative contact area δ, justifying the claim that $\alpha = O\left(\mathcal{B}o^{1/2}\right)$.

Using (2.13) we can now write the expressions for the surface and gravitational potential energy *increments*, that is, their change due to the drop deformation. It will be useful later on to include also the next order correction to these expressions, in order to obtain a better match for $\mathcal{B}o$ near 1. We have solved for the static shape numerically and, by subtracting the analytically derived first order dependence, were able to find that the second order correction is well approximated by $2\pi\sigma R_0^2 \frac{\mathcal{B}o^3}{18\mathcal{R}}$. Thus

$$\frac{\Delta\mathcal{S}.\mathcal{E}.}{2\pi\sigma R_0^2} \approx +\frac{1}{9}\mathcal{B}o^2\left[\ln\frac{6\mathcal{R}}{\mathcal{B}o} - \frac{4}{3} + \frac{\mathcal{B}o}{2\mathcal{R}}\right] ,$$
$$\frac{\Delta\mathcal{P}.\mathcal{E}.}{2\pi\sigma R_0^2} \approx -\frac{2}{9}\mathcal{B}o^2\left[\ln\frac{6\mathcal{R}}{\mathcal{B}o} - \frac{5}{6} + \frac{3\mathcal{B}o}{8\mathcal{R}}\right] . \qquad (2.14)$$

Expression (2.14) is in accord with the result of Morse & Witten [81], who found that the surface energy of a drop subject to a point force f increases by an amount proportional to $f^2 \ln(1/f)$.

2.2.2 Spherical harmonic decomposition

In order to compute the kinetic energy of the quasi-static drop in the next section, we will need the spherical harmonic decomposition of the static axisymmetric profile:

$$R(\theta) = R_0\left(1 + \mathcal{B}o f(\cos\theta)\right) = R_0\left(1 + \mathcal{B}o\sum_{n=2}^{\infty} b_n P_n(\cos\theta)\right) \quad , \qquad (2.15)$$

where P_n is the n-th Legendre polynomial. The sum begins with $n = 2$ because $b_0 = 0$ from volume conservation (2.4) and $b_1 = 0$ from (2.5). A static drop minimizes the sum of its surface energy and gravitational potential energy.

In order to obtain the surface energy in terms of the spherical harmonic components, we substitute $f(x) = \sum_{n=2}^{\infty} b_n P_n(\cos x)$ from (2.15) into (2.7), which yields

$$\frac{\mathcal{S}.\mathcal{E}.}{2\pi\sigma R_0^2} = 2 + \mathcal{B}o^2\sum_{m,n=2}^{\infty} b_m b_n \int_{-1}^{1}\frac{1}{2}(1-x^2)P_m' P_n' - P_m P_n dx + O\left(\mathcal{B}o^3\right) \quad . \qquad (2.16)$$

Orthogonality of the Legendre polynomials and integration by parts yields

$$\mathcal{S}.\mathcal{E}. = 4\pi\sigma R_0^2 + 2\pi\sigma R_0^2\mathcal{B}o^2\sum_{m=2}^{\infty}\frac{(m-1)(m+2)}{2m+1}b_m^2 + O\left(\mathcal{B}o^3\right) \quad . \qquad (2.17)$$

Obtaining the gravitational potential energy is less straightforward. It might be tempting to simply use (2.3) and write $\mathcal{P}.\mathcal{E}. = \frac{4}{3}\pi\rho g R_0^4\left[1+\mathcal{B}o\sum_{m=2}^{\infty} b_m P_m(1-\delta)-\delta\mathcal{R}\right]$ with δ given by (2.13). This is equivalent to a drop resting on a circular wire of radius $R_0\sqrt{2\delta}$. An alternative choice would be to set $\delta = 0$ in the previous expression, which is equivalent to constraining the drop at just one point. Both approaches are unsatisfactory, especially the latter, as indicated in Fig. 2-3. Although they both give correct values of b_m in the limit of $\delta \to 0$ (i.e. $\mathcal{B}o \to 0$), we want a good approximation to

the next order corrections, which will be used in calculating the kinetic energy and also in the reference numerical simulation. To that end, we must somehow constrain the drop over the whole contact area. A simple way to do that is to use the average over that region:

$$\mathcal{P}.\mathcal{E}. = \frac{4}{3}\pi\rho g R_0^4 \left[1 + \frac{1}{\delta}\int_{1-\delta}^{1} \mathcal{B}o \sum_{m=2}^{\infty} b_m P_m(x) - (1-x)\mathcal{R}\mathrm{d}x\right] \quad . \tag{2.18}$$

Since $\int_{1-\delta}^{1} P_m(x)\mathrm{d}x = \frac{2\delta-\delta^2}{m(m+1)}P'_m(1-\delta)$, (2.18) can be written

$$\mathcal{P}.\mathcal{E}. \approx \frac{4}{3}\pi\rho g R_0^4 \left[1 + 2\mathcal{B}o \sum_{m=2}^{\infty} b_m \frac{P'_m(1-\delta)}{m(m+1)}\right] \quad . \tag{2.19}$$

Minimizing the sum of (2.17) and (2.19) with respect to each b_m immediately yields

$$b_m \approx -\frac{2}{3}\frac{(2m+1)P'_m(1-\delta)}{(m-1)m(m+1)(m+2)} \quad \text{with } \delta = \frac{\mathcal{B}o}{3\mathcal{R}} \quad . \tag{2.20}$$

As $\mathcal{B}o \to 0$, $b_m \to -\frac{1}{3}\frac{2m+1}{(m-1)(m+2)}$, the result obtained from the point constraint for all $\mathcal{B}o$. Including more modes obtained by the point constraint method therefore leads to a shape that diverges logarithmically at $x = 1$ (see Fig. 2-3a). This divergence is avoided by our averaging method (2.20) which produces a good representation of the contact area even for large values of $\mathcal{B}o$. In Fig. 2-3a, it is evident that the form obtained by our averaging method is nearly flat over the contact area, instead of bulging outwards as does the form obtained by the rim constraint method, or curving inwards as does the form obtained by the point constraint method. In Fig. 2-3b, we show the static drop shape obtained by the averaging method for several values of $\mathcal{B}o$. Once again, the curves are close to flat throughout the contact area for all values of $\mathcal{B}o$ considered.

2.3 Quasi-static droplet

We now assume that the drop shape is given by

$$R(\theta,t) = R_0\left(1 + B(t)f(B,\cos\theta)\right) = R_0\left(1 + B(t)\sum_{n=1}^{\infty} b_n(B)\,P_n(\cos\theta)\right) \quad , \tag{2.21}$$

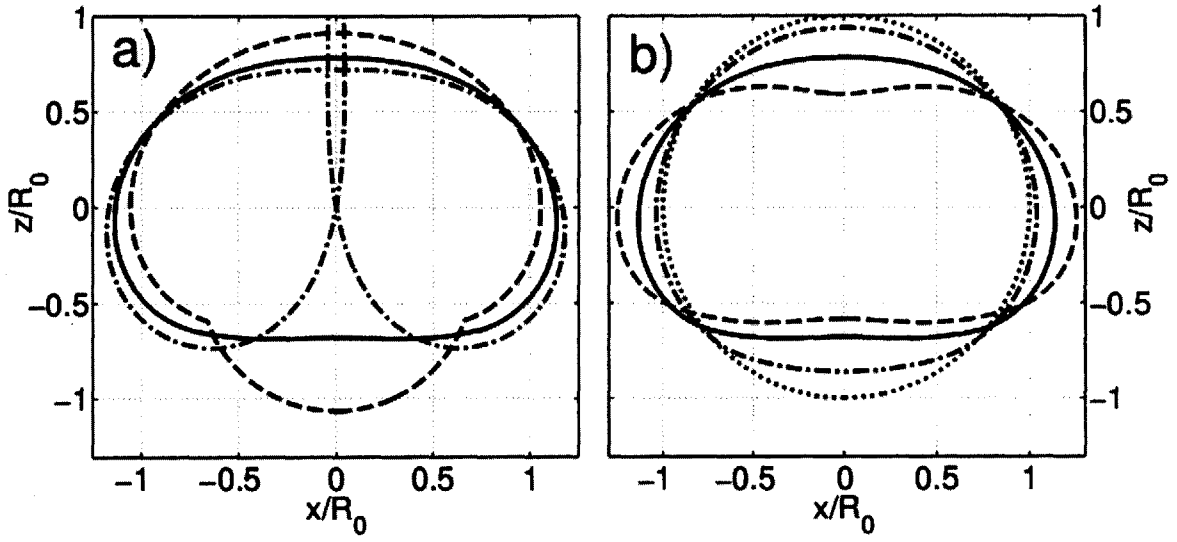

Figure 2-3: **a)** The static profiles of a liquid drop with $\mathcal{B}o = 1$ on a flat surface. The three profiles are the sum of the first 50 spherical harmonic modes obtained by minimizing the surface and gravitational potential energy of a drop constrained in different ways, by averaging the reaction force over: the contact area (equation (2.19)) (*solid line*), the contact area rim (*dashed line*), and the center of the contact area (*dash-dot line*). We see that even for an $O(1)$ Bond number, the averaging method provides a good approximation to the actual drop shape, which has a perfectly flat base. **b)** The static profile of a drop obtained from the first 50 spherical harmonics using the averaging method (2.20) for several values of $\mathcal{B}o$: $\mathcal{B}o = 0$ (*dotted line*), $\mathcal{B}o = 0.5$ (*dash-dot line*), $\mathcal{B}o = 1$ (*solid line*) and $\mathcal{B}o = 1.5$ (*dashed line*).

that is, it corresponds to that of a static drop with instantaneous effective Bond number $\mathcal{B}o_{eff} = B(t)$. The surface and gravitational potential energy of the drop are obtained by simply replacing $\mathcal{B}o$ by $B(t)$ in (2.14). We want to calculate the kinetic energy and rate of viscous dissipation corresponding to this motion in the center-of-mass frame of reference. Let us first consider the limit of small viscosity, which is most accessible analytically.

2.3.1 $\mathcal{O}h \ll 1$: low viscosity drops

When the ratio of the viscous to surface tension forces, as prescribed by the Ohnesorge number $\mathcal{O}h = \mu\,(\rho\sigma R_0)^{-1/2}$, is sufficiently small, we can approximate the flow inside the drop by a potential flow. Axisymmetric solutions of the Laplace equation $\nabla^2\phi = 0$ in spherical coordinates for the velocity potential ϕ, which are continuous at the origin, are of the form $r^n P_n(\cos\theta)$. We can thus write

$$\phi(r,\theta,t) = \sum_{n=1}^{\infty} R_0^2 \left(\frac{r}{R_0}\right)^n \dot{\Phi}_n(t) P_n(\cos\theta) \quad . \tag{2.22}$$

The radial component of velocity is then given by

$$\boldsymbol{u}_r(r,\theta,t) = \boldsymbol{e}_r \frac{\partial\phi}{\partial r} = R_0 \boldsymbol{e}_r \sum_{n=1}^{\infty} n \left(\frac{r}{R_0}\right)^{n-1} \dot{\Phi}_n(t) P_n(\cos\theta) \; . \tag{2.23}$$

Application of boundary conditions at the surface yields

$$u_r(R_0,\theta,t) = \frac{\partial R(\theta,t)}{\partial t} = R_0 \dot{B}(t) \sum_{n=1}^{\infty} b_n P_n(\cos\theta) \quad , \tag{2.24}$$

using (2.22) and ignoring the terms $B(t)\dot{b}_n$ which are of order B^2. Therefore $\Phi_n(t) = B(t)b_n/n$. The kinetic energy of the drop is given by

$$\begin{aligned} \mathcal{K}.\mathcal{E}._0 &= \tfrac{1}{2}\rho \int_V \nabla\phi\cdot\nabla\phi dV = \tfrac{1}{2}\rho \int_V \nabla\cdot(\phi\nabla\phi)\,\mathrm{d}V = \tfrac{1}{2}\rho \int_S \phi \boldsymbol{u}_r \mathrm{d}S = \\ &= \pi\rho R_0^5 \int_0^{\pi} \left(\sum_m \dot{B} b_m P_m \frac{1}{m}\right)\left(\sum_n \dot{B} b_n P_n\right) \sin\theta \mathrm{d}\theta = \pi\rho R_0^5 \dot{B}^2(t) \sum_{m=2}^{\infty} \frac{2b_m^2}{m(2m+1)} \; , \end{aligned} \tag{2.25}$$

where we have used $\nabla^2\phi = 0$ and the orthogonality of the Legendre polynomials. Using the rotational symmetry, the viscous dissipation in the drop can be written as

$$\mathcal{D} = 2\mu \int_V \left(\frac{\partial u_r}{\partial r}\right)^2 + \left(\frac{1}{r}\frac{\partial u_\theta}{\partial \theta} + \frac{u_r}{r}\right)^2 + \left(\frac{u_r}{r}\right)^2 + \tfrac{1}{2}\left(r\frac{\partial}{\partial r}\frac{u_\theta}{r} + \frac{1}{r}\frac{\partial u_r}{\partial \theta}\right)^2 \mathrm{d}V \quad . \quad (2.26)$$

For small $\mathcal{O}h$, we can substitute for $\boldsymbol{u} = \nabla\phi$ from (2.22) into the general formula above, and so derive the expression

$$\mathcal{D}_0 = 8\pi\mu R_0^3 \dot{B}^2(t) \sum_{m=2}^{\infty} \frac{m-1}{m} b_m^2 \quad . \quad (2.27)$$

Having computed the coefficients b_m we can now derive closed-form expressions for the kinetic energy and energy dissipation rate. In the $\mathcal{B}o \to 0$ limit , we have $b_m = -\frac{1}{3}\frac{2m+1}{(m-1)(m+2)}$, which implies

$$\mathcal{K}.\mathcal{E}._0 = \frac{2}{9}\pi\rho R_0^5 \dot{B}^2 \sum_{m=2}^{\infty} \frac{2m+1}{m(m-1)^2(m+2)^2} = \frac{2}{9}\pi\rho R_0^5 \dot{B}^2 C_{K0} \quad \mathcal{B}o \ll 1 \quad , \quad (2.28)$$

where $C_{K0} = \frac{\pi^2}{12} - \frac{17}{27} = 0.19284\ldots$, and the energy dissipation rate is

$$\mathcal{D}_0 = \frac{8}{9}\pi\mu R_0^3 \dot{B}^2 \sum_{m=2}^{\infty} \frac{(2m+1)^2}{m(m+2)^2(m-1)} = \frac{8}{9}\pi\mu R_0^3 \dot{B}^2 C_{D0} \quad \mathcal{B}o \ll 1 \quad , \quad (2.29)$$

where $C_{D0} = \frac{\pi^2}{4} - \frac{5}{12} = 2.0507\ldots$.

For a finite B, we substitute (2.20) into (2.25) and (2.27). It is found that the formulae (2.28) and (2.29) overestimate the kinetic energy and dissipation rate for $B = O(1)$. Although no closed-form expressions could be found for these two quantities at finite B, a reasonable approximation is given by

$$\mathcal{K}.\mathcal{E}._0(B) \approx \tfrac{2}{9}\pi\rho R_0^5 \dot{B}^2 C_{K0}\,(1 - M(B)) \quad \text{and} \quad \mathcal{D}_0(B) \approx \tfrac{8}{9}\pi\mu R_0^3 \dot{B}^2 C_{D0}\left(1 - \sqrt{M(B)}\right) \quad , \quad (2.30)$$

where $M(B) = \frac{8B}{27\mathcal{R}} \ln\frac{9\mathcal{R}}{B}$.

2.3.2 Arbitrary $\mathcal{O}h$

For arbitrary $\mathcal{O}h$, the potential flow approximation ceases to be valid and one has to use a more general method to derive the kinetic energy and viscous dissipation. For

small B, the spherical harmonic modes are still uncoupled, but now we have

$$\mathcal{K}.\mathcal{E}.=\pi\rho R_0^5\dot{B}^2(t)\sum_{m=2}^{\infty}A_m(\mathcal{O}h_m)\frac{2b_m^2}{m(2m+1)} \quad \mathcal{D}=8\pi\mu R_0^3\dot{B}^2(t)\sum_{m=2}^{\infty}D_m(\mathcal{O}h_m)\frac{m}{2m+1}b_m^2 \ . \tag{2.31}$$

The scaled Ohnesorge number $\mathcal{O}h_m \equiv \mathcal{O}h\sqrt{m}$ is introduced for the sake of convenience. The coefficients A_m and D_m are such that the roots of the equation

$$A_m b^2 - 2aD_m b + 1 = 0 \quad \text{, where } \ a = \frac{\mathcal{O}h}{\sqrt{m(m-1)(m+2)}} \ , \tag{2.32}$$

are the two roots with the largest real part of the transendental equation

$$b^2-2a(m-1)\frac{[(2m+1)-2m(m+2)W(b/a)]}{1-2W(b/a)}b+1=0 \ \text{ where } W(x)=\frac{J_{m+3/2}(\sqrt{x})}{\sqrt{x}J_{m+1/2}(\sqrt{x})} \ . \tag{2.33}$$

Here $J_k(x)$ is the Bessel function of the first kind of order k and a is defined in (2.32). For the derivation of (2.33), see Chandrasekhar [11] or Miller & Scriven [76]. The dependence of A_m and D_m on $\mathcal{O}h_m$ is shown on Fig. 2-4. From the properties of the Bessel functions, it follows that $W(x) \to \frac{1}{2m+3}$ as $x \to 0$ and $W(x) \to 0$ as $x \to \infty$. This allows one to approximate (2.32) in the limits of $\mathcal{O}h \to 0$ and $\mathcal{O}h \to \infty$ [76]. For low viscosity ($\mathcal{O}h_m < 0.03$) $A_m \to 1$ (as derived in Section 3.1) and $D_m \to \frac{(2m+1)(m-1)}{m^2}$. For high viscosity ($\mathcal{O}h_m > 1$), $D_m \to \frac{(m-1)(2m^2+4m+3)}{m^2(2m+1)}$ and the kinetic energy term is negligible relative to the surface energy term and so can be discarded. As $m \to \infty$, the values of $A_m(\mathcal{O}h_m)$ and $D_m(\mathcal{O}h_m)$ approach limiting values, denoted $A_\infty(\mathcal{O}h_m)$, $D_\infty(\mathcal{O}h_m)$, which coincide with the values obtained for small surface capillary waves on a planar surface. Note that $D_\infty(0) = 2$, while $D_\infty(\infty) = 1$ (see Fig. 2-4).

As in the previous section, we substitute for b_m from (2.20) into (2.31) to find that

$$\mathcal{K}.\mathcal{E}.(B,\mathcal{O}h)\approx \tfrac{2}{9}\pi\rho R_0^5\dot{B}^2C_K(\mathcal{O}h)\,(1-M) \ , \ \mathcal{D}(B,\mathcal{O}h)\approx \tfrac{8}{9}\pi\mu R_0^3\dot{B}^2C_D(\mathcal{O}h)\left(1-\sqrt{M}\right) \ , \tag{2.34}$$

where $M(B) = \frac{8B}{27\mathcal{R}}\ln\frac{9\mathcal{R}}{B}$.

C_K is a monotonically increasing function of $\mathcal{O}h$, but since $C_K(0) = C_{K0} = 0.192$ while $C_K(\infty) = 0.212$, we can approximate the kinetic term by C_{K0} henceforth while incurring no more than a 5% error. On the other hand, C_D is a monotonically decreasing function of $\mathcal{O}h$ (see Fig. 2-5) with $C_D(0) = \frac{\pi^2}{4} - \frac{5}{12} = 2.051$ and $C_D(\infty) = \frac{\pi^2}{12} + \frac{19}{36} = 1.350$, so for problems with $0.01 \le \mathcal{O}h \le 1$ one cannot use either

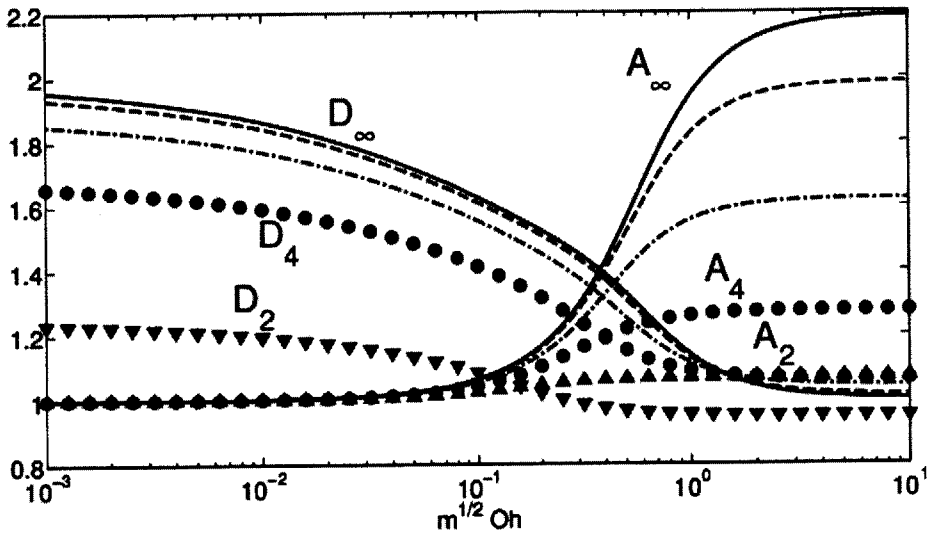

Figure 2-4: The dependence of the coefficients A_m and D_m from equation (2.31) on the scaled Ohnesorge number $\mathcal{O}h_m = m^{1/2}\mathcal{O}h$. Curves for $m = 2, 4, 10, 40$ (*triangles, circles, dash-dot and dashed lines respectively*) are shown, together with the limiting curves for $m \to \infty$ (*solid lines*) corresponding to planar surface capillary waves.

of the limiting values without sacrificing accuracy. Prosperetti [94, 95] treats this complication in greater detail.

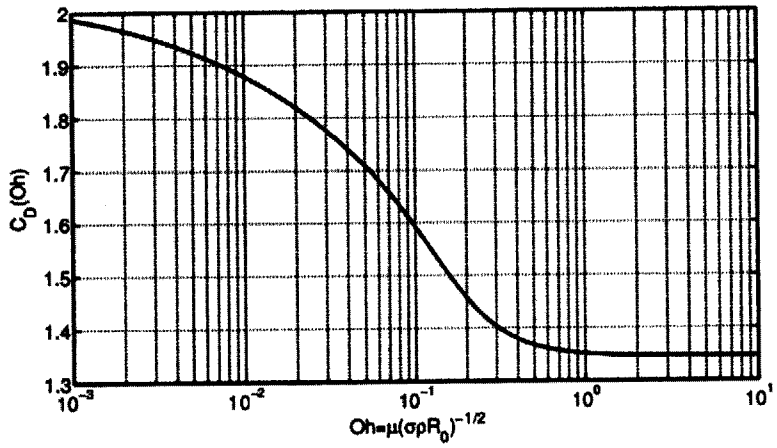

Figure 2-5: The dependence of the dissipation coefficient C_D in equation (2.34) on the Ohnesorge number $\mathcal{O}h$.

2.3.3 Equation of motion

Having derived the surface, kinetic and gravitational potential energies of the drop, as well as the viscous dissipation inside it, we can now construct the Lagrangian

$\mathsf{L} = \mathcal{K}.\mathcal{E}. - \Delta\mathcal{S}.\mathcal{E}. - \Delta\mathcal{P}.\mathcal{E}.$ We switch to a coordinate system fixed to the impacted surface, and assume that it is stationary. The kinetic energy must thus also include a contribution from movement of the drop's center of mass. We define $R_0 b_1$ to be the vertical displacement of the center of mass relative to where it would be if the drop remained spherical. Its dependence on B can be obtained from (2.14) since $\Delta\mathcal{P}.\mathcal{E}. = -\frac{4}{3}\pi\rho g R_0^4 b_1$:

$$b_1 = \frac{B}{3}\left[\ln\frac{6\mathcal{R}}{B} - \frac{5}{6} + \frac{3B}{8\mathcal{R}}\right] \quad . \tag{2.35}$$

Then, as $\frac{d}{dt}b_1 = b_1'(B)\dot{B}$, the Lagrangian is

$$\mathsf{L} = \pi\rho R_0^5\left[\frac{2}{3}\left(b_1'\dot{B}\right)^2 + \frac{2}{9}C_{K0}(1-M(B))\dot{B}^2\right] - \Delta S.E.(B) + \frac{4}{3}\pi\rho g R_0^4 b_1 \quad . \tag{2.36}$$

We obtain the drop's equation of motion using the Euler-Lagrange equation with dissipation [122]

$$\frac{d}{dt}\left[\frac{\partial\mathsf{L}}{\partial\dot{B}}\right] + \frac{1}{2}\frac{\partial\mathcal{D}}{\partial\dot{B}} = \frac{\partial\mathsf{L}}{\partial B} \quad . \tag{2.37}$$

After nondimensionalizing the time with $\tau = t\,(\sigma/\rho R_0^3)^{1/2}$, we deduce

$$\left[b_1'^2 + \frac{1-M}{3}C_{K0}\right]B_{\tau\tau} + \left[b_1'b_1'' - \frac{M'}{6}C_{K0}\right]B_\tau^2 + 2\mathcal{O}h\frac{1-\sqrt{M}}{3}C_D B_\tau + b_1'(B-\mathcal{B}o) = 0 \ , \tag{2.38}$$

where dashes indicate derivatives with respect to B. $M(B)$ is given by (2.34), $C_{K0} = \frac{\pi^2}{12} - \frac{17}{27} = 0.1928$ and $C_D(\mathcal{O}h)$ is shown on Fig. 2-5. We have used the relation $\frac{d\Delta S.E.}{dB} = -\frac{4}{3}\pi\sigma R_0^2 b_1' B$, which follows from the fact that the stationary droplet shape minimizes the sum of potential and surface energy. Differentiating (2.35), we obtain

$$b_1'(B) = \frac{1}{3}\left[\ln\frac{6\mathcal{R}}{B} - \frac{11}{6} + \frac{3B}{4\mathcal{R}}\right] \quad \text{and} \quad b_1''(B) = \frac{3B/4\mathcal{R} - 1}{3B} \quad . \tag{2.39}$$

When $\ln(6\mathcal{R}/B) \gg 1$, (2.38) can be greatly simplified by neglecting higher order terms in B, giving

$$\left[\ln\frac{6\mathcal{R}}{B} - \frac{11}{6}\right]B_{\tau\tau} - B_\tau^2/B + 3\,(B - \mathcal{B}o) = 0 \quad . \tag{2.40}$$

Equation (2.38), or its small $\mathcal{B}o$ approximation (2.40), is our final equation describing the dynamics of a quasi-static droplet. In terms of simplicity and speed of numerical solution, it is surpassed only by the linear spring model of Okumura *et al.* In contrast to the latter model however, it compares favourably even with extensive

numerical simulations and experiments, as will be shown in what follows.

2.4 Results

In this section we compare the results obtained with our quasi-static model with previous models and, most decisively, experimental results reported in the literature. In order to evaluate the accuracy of the model for parameters not found in the literature (e.g. different values of $\mathcal{R}$), we have also created a numerical model by considering the spherical harmonic decomposition of the drop (2.15). The Lagrangian constructed from the surface energy (2.17), potential energy (2.19) and kinetic energy (2.31), together with the constraint

$$\int_{1-\delta}^{1} \sum b_m P_m(x) - (1-x)\mathcal{R}\, \mathrm{d}x = 0 \quad , \tag{2.41}$$

allows one to obtain the equation of motion for each of the modes:

$$A_m b_{m\tau\tau} + 2m^2 \mathcal{O}h D_m b_{m\tau} + m(m-1)(m+2)b_m + \delta_{1m}\mathcal{B}o + \lambda \frac{2m+1}{m+1} P'_m(1-\delta) = 0 \, , \tag{2.42}$$

where $\tau = t(\sigma/\rho R_0^3)^{1/2}$ and δ_{ij} is the Kronecker delta function. δ is defined as the largest solution of $f(1-x) = \mathcal{R}x$ (the length over which the drop surface conforms to that of the substrate), where $f(x) = \sum_{m=1}^{M} b_m P_m(x)$. λ is the Lagrange multiplier corresponding to the constraint (2.41) and its value is determined at each step so that the value of the left-hand side of (2.41) remains constant except possibly for discrete jumps when δ changes discontinuously. We used $M = 150$ modes in our calculations, but as few as 20 modes are sufficient to achieve good accuracy (relative to the full $M = 150$ simulations) within the range of Weber and Bond numbers examined.

2.4.1 Contact time of an impacting drop

Our quasi-static model provides a simple way of treating the vibrations and impact of small drops on a rigid surface for small Weber numbers. Drops impacting with speed V can be modeled by the equation (2.38) with initial conditions $B(0) = \epsilon$, $B_\tau(0) = \mathcal{W}e^{1/2}/b'_1(\epsilon)$ with $\epsilon \to 0$. The contact time of impacting drops has been studied experimentally by Richard *et al.* [109], Okumura *et al.* [84], and numerically by Foote [42] and Gopinath and Koch [53]. Comparing the contact time obtained by

solving (2.38) numerically with their results will allow us to determine the range of validity of our quasi-static model.

Note that from (2.40) we can obtain T_C in the low speed limit $We \to 0$, where we expect $B = O\left(We^{1/2}\right)$ from conservation of energy. For $Bo \ll We^{1/2}$, the influence of gravity on the droplet dynamics can be neglected. By assuming $B(\tau) = A\sin\omega\tau$ with $A \ll 1$ and approximating $\ln(\mathcal{R}/B(t)) \approx \ln(\mathcal{R}/A)$, one can reduce (2.40) to $\omega^2 \ln(\mathcal{R}/A) \approx 3$, thus $\tau_C = \frac{\pi}{\omega} \approx \pi\sqrt{\frac{\ln(\mathcal{R}/A)}{3}}$. From the initial condition $A\omega = B_\tau(0) \approx 3We^{1/2}\ln^{-1}(\mathcal{R}/A)$, it follows that $A\ln^{1/2}(\mathcal{R}/A) \approx \sqrt{3}We^{1/2}$ and so $\tau_C \approx \frac{\pi}{\sqrt{3}}\left[\ln\frac{\mathcal{R}}{We^{1/2}} + \ln\ln^{1/2}\frac{\mathcal{R}}{We^{1/2}} + \gamma\right]^{1/2}$. Analysis of numerical solutions to (2.40) allows us to determine γ and so deduce:

$$T_C = \pi\sqrt{\frac{\rho R_0^3}{3\sigma}}\left[\ln\frac{\mathcal{R}}{We^{1/2}} + \ln\ln^{1/2}\frac{\mathcal{R}}{We^{1/2}} + 0.55\right]^{1/2} + O\left(\ln^{-1}\frac{\mathcal{R}}{We^{1/2}}\right) \quad \text{for } Bo \ll We^{1/2}. \tag{2.43}$$

The expression (2.43) represents an improvement on the first analytic expression for the contact time, formula (2.19) from Gopinath & Koch [53], which states $T_C = \pi\sqrt{\frac{\rho R_0^3}{3\sigma}}\left[\ln We^{-1/2} + O\left(\ln\ln^{1/2} We^{-1/2}\right)\right]^{1/2}$ for the case of a flat impactor $\mathcal{R} = 1$. (2.43) implies that the nondimensional contact time increases without bound as the Weber number approaches zero; however, in reality the effects of viscosity and other body forces will alter this result for sufficiently small Weber numbers.

When $1 \gg Bo \geq We^{1/2}$, we assume that the drop's center of mass will oscillate around its equilibrium position: $B(\tau) = Bo\,(1 + A\cos\omega\tau)$. The value of the amplitude A is determined from conservation of energy. The kinetic energy associated with the internal circulation is negligible relative to its translational kinetic energy, as can be seen from (2.38), their ratio being $3C_{K0}/\ln^2\frac{6\mathcal{R}}{B} \ll 1$. Thus the initial kinetic energy of the drop $\frac{2}{3}\pi\rho R_0^3 V^2$ must equal the sum of surface and gravitational potential energy at the instant of maximal drop deformation, i.e. when $B = Bo(1 + A)$. Substituting for B into (2.14) yields $A^2 = 1 + 3We/\left(Bo^2\ln\frac{\mathcal{R}}{Bo}\right)$, provided $\ln\frac{\mathcal{R}}{Bo} \gg 1$. The contact time equals the difference between the two times when $0 = B(\tau) = Bo\,(1 + A\cos\omega\tau)$, so $\tau_c = \frac{2}{\omega}\left(\pi - \cos^{-1}A^{-1}\right)$. In order to obtain ω, we calculate the frequency of small oscillations around the equilibrium drop shape. Substituting $B(\tau) = Bo\,(1 + \epsilon e^{i\omega\tau})$ into (2.40) with $\epsilon \ll 1$, gives $\omega \approx \sqrt{\frac{1}{3}\ln(\mathcal{R}/Bo) + C_K\ln^{-1}(\mathcal{R}/Bo)}$. Therefore

$$T_C \approx 2\left[\frac{\rho R_0^3}{\sigma}\left(\frac{\ln\frac{\mathcal{R}}{Bo}}{3} + \frac{C_K}{\ln\frac{\mathcal{R}}{Bo}}\right)\right]^{1/2}\left[\pi - \arccos\left(1 + \frac{3We}{Bo^2\ln\frac{\mathcal{R}}{Bo}}\right)^{-1/2}\right] \quad \text{for} \quad Bo \geq We^{1/2}. \tag{2.44}$$

The results are shown in Figures 2-6–2-8. In Fig. 2-6 we see that the numerical model (2.42), the quasi-static models (2.38) and (2.40), and the predictions of Gopinath & Koch [53] all converge for small We, as expected. Our numerical model is also in good agreement with the numerical results of Foote [42], the difference for $We \sim 1$ being due to the fact that the drop becomes elongated upon detachment from the surface, thus prolonging the contact time. This effect was included in Foote's model, but to capture it within the quasi-static framework, one would need to decouple the contact area size from the overall drop deformation and solve for the static shape in negative gravity. While such decoupling would represent an interesting extension of the quasi-static model and presumably would allow one to better capture the dynamics for $We = O(1)$, as our primary focus was the small We limit, this direction was not pursued. Note also that in the numerical simulation using (2.42), we set the contact time to be the time necessary for b_1 to pass zero, i.e. for the center of mass to return to its initial position before the contact. This alternative definition of contact time, while making no difference within the quasi-static framework, was made to eliminate the effects of the oscillations of higher spherical modes on the actual contact time (inevitable for $Oh \to 0$) and thus show the general trends more clearly.

We can see from Fig. 2-6 that the full quasi-static model is within 12% of the other results for the entire range of Weber numbers studied, while the simplified quasi-static model (2.40) is within 10% for $We \lesssim 0.1$. The spring model of Okumura *et al.* [84] predicts $\tau_C = \pi\sqrt{13/24} = 2.312$, which we see is only approximately valid for $0.2 < We \lesssim 1$. For smaller Weber numbers, one needs to include more spherical harmonic modes. In fact, one finds that modeling the first N spherical harmonic modes together with the constraint $\sum_{n=1}^{N} b_n = 0$ (drop pinned at one point) gives $\tau_c \approx \pi\sqrt{\frac{2}{3}\ln N}$. By comparison with formula (2.43) we see that one should include at least $N \approx \frac{\sqrt{\mathcal{R}}}{We^{1/4}} \ln^{1/4} \frac{\mathcal{R}}{We^{1/2}}$ modes for reliable results.

The analytic expression (2.43) suggests that one should use the rescaled Weber number $We/\mathcal{R}^2$ to incorporate the effects of curvature and Weber number into a single nondimensional group; indeed, the numerical results for different $\mathcal{R}$ then collapse onto a single curve (see Fig. 2-7). It can be shown that this collapse follows from the nature of the linearized boundary conditions and equations employed, which are valid approximations provided the contact area, that is, the size of the region over which the drop's shape conforms to that of the substrate, remains small relative to the total drop area. This relative contact area is proportional to δ, which we know from (2.13) to be $B/3\mathcal{R}$. This last expression can be quickly derived by considering

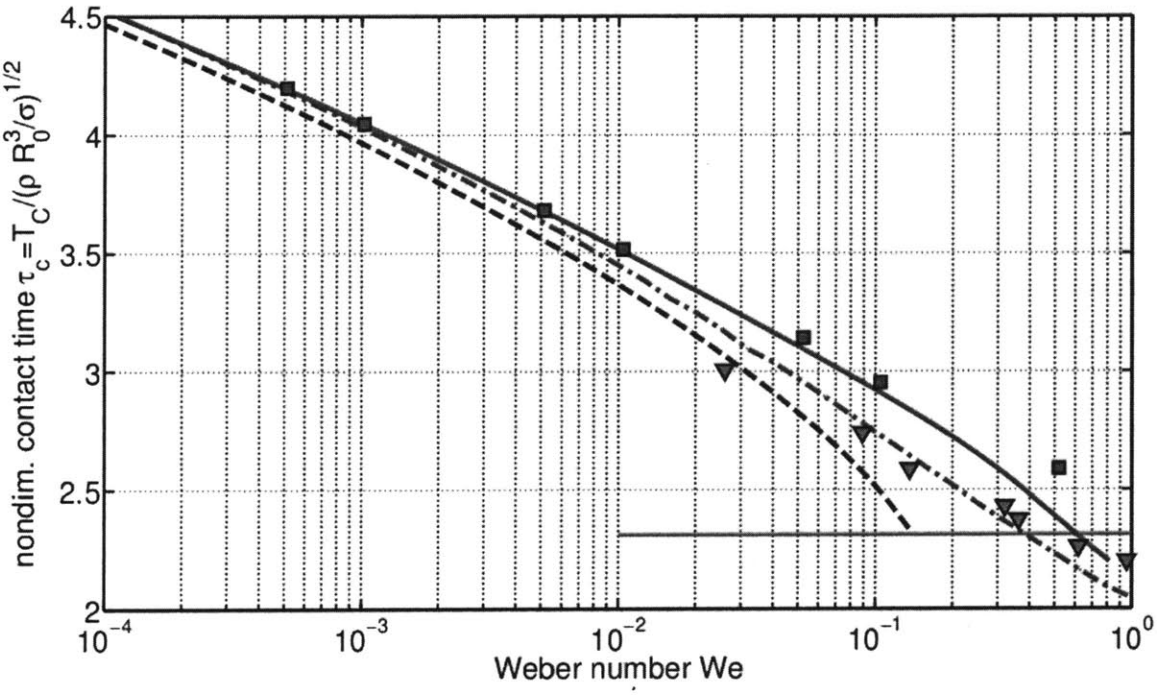

Figure 2-6: Comparison of the nondimensional contact time $\tau_c = T_C/\left(\rho R_0^3/\sigma\right)^{1/2}$ as a function of the Weber number $\mathcal{W}e = \rho R_0^2 V_{in}^2/\sigma$ for $\mathcal{O}h = \mu/\left(\rho\sigma R_0\right)^{1/2} = 0.005$ and $\mathcal{B}o = \rho g R_0^2/\sigma = 0$, obtained with our quasi-static model (2.38) (*solid line*), the simplified model (2.40) (*dashed line*) and numerical simulation of the first 250 spherical harmonic modes (2.42) (*dash-dot line*). The predictions of Gopinath & Koch [53] (■), Foote [42] (▼) and Okumura [84] (*horizontal line*) are included for the sake of comparison.

the pressure jump across the drop interface in the contact region, approximating the internal pressure by $2\sigma/R_0$, and calculating the external pressure by balancing the drop's weight and the total reaction force. Since $B = O(We^{1/2})$ from conservation of energy, the maximum relative contact area scales as $We^{1/2}/\mathcal{R}$, the square root of the rescaled Weber number. Therefore, our model should break down when $We/\mathcal{R}^2 \approx 1$, i.e., when the impact speed becomes sufficiently high, or the substrate curvature sufficiently close to that of the drop, that the contact area becomes comparable to the drop area and the nonlinear effects become important. Little can be said at this point about the drop dynamics in the $We/\mathcal{R}^2 > 1$ regime.

Our quasi-static and numerical models clearly indicate that both the contact time (Fig. 2-7) and the coefficient of restitution (Fig. 2-9) increase logarithmically with decreasing values of the rescaled Weber number. The reason for both of these effects is the logarithmic divergence of the static shape for small contact areas (see eqn. (2.10)), which allows the drop to localize its deformation to a small region around the contact area. Viscous dissipation is then similarly localized and therefore restricted in its total amount, leading to a higher coefficient of restitution. On the other hand, the divergence of the static shape allows the drop to deform further with the same increase in total surface energy, reducing the effective spring constant associated with the deformation and thus increasing the rebound time. From (2.36) we see that the total mechanical energy of the drop scales like $\rho R_0^5 \ln^2(1/B)\dot{B}^2$, while the kinetic energy associated with the internal circulation is only of order $\rho R_0^5 \dot{B}^2$ (see eqn. 2.28). Viscosity can only dissipate the latter component, with viscous dissipation scaling as $\mu R_0^3 \dot{B}^2$ (2.29). Integrating the dissipation over the contact time, which scales like $(\rho R_0^3/\sigma)^{1/2} \ln(1/B)$, we thus expect the relative energy loss during rebound to scale as $\mathcal{O}h/\ln(1/B) \sim \mathcal{O}h/\ln(1/We)$ (see Fig. 2-9).

The effects of gravity have also been studied by Okumura *et al.* [84], whose experimental results are shown in Fig. 2-8, together with our analytical expression (2.44), the quasi-static model (2.38) and the numerical model (2.42). The quasi-static model stays within 12% of the experimental data for the whole range of Weber numbers considered. As a reference, we include the line for zero gravity. We see that the increase in contact time with decreasing We found experimentally by Okumura *et al* may be attributed to the effects of small We and not to gravity.

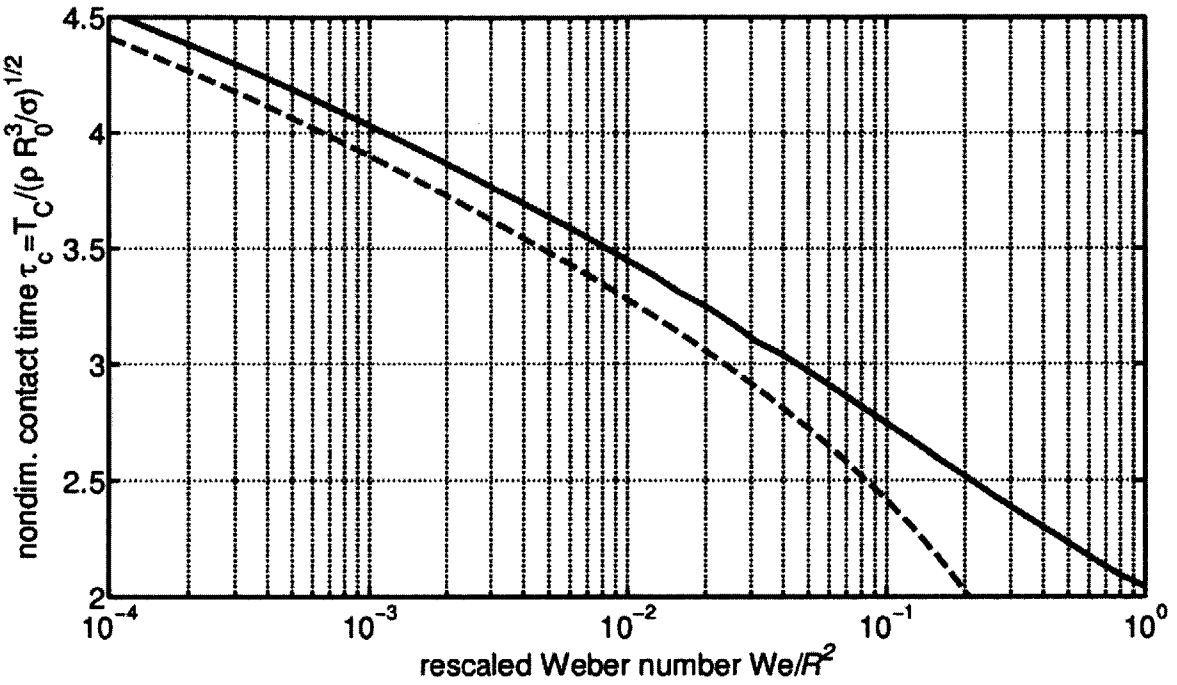

Figure 2-7: The dependence of the nondimensional contact time $\tau_c = T_C\,(\sigma/\rho R_0^3)^{1/2}$ on the rescaled Weber number $We/\mathcal{R}^2 = \rho R_0 V_{in}^2/\sigma(1 - R_0/R_2)^2$. Results of the numerical model (2.42) for several values ($0.1 \leq \mathcal{R} \leq 10$) of the curvature parameter $\mathcal{R} = 1 - R_0/R_2$ follow a single curve (*solid line*). The analytic expression (2.43) (*dashed line*) is shown for the sake of comparison.

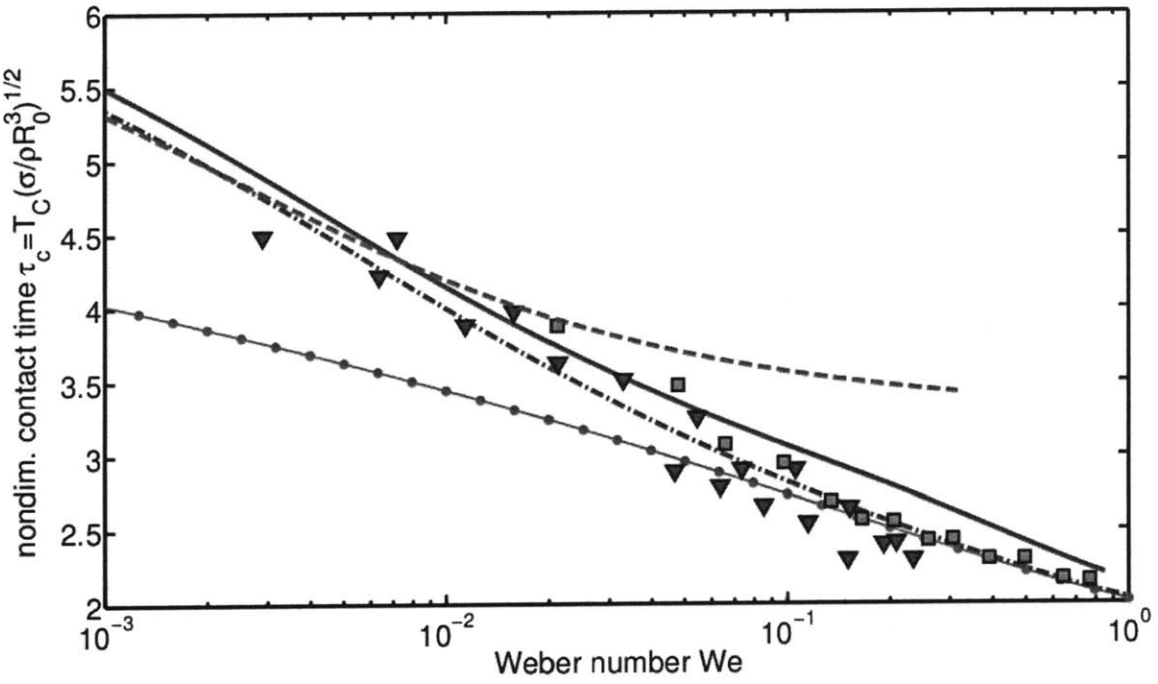

Figure 2-8: The effects of gravity on the nondimensional contact time $\tau_C = T_C\sqrt{\frac{\sigma}{\rho R_0^3}}$ as a function of the Weber number $\mathcal{W}e = \rho R_0 V_{in}^2/\sigma$. The results of the numerical model (2.42) (*dash-dot line*), quasi-static model (2.38) (*solid line*) and the analytical expression (2.44) (*dashed line*), all for $\mathcal{B}o = 0.05$ are plotted, together with the experimental results of Okumura *et al*, for $\mathcal{B}o = 0.02$ (▼) and $\mathcal{B}o = 0.05$ (■). For reference, the result of the numerical model (2.42) for $\mathcal{B}o = 0$ (i.e. no gravity) is also shown (•).

2.4.2 Coefficient of restitution

The quasi-static model (2.38) provides a fast way of estimating the coefficient of restitution. The velocity of the droplet center of mass can be obtained from (2.38) and (2.39) as $b_1'(B)\dot{B}$, giving

$$C_R = \frac{b_1'(B(\tau_c))\dot{B}(\tau_c)}{b_1'(B(0))\dot{B}(0)} \quad , \tag{2.45}$$

where τ_c is the contact time. The dependence of C_R on Ohnesorge number, Weber number and Bond number for a flat surface ($\mathcal{R} = 0$) is shown in Fig. 2-9. In order to check the accuracy of the quasi-static model, we include the results of the full numerical model (2.42). As expected, C_R decreases uniformly with increasing viscosity. Nevertheless, as $\mathcal{O}h \to 0$, it does not approach 1, but a somewhat smaller value due to a transfer of the kinetic energy into the vibrational modes, as observed by Richard & Quéré. This transfer cannot be captured by the quasi-static model and therefore the model overestimates C_R for low $\mathcal{O}h$ and high $\mathcal{W}e$. The match improves with decreasing $\mathcal{W}e$ and increasing viscosity. In absence of gravity, C_R uniformly increases with decreasing Weber number, but when $\mathcal{B}o > 0$, it reaches a peak and then sharply drops to zero near $\mathcal{W}e \approx \mathcal{B}o \cdot \mathcal{O}h$ as the drop fails to detach. Both of these phenomena are captured well by our model.

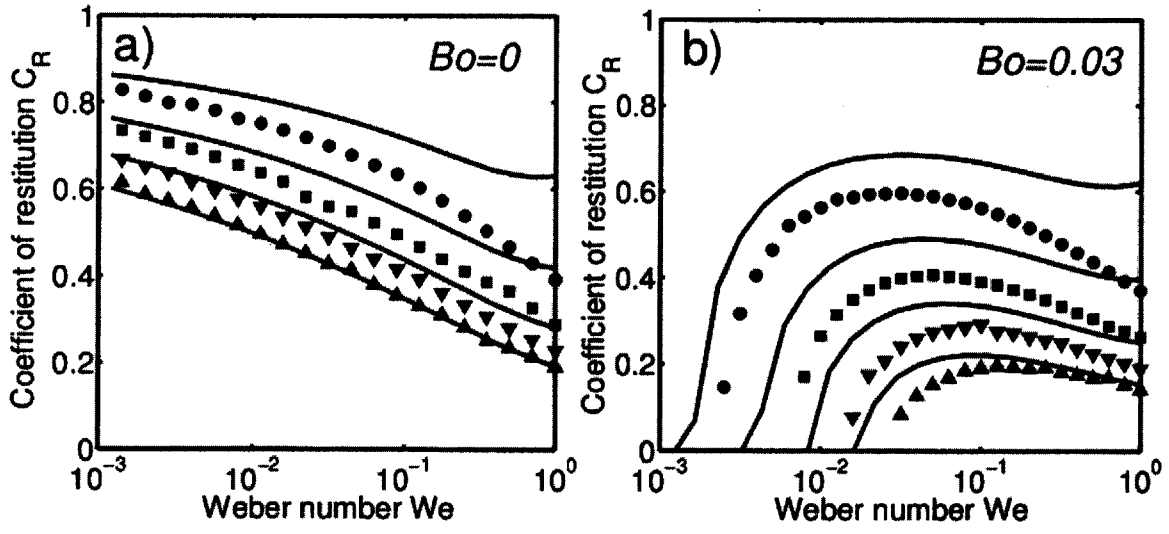

Figure 2-9: The dependence of the coefficient of restitution C_R on the Weber number $\mathcal{W}e = \rho R_0 V_{in}^2/\sigma$ with (a) and without (b) gravity, for a drop impacting a flat substrate ($\mathcal{R} = 1$). Results of the quasi-static model (2.38) (*solid lines*) and the full numerical model (2.42) (*points*) are shown for four values of the Ohnesorge number $\mathcal{O}h = \mu/\sqrt{\rho\sigma R_0}$: $\mathcal{O}h = 0.1$ (•), $\mathcal{O}h = 0.2$ (■), $\mathcal{O}h = 0.3$ (▼) and $\mathcal{O}h = 0.4$ (▲).

2.5 Discussion

We have presented a conceptually simple theoretical model for the dynamics of a drop impacting a rigid substrate, which is valid when the drop deformation remains small and the effects of contact line dynamics and dissipation in the surrounding gas can be neglected. It has allowed us to characterize the effects of both the Weber number and substrate curvature on the dynamics. The form of the equation of motion suggests that in the small deformation limit these two effects are captured by a single nondimensional group - square root of the rescaled Weber number $We^{1/2}/\mathcal{R}$, where $\mathcal{R} = 1 - R_0/R_2$, which is proportional to the ratio of the maximum contact area to the drop's total area. When $We^{1/2}/\mathcal{R} < 0.3$, the dynamics can be approximated by a simple differential equation (2.40), which can be interpreted as a logarithmic spring. The model reproduces all the qualitative features of the drop dynamics and is in good quantitative agreement (within 10%) with previously reported experiments and numerical results when $We^{1/2}/\mathcal{R} < 0.1$. It removes the need to deal with the complicated interaction between the drop and the impacted substrate considered in the usual numerical simulations, and is very fast to solve numerically. The relatively simple form of the equation of motion (2.40) also allows analytical treatment in the $We^{1/2}/\mathcal{R} \ll 1$ limit.

Both the coefficient of restitution and the contact time of the impacting drop increase with decreasing rescaled Weber number. For a fixed impact speed, the rescaled Weber number is reduced by decreasing the radius of curvature of the substrate. We note that the wettability of the surface will in general depend not only on the rescaled Weber number through its influence on the impact dynamics, but also on the surface microsctructure and its influence on the sustenance of the lubricating air layer. The spacing and shape of the microstructure for optimal water-repellency has been considered in the context of static drops [89, 86, 102, 57]. An equivalent study of optimal water-repellent design in this dynamic setting, wherein both micro- and macrostructure are important, is left for future consideration.

Approximating the shape of a deformable substrate by its quasi-static shape would presumable allow one to extend the quasi-static model presented here to a more general scenario of liquid drops impacting a liquid bath. Such a model would prove useful in rationalizing the coalescence criteria for impacting liquid drops [18] and the phase diagrams of drops bouncing on a vertically vibrated liquid bath [33, 98]. The development of such a model will be the subject of the next chapter.

Chapter 3

Drops Bouncing on a Liquid Bath

3.1 Background

In this chapter, we generalize the model developed in Chapter 2 to impacts on a fluid bath, again considering relatively low energy impacts in which both the droplet and bath are only weakly distorted.

The dynamics of the drop impact depends in general on the drop inertia, surface tension, viscous forces within the drop, bath and surrounding air, and gravity. Restricting attention to the case of a drop's normal impact on a quiescent bath of the same liquid reduces the number of relevant physical variables to 6: the gravitational acceleration g, the droplet radius R_0 and impact speed V_{in}, the liquid density ρ, dynamic viscosity μ and surface tension σ (see Table 3.1). These give rise to three dimensionless groups. The Weber number $We = \rho R_0 V_{in}^2/\sigma$, Bond number $Bo = \rho g R_0^2/\sigma$ and Ohnesorge number $Oh = \mu\left(\sigma\rho R_0\right)^{-1/2}$ prescribe the relative magnitudes of, respectively, inertial and gravitational pressure and viscous stresses to curvature pressures associated with surface tension (see Table 3.1 for a summary of our notation). Considering the effects of the surrounding gas on the drop dynamics requires the inclusion of two more physical variables, the gas density ρ_g and gas viscosity μ_g, that require in turn two additional dimensionless groups, ρ_g/ρ and $Oh_g = \mu_g\left(\sigma\rho R_0\right)^{-1/2}$. For the parameter range of interest in our study, $\rho_g/\rho \ll 1$ and $Oh_g \ll Oh$. Thus, beyond providing the lubrication layer between drop and bath that allows the bouncing states, the influence of air on the dynamics is negligible. When the bath is shaken vertically, two additional parameters enter into the dynamics, the frequency f and peak acceleration γ of the bath vibration. These give rise to two new dimensionless groups, the first being the dimensionless bath acceleration $\Gamma = \gamma/g$, the second being the ratio of the driving angular frequency $\omega = 2\pi f$ and

the characteristic drop oscillation frequency $\omega_D = (\sigma/\rho R_0^3)^{1/2}$ [103]. We call this ratio the *vibration number* $\Omega = \omega/\omega_D$.

At low forcing amplitude, the drop comes to rest on the vibrating bath, oscillating with the driving frequency while the air layer drains beneath it. Once the thickness decreases below the range of molecular forces, the two interfaces connect and the drop is absorbed into the bath. When the driving acceleration reaches a value corresponding to the bouncing threshold, the bath can transfer enough momentum during impact to compensate for the energy lost; consequently, the drop can be sustained indefinitely in a periodic bouncing motion [124]. In this bouncing regime, the drop and the bath never come into contact, which would lead to coalescence; instead, they remain separated by an air layer that is replenished after each collision [18]. We note that there is also a strict upper bound on the bath acceleration that will permit stable bouncing states: beyond a critical value γ_F, known as the Faraday threshold, the entire bath surface becomes unstable to a standing field of Faraday waves with frequency $f/2$ [38, 4]. For a theory describing the dependence of the Faraday threshold on viscosity, see Kumar [69]. All experiments reported here were performed below the Faraday threshold.

As the amplitude of the bath oscillation is increased beyond the bouncing threshold, the drop's periodic bouncing may become unstable and undergo a period-doubling cascade leading to a chaotic vertical motion, a feature common to systems involving bouncing on vibrating substrates. The most commonly studied scenario, first proposed by Fermi [39] as a model of cosmic rays, is the dynamics of a ball bouncing on a vibrating rigid surface [90, 91, 37, 73, 21], one of the simplest systems that exhibits a transition to chaos via a period-doubling cascade. A simple theoretical model thereof considers an elastic ball with coefficient of restitution equal to 1 and zero contact time (that is, instantaneous rebound) bouncing on a flat, horizontal rigid plate vibrating vertically in a uniform gravitational field. Between this idealized scenario and that considered in this chapter are various intermediate cases possessing some but not all of the complications of the bouncing drop problem of interest.

Luck & Mehta [72] considered a bouncing ball with finite coefficient of restitution C_R, and derived analytic expressions for the regions where the ball bounces with a simple period. In general, when $C_R < 1$, the trajectories were found to be periodic, owing to the existence of locking regions, where the ball performs an infinite series of ever-decreasing jumps until the information concerning its initial conditions is lost. Mehta *et al.* [74] and Gilet *et al.* [49] considered the dynamics of a completely inelastic bouncing ball, Naylor *et al.* [82] examined the role of air drag on the bouncing ball

dynamics, Wright *et al.* [130] examined the role of the surface curvature, and Dorbolo *et al.* [26] considered two connected balls. The dynamics of a drop bouncing on a highly viscous liquid bath have been examined by Terwagne *et al.* [117], and that of a rigid ball bouncing on an vibrated elastic membrane by Eichwald *et al.* [35]. Gilet & Bush [45, 46] examined the dynamics of a liquid drop bouncing on a soap film and noted the coexistence of multiple bouncing states for a given set of system parameters, an effect to arise also in our system.

For drops within a certain size range, the interplay between the drop and the waves it excites on the liquid surface causes the vertical bouncing to become unstable; as a result, the drop begins to move horizontally, an effect first reported by Couder *et al.* [19]. As the bath acceleration approaches the Faraday threshold from below, the decay rate of the surface waves created by the drop impacts is reduced and a particular wavelength is selected, corresponding to the most unstable Faraday wavenumber. Interaction of walking drops and the surface waves reflected from the boundaries [16, 30] or from other drops [100, 98, 97, 29, 28, 32, 43, 99] leads to a variety of interesting phenomena reminiscent of quantum mechanics [6]. Examples include tunneling across a sub-surface barrier [30], single-particle diffraction in both single- and double-slit geometries [16], quantized orbits analogous to Landau levels in quantum mechanics [43], and orbital level splitting [31]. Harris *et al.* [59] considered a drop walking in confined geometries, and demonstrated that the resulting probability distribution function is simply related to the most unstable Faraday wave mode of the cavity. Rationalizing these remarkable macroscopic quantum-like phenomena provided the motivation for this study. In the next chapter, we shall focus on the dynamics of the walking drops. Our studies will make clear that in order to understand the role of drop size and driving frequency on the horizontal dynamics, a model of both the vertical and horizontal drop motion is required. The former will be developed herein.

Gilet & Bush [46] demonstrated that for the case of a drop bouncing on a soap film, the surface energy of the film increases quadratically with the drop's penetration depth and thus the film's effect on the drop is analogous to that of a linear spring with a spring constant proportional to the surface tension. When a drop impacts a rigid surface, one can approximate the drop's shape by its first two spherical harmonics, leading to a linear dependence of reaction force on the deformation amplitude and of the viscous drag on the speed of the drop's centre of mass [84]. Thus, the interactions in these two disparate systems can both be modeled in terms of a damped linear spring. To model drop impact on a liquid bath, Terwagne [116] augmented the model of Okumura *et al.* [84] by adding a second spring that captures the role of surface

energy stored in the bath deformation. Such linear spring models break down when the inertial stresses become comparable to the surface tension ($We \gtrsim 1$), or when the surface deformation ceases to be small relative to the drop radius. The range of Weber numbers encountered in the current study extends beyond 1, motivating the introduction of a more complex model.

Protière *et al.* [98] were the first to publish a regime diagram indicating the behaviour of liquid drops bouncing on a liquid bath (specifically, 20 cS silicone oil), followed by Eddi *et al.* [33] who used 50 cS oil. We here extend their measurements, covering a wider range of drop size and driving frequencies, in order to have a firmer experimental basis for building our theoretical model of the drop dynamics. The goal of this chapter is to rationalize the regime diagrams for the vertical motion of the bouncing drops, such as that shown in Fig. 3-3. In addition to providing a consistent means by which to describe the vertical dynamics, the model presented here will provide a crucial prerequisite to rationalizing the drop's horizontal motion, which will be the subject of the next chapter.

In §3.2 we describe our experimental arrangement and present our data on the transitions between different vertical bouncing states. In §3.3 we develop a theoretical description of the vertical dynamics of drops bouncing on a vertically vibrated bath. We first consider a linear spring model, and examine its range of validity and shortcomings, which motivate the development of a "logarithmic spring" model in §3.3.2. The logarithmic spring model best rationalizes the experimentally measured regime diagrams; moreover, it reproduces the observed dependence of the coefficient of restitution and contact time on the Weber number. Future directions are outlined in §3.4.

3.2 Experiments

In order to extend the data set reported by Protière *et al.* [98] and Eddi *et al.* [33], we have recorded the behaviour of droplets of silicone oil of viscosity 20 and 50 cS over a wide range of drop sizes and driving frequencies. A schematic illustration of the experimental apparatus is shown in Fig. 3-1. A liquid drop of undeformed radius R_0 bounces on a bath of the same liquid (Fig. 3-2), in our case silicone oil with density $\rho = 949$ kg·m^{-3}, surface tension $\sigma = 20.6 \cdot 10^{-3}$ N/m and kinematic viscosity $\nu = 20$ cS, or a more viscous silicone oil with $\rho = 960$ kg·m^{-3}, $\sigma = 20.8 \cdot 10^{-3}$ N/m and $\nu = 50$ cS. The bath, of depth $h_B \approx 9$ mm, is enclosed in a cylindrical container with diameter $D = 76$ mm. The container is shaken vertically, sinusoidally in time, with

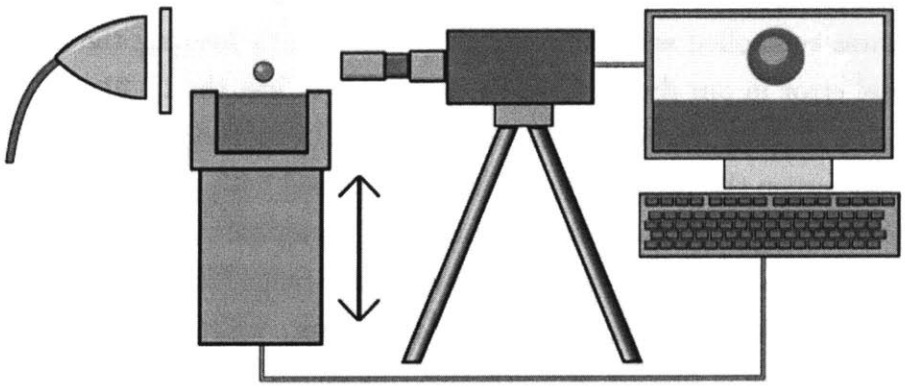

Figure 3-1: A schematic illustration of the experimental set-up. A liquid drop bounces on a liquid bath enclosed in a circular container shaken vertically. The drop is illuminated by a strong LED lamp through a diffuser, and its motion recorded by a high-speed camera that can be synchronized with the shaker.

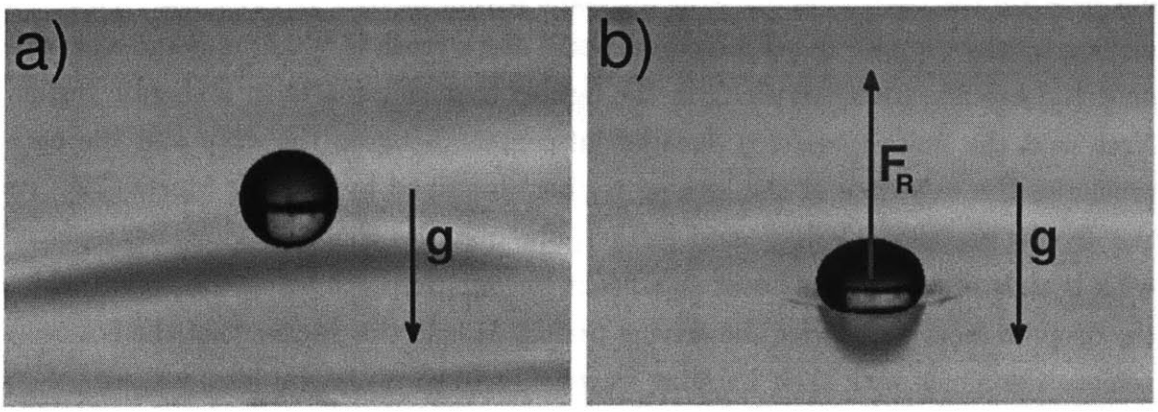

Figure 3-2: A droplet of radius $R_0 = 0.38$mm **(a)** in flight and **(b)** during contact with the bath. The drop motion is determined by the gravitational force $\boldsymbol{g}$ and the reaction force $\boldsymbol{F_R}$ generated during impact.

peak acceleration γ and frequency f, so that the effective gravity in the bath frame of reference is $g + \gamma \sin(2\pi f t)$.

The motion of the drop was observed using a high-speed camera synchronized with the shaker. The camera resolution is 86 px/mm and the distance of the drop from the camera was controlled with approximately 1% error by keeping the drop in focus, giving a total error in our drop radius measurement of less than 0.01mm. The drops were created by dipping a needle in the bath followed by its fast retraction. In order to systematically sweep the range of drop radii, we started with a drop at the lower end of the spectrum (radius of roughly 0.1 mm), and repeatedly enlarged it by merging it with other small drops. We limit ourselves to the range 0.07 mm$< R_0 <$ 0.8 mm, since larger drops do not exhibit any novel behaviour, while smaller drops tend to coalesce for the range of driving accelerations considered ($0 < \gamma < 7g$). The notation adopted in this chapter together with the range of physical variables considered are defined in Table 3.1.

3.2.1 Regime Diagrams

A typical regime diagram is shown in Fig. 3-3, where we adopt the nomenclature used by Protière *et al.* [98]. For a droplet of fixed size, below a certain driving acceleration γ_B, the vibrating bath is unable to compensate for the drop's loss of mechanical energy during impact, and the droplet coalesces after a series of increasingly small jumps. For $\gamma > \gamma_B$, the drop bounces with the same period as that of the bath. When the driving acceleration is further increased, small drops (with $\Omega \lesssim 0.6$) undergo a period-doubling cascade (denoted *PDC* in the figure) that culminates in a chaotic region. Note that the finite (nonzero) duration of contact between the drop and the bath precludes the existence of the locking regions described by Luck & Mehta [72]. As the driving amplitude is increased further, one observes chaotic regions interspersed with islands of periodicity, most significant for our purposes being the region where the drop bounces with twice the driving period. It is in this regime that the bouncers achieve resonance with their Faraday wavefield and so transform into walkers.

Compared to the previously published regime diagrams [98, 33], our data offer the first insight into the behaviour of the threshold curves for small drop sizes. The bouncing and period-doubling threshold curves are not nearly vertical for small drops, as previously suggested, but in fact curve towards higher values of Γ as $R_0 \to 0$. Other novel features are the discontinuity of the bouncing threshold curve at $R_0 = 0.25$mm and the realization that the region between the first and second period-doubling

Symbol	Meaning	Typical value	
R_0	drop radius	$0.07 - 0.8$	mm
ρ	silicone oil density	$949 - 960$	kg/m^3
ρ_a	air density	1.2	kg/m^3
σ	drop surface tension	$20 - 21$	mN/m
g	gravitational acceleration	9.81	m/s^2
V_{in}	drop incoming speed	$0.1 - 1$	m/s
V_{out}	drop outgoing speed	$0.01 - 1$	m/s
μ	drop dynamic viscosity	$10^{-3} - 10^{-1}$	kg/(m·s)
μ_a	air dynamic viscosity	$1.84 \cdot 10^{-5}$	kg/(m·s)
ν	drop kinematic viscosity	$10 - 100$	cS
ν_a	air kinematic viscosity	15	cS
T_C	contact time	$1 - 20$	ms
C_R	$= V_{in}/V_{out}$ coefficient of restitution	$0 - 0.4$	
f	bath shaking frequency	$40 - 200$	Hz
γ	peak bath acceleration	$0 - 70$	m/s^2
ω	$= 2\pi f$ bath angular frequency	$250 - 1250$	rad·s$^-$1
ω_D	$= (\sigma/\rho R_0^3)^{1/2}$ charact. drop oscillation freq.	$300 - 5000$	s^{-1}
$\mathcal{W}e$	$= \rho R_0 V_{in}^2/\sigma$ Weber number	$0.01 - 1$	
$\mathcal{B}o$	$= \rho g R_0^2/\sigma$ Bond number	$10^{-3} - 0.4$	
$\mathcal{O}h$	$= \mu\,(\sigma\rho R_0)^{-1/2}$ drop Ohnesorge number	$0.004 - 2$	
$\mathcal{O}h_a$	$= \mu_a\,(\sigma\rho R_0)^{-1/2}$ air Ohnesorge number	$10^{-4} - 10^{-3}$	
Ω	$= 2\pi f\sqrt{\rho R_0^3/\sigma}$ vibration number	$0 - 1.4$	
Γ	$= \gamma/g$ peak nondim. bath acceleration	$0 - 7$	

Table 3.1: List of symbols used together with the typical values encountered in our experiments, as well as those reported by Eddi *et al.* [32] and Protière *et al.* [98].

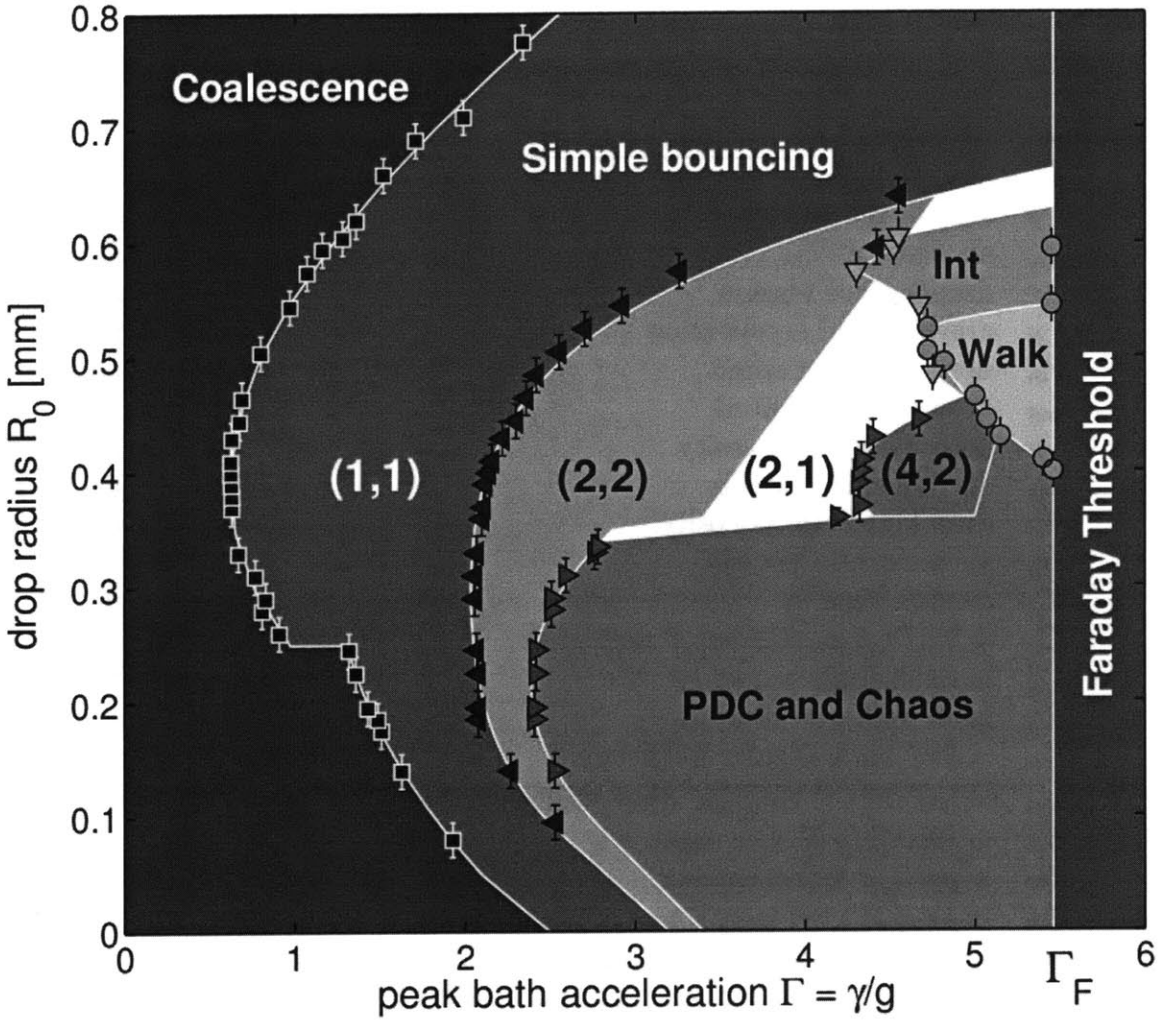

Figure 3-3: Regime diagram describing the motion of a silicone oil droplet of viscosity 50 cS on a bath of the same fluid vibrating with frequency 60Hz. The horizontal axis is the dimensionless peak acceleration of the bath $\Gamma = \gamma/g$, while the vertical axis is the drop radius. The bath surface becomes unstable when Γ exceeds the Faraday threshold $\Gamma_F = 5.46$ (vertical line). Only the major dynamical regimes are shown: *PDC* signifies the period-doubling cascade, *Int* the region of intermittent horizontal movement and *Walk* the walking regime. Lines indicate best fits to threshold curves.

transitions contains both the $(2,2)$ and the $(2,1)$ modes.

Following Gilet & Bush [46], we adopt the (m,n) notation to distinguish between different bouncing modes. In the (m,n) mode, the drop's vertical motion has period equal to m driving periods, and within this period the drop contacts the bath n times. By *contact* we refer to that part of the drop's motion when the drop and bath are being deformed and the air pressure beneath the drop is significantly elevated above that of the ambient air. We stress that the drop and the bath always remain separated by an intervening air layer and thus never actually come into contact. Provided the rebound time is shorter than the time required for the intervening layer to thin below a certain critical thickness, the drop will detach without coalescing. The chaotic region is thus difficult to observe experimentally for small drops (i.e. $\Omega \lesssim 0.6$): once the bouncing becomes chaotic, the drop will eventually undergo a chattering sequence and coalesce.

An interesting feature of the system is that there can be more than one stable bouncing mode for a given combination of drop size and driving [118]. Indeed, several stable periodic motions may coexist, corresponding to the same mode (m,n) but having different average mechanical energy (see Figs. 3-4, 3-16 and 3-17) and average contact time. In order to distinguish between different bouncing states with the same mode number (m,n), we denote them by $(m,n)^p$. $(m,n)^1$ signifies the motion with the least average energy (corresponding usually to the longest average contact time) and the p-index increases with increasing average energy. Larger drops do not undergo a full period-doubling cascade (refer to Fig. 3-3): after transitioning from the $(1,1)$ mode to the $(2,2)$ mode, further increase of γ leads to increasing disparity between the large and small jumps, until the smaller jump disappears completely. Thus the drop transitions from the $(2,2)$ mode into the $(2,1)$ mode. This mode then undergoes a period-doubling cascade and only then enters a chaotic regime. Near the Faraday threshold (as occurs at $\Gamma = 5.46$ for 50 cS oil at $f = 60$ Hz), the interaction between the drop and the slowly decaying standing waves created by its previous impacts may lead either to walking or to an intermittent behaviour (denoted *Int* in Fig. 3-3), where the drop performs a complicated aperiodic horizontal motion and does not settle into a steady walking state.

In Fig. 3-4, we show the vertical motion of 50 cS silicone oil droplets for several driving accelerations over the course of 5 driving periods. We show the 5 most prevalent modes, specifically, the $(1,1)^1$, $(1,1)^2$, $(2,2)$, $(2,1)^1$ and $(2,1)^2$ modes, that emerge as the driving acceleration is increased progressively. Note that the amplitude of the drop's motion increases with driving acceleration. The motion of the bath

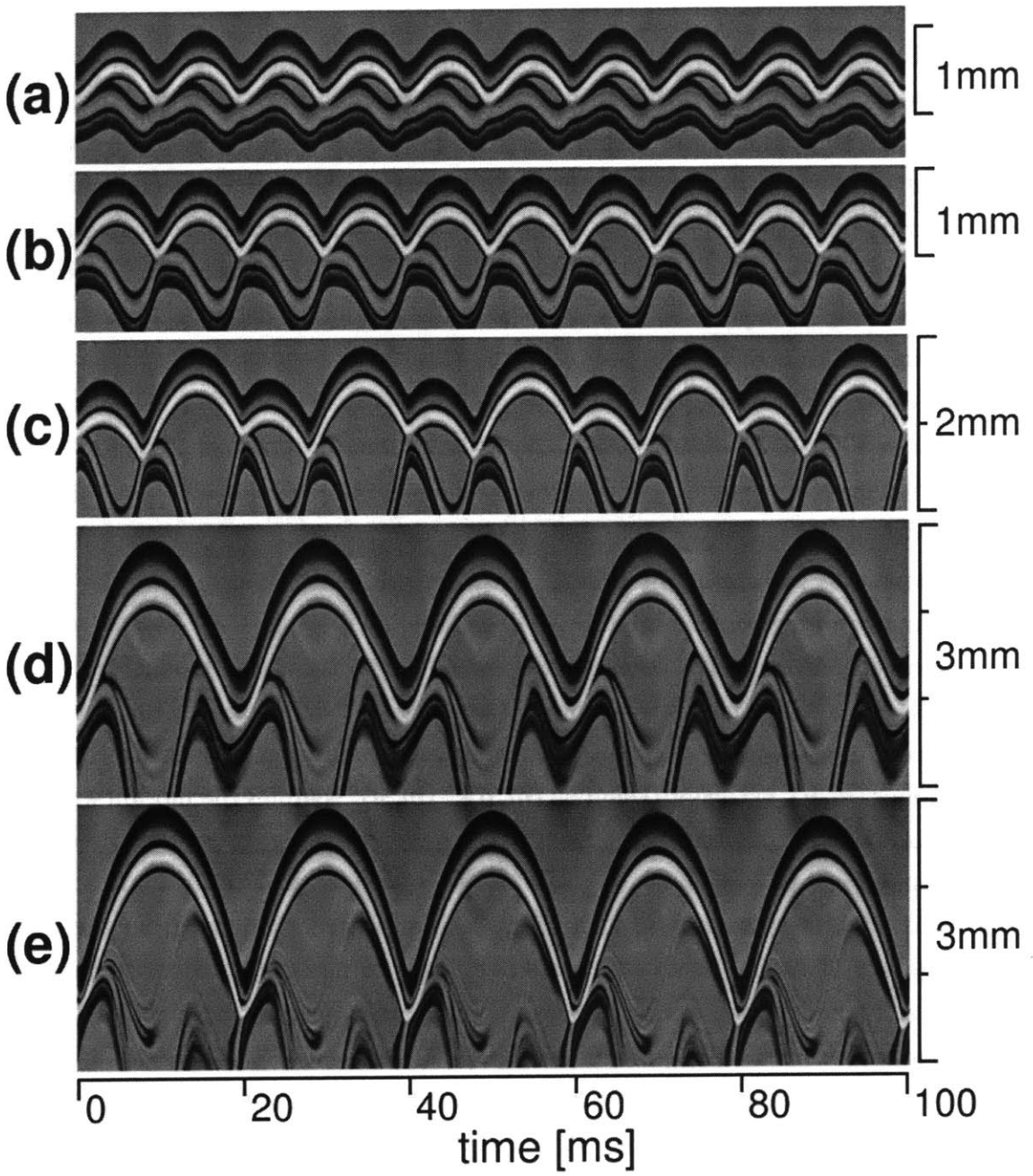

Figure 3-4: The simplest modes of vertical motion for 50 cS silicone oil drops bouncing on a liquid bath vibrating with frequency 50 Hz. These are, in order of increasing dimensionless forcing $\Gamma = \gamma/g$: **(a)** the $(1,1)^1$ mode, $\Gamma = 1.3$; **(b)** the $(1,1)^2$ mode, $\Gamma = 1.4$; **(c)** the $(2,2)^2$ mode, $\Gamma = 2.35$; **(d)** the $(2,1)^1$ mode, $\Gamma = 3.6$ and **(e)** the $(2,1)^2$ mode, $\Gamma = 4.1$. The drop radii are $R_0 = 0.28$mm in **(a-c)** and $R_0 = 0.39$mm in **(d-e)**. The images were obtained by joining together vertical sections from successive video frames, each one 1 pixel wide and passing through the drop's centre. The camera was recording at 4000 fps. Note that in both the $(2,1)$ modes shown **(d-e)**, the drop was walking.

surface cannot be directly observed in Fig. 3-4 due to the nature of the illumination; nevertheless, one can determine the contact time from the relative positions of the drop and its reflection in the bath.

We measured the bouncing threshold and the first two period-doubling thresholds of silicone oil droplets with $\nu = 20$ cS and 40 Hz $\leq f \leq$ 200 Hz, and with $\nu = 50$ cS and 60 Hz $\leq f \leq$ 100 Hz. The results are shown in Figs. 3-5-3-8. In Fig. 3-5, the bouncing threshold $\Gamma_B = \gamma_B(R_0, f, \nu)/g$, the minimum driving acceleration needed to prevent the drop from coalescing, is shown as a function of the drop size (*vertical axis*). We observe that the size of the drop that attains a bouncing state at the lowest Γ decreases with increasing frequency, while the minimum of Γ_B remains roughly constant. One expects that the minimum of Γ_B corresponds to the drop size for which the driving frequency equals the resonant frequency of the drop-bath system, with a shift due to the effects of viscosity. Using the vibration number $\Omega = \omega/\omega_D$ instead of R_0 on the vertical axis, we see that the data for different frequencies nearly collapse onto a single curve (Fig. 3-6). Henceforth, we shall use Ω in order to display data for different frequencies in a single diagram.

In Fig. 3-6, we observe that the minimum of Γ_B occurs at $\Omega \approx 0.65$ for both viscosities, which corresponds to $R_0 \approx 0.47\,(\sigma/\rho f^2)^{1/3}$. We note that the minimum of Γ_B does depend weakly on the driving frequency (Fig. 3-6b): at higher frequencies, the typical drop radius near the minimum is smaller and the increasing influence of air drag and dissipation in the intervening air layer results in a shift of the bouncing threshold curve towards higher driving amplitudes (e.g. $f = 200$ Hz in Fig. 3-6). On the other hand, at lower frequencies the typical drop radius near the minimum is larger and a relatively large portion of the mechanical energy is lost to the outgoing surface waves created by the drop motion. Thus there is an optimal frequency, in our case $f = 80$ Hz, for which the sum of these two effects is minimized and the global minimum of Γ_B is achieved. We observe $\Gamma_B \geq 0.47$ for $\nu = 20$ cS and $\Gamma_B \geq 0.59$ for $\nu = 50$ cS.

In Figs. 3-6b and 3-7, we see that the bouncing curves exhibit a discontinuity at approximately $\Omega = 0.2 - 0.4$. This discontinuity arises because smaller droplets can only exist in the higher energy $(1,1)^2$ mode and coalesce when this mode can no longer be sustained by the bath vibration. Larger drops can persist in the lower energy $(1,1)^1$ mode without coalescing because the intervening air layer takes a relatively long time to drain. Although determining the exact form of the bouncing threshold curve theoretically would require a detailed analysis of the intervening air layer dynamics [60, 62, 68], we will demonstrate in §3.3 that the majority of the bouncing threshold

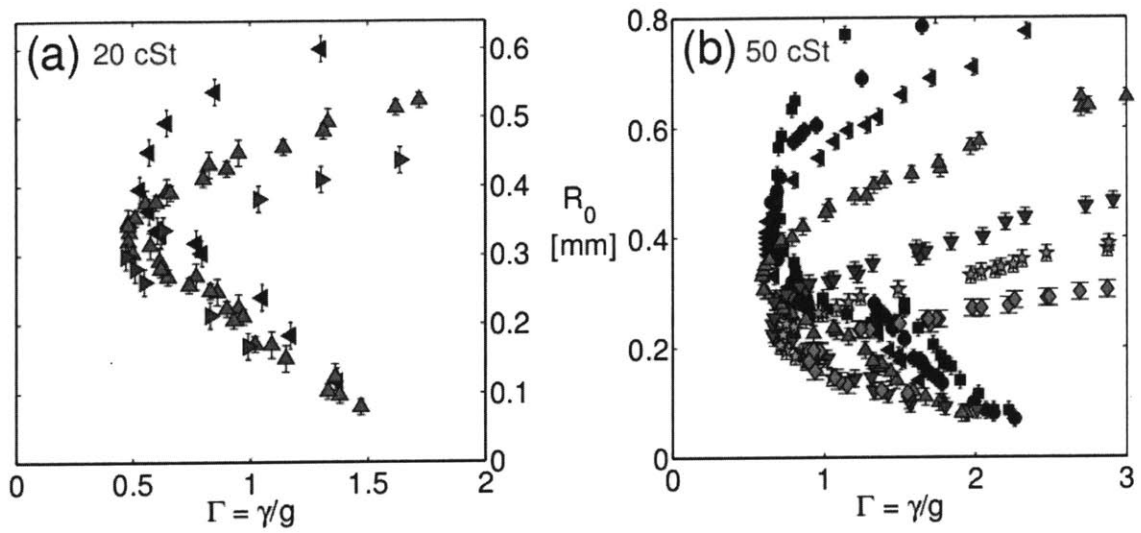

Figure 3-5: Bouncing thresholds measured for silicone oil droplets of viscosity **(a)** 20 cS and **(b)** 50 cS on a vibrating bath of the same oil. The minimum driving acceleration $\Gamma = \gamma/g$ (horizontal axis) required for sustained bouncing is shown as a function of the drop radius R_0 (vertical axis). Experimental results are shown for several driving frequencies f: 40 Hz (■), 50 Hz (•), 60 Hz (◄), 80 Hz (▲), 100 Hz (►), 120 Hz (▼), 150 Hz (★) and 200 Hz (♦).

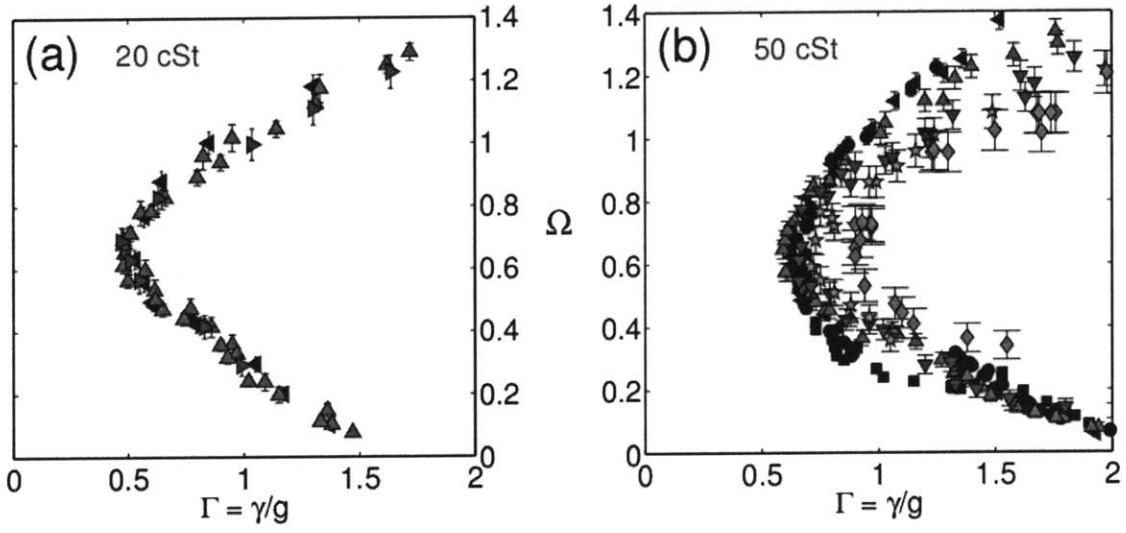

Figure 3-6: Bouncing thresholds. The same experimental data shown in Fig.3-5 is now plotted as a function of the vibration number $\Omega = \omega/\omega_D$ (vertical axis) instead of drop diameter R_0. Data for different frequencies collapse nearly onto a single curve.

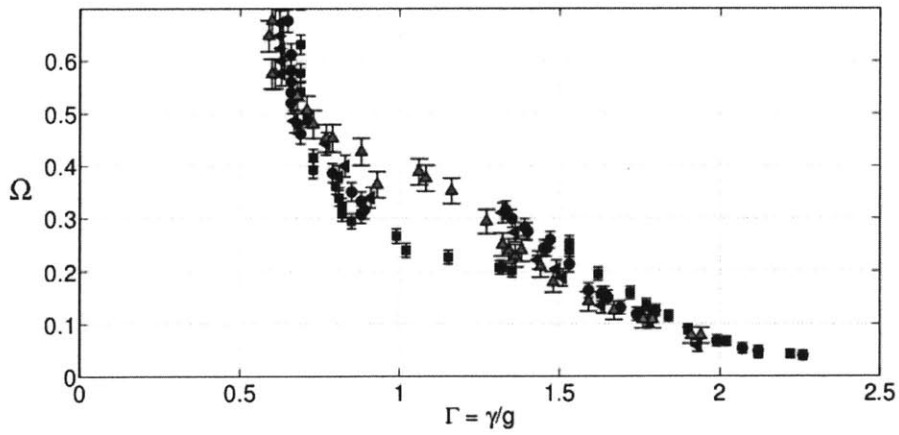

Figure 3-7: Detail of Fig. 3-6 showing the bouncing thresholds for silicone oil droplets of viscosity 50 cS on a vibrating bath of the same oil. The minimum driving acceleration $\Gamma = \gamma/g$ (horizontal axis) needed to prevent the drop from coalescing with the bath is shown as a function of the vibration number $\Omega = \omega/\omega_D$ (vertical axis). Experimental results are shown for several driving frequencies f: 40 Hz (■), 50 Hz (•), 60 Hz (◀), 80 Hz (▲). The discontinuity of the bouncing thresholds between $\Gamma = 1$ and $\Gamma = 1.2$ is clearly apparent.

curve runs along a mode threshold obtainable by relatively simple means.

Fig. 3-8 shows the first two period-doubling thresholds. Smaller drops ($\Omega < 0.6$) undergo a period-doubling cascade, so the first two thresholds correspond to $(1,1) \rightarrow (2,2)$ and $(2,2) \rightarrow (4,4)$ transitions. Larger drops ($\Omega > 0.6$) transition from $(1,1)$ to $(2,2)$, then reduce the amplitude of their smaller bounce until a simple period-doubled bouncing mode $(2,1)$ is reached, and only then commence the period-doubling cascade $(2,1) \rightarrow (4,2) \rightarrow (8,4) \rightarrow \ldots$. Note that the low frequency curves are shifted to the right of their high frequency counterparts (60 Hz curve for 20 cS; $50 - 60$ Hz for 50 cS), an effect due to the influence of the standing waves created on the bath by previous drop impacts. At lower frequencies, the Faraday threshold is closer to the period-doubling threshold; thus, the drop impacts create more slowly decaying standing waves on the bath surface. By reducing the relative speed between the drop and bath at impact, the standing waves appear to stabilize the vertical motion, and so delay the period-doubling transitions.

The bounds of the frequency range explored were prescribed by experimental constraints. The presence of the Faraday threshold provides a lower limit on the range of frequencies over which the period-doubled modes can arise. For example, for 20 cS silicone oil, period-doubling occurs only for $\Gamma > 1.58$ (Fig. 3-8), while $\Gamma_F < 1.58$ for $f \leq 45$ Hz. Thus, for $f \leq 45$ Hz, the period-doubling transitions disappear. The

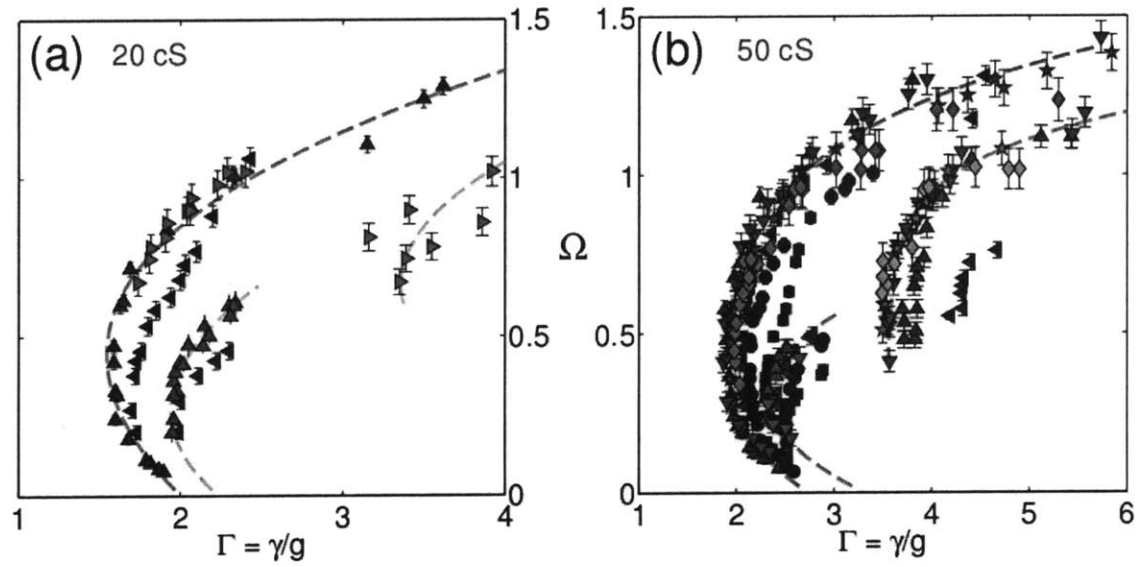

Figure 3-8: First two period-doubling thresholds for silicone oil droplets of viscosity **(a)** 20 cS and **(b)** 50 cS on a vibrating bath of the same oil. For smaller droplets ($\Omega < 0.6$) these are $(1,1) \rightarrow (2,2)$ and $(2,2) \rightarrow (4,4)$ transitions, while for larger drops ($\Omega > 0.6$) they are $(1,1) \rightarrow (2,2)$ and $(2,1) \rightarrow (4,2)$ transitions. The experimentally measured threshold acceleration $\Gamma = \gamma/g$ (horizontal axis) is shown as a function of the vibration number $\Omega = \omega/\omega_D$ (vertical axis) for several driving frequencies: $f = 40$ Hz (■), 50 Hz (•), 60 Hz (◄), 80 Hz (▲), 100 Hz (►), 120 Hz (▼), 150 Hz (★) and 200 Hz (♦) .

upper limit on the frequency range is imposed by the finite resolution of our camera. Since the walking region of ultimate interest is given by $\Omega = 2\pi f\sqrt{\rho R_0^3/\sigma} \lesssim 1.5$ (see the next chapter), the typical size of a walker $R_0 \sim f^{-2/3}$. Thus, for higher frequencies, the constant error in drop size measurement leads to increasing relative error in Ω. Similarly, at high frequency, it becomes increasingly difficult to distinguish between the different bouncing modes, as the motion itself happens over a distance of at most $g(T/2)^2/2 \leq gf^{-2}/2$, which is of order 0.1mm for $f = 200$ Hz.

3.3 Vertical dynamics

3.3.1 Linear spring model

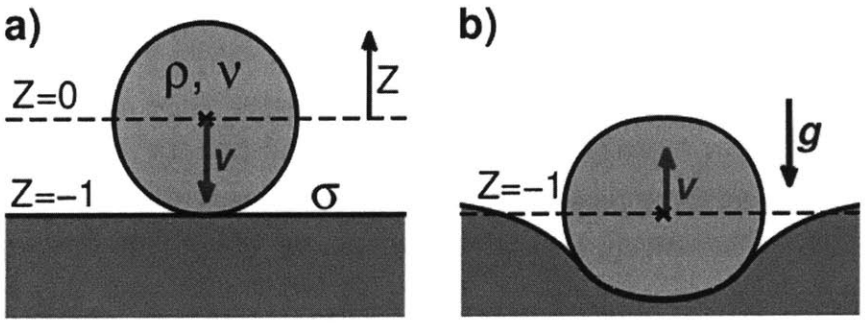

Figure 3-9: A schematic illustration of our choice of coordinates. The vertical position of the drop's centre of mass Z is equal to 0 at the initiation of impact **(a)**, and would be -1 if it reached the equilibrium level of the bath **(b)**.

We proceed by describing the simplest model of the drop's vertical dynamics, analogous to works by Okumura *et al.* [84], Gilet & Bush [46] and Terwagne [116], in which the drop-impactor interaction is described in terms of a linear spring. We nondimensionalize the vertical displacement of the drop by its radius (see Table 3.2 for a list of dimensionless variables) and time by the characteristic frequency of drop oscillations $\omega_D = \sqrt{\sigma/\rho R_0^3}$ [103]. We shall always consider the frame of reference fixed relative to the shaking platform, and place the origin so that the undisturbed bath surface is at $Z = -1$ (see Fig. 3-9). Thus, a drop impacting an undisturbed surface will make a contact with the bath when its centre of mass is at $Z = 0$ and its base at $Z = -1$. When the drop is not in contact with the bath ($Z > 0$), it is acted upon only by gravity (we neglect the air drag, an approximation to be justified later). Conversely, when it deforms the bath below its equilibrium height, we assume that the drop experiences an additional reaction force proportional to the penetration

depth (CZ) and its energy is dissipated at a rate proportional to its speed relative to the bath ($D\frac{\partial Z}{\partial \tau}$ term). We thus expect the drop center of mass $Z(\tau)$ to be governed by the following equation of motion:

$$\frac{\partial^2 Z}{\partial \tau^2} + \mathrm{H}(-Z) \cdot \left(D\frac{\partial Z}{\partial \tau} + CZ \right) = -\mathcal{B}o^*(\tau) \quad . \tag{3.1}$$

Here $\mathrm{H}(x)$ is the Heaviside step function, which indicates that the bath acts on the drop only when they are in contact. $\mathcal{B}o^*(\tau) = \mathcal{B}o \cdot (1 + \Gamma \sin \Omega\tau)$ is the effective Bond number, which reflects the effective gravity in the vibrating bath frame of reference. The constants C and D can be determined from experiments by measuring, respectively, the coefficient of restitution C_R and the dimensionless contact time τ_C of the drop impacting a quiescent bath ($\Gamma = 0$). For small $\mathcal{B}o$ ($\mathcal{B}o \ll Z_\tau(0)$), one can solve (3.1) over the duration of contact subject to the initial condition $Z(0) = 0$ and $Z_\tau(0) = Z_{\tau 0}$ and so obtain $Z(\tau) \approx Z_{\tau 0} \exp(-D\tau/2) \sin\left(\sqrt{C'}\tau\right)/\sqrt{C'}$, where $C' = C - D^2/4$. Then we have the approximate relations $\tau_C = \pi/\sqrt{C'}$ and $C_R = \exp\left\{-\pi D/2\sqrt{C'}\right\}$, or conversely, $D = -2\ln C_R/\tau_C$ and $C = (\pi^2 + \ln^2 C_R)/\tau_C^2$. As there is a one-to-one correspondence between pairs (C, D) and (C_R, τ_C) and the latter pair is easier to grasp intuitively, we shall henceforth use (C_R, τ_C) to characterize our linear spring model.

The crucial assumption underlying equation (3.1) is that each time the drop strikes the vibrating bath, the disturbances created by its previous impacts have decayed sufficiently to be negligible. Similarly, it is assumed that any distortions and internal motions of the drop have decayed to the point where we can approximate the drop at impact as being spherical and in rigid-body motion. To check whether this assumption is reasonable for the range of parameters examined experimentally, we first look at the decay rate of drop oscillations. For small oscillations, this problem can be adequately described with a linear theory and has been treated in several classic papers [11, 76, 95]. The instantaneous drop shape can then be decomposed into spherical harmonics and the evolution of each mode treated separately by virtue of the linearity. It is found that the second harmonic mode (corresponding to ellipsoidal deformation) decays the slowest and the rate of decay is equal to $3.8\mu/\rho R_0^2$ [76]. Even if the oscillations are large and the linear theory is no longer accurate, we expect the deformations to decay at a comparable rate. The typical time between two subsequent excitations of the drop is given by $1/f$; therefore, provided that $(\mu/\rho f R_0^2) > 0.5$, the oscillations will decay to less than $\exp(-19/10) \approx 0.15$ of their original magnitude and our assumption will

be valid. This condition can be written in dimensionless form as

$$\mathcal{O}h > \frac{\Omega}{4\pi} \quad . \tag{3.2}$$

Since we are interested only in the parameter regime for which $\Omega \lesssim 1.5$, we thus arrive at the condition $\mathcal{O}h > 0.12$. For silicone oil of viscosity 50 cS and 20 cS, this is equivalent to requiring $R_0 < 8$ mm and $R_0 < 1.3$ mm, respectively, both of which are amply satisfied in our experiments.

When the driving amplitude is sufficiently far from the Faraday threshold, a similar argument can be made for the decay rate of the local bath deformation near the drop, composed of waves with wavelength comparable to or smaller than the drop radius. Note that each drop impact also creates a propagating wave on the bath, which decays relatively slowly due to its relatively long wavelength. We assume that this propagating wave is sufficiently far from the drop on its next impact that it has negligible influence on its dynamics. These inferences that the drop returns to a spherical form and the local interface to a plane between impacts are consistent with our observations, provided the system is sufficiently far from the Faraday threshold.

We now examine the region of validity of the second assumption used to derive (3.1), namely, that the influence of air drag on the vertical drop dynamics is negligible. When the drop is not in contact with the bath and $\mathcal{R}e < 1$, approximating the air-drag using the well-known Stokes formula for a rigid sphere gives

$$Z_{\tau\tau} = -\mathcal{B}o^*(\tau) - \tfrac{9}{2}\mathcal{O}h_a Z_\tau. \tag{3.3}$$

Here $\mathcal{O}h_a = \mu_a/\sqrt{\rho\sigma R_0}$ is the air Ohnesorge number, with μ_a being the dynamic viscosity of air. The Reynolds number is given by $\mathcal{R}e = 2R_0V/\nu_a = 2(|Z_\tau|/\mathcal{O}h_a)(\rho_a/\rho)$, ν_a and ρ_a being the kinematic viscosity and density of the air. Since the maximum value of the Reynolds number during the bouncing motion is $\mathcal{R}e_{max} \sim 2gR_0/f\nu_a$, we have $\mathcal{R}e_{max} \sim 4$ for $f = 100$ Hz and $R_0 = 0.3$ mm, and $\mathcal{R}e_{max} \sim 16$ for $f = 40$ Hz and $R_0 = 0.5$ mm. Therefore the Stokes formula cannot be applied and we must use an approximation to the drag in the regime $1 < \mathcal{R}e \leq 20$. A good approximation (accurate to within 10% in the range $1 < \mathcal{R}e < 50$) is given by Flemmer & Banks [40]:

$$Z_{\tau\tau} = -\mathcal{B}o^*(\tau) - \tfrac{9}{2}\mathcal{O}h_a Z_\tau \left(1 + \tfrac{1}{12}\mathcal{R}e\right) \quad . \tag{3.4}$$

Thus the air drag is negligible provided that $\frac{9}{2}\mathcal{O}h_a Z_\tau(1 + 18/12) \ll \mathcal{B}o$. Since $Z_\tau \leq$

Dim. variable	Nondim. variable	Meaning
z	$Z = z/R_0$	drop's vertical displacement
x	$X = x/R_0$	drop's horizontal displacement
h	$H = h/R_0$	bath distortion
t	$\tau = \omega_D t$	time
T_C	$\tau_C = \omega_D T_C$	dimensionless contact time
f	$\Omega = 2\pi f/\omega_D$	vibration number

Table 3.2: List of variables used, along with their dimensionless counterparts. R_0 is the drop radius and $\omega_D = (\sigma/\rho R_0^3)^{1/2}$ the characteristic drop oscillation frequency.

$\mathcal{B}o(2\pi/\Omega)$ (acceleration times time), we arrive at the condition that

$$\tfrac{45\pi}{2}\mathcal{O}h_a \ll \Omega \qquad \text{or} \qquad \frac{\mu_a}{\rho R_0^2 f} \ll 0.09 \ . \tag{3.5}$$

As $R_0 \geq 0.07$ mm, we have $\mathcal{O}h_a \leq 5 \cdot 10^{-4}$, and so require $\Omega \gg 0.035$. This condition is satisfied in our experiments except for the smallest drops at the lowest frequencies. We proceed by neglecting the air drag, but bear in mind that for $\Omega < 0.2$, its influence may become significant.

Note that because equation (3.1) is linear, the coefficient of restitution C_R and contact time τ_C should be independent of the impact speed $X_\tau(0) = \mathcal{W}e^{1/2}$. This independence has been experimentally observed for liquid drops impacting a soap film [46], a rigid substrate [109, 108] and a liquid bath [67, 133], but only when $\mathcal{W}e \geq 1$. For $\mathcal{W}e < 1$, C_R and τ_C increase with decreasing impact speed, albeit quite weakly, as has been demonstrated numerically by Foote [42] and Gopinath & Koch [52], and experimentally by Okumura *et al.* [84] for the case of a drop impacting a rigid superhydrophobic surface.

In order to see the dependence of the dynamics on the Weber number in the liquid-liquid setting of interest, we have measured C_R and τ_C for silicone oil drops of viscosity 20 cS and 50 cS. The contact time was determined as the interval between the time when the bath beneath the drop first deforms and when the drop visibly detaches from the bath. The time of detachment is relatively difficult to pinpoint, due to the small relative speed of the drop and underlying bath at that time. The measurement error was thus typically larger than the time difference of successive video frames. In order to determine C_R, we fitted the drop motion before and after the contact to parabolic trajectories, allowing us to calculate the instantaneous drop speed at both impact and detachment. With decreasing $\mathcal{W}e$, the amplitudes of the drop motion

and bath deformation decrease, leading to a larger relative error in measurement of C_R and τ_C.

The results are shown in Figs. 3-10 and 3-11. We observe a logarithmic decrease of both contact time and coefficient of restitution with increasing Weber number, in line with the numerical predictions of Gopinath & Koch [52]. For small drops with $\mathcal{W}e > 1$, the coefficient of restitution tends to a value of about 0.11 for 50 cS oil and about 0.19 for 20 cS oil, which should be compared to the value 0.22 obtained by Jayaratne & Mason [67] for water (1 cS). Fig. 3-11 indicates that there is not an appreciable difference in the contact time between the two oils, unlike for a linear spring, for which larger damping leads to a longer period. As the Weber number is decreased, the contact time increases progressively until the point (around $\mathcal{W}e \approx 0.03$) where gravity prevents drop detachment.

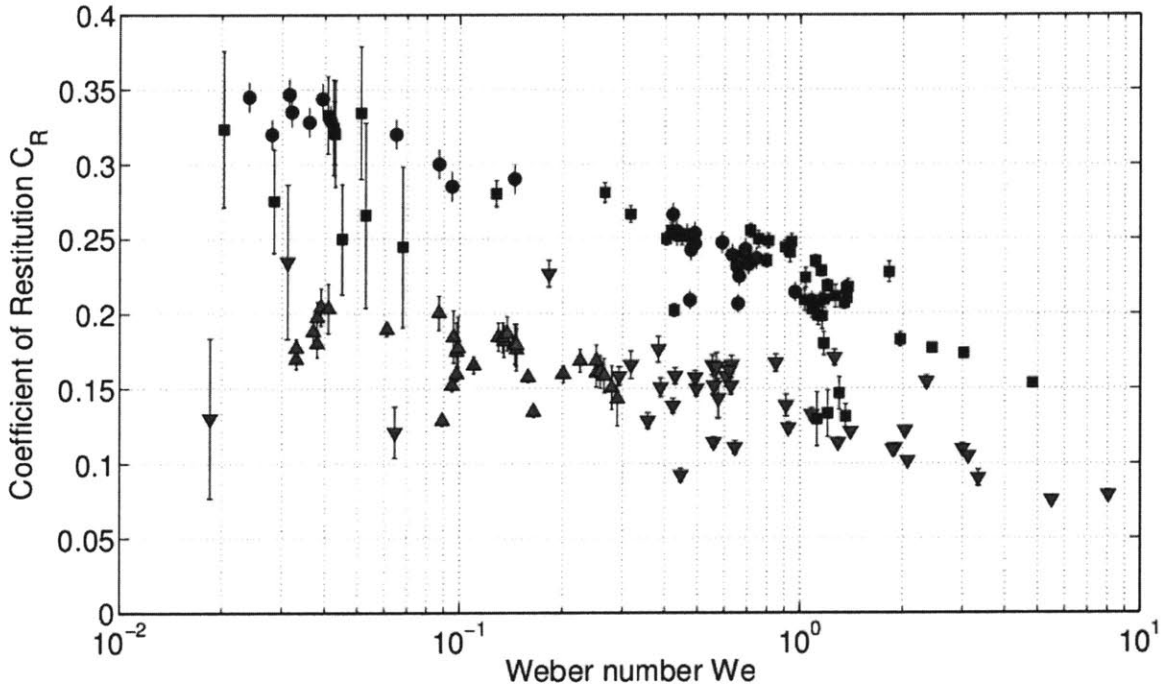

Figure 3-10: Normal coefficient of restitution $C_R = V_{out}/V_{in}$ of silicone oil droplets impacting a bath of the same liquid, as a function of the Weber number $\mathcal{W}e = \rho R_0 V_{in}^2/\sigma$. Shown are results for 20 cS (■) and 50 cS (▼) droplets impacting a quiescent bath, together with values measured from drops impacting a vibrating bath just above the bouncing threshold, (•) and (▲), respectively.

Within a single regime diagram (i.e. for a fixed driving frequency and oil viscosity) the Weber number changes significantly with drop size and bouncing mode, while generally remaining below 1 (the lower extreme being $\mathcal{W}e \approx 0.003$ for small drops in the $(1,1)$ mode at $f = 200$ Hz, the upper extreme being $\mathcal{W}e \approx 2$ for large drops

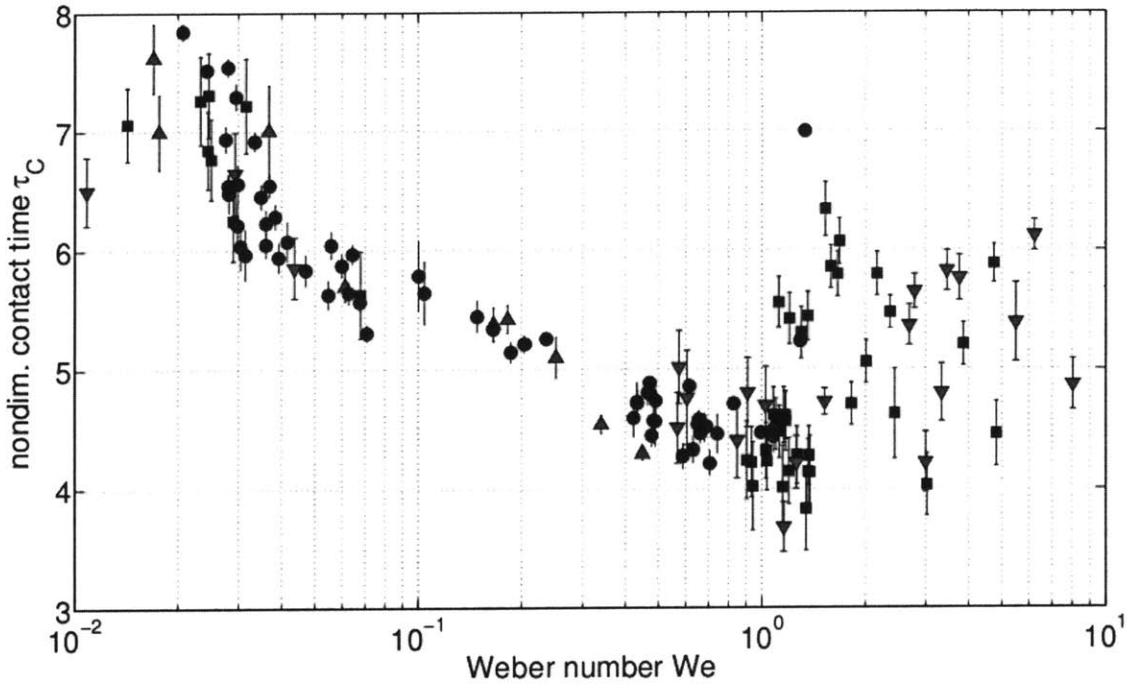

Figure 3-11: Dimensionless contact time $\tau_C = T_C / \left(\rho R_0^3/\sigma\right)^{1/2}$ of silicone oil droplets impacting a bath of the same liquid, as a function of the Weber number $\mathcal{W}e = \rho R_0 V_{in}^2/\sigma$. Shown are results for 20 cS (■) and 50 cS (▼) droplets impacting a quiescent bath, together with values measured from drops impacting a vibrating bath just above the bouncing threshold, (•) and (▲), respectively.

in the $(2,1)^2$ mode at $f = 50$ Hz). It is not surprising that the linear spring model with constant (C_R, τ_C) does not compare favourably with the experiments, since one expects both C_R and τ_C to depend on We. For example, using constant values of C_R within the experimentally observed range, that is, $C_R < 0.22$ for 50 cS oil and $C_R < 0.35$ for 20 cS, leads to a poor match. Note that changing τ_C (or C) has the effect of stretching the threshold curves vertically, so by choosing $\tau_C \approx 4.5$ we can match the curvature of the threshold curves. Changing C_R (or D) leads mainly to horizontal translation of the threshold curves on the regime diagram, so by picking the right value we can hope to fit one of the threshold curves. Fig. 3-12 shows the results of the model with $C_R = 0.32$ (for $\nu = 50$ cS) and $C_R = 0.42$ (for $\nu = 20$ cS). We note that the upper parts of the other threshold curves are also well fit by the model, likely due to the fact that those parts of the regime diagram are already in the $We \geq 1$ regime, which is nearly linear. Nevertheless, the match for $\Omega < 0.4$ is less satisfactory and the values of C_R are unrealistic when compared to those reported in Fig. 3-10.

A closer examination of the reaction force acting on the drop during rebound (see Fig. 3-21) provides rationale for the unrealistically high values of C_R required to best fit the data with our linear spring model. During the late stages of contact, the viscous damping term dominates the spring term in (3.1) and the reaction force acting on the droplet pulls it towards the bath, a clearly unphysical effect if one neglects the intervening air layer dynamics. Therefore, a better model would be one in which the reaction force acting on the drop is always nonnegative:

$$\frac{\partial^2 Z}{\partial \tau^2} = -\mathcal{B}o^*(\tau) + \mathrm{H}(-Z) \cdot \max\left\{-D\frac{\partial Z}{\partial \tau} - CZ, 0\right\} \quad . \tag{3.6}$$

With such a condition, the best match with the experimental data is indeed achieved with realistic values of C_R (specifically $C_R = 0.3$ for 20 cS oil and $C_R = 0.19$ for 50 cS oil), but now the threshold curves in the regime diagrams are matched less well (see Fig. 3-13), especially the bouncing threshold. This shortcoming strongly suggests a Weber number dependence of C_R.

While the linear spring models presented in (3.1) and (3.6) do not provide satisfactory quantitative agreement with the experiments and so will be superseded by an improved model to be developed in §3.3.2, they have one major advantage. Specifically, the simple form of the equation of motion for the drop (3.1) allows one to obtain an analytic expression for the drop motion during both flight and contact. It is thus only necessary to obtain numerically the points of first impact and detachment; the

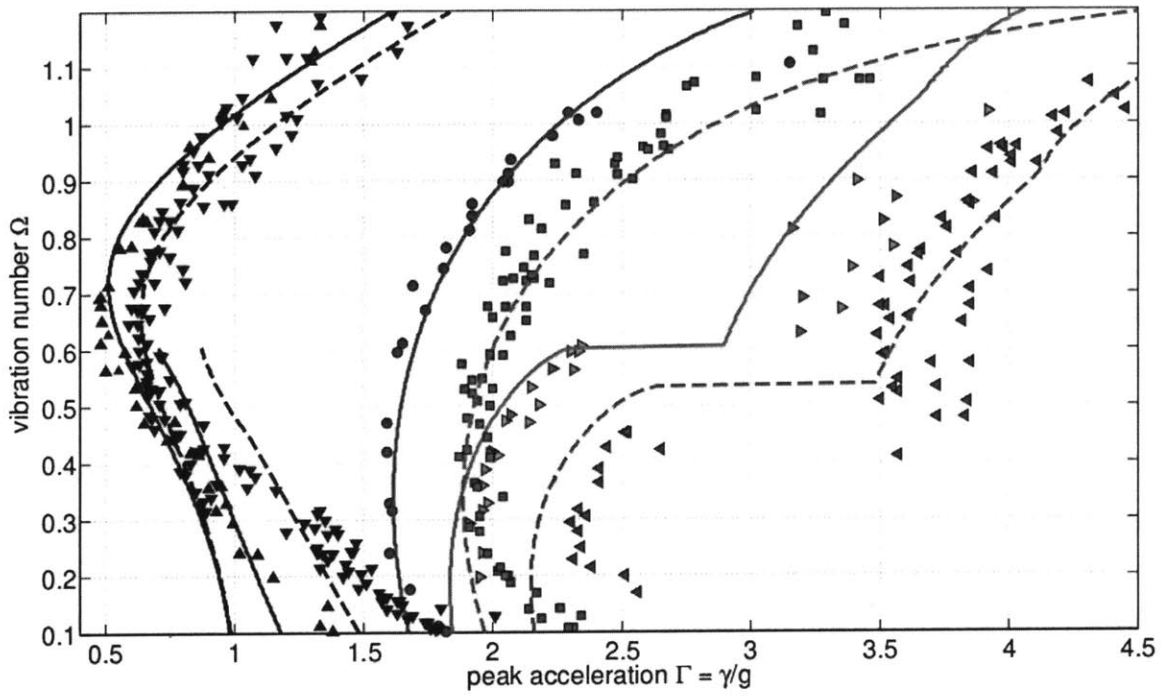

Figure 3-12: Comparison of the bouncing thresholds and first two period-doubling transitions measured experimentally and calculated using the linear spring model (3.1). Refer to Fig. 3-3 to see where these transitions fit into the regime diagram. The linear model predictions with $C_R = 0.42$ and $\tau_C = 4.2$ (*solid lines*) are compared to experiments with 20 cS oil in which coalescence (▲), 1st period doubling (•) and 2nd period doubling (►)) were measured. The predictions of the model with $C_R = 0.32$ and $\tau_C = 4.4$ (*dashed lines*) are compared to experiments with 50 cS oil in which coalescence (▼), 1st period doubling (■) and 2nd period doubling (◄)) were measured. The lines shown are, from the left, the bouncing thresholds, $(1,1)^1 \leftarrow (1,1)^2$ mode transitions, first period-doubling $(1,1) \rightarrow (2,2)$ and second period-doubling $(2,2) \rightarrow (4,4)$ or $(2,1) \rightarrow (4,2)$.

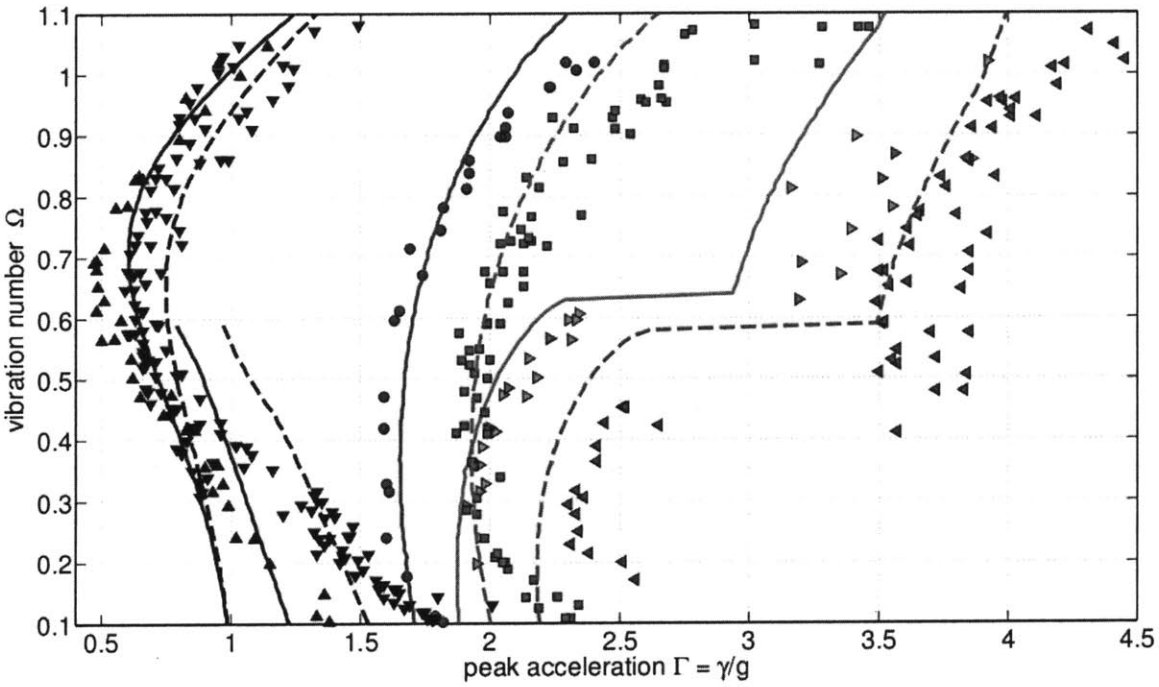

Figure 3-13: Comparison of the same experimental data as in Fig.3-12 and the predictions of the second linear spring model (3.6) with $C_R = 0.3$ and $\tau_C = 4.2$ (*solid lines*), and with $C_R = 0.19$ and $\tau_C = 4.4$ (*dashed lines*). The lines shown are, from the left, the bouncing thresholds, $(1,1)^1 \leftarrow (1,1)^2$ mode transitions, first period-doubling $(1,1) \rightarrow (2,2)$ and second period-doubling $(2,2) \rightarrow (4,4)$ or $(2,1) \rightarrow (4,2)$.

motion in between can then be calculated with great speed, which makes it possible to obtain qualitatively correct regime diagrams with great resolution. One such regime diagram is shown in Fig. 3-14, obtained by choosing $C_R = 0.42$ and $\tau_C = 4.2$ in (3.1). The predicted bouncing thresholds shown in Figs. 3-12-3-13 and 3-14 correspond to the highest driving acceleration for which the drop never detaches from the bath surface (so that $Z(\tau) \leq 0$ always).

As mentioned previously, there can be several kinds of vertical motion corresponding to the same bouncing mode number (m, n), which can be thought of as different energy levels. The lowest energy mode tends to be the one where the drop spends the most time in contact with the bath. When average mechanical energy is increased, the drop spends more time in the air and less in contact with the bath. Fig. 3-15 depicts the relative contact time as predicted by the linear spring model (3.1), for the highest stable energy mode. We see two sharp transitions. The first arises for small drops ($\Omega < 0.55$), when the higher energy $(1,1)^2$ bouncing mode can no longer be sustained and collapses to the least energetic vibrating mode $(1,1)^1$, in which the drop oscillates on the bath surface with a large portion of the period spent in contact with the bath. The second arises for larger drops ($\Omega > 0.6$), when the higher energy $(2,1)^2$ mode cannot be sustained and only the base energy mode $(2,1)^1$ exists. Both of these transitions are prominent in our regime diagrams (Figs. 3-3-3-8): the former constitutes the lower part of the bouncing threshold, while the latter constitutes the upper half of the walking threshold, as will be seen in Chapter 4.

In Figs. 3-16-3-18 we show the two different $(1,1)$ modes, the two $(2,1)$ modes and the $(3,2)$ bouncing mode, respectively. The dimensionless height of the drop in the lab frame of reference (*solid line*) and the equilibrium height of the vibrating bath (*dashed line*) are shown as functions of dimensionless time $\tau = f \cdot t$. In order to highlight the difference between the vibrating and bouncing states, the periods of contact between the drop and the bath are marked by a darker shading. In the vibrating state (Fig. 3-16a,3-17a) the contact lasts roughly half the period of the drop's vertical motion, whereas in the bouncing state (Fig. 3-16b,3-17b) the contact is significantly shorter. The $(3,2)$ mode shown in Fig. 3-18 consists of one long and one short contact.

3.3.2 Logarithmic Spring Model

We have seen that the coefficient of restitution and the contact time of a drop interacting with a quiescent liquid bath are independent of the Weber number for $We > 1$,

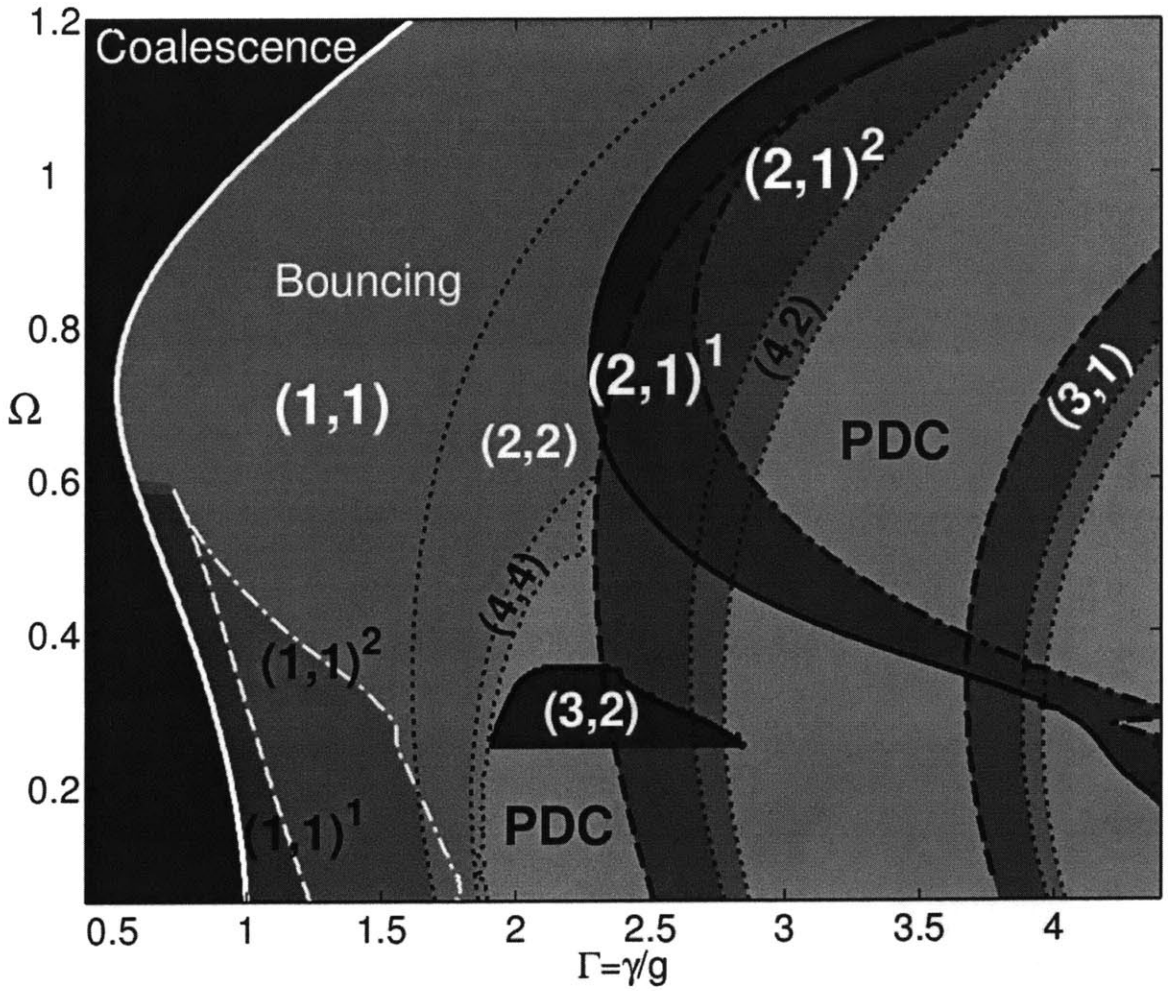

Figure 3-14: Regime diagram indicating the behaviour of a bouncing drop in the $\Gamma - \Omega$ plane, as predicted by the linear spring model (3.1) with $C_R = 0.42$ and $\tau_C = 4.2$. $\Omega = \omega/\omega_D$ is the vibration number and $\Gamma = \gamma/g$ the dimensionless driving acceleration. In the (m, n) mode, the drop's motion has period equal to m driving periods, during which the drop hits the bath n times. *PDC* indicates a region of period-doubling cascade and chaos. Solid lines indicate lower boundaries of existence (or stability) of lower energy modes, dash-dot lines indicate upper boundaries. Similarly, dashed lines indicate lower boundaries of existence of higher energy modes, their upper boundaries being period-doubling transitions marked by dotted lines.

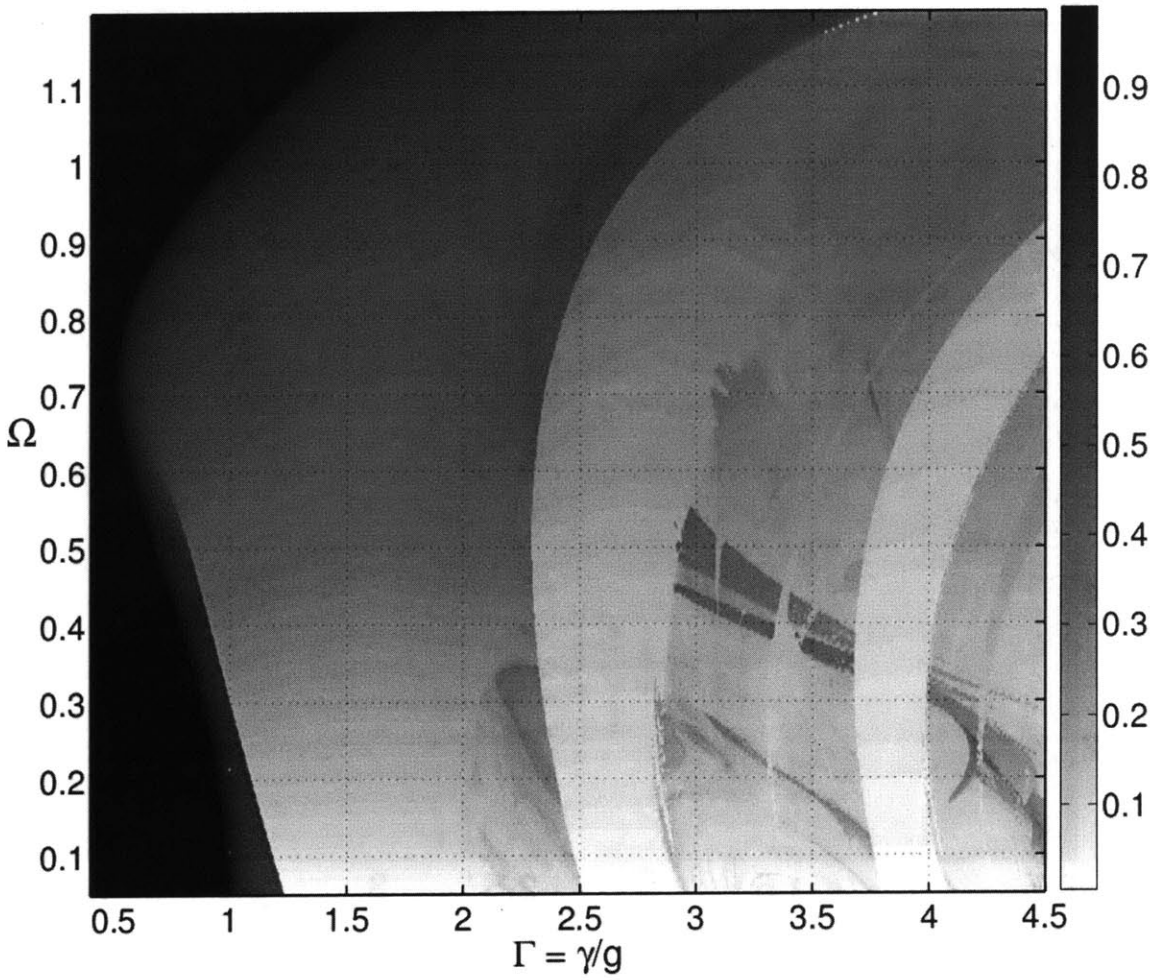

Figure 3-15: The relative contact time (fraction of the bouncing period spent in contact with the bath) of a bouncing drop in the Γ-Ω plane, as predicted by the linear spring model (3.1) with $C_R = 0.42$ and $\tau_C = 4.2$. Ω is the vibration number and Γ the dimensionless driving acceleration. Sharp changes of the relative contact time are evident near $\Gamma \approx 1$ (the bouncing to oscillating transition, or the $(1,1)^2 \rightarrow (1,1)^1$ mode transition), $\Gamma \approx 2.4$ (onset of the $(2,1)^2$ mode) and $\Gamma \approx 3.7$ (onset of the $(3,1)$ mode).

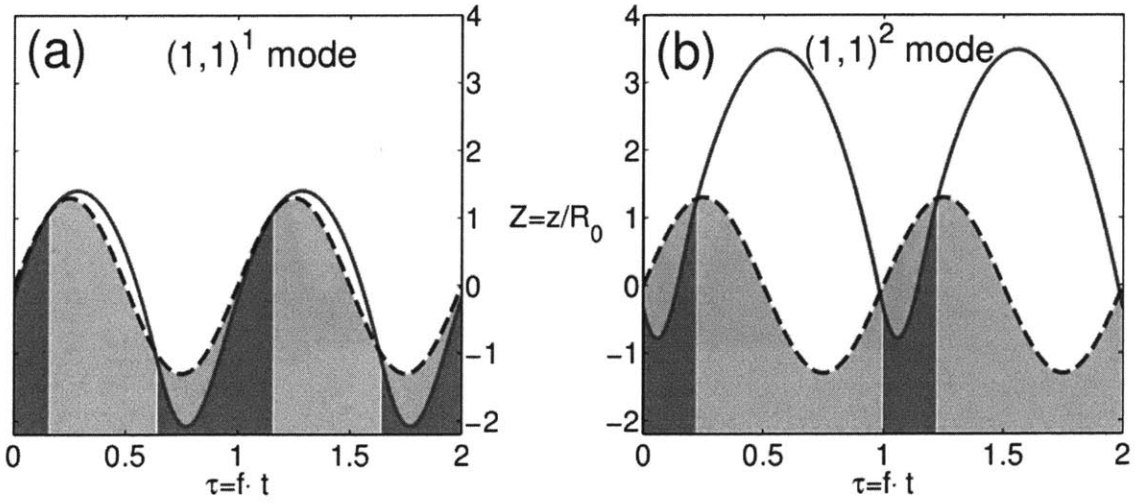

Figure 3-16: Comparison of **(a)** the low energy "vibrating" $(1,1)^1$ mode and **(b)** the high energy "bouncing" $(1,1)^2$ mode, as predicted by the linear spring model (3.1) with $\tau_C = 4.2$, $C_R = 0.42$ for $(\Gamma, \Omega) = (1.3, 0.35)$. The dimensionless vertical position of the oscillating bath (*dashed line*) and the droplet's center of mass shifted down by one radius (*solid line*) are shown as functions of the dimensionless time $\tau = ft$, where f is the bath's driving frequency. See Fig. 3-4 **(a-b)** for the experimental realizations of these modes.

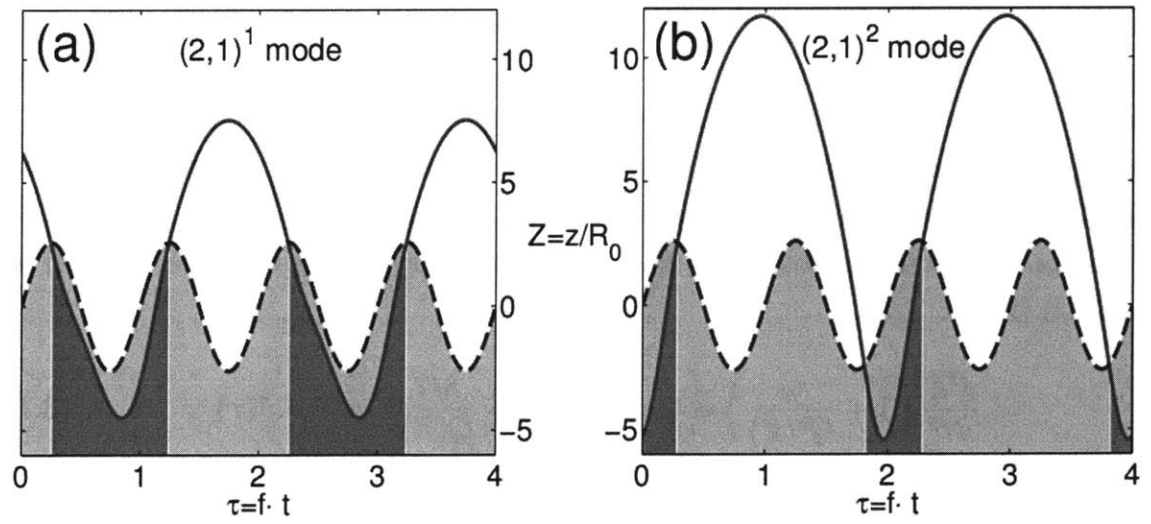

Figure 3-17: Comparison of **(a)** the lower energy $(2,1)^1$ mode and **(b)** the higher energy $(2,1)^2$ mode, as predicted by the linear spring model (3.1) with $\tau_C = 4.2$, $C_R = 0.42$ for $(\Gamma, \Omega) = (2.6, 0.7)$. The dimensionless vertical position of the oscillating bath (*dashed line*) and the droplet's center of mass shifted down by one radius (*solid line*) are shown as functions of the dimensionless time $\tau = ft$. See Fig. 3-4 **(d-e)** for the experimental realizations of these modes.

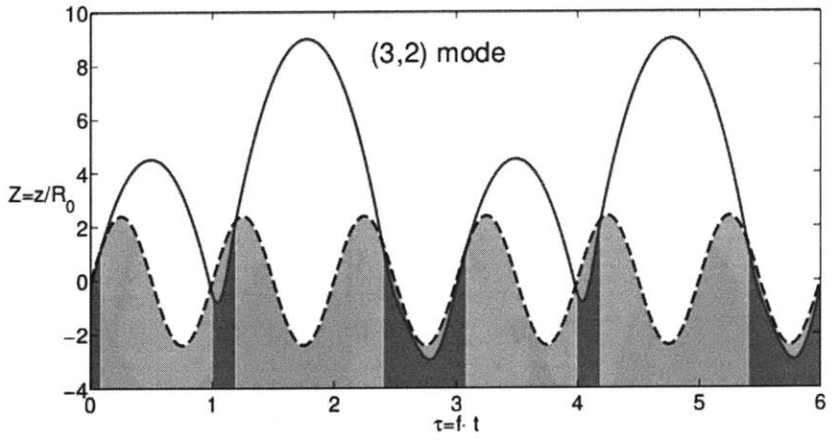

Figure 3-18: The $(3,2)$ mode, as predicted by the linear spring model (3.1) with $\tau_C = 4.2$, $C_R = 0.42$ for $(\Gamma, \Omega) = (2.4, 0.32)$. The dimensionless vertical position of the oscillating bath (*dashed line*) and the droplet's center of mass shifted down by one radius (*solid line*) are shown as functions of the dimensionless time $\tau = ft$.

while for $\mathcal{W}e \leq 1$ they depend logarithmically on $\mathcal{W}e$ (see Figs. 3-10-3-11). Therefore, while in the former regime we can model the drop by a linear spring, in the latter we need a nonlinear model in order to capture, above all, the dependence of C_R on $\mathcal{W}e$. We derive such a model in Appendix B, using a quasi-static approximation similar to that developed previously for drop impact on a rigid substrate [77]. The key idea of the resulting "quasi-static" model is the approximation of the actual instantaneous shape of the drop and the bath by relatively simple shapes, specifically their quasi-static forms, that may be characterized by a small number of variables. By calculating the Lagrangian of the system we can then derive the system of equations of motion for these variables. We then simplify the system to a single differential equation (B.14):

$$\frac{d^2Z}{d\tau^2}\left(1+\frac{c_3}{Q^2(Z)}\right)+\mathcal{O}h\frac{c_2(\nu)}{Q(Z)}\frac{dZ}{d\tau}+\frac{3/2}{Q(Z)}Z=-\mathcal{B}o^*(\tau)\ , \tag{3.7}$$

where $Q(Z) = \ln(c_1/|Z|)$. c_3 prescribes the kinetic energy associated with the fluid motion within the two liquid bodies, $c_2(\nu)$ the amount of viscous dissipation within them, and c_1 the nonlinearity of the spring. For higher values of c_1, $\ln(c_1/|Z|)$ is less dependent on Z, thus making the spring more linear. The constants c_i are determined from matching to the observed dependence of the normal coefficient of restitution C_R on $\mathcal{W}e$ (Fig. 3-10). The best match found is shown in Fig. 3-19, which was obtained by solving (B.13) for $R_0 = 0.15$mm and two viscosities ($\nu = 20$ cS and $\nu = 50$ cS), with

the initial conditions $Z(0) = 0$, $dZ/d\tau = -\mathcal{W}e$. The constants used were $c_2 = 12.5$ for 20 cS and $c_2 = 7.5$ for 50 cS, and $c_1 = 2$, $c_3 = 1.4$ were used for both viscosities. Changing c_1 alters the slope of the line in Fig. 3-19, while changing c_2 shifts the line vertically. The fits were found to be quite insensitive to the value of c_3, suggesting that the internal fluid motion does not play a significant role in the impact dynamics, which is consistent with the scaling argument presented in the previous chapter.

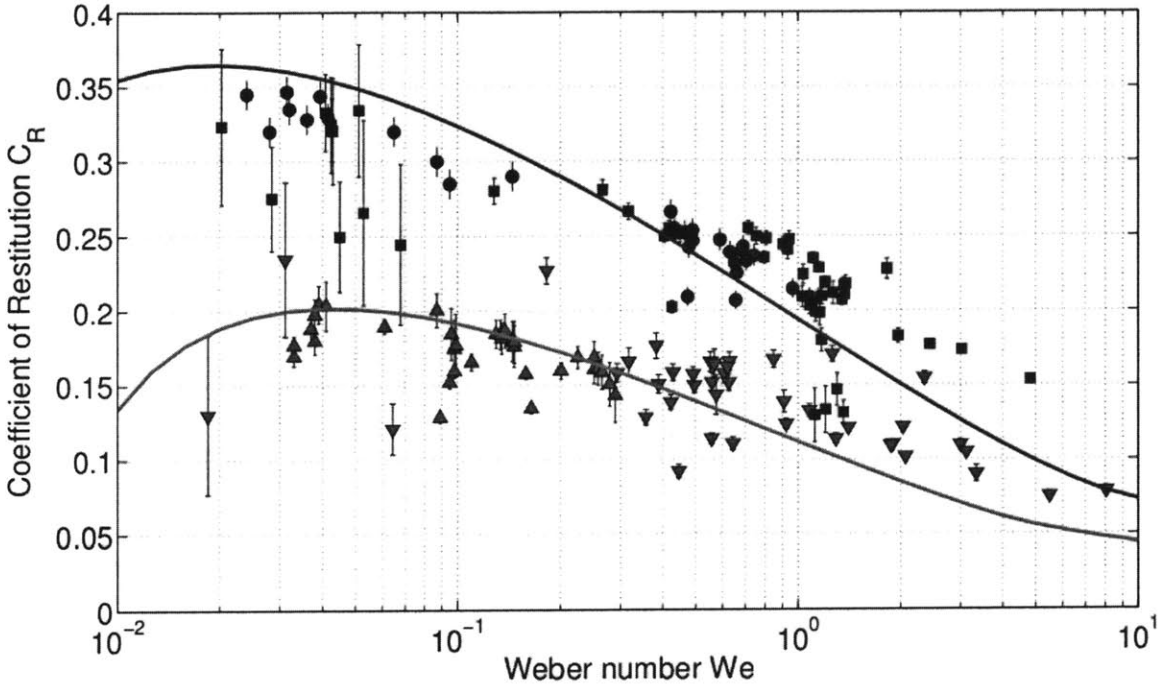

Figure 3-19: The dependence of the normal coefficient of restitution $C_R = V_{out}/V_{in}$ for silicone oil droplets impacting a bath of the same liquid, on the Weber number $\mathcal{W}e = \rho R_0 V_{in}^2/\sigma$. Shown are the experimental results for 20 cS (■) and 50 cS (▼) droplets impacting a quiescent bath. (•) and (▲) denote analogous C_R values for droplets impacting a vibrating bath just above the bouncing threshold. Solid lines indicate the values obtained using the logarithmic spring model (B.13) with $R_0 =$ 0.15mm for $c_1 = 2$, $c_2(20\text{ cS}) = 12.5$, $c_2(50\text{ cS}) = 7.5$ and $c_3 = 1.4$.

In Fig. 3-20, the model predictions for the temporal evolution of the penetration depth are compared to the experimental data for $0.68 \leq \mathcal{W}e \leq 0.96$. Clearly, the linear spring model (3.1) overestimates C_R and both linear models (3.1) and (3.6) underestimate the time elapsed until $|Z| = 0$, the drop's "rebound time". Note that the actual dimensionless contact time for $\mathcal{W}e \approx 0.8$ is approximately 4.3, as the drop detaches while the bath is still deformed. In Fig. 3-21, we compare the predictions of the three models for the evolution of the dimensionless drop acceleration during contact. The linear models produce substantially different curves from the logarithmic

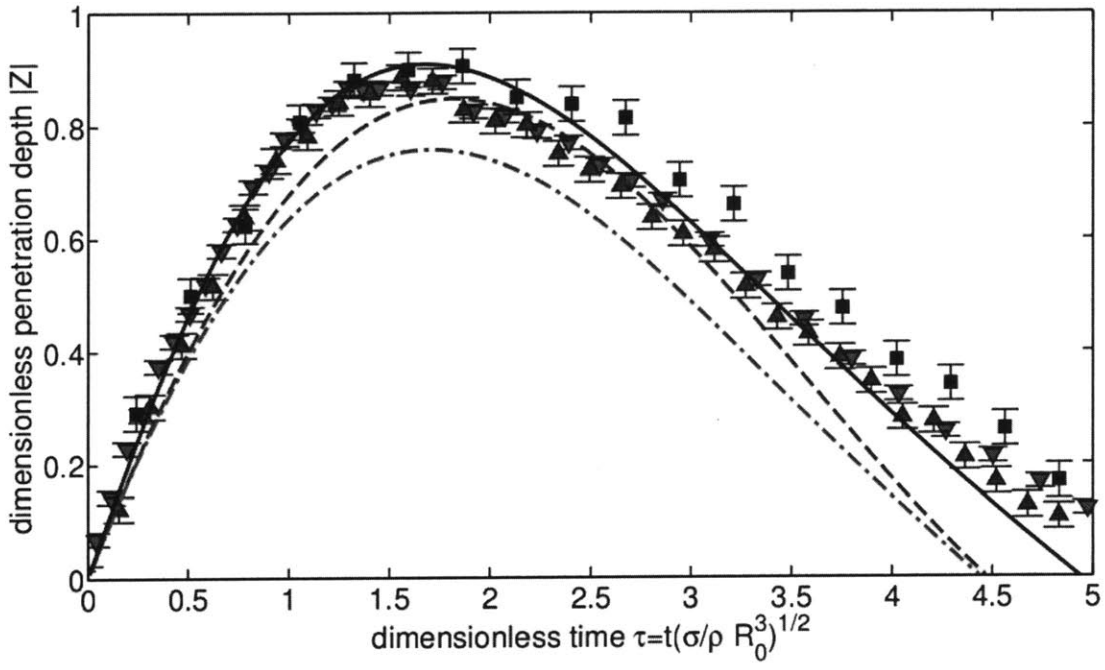

Figure 3-20: The dimensionless depth of penetration $|Z| = |z|/R_0 We^{1/2}$ of the drop's center of mass below its height at the outset of contact (see Fig. 3-9), as a function of the dimensionless time $\tau = t\,(\sigma/\rho R_0^3)^{1/2}$. The predictions of the linear spring model (3.1) (*dashed line*), alternative linear spring model (3.6) (*dash-dot line*) and the logarithmic spring model (3.7) (*solid line*) for $R_0 = 0.3$mm and $We = 0.8$ are compared to the experimental values for $R_0 = 0.14$mm, $We = 0.73$ (■), $R_0 = 0.20$mm, $We = 0.68$ (▲) and $R_0 = 0.33$mm, $We = 0.96$ (▼).

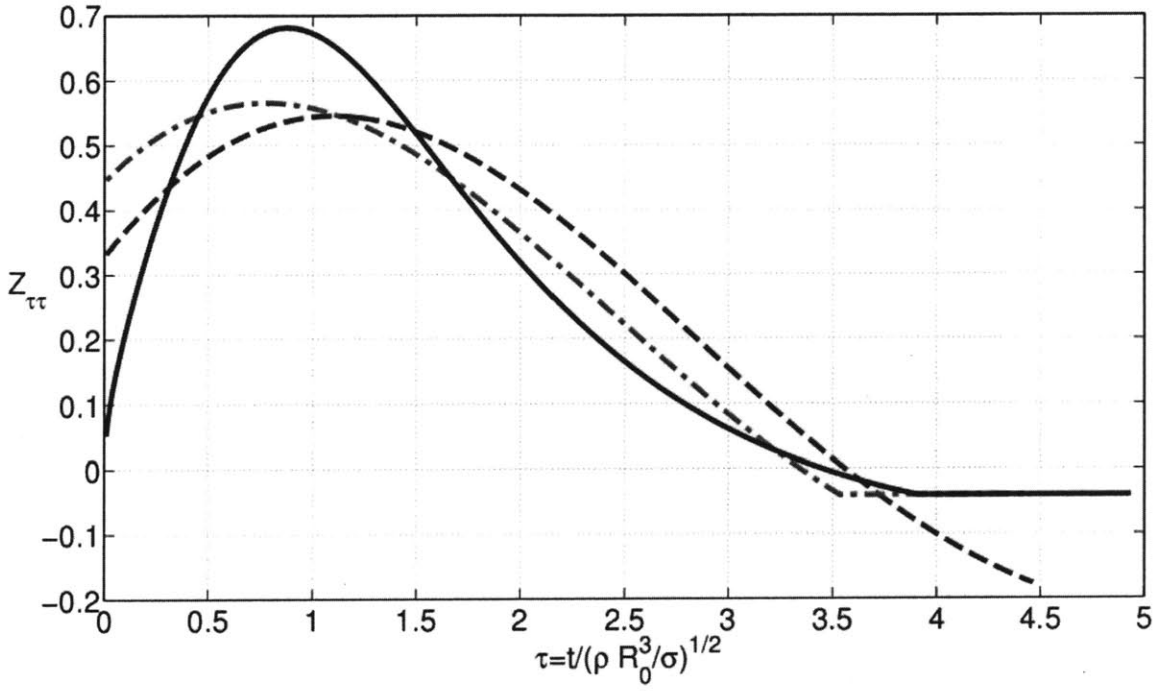

Figure 3-21: The dimensionless acceleration $Z_{\tau\tau} = (d^2z/dt^2)\,(\rho R_0^3/\sigma V_{in}^2)^{1/2}$ of the drop's center of mass as a function of the dimensionless time $\tau = t\,(\sigma/\rho R_0^3)^{1/2}$. The predictions of the linear spring model (3.1) (*dashed line*), alternative linear spring model (3.6) (*dash-dot line*) and the logarithmic spring model (3.7) (*solid line*) are shown for $R_0 = 0.3$mm and $\mathcal{W}e = 0.8$.

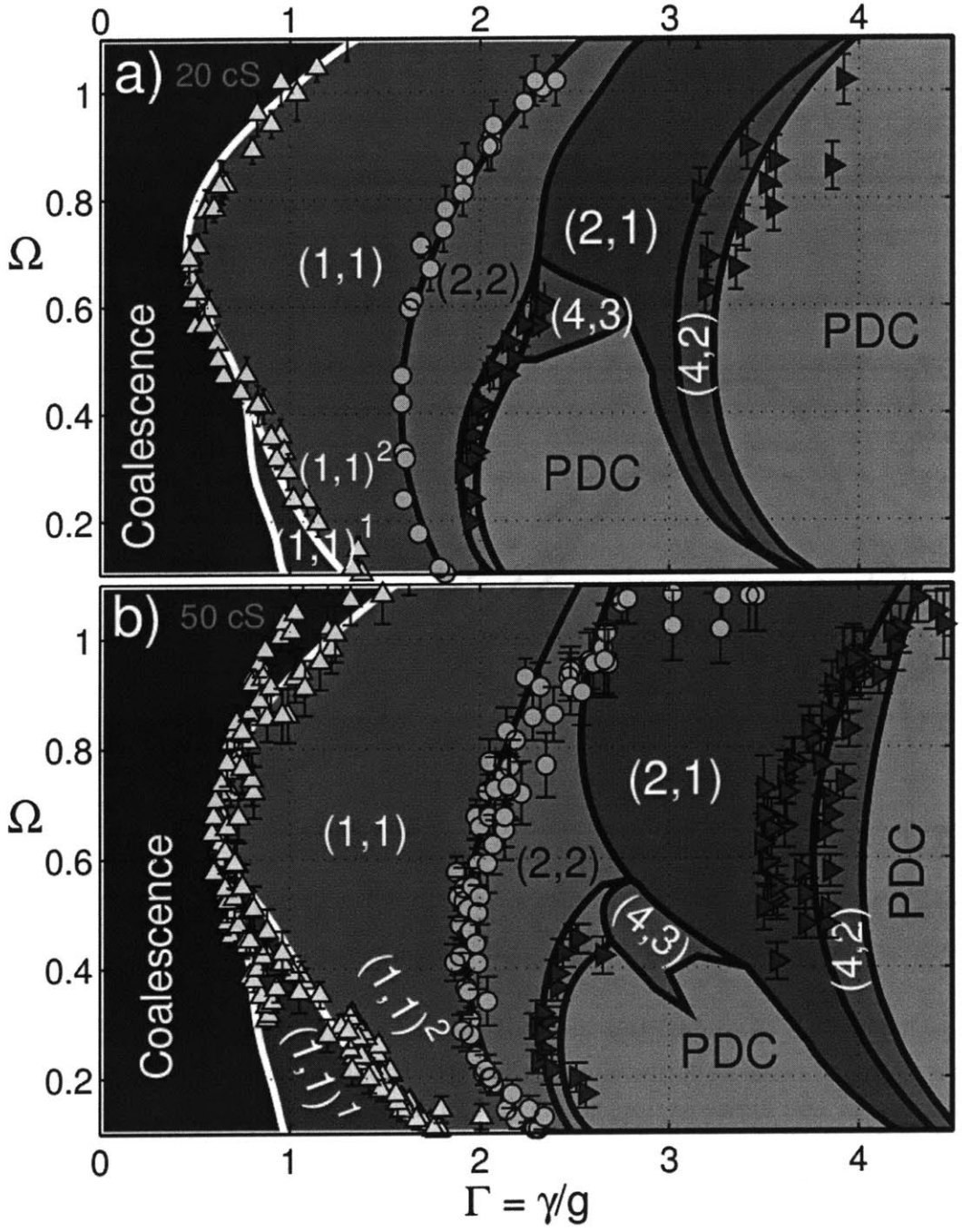

Figure 3-22: Comparison of the regime diagrams measured experimentally and those calculated using the logarithmic spring model (3.7). **(a)** The model predictions with $c_1 = 2$, $c_3 = 1.4$, $c_2 = 12.5$ and $f = 80$ Hz (*solid lines*) are compared to experiments with 20 cS oil in which coalescence (▲), 1st period doubling (•) and 2nd period doubling (►) were measured. **(b)** The predictions of the model with $c_1 = 2$, $c_3 = 1.4$, $c_2 = 7.5$ and $f = 80$ Hz (*dashed lines*) are compared to experiments with 50 cS oil in which coalescence (▲), 1st period doubling (•) and 2nd period doubling (►) were measured.

model, predicting a significant acceleration immediately after impact and a stronger reaction force during the later stages of contact. The first linear model (3.1) also shows an unphysical negative reaction force during the late stages of contact, as indicated by the dip below the gravitational acceleration for $\tau > 3.8$.

Using the same combination of constants c_i as in Fig. 3-19, the regime diagram predicted using the logarithmic spring model (3.7) matches well with the experimental data (Fig. 3-22). Specifically, the lower part of the experimentally observed bouncing threshold curve now corresponds to the $(1,1)^1 \leftarrow (1,1)^2$ mode transition, which was not the case for the previous models. The mode transition $(2,1) - (4,2)$ for 20 cS (upper-right corner of Fig. 3-22a,b) is matched least well; however, the match is still better than that produced by either of the linear models. Note that we had no freedom in choosing the curvature (vertical scale) of the threshold curves in Fig. 3-22 unlike the previous cases (Figs. 3-12 and 3-13), where it was determined by the parameter τ_C (or spring constant C). In the logarithmic spring model (3.7), the spring constant is $1.5/Q(Z)$ and therefore, apart from the weak nonlinear contribution from $Q(Z)$, is determined from the low Weber number analysis. The fact that the curvature and peaks of the predicted threshold curves correspond to those measured experimentally provides additional verification of our model.

A useful way to characterize the drop's impact in relation to the bath vibration is provided by the *impact phase* relative to the driving, defined as the weighted average of the driving phase $\Omega\tau$ over the contact time:

$$\Phi = \int_{\tau_C} F(\tau)\,(\Omega\tau)\,\mathrm{d}\tau \Big/ \int_{\tau_C} F(\tau)\mathrm{d}\tau \qquad (\mathrm{mod}\ 2\pi)\ , \tag{3.8}$$

where $F(\tau) = \partial^2 Z/\partial\tau^2 + \mathcal{B}o^*(\tau) = Z_{\tau\tau}(\tau) + \mathcal{B}o\,(1 + \Gamma\sin\Omega\tau)$ is the dimensionless reaction force acting on the drop during contact. Thus, $\Phi = \pi$ corresponds to impact at maximum upward bath velocity, whereas $\Phi = 0$ corresponds to the impact at maximum downward bath velocity. The impact phase Φ divided by π is shown in Fig. 3-23 as a function of the driving acceleration $\Gamma = \gamma/g$ for three values of Ω, specifically, $\Omega = 0.2, 0.5$ and 0.8. The results were obtained using the model (3.7) with $c_1 = 2$, $c_3 = 1.4$, $c_2 = 7.5$ and $f = 80$ Hz. The weighted average of Φ/π is indicated by dark lines and dots, while the extent of contact is marked by shaded regions with lighter shading indicating that the droplet is in contact during the corresponding phase only on a small number of impacts per its period of motion.

For $\Omega = 0.8$ (Fig. 3-23c), the drop coalesces with the bath when $\Gamma < 0.49$. As the driving is increased above this value, the drop begins to detach from the surface

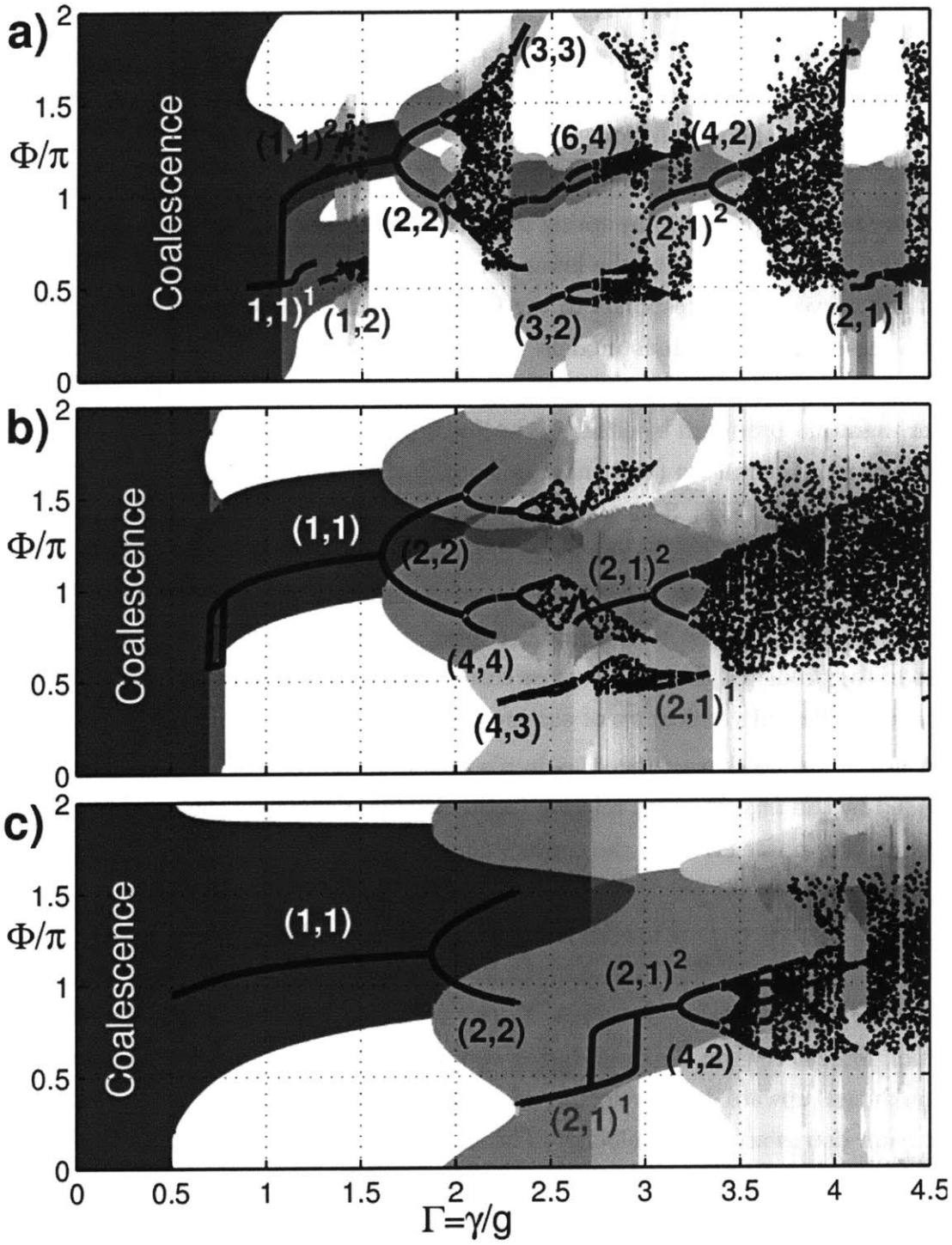

Figure 3-23: The dependence of the impact phase Φ (*solid lines, points*), defined in (3.8), on the driving acceleration $\Gamma = \gamma/g$ for three values of the vibration number Ω: **(a)** $\Omega = 0.2$, **(b)** $\Omega = 0.5$ and **(c)** $\Omega = 0.8$ (refer to Fig. 3-22a). Contact is marked by the shaded regions, wherein darkness of the shading indicates the relative number of contacts including the given phase. Where possible, the periodic bouncing modes (m, n) are indicated.

(white regions), and the contact time decreases as indicated by the vertical extent of the shaded region. The impact phase slowly increases from approximately π at $\Gamma = 0.5$ to 1.2π at $\Gamma = 1.9$, where the first period-doubling occurs. There, the even and odd contacts separate, with the impact phase of one increasing and of the other decreasing. At $\Gamma \approx 2.3$, one of the ends of contact joins with the beginning of the following contact and the completely period-doubled $(2,1)^1$ mode is formed (note the discrete change of impact phase by π). Increasing the driving to $\Gamma \approx 2.95$, the $(2,1)^1$ vibrating mode becomes unstable to the $(2,1)^2$ bouncing mode, with markedly shorter contact time. Once in this mode, we can decrease the driving acceleration to $\Gamma \approx 2.7$ before we switch back to the $(2,1)^1$ mode. Further increase of Γ beyond $\Gamma = 3$ leads to a period-doubling cascade and the onset of chaos at $\Gamma \approx 3.45$.

The most common bouncing modes are labeled in Fig. 3-23, where we observe that the impact phase is higher for higher energy (bouncing) states than their lower energy counterparts, with the higher energy state disappearing once the phase dips below π. This disappearance can be rationalized by considering the vertical bath speed in an inertial frame of reference, given by $-(Bo/\Omega)\cos(\Omega\tau)$, which achieves its maximum value when $\Phi = \pi$. Thus, when $\Phi = \pi$, the bath transfers the maximum momentum possible to the drop during contact; below this value the drop cannot maintain the higher energy level and collapses to a lower energy bouncing mode. We note that with increasing vibration number Ω (or, equivalently, increasing drop size), the duration of contact increases, chaotic bouncing states are replaced by periodic states, and the lower energy modes $(1,1)^1$ and $(2,1)^1$ shift to lower driving accelerations.

3.4 Discussion

In our experiments, we have classified the drop dynamics for a wide range of driving frequencies and drop sizes, and reported a number of new bouncing states. We have reported the full bouncing threshold curve and shown that it can be discontinuous. We observed the existence of two distinct bouncing states corresponding to the same mode number (m,n), which we dubbed bouncing and vibrating. The transition between these two energy levels of the same mode plays a crucial role in the coalescence of small drops and in the onset of walking for larger drops. For small drops, the contact time in the $(1,1)^1$ mode, being roughly half the oscillation period, is longer than the thinning time of the intervening air layer, resulting in coalescence. The lower part of the bouncing threshold curve therefore lies along the $(1,1)^1 - (1,1)^2$ transition curve. The peak of the walking region typically occurs on the transition curve between the

$2,1)^1$ and the $(2,1)^2$ mode, as will be shown in Chapter 4. The dominance of the $(2,1)^2$ mode beyond this point is responsible for the walking region having only finite extent.

We have thus delineated the different regimes arising in the vertical dynamics of a drop bouncing on a vibrating bath and rationalized them using a logarithmic spring model for the drop-bath interaction. For small driving accelerations, the bath cannot transfer energy to the drop at a rate sufficient to compensate for viscous dissipation and wave creation; consequently, the drop coalesces when the intervening air layer thins below a critical thickness. For higher driving accelerations, simple periodic bouncing is observed, which tends to become unstable to more complex bouncing states with longer period, as the driving amplitude is further increased. Generally, as the driving acceleration is raised, the average contact time of the drop decreases and the amplitude of its bounce increases, but the change between bouncing modes is sometimes discrete. For even higher accelerations, chaotic bouncing is the norm, interspersed with windows of periodicity. Nevertheless, the chaotic regions disappear for larger drops and near the Faraday threshold, where the standing wave pattern created by the drop's impacts acts to stabilize the vertical motion by reducing the relative speed of the drop and bath at impact.

We have developed a series of models of increasing sophistication to describe the dynamics of drops bouncing on a vibrating fluid bath. The dynamics involve a complex interplay of the drop and bath deformation and also of the air flow in the intervening layer during contact. However, provided there is no coalescence, the air film between the drop and the bath serves only to communicate normal stresses between the two. We have shown that in the parameter regime of interest, many factors can be neglected, such as the role of air drag during flight and the residual bath deformation generated by previous drop impacts. This allowed us to simplify the dynamics to the point that it could be captured by a single differential equation, with the reaction force acting during contact modeled as a linear or logarithmic spring. The linear spring model, which has been used previously to model drop rebound from a rigid substrate [84], has two free parameters, the spring and dissipation constants, which can be determined experimentally by measuring the contact time T_C and coefficient of restitution C_R.

The linear spring models, by virtue of their linearity, were unable to correctly model the dependence of C_R on the impact speed. Nevertheless, their integrability allows fast numerical solution, which might make them preferable in some cases where speed takes precedence over accuracy. The logarithmic spring model is new, derived

by analysis of the dynamics at very small Weber numbers and extension to the parameter regime of interest. It has 3 free parameters, which can be determined by measuring T_C and C_R for two different impact speeds. Only the logarithmic spring model was found to be consistent with the experimental data for Weber numbers smaller than one. Even the bouncing threshold, which in general requires understanding of the intervening layer dynamics, could be almost entirely rationalized by considering mode transitions and contact time. For applications requiring a highly accurate representation of the temporal dependence of the reaction force, as will be the case for the model of walking drops treated in the subsequent chapter, the logarithmic spring model will be invaluable.

Throughout our analysis, we have assumed that both the drop and bath deformations are dissipated between impacts, an assumption that breaks down as one approaches the Faraday threshold. Then, the purely vertical bouncing states can be destabilized by the standing waves, giving rise to walking states, an effect to be treated in Chapter 4. There, we couple the drop's vertical dynamics, as described herein, to its horizontal dynamics. In order to determine the amplitude of the standing waves created and the tangential acceleration they impart to the drop, it is necessary to know the impact phase and the temporal dependence of the reaction force. The model for the vertical dynamics developed herein provides this information, the absence of which is responsible for the shortcomings of previous theoretical descriptions [19, 32] of this relatively subtle system.

Chapter 4

Drops Walking on a Vibrating Bath

4.1 Background

A liquid drop placed on a vibrating liquid bath can achieve a vertical bouncing motion by virtue of the sustenance of an air layer between the drop and bath [124, 18]. For drops within a certain size range, the interplay between the drop and the waves it excites on the liquid surface causes the vertical bouncing state to become unstable to a walking state [19]. The interaction of the walking drops and their guiding wave field leads to a variety of phenomena reminiscent of quantum mechanics, including tunneling across a sub-surface barrier [30], single-particle diffraction in the single- and double-slit geometries [16], quantized orbits [43] and orbital level splitting [31]. This hydrodynamic system bears a remarkable similarity to an early model of quantum dynamics, the pilot-wave theory of Louis de Broglie [23, 6, 59].

Protière *et al.* [98] presented a regime diagram of liquid drops bouncing on a liquid bath (specifically, 20 cS silicone oil), as did Eddi *et al.* [33] for 50 cS oil. In the previous chapter, we have extended their measurements to cover a wider range of drop size and driving frequency, in order to have a firmer experimental basis for building a theoretical model for the drop's vertical dynamics. In section §3.3, we developed a hierarchy of theoretical models and showed that the experimental results are best matched by describing the interaction as a logarithmic spring, analogously to impacts on rigid substrates (Chapter 2). We noted the existence of two distinct modes with the same period and number of jumps per period, which we refer to as "vibrating" and "bouncing" modes. In the lower energy vibrating mode, the contact

time of the drop is set by the vibration frequency of the bath, while in the higher energy bouncing mode, by the drop's characteristic frequency of oscillations. The possible coexistence of these two vertical modes for the same parameter combination will be relevant here.

In order to understand the role of drop size and driving frequency on the bouncing dynamics, a model of both the vertical and horizontal drop motion is required. No satisfactory quantitative model exists to date. Couder *et al.* [19] introduced a simple model of walking drops that was further developed by Protière *et al.* [98], both models being based on the approximation that the wavefield is sinusoidal and centered on the last impact. The shear drag in the intervening air layer was misidentified as the major force resisting the drop's horizontal motion, an assumption to be corrected here. We also point out the shortcomings of their scaling for the averaged reaction force acting on the drop $F \sim m\gamma(\tau/T_F)$, where m is drop mass, γ the driving acceleration, τ the contact time and T_F the Faraday period. If the drop is to keep bouncing, the average reaction force must equal the drop weight: $F = mg$. It will be shown here that the horizontal force on the drop increases with driving acceleration not because of an increasing vertical reaction force, but due to an increase in the magnitude of the standing wave pattern induced as one approaches the Faraday threshold.

Eddi *et al.* [32] presented a more detailed model which included the contributions to the wavefield from all previous impacts, but the divergence of their wavefield approximation at the centre of the impact precludes its suitability for modeling the transition from simple bouncing to walking. While the theoretical models of Couder's group capture certain key features of the walker dynamics, they contain a number of free parameters that can only be eliminated by careful consideration of the impact dynamics. More recently, Shirokoff [113] treated the wavefield created by drop impacts in more detail, but only the most recent impact was considered; moreover, no connection was made between the model's free parameters and the experiments.

The goal of this chapter is to develop a theoretical model capable of providing quantitative rationale for the regime diagrams of the bouncing drops, such as that shown in Fig. 4-4. In addition to rationalizing the limited extent of the walking regime, the model should allow us to understand the observed dependence of the walking speed on the bath acceleration. By time-averaging over the vertical dynamics described in §3.3, we here develop a trajectory equation for the walking drops. Our model predicts the existence of several of the experimentally observed walking states, such as low and high energy resonant walking, limping and chaotic walking. The possible coexistence of these states at the same parameter combination may give rise

to a complex mode-switching dynamics.

In §4.2 we describe our experimental arrangement and present our data describing the observed dependence of the walking thresholds and speeds on the system parameters. In §4.3 we analyze the spatio-temporal evolution of the standing waves created by a drop impact on the liquid bath for peak driving accelerations near the Faraday threshold. In §4.4, we consider all the major forces acting on the drop during flight and rebound and so obtain a consistent model for the drop's horizontal and vertical dynamics. By analysing the model in the limit of short contact time relative to the driving period, we obtain a trajectory equation appropriate for small walking drops. In §4.5 we present the model predictions and compare them to the experimental data. Specifically, we examine the role of drop size and driving acceleration on the walking speed and the role of oil viscosity and driving frequency on the extent of the walking regime. We also highlight the role of the vertical dynamics in setting the boundaries of the walking regime. Some simplifications of the full model are made in order to obtain a relatively simple scaling for the walking speed and insight into the walking thresholds. Future research directions are outlined in §4.6.

4.2 Experiments

In order to extend the data sets reported by Protière *et al.* [98] and Eddi *et al.* [32], we measured the walking thresholds and walking speeds of droplets of silicone oil of kinematic viscosity 20 and 50 cS, for a broad range of drop sizes and driving frequencies. A schematic illustration of the experimental apparatus is shown in Fig. 4-1. A liquid drop of undeformed radius R_0 bounces on a bath of the same liquid (Fig. 4-2), in our case silicone oil with density $\rho = 949$ kg·m^{-3}, surface tension $\sigma = 20.6 \cdot 10^{-3}$ N/m and kinematic viscosity $\nu = 20$ cS, or a more viscous silicone oil with $\rho = 960$ kg·m^{-3}, $\sigma = 20.8 \cdot 10^{-3}$ N/m and $\nu = 50$ cS. The bath of depth $h_B \approx 9$ mm is enclosed in a cylindrical container with diameter $D = 76$ mm. The container is shaken vertically, sinusoidally in time, with peak acceleration γ and frequency f, so that the effective gravity in the bath frame of reference is $g + \gamma \sin(2\pi f t)$. The motion of the drop was observed using a high-speed camera synchronized with the shaker. The camera resolution is 86 px/mm and the distance of the drop from the camera was controlled with approximately 1% error by keeping the drop in focus, giving a total error in our drop radius measurement of less than 0.01mm. The drops were created by dipping a needle in the bath then quickly retracting it [98]. The drop's initial conditions play little role in its subsequent dynamics, provided coalescence is

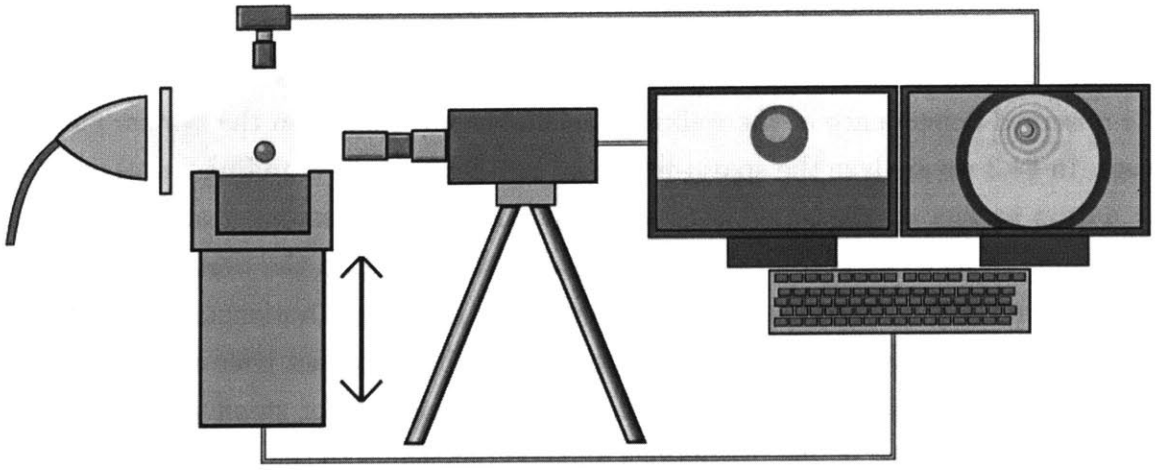

Figure 4-1: The experimental setup. A liquid drop bounces on a vibrating liquid bath enclosed in a circular container. The drop is illuminated by an LED lamp, its vertical motion recorded on a high-speed camera and its horizontal motion recorded on a top view camera. Both cameras are synchronized with the shaker.

avoided. However, a certain amount of hysteresis may arise as the various thresholds are crossed.

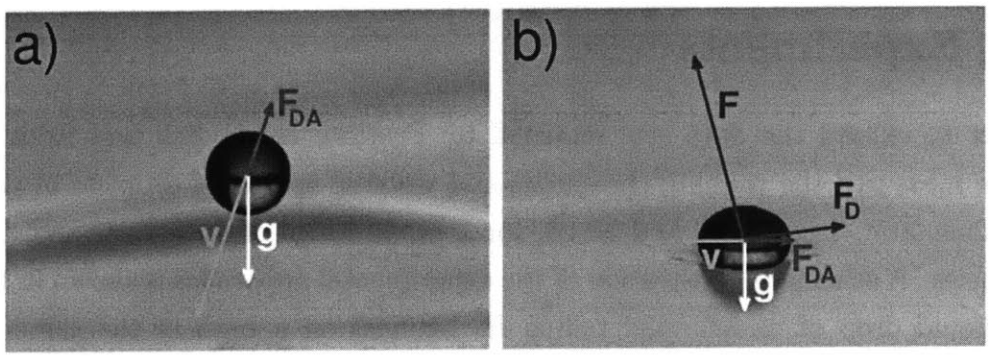

Figure 4-2: A droplet of radius $R_0 = 0.38$mm **(a)** in flight and **(b)** during contact with the bath. During flight, its motion is accelerated by the gravitational force $\boldsymbol{g}$ and resisted by the air drag $\boldsymbol{F}_{DA}$ that opposes its motion $\boldsymbol{v}$. During contact, two additional forces act on the drop; the reaction force $\boldsymbol{F}$ normal to the bath surface and the momentum drag force $\boldsymbol{F}_D$ tangential to the surface and proportional to the tangential component of $\boldsymbol{v}$.

We continue to use the notation adopted in the previous chapter and summarised in Table 3.1. We shall also keep using the (m, n) notation to distinguish between different bouncing modes, following Gilet & Bush [46], and use a superscript to differentiate between the different energy levels. The $(2,1)^1$, $(2,1)^2$ and $(2,2)$ walking modes are shown in Fig. 4-3, together with more complex behaviours observed in

walking drops.

4.2.1 Walking thresholds and speeds

Each impact of the drop on the vibrating liquid bath creates a transient wave that propagates outwards from the centre of impact, leaving in its wake a standing Faraday wave pattern that decays exponentially with both time and distance from the impact centre [32]. As the driving is increased, the temporal decay rate of the standing wave pattern decreases and the total amplitude of the surface deformation increases, being the sum of the standing waves generated by all previous impacts. When the drop is in the $(2,1)$ bouncing mode, it lands on the bath when the standing wave beneath it is convex, bulging upwards: the drop lands on the crest of its associated wave. Consequently, a small perturbation of the horizontal position of the drop during flight leads to a horizontal component of the reaction force imparted during impact that may destabilize the pure bouncing state.

Below a certain driving threshold, which we denote by the walking threshold Γ_W, the drop's horizontal movement is stabilized by air drag, shear drag in the intervening air layer and the force resulting from the transfer of horizontal momentum imparted by the drop to the surface waves. Mechanically, the latter arises since the non-axisymmetric deformation of the drop and bath induced by an oblique impact leads to a horizontal pressure gradient in the contact area due to fluid inertia. For $\Gamma > \Gamma_W$ these stabilizing forces can no longer offset the destabilizing wave force and the drop begins to walk. We henceforth shall refer to drops walking in the $(2,1)$ bouncing mode as *resonant* walkers, due to the periodicity of their vertical motion precisely matching that of the Faraday wavefield. In certain regimes, the drop then settles into a state of straight-line walking with a steady speed. The walking thresholds have been investigated by Protière *et al.* [100] for silicone oil with viscosities ranging from $\mu = 10$ to 100 cS. They found that the walking regime exists only for a small range of driving frequencies, with the typical frequency decreasing with increasing viscosity, as indicated in Table 4.1.

We have measured the walking thresholds for oil with viscosity 20 cS and 50 cS, in both cases spanning the whole range of frequencies over which walking occurs. The experimental results are shown in Fig. 4-4. The vertical axis denotes the *vibration number* $\Omega = \omega/\omega_D$, the ratio of the driving angular frequency $\omega = 2\pi f$ to the characteristic oscillation frequency of the drop $\omega_D = (\sigma/\rho R_0^3)^{1/2}$ (see §3.2). We first note that the walking threshold curves are composed of two distinct parts joined at

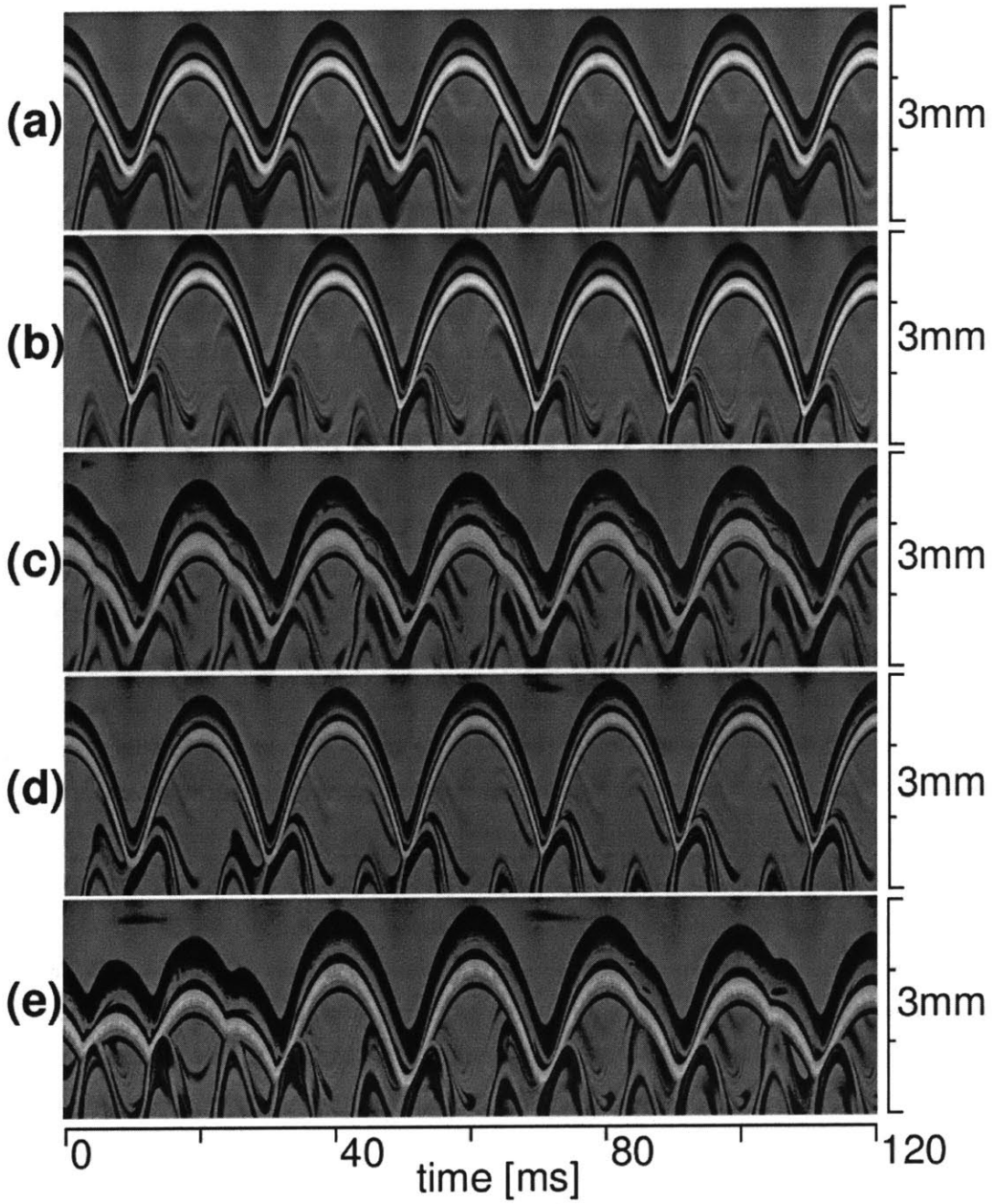

Figure 4-3: Examples of the vertical motion of 50 cS silicone oil drops walking on a liquid bath vibrating with frequency 50 Hz. These are, in order of increasing complexity: **(a)** the $(2,1)^1$ mode, $R_0 = 0.39$mm, $\Gamma = 3.6$; **(b)** the $(2,1)^2$ mode, $R_0 = 0.39$mm, $\Gamma = 4.1$; **(c)** the $(2,2)$ limping mode, $R_0 = 0.57$mm, $\Gamma = 4.0$; **(d)** switching between the $(2,1)^1$ and $(2,1)^2$ modes that arises roughly every 20 forcing periods, $R_0 = 0.35$mm, $\Gamma = 4.0$; **(e)** chaotic bouncing, $R_0 = 0.57$mm, $\Gamma = 4.0$. Here R_0 is the drop radius and $\Gamma = \gamma/g$ the dimensionless driving acceleration. The images were obtained by joining together vertical sections from successive video frames, each 1 pixel wide and passing through the drop's centre. The camera was recording at 4000 fps.

Viscosity [cS]	f_{min} [Hz]	f_{opt} [Hz]	f_{max} [Hz]
10	100	110	125
20	60	80	90
50	40	55	60
100	35	45	50

Table 4.1: The range of driving frequencies for which drops can walk, for various values of the oil viscosity, as reported by Protière *et al.* [100]. Walking occurs for $f_{min} \leq f \leq f_{max}$, with the minimum value of Γ_W/Γ_F occurring at $f = f_{opt}$. For $f = f_{opt}$, the smallest relative driving acceleration Γ_W/Γ_F is required to produce a walking drop. The resolution of their frequency sweep was 5 Hz.

$\Gamma_{WM} = \min_\Omega \{\Gamma_W\}$, the minimum driving acceleration required to produce walking. While the lower branches of the threshold curves seem to have similar slopes for all frequencies, the slopes of the upper branches decrease dramatically with increasing frequency, until disappearing completely as f approaches f_{max}. We also observe that the peak of the walking regime moves to higher Ω with increasing frequency, but never greatly exceeds $\Omega = 1$.

The dependence of the horizontal walking speed on the driving acceleration is shown in Fig. 4-5. The walking speed generally increases with increasing drop size, but this trend may be violated for larger drops due to complications associated with the vertical dynamics, an effect to be discussed in §4.5.

4.3 Waves on the Bath Surface

The purpose of this section is to describe the evolution of the bath deformation caused by a single drop impact. We will assume the deformations to be small and additive, so that the bath shape after multiple drop impacts can be simply obtained by adding the contributions from successive impacts. We are particularly interested in the long-term evolution of the surface waves, which is important in the dynamics of walkers close to the Faraday threshold. Of course, the bath surface profile only influences the drop dynamics when the drop is in contact with the bath; thus, any transient behaviour arising between impacts is irrelevant to our model and need not be considered.

We thus consider a single, normal impact of a liquid drop on a flat vibrating liquid bath. We assume that the drop is initially spherical and therefore the wavefield is radially symmetric about the point of impact. The dimensional height of the bath surface will thus depend only on time and distance from the axis of symmetry:

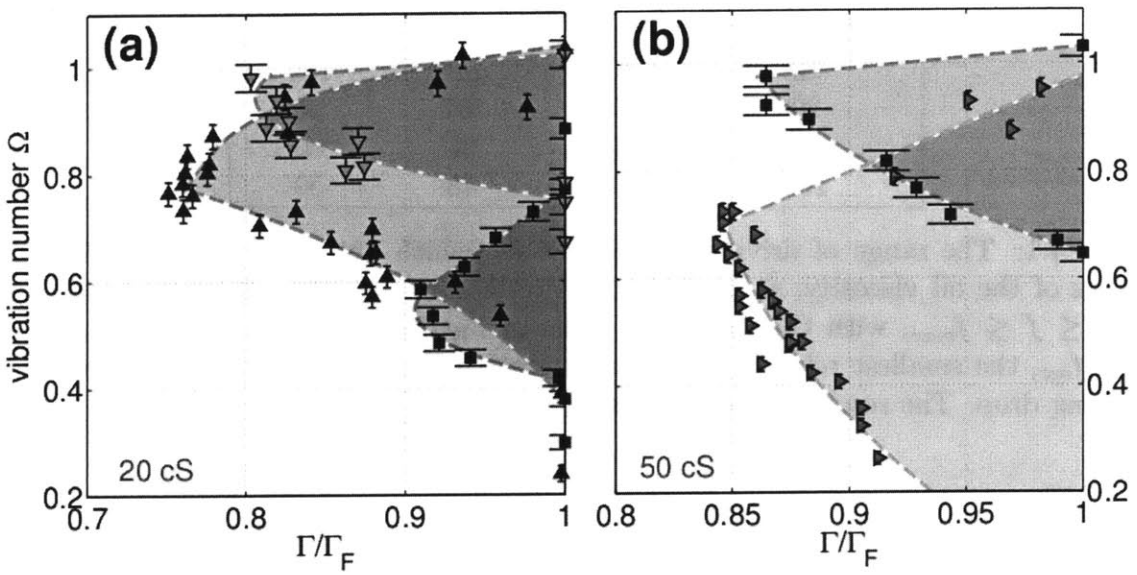

Figure 4-4: The walking thresholds for silicone oil droplets of viscosity **(a)** 20 cS and **(b)** 50 cS on a vibrating bath of the same oil. The experimentally measured threshold acceleration $\Gamma = \gamma/g$ (horizontal axis) is shown as a function of the vibration number $\Omega = \omega/\omega_D$ (vertical axis) for several values of the driving frequency f: 50 Hz (▶), 60 Hz (■), 80 Hz (▲) and 90 Hz (▼). The dashed lines are best-fit curves provided to guide the eye.

$h'(x, y, t) = h'(r', t)$. We nondimensionalize the governing equations using length- and timescales deduced from the drop radius R_0 and the characteristic oscillation frequency of the drop $\omega_D = (\sigma/\rho R_0^3)^{1/2}$:

$$h = h'/R_0 \ , \ r = r'/R_0 \ , \ \tau = \omega_D t = t\left(\sigma/\rho R_0^3\right)^{1/2} \ , \ Z = z/R_0 \ , \ k = k' R_0 \ . \quad (4.1)$$

The Hankel transform $H(k, \tau)$ of the dimensionless surface height $h(r, \tau)$ is defined by

$$H(k,\tau) = \int_0^\infty h(r,\tau) J_0(kr) r dr \text{ so that } \ h(r,\tau) = \int_0^\infty H(k,\tau) J_0(kr) k dk \ . \quad (4.2)$$

Here, and throughout the chapter, $J_i(x)$ denotes the Bessel function of the first kind and order i. The effective gravity in the bath frame of reference, defined as the sum of gravity and the fictitious force arising in this vibrating reference frame, is given by

$$\mathcal{B}o^*(\tau) = \mathcal{B}o\,(1 + \Gamma \sin \Omega\tau) \ . \quad (4.3)$$

In the frame of reference fixed with the oscillating bath, the quiescent bath surface

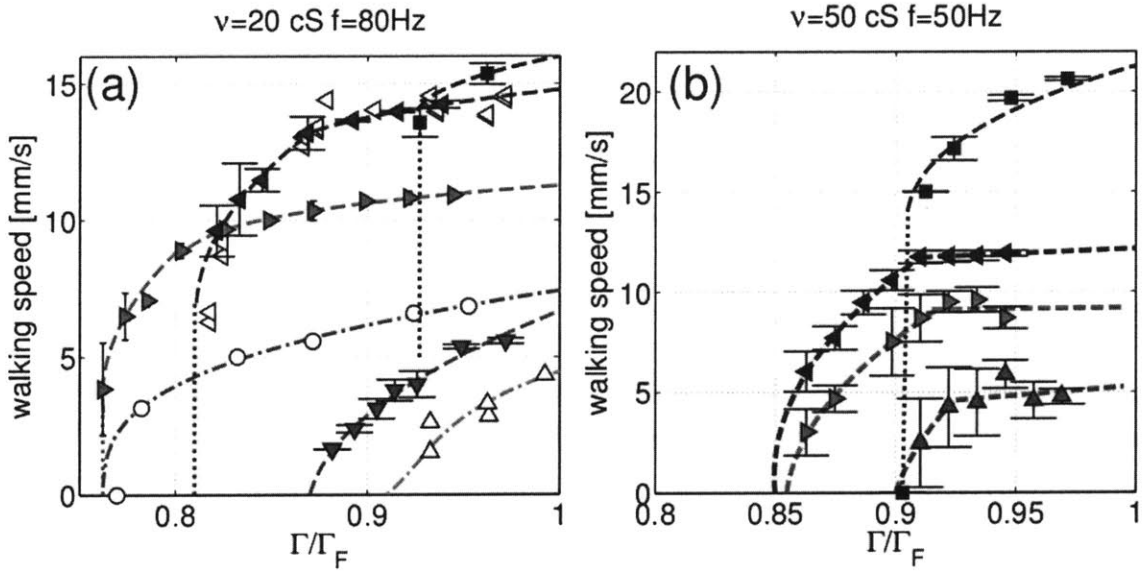

Figure 4-5: The walking speed of silicone oil droplets for **(a)** $\nu = 20$ cS, $f = 80$ Hz and **(b)** $\nu = 50$ cS, $f = 50$ Hz, bouncing on a vibrating bath of the same oil, as a function of the driving acceleration. The experimentally measured speeds are shown for several droplet radii R_0. For 20 cS, $R_0 = 0.31$ mm (▼), 0.38 mm (►) , 0.40 mm (◄) and 0.43 mm (■), while for 50 cS, $R_0 = 0.25$ mm (▲), 0.34 mm (►), 0.39 mm (◄) and 0.51 mm (■). In **(a)**, the walking speeds reported by Protière *et al.* [98] are shown for comparison, for drop radii 0.28 mm (△), 0.35 mm (◯) and 0.41 mm (◁).

is located at $Z = 0$ at all times. The vertical position $Z(\tau)$ of the drop will be represented by its centre of mass shifted down by one radius, so that $Z(\tau) = 0$ when the drop first makes contact with the unperturbed bath. $Z(\tau)$ is then governed by

$$\frac{\partial^2 Z}{\partial \tau^2} = F(\tau) - \mathcal{B}o^*(\tau) \quad , \tag{4.4}$$

where F is the dimensionless reaction force acting on the drop. The Hankel transform of the surface height can be modeled by the following equation:

$$H_{\tau\tau} + 2\mathcal{O}h_e k^2 H_\tau + H\left[k^3 + k\mathcal{B}o^*(\tau)\right] = -\frac{4}{3}F(\tau)\frac{J_1(wk)}{w} \quad , \tag{4.5}$$

where w is the dimensionless extent of the contact region and $\mathcal{O}h_e = \mu_e/\left(\sigma\rho R_0\right)^{1/2}$ is an effective Ohnesorge number (see Appendix C, §C.0.2). When $\mathcal{B}o \ll 1$, we can approximate the forcing term in (4.5) by a point forcing (see §C.0.3) and so obtain

$$H_{\tau\tau} + 2\mathcal{O}h_e k^2 H_\tau + H\left(k^3 + k\mathcal{B}o^*(\tau)\right) = -\frac{2}{3}kF(\tau) \; . \tag{4.6}$$

In §C.0.4 we analyze the long-term evolution of the bath surface following a single drop impact when the forcing is close to the Faraday threshold Γ_F. We find (see eqn. (C.50)) that the impact creates a standing wave with nearly sinusoidal time-dependence and Bessel function spatial-dependence, which decays exponentially in time. The rate of decay is proportional to the relative distance from the Faraday threshold $1-\Gamma/\Gamma_F$. The amplitude of the wave is given by the integral of the reaction force F over the contact time, multiplied by the Green's function for (4.5), which is approximately $\sin\Omega\tau/2$:

$$h(r,\tau) \approx \frac{4\sqrt{2\pi}}{3\sqrt{\tau}}\frac{k_C^2 k_F \mathcal{O}h_e^{1/2}}{3k_F^2 + \mathcal{B}o}\left[\int_{\tau_C} F(u)\sin\frac{\Omega u}{2}\mathrm{d}u\right]\cos\frac{\Omega\tau}{2}\exp\left\{\left(\frac{\Gamma}{\Gamma_F}-1\right)\frac{\tau}{\tau_D}\right\}J_0(k_C r) \; . \tag{4.7}$$

The critical (most unstable) wavenumber k_C is found to be close to the Faraday wavenumber k_F, given by the dispersion relation [4]

$$k_F^3 + \mathcal{B}o \cdot k_F = \frac{1}{4}\Omega^2 \quad . \tag{4.8}$$

Eqn. (4.7) is found to be a good approximation provided that $\left(\mu^3 f/\rho\sigma^2\right)^{1/3} \ll 2$ (C.51), which is satisfied for the parameter range of interest. In order to obtain a closer match with experimental data, the analytic expression (4.7) is superceded by a

slightly more complex relation, derived in §C.0.5 using a more complete description of the wavefield:

$$h(r,\tau) \approx \frac{4\sqrt{2\pi}}{3}\frac{k_C^2 k_F \mathcal{O}h_e^{1/2}}{3k_F^2+\mathcal{B}o}\left[\int F(u)\sin\frac{\Omega u}{2}\mathrm{d}u\right]\frac{\bar{H}(\tau)}{\sqrt{\tau}}\exp\left\{\left(\frac{\Gamma}{\Gamma_F}-1\right)\frac{\tau}{\tau_D}\right\}J_0(k_C r)\ , \tag{4.9}$$

with $\bar{H}(\tau)$, k_c and τ_D now determined by a numerical scheme described in §C.0.5. To illustrate the accuracy of (4.9), we compare it to a full numerical solution of (4.6) in Fig. 4-6.

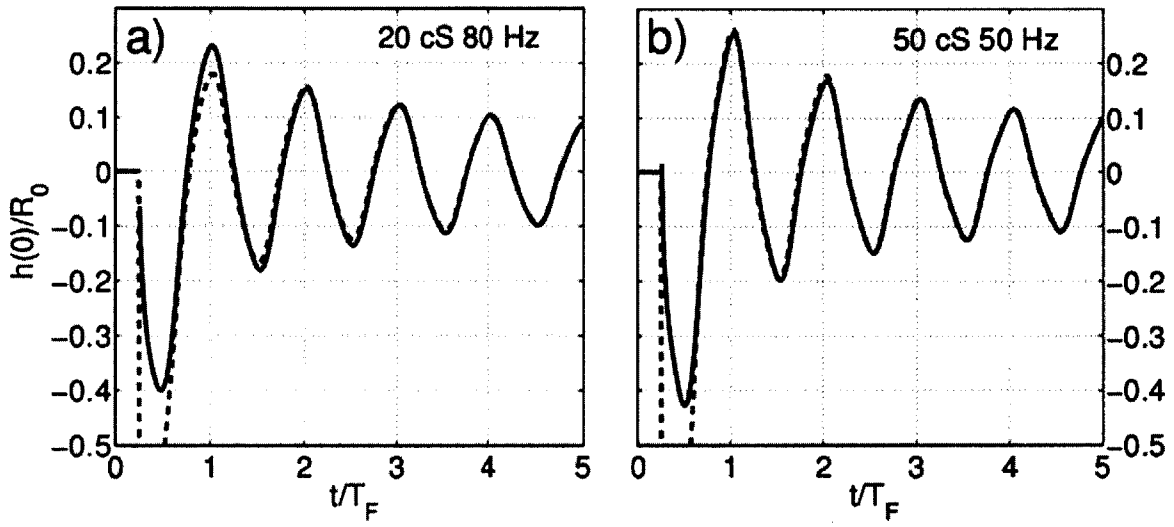

Figure 4-6: Comparison between the full numerical model (*dashed line*) and the long-term approximation (C.50) (*solid line*) for **(a)** 20 cS oil and **(b)** 50 cS oil. The dimensionless height of the surface $h(0,\tau)$ at the centre of drop impact is shown as a function of time, nondimensionalized by the Faraday period $T_F = 2/f$. The surface is forced at $t = T_F/4$ and then evolves freely.

4.4 Horizontal Dynamics

In this section, we combine our models for the vertical drop dynamics developed in §3.3.2 and the standing wave evolution (from §4.3) in order to describe the complete drop dynamics. The model presented here is readily generalizable to a full three-dimensional model; however experimental evidence indicates the prevalence of a 2-dimensional motion, in which the drop is confined within a vertical plane unless perturbed transversely by an external force or through interaction with boundaries. We thus expect that a 2-D model will suffice in describing the behaviour of a drop

bouncing on an unbounded vibrating liquid bath.

We nondimensionalize the position and time as in §4.3, and denote the horizontal drop position by $X(\tau) = x(\tau)/R_0$.

4.4.1 Horizontal drag during contact

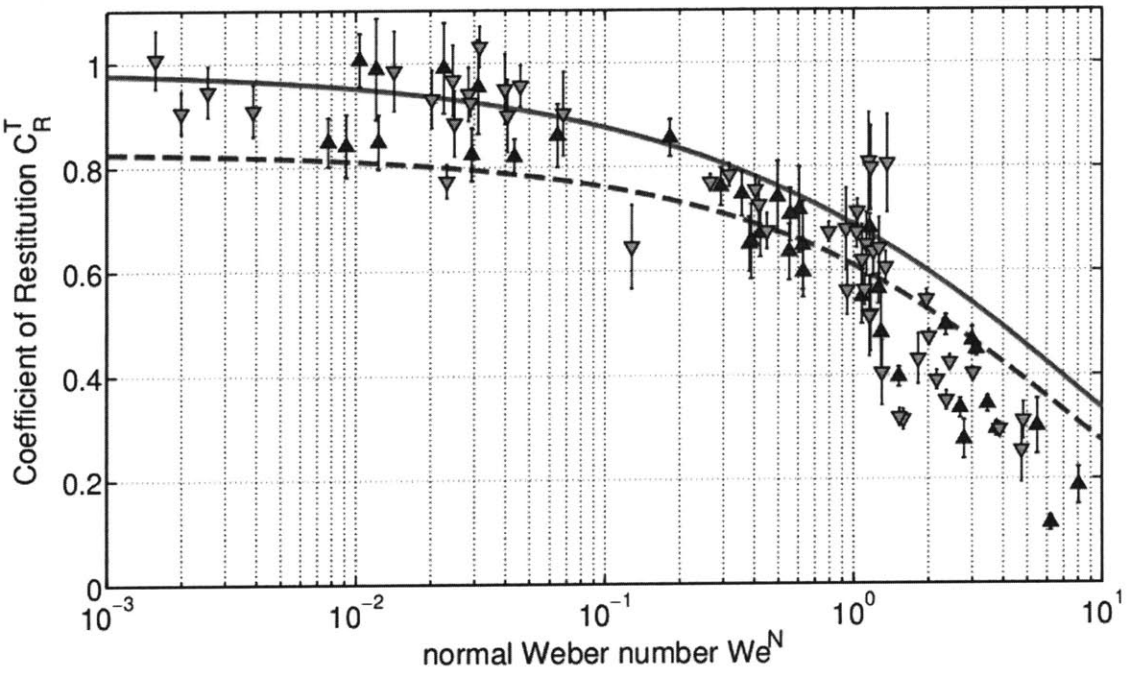

Figure 4-7: The tangential coefficient of restitution $C_R^T = v_{out}^T/v_{in}^T$ as a function of the normal Weber number $\mathcal{W}e^N = \rho R_0(v_{in}^N)^2/\sigma$, where v^T, v^N are the tangential and normal components of the drop velocity relative to the bath surface. Data for 20 cS (▼) and 50 cS (▲) silicone oil are shown, together with the values obtained with the model (4.10) with $C = 0.3$ for $R_0 = 0.1$ mm (*solid line*) and $R_0 = 0.4$ mm (*dashed line*). The impact angle with respect to the bath surface ranged from 45° to nearly 90°.

All previous models of walking drops have assumed, following the argument first proposed by Protière *et al.* [98], that the shearing inside the intervening air layer provides the principal contribution to the horizontal drag during impact. Instead, we propose that the dominant contribution comes from the direct transfer of momentum from the drop to the bath during impact. The resulting horizontal force is difficult to characterize analytically or numerically, due to the asymmetry of the drop and bath surfaces involved, but the resulting tangential coefficient of restitution $C_R^T = v_{out}^T/v_{in}^T$ is straightforward to measure experimentally.

We have recorded C_R^T for silicone oil drops with 0.1mm $\leq R_0 \leq$ 0.6mm, $\nu = 20$ cS and $\nu = 50$ cS and a wide range of normal and tangential velocities (0.01 m/s $\leq v_{in}^T, v_{in}^N \leq$ 0.8 m/s). The results are shown in Fig. 4-7 as a function of the normal Weber number $We^N = \rho R_0 (v_{in}^N)^2/\sigma$. The data indicate that C_R^T depends only weakly on the oil viscosity. Note that we have controlled neither the tangential velocity v_{in}^T nor the normal velocity v_{in}^N and the incident angle θ thus ranged from nearly 90° (for normal impact) to 45°. The near collapse of the data onto a single curve implies that, over the parameter regime of interest, C_R^T does not depend appreciably on either θ or v_{in}^T, which indicates that the tangential drag force depends linearly on v_{in}^T. We conclude that the dimensionless tangential force on the drop $\bar{F}_D$ is a function of the drop position Z, normal velocity Z_τ and the normal force F, multiplied by the tangential velocity: $\bar{F}_D = C(Z, Z_\tau, F) \cdot X_\tau$. For the sake of simplicity, we assume $\bar{F}_D = C \cdot F^a \cdot X_\tau$. The coefficients C and a can be determined by matching the experimental data; the best match is achieved for $1 \lesssim a \lesssim 1.5$. We shall use $a = 1$, and so write

$$\bar{F}_D = C \cdot F \cdot X_\tau \qquad \text{where} \quad F = Z_{\tau\tau} + \mathcal{B}o^* \ . \tag{4.10}$$

The experimental data is best fit by choosing $C = 0.3$, as is shown in Fig. 4-7, where the two curves indicate the model predictions for $R_0 = 0.1$ mm and $R_0 = 0.3$ mm. Using the shearing force in the air layer as the dominant drag force gives $\bar{F}_D \sim F^{1/2}$ (see Appendix D), leading to an underestimation of the tangential drag for high Weber numbers (since $F^{1/2} < F$).

4.4.2 Horizontal drag during flight

When the drop is in flight (specifically, not experiencing a reaction force from the bath), its dynamics may be approximated by the system

$$\begin{aligned} X_{\tau\tau} &= -F_{DA}(\bar{V})\frac{X_\tau}{\bar{V}} \\ Z_{\tau\tau} &= -\mathcal{B}o^*(\tau) - F_{DA}(\bar{V})\frac{Z_\tau}{\bar{V}} \ , \end{aligned} \tag{4.11}$$

where, as previously, $\mathcal{B}o^*(\tau) = \mathcal{B}o(1 + \Gamma \sin \Omega\tau)$ is the effective gravity in our vibrating frame of reference, $\bar{V} = (X_\tau^2 + Z_\tau^2)^{1/2}$ is the dimensionless droplet speed, and F_{DA} is the air drag. We assume that the drag is always opposite to the velocity and its magnitude is a function of speed only, thus neglecting the effect of the bath on the air flow around the drop [50]. The maximum value of the Reynolds number $\mathcal{R}e_{max} = 2R_0 V_{max}/\nu_a = 2gR_0/f\nu_a$ varies between 4 for $f = 100$ Hz and $R_0 = 0.3$ mm

and 16 for $f = 40$ Hz and $R_0 = 0.5$ mm, so the Stokes formula for the air drag on a rigid sphere is no longer accurate. Moreover, the motion of drop is unsteady and we need to take into account the variable flow profile around the drop. The Strouhal number $\mathcal{S}t = \omega R_0/V_{max} = \pi R_0 f^2/g$, a measure of the flow unsteadiness, is typically between 0.1 and 1 in our system. Chang & Maxey [12] showed that the relative magnitude of the correction to the Stokes drag is on the order of $\mathcal{R}e \cdot \mathcal{S}t/6$ when both of these dimensionless numbers achieve small or moderate values:

$$F_{DA} = \frac{9}{2}\mathcal{O}h_a \bar{V} \left[1 + O\left(\frac{1}{6}\mathcal{R}e\mathcal{S}t\right)\right] \tag{4.12}$$

We shall show that the correction in (4.12) is negligible in its effect on the horizontal drop dynamics relative to the sum of the Stokes drag and the momentum drag during impact. To that end, we average the horizontal equation of motion over the period of drop's motion P, giving us the average drag on the drop. Integrating (4.10), we derive that the momentum drag contribution to the average drag scales like $X_\tau \cdot C(\int F)/P = C \cdot X_\tau \mathcal{B}o$, since by periodicity the integral of the reaction force on the drop $\int F$ must equal the integral of the gravitational force $\int \mathcal{B}o = \mathcal{B}o \cdot P$ over the period. The contribution of the air drag scales simply like $X_\tau \cdot \left[\frac{9}{2}\mathcal{O}h_a + O\left(\frac{3}{4}\mathcal{O}h_a\mathcal{R}e\mathcal{S}t\right)\right]$. The relative magnitude of the Stokes drag to the momentum drag contribution is therefore given by $9\mathcal{O}h_a/2C\mathcal{B}o \approx 20\mu_a\sigma^{1/2}\rho^{-3/2}g^{-1}R_0^{-5/2}$, which varies between 0.36 for $R_0 = 0.2$ mm, and 0.02 for $R_0 = 0.6$ mm. As expected, the air drag plays much smaller role for larger drops and is never the dominant source of momentum loss, but for drops below $R_0 = 0.4$ mm it cannot be neglected. However, the relative magnitude of the air drag correction to the momentum drag, given by $3\mathcal{O}h_a\mathcal{R}e\mathcal{S}t/4C\mathcal{B}o = 25\rho_a\sigma^{1/2}f\rho^{-3/2}g^{-1}R_0^{-1/2}$, varies between 0.08 for $R_0 = 0.2$ mm and $f = 80$ Hz and 0.03 for $R_0 = 0.6$ mm and $f = 50$ Hz. Therefore we shall from now on neglect the correction term.

It is also straightforward to check that in the vertical direction the drag is negligible relative to gravity, their ratio being at most $9\mu_a/2\rho f R_0^2$, which is at most 0.04 for $R_0 \geq 0.2$ mm and $f \geq 50$ Hz. Therefore (4.11) can be simplified to

$$X_{\tau\tau} = -\frac{9}{2}\mathcal{O}h_a X_\tau \ , \quad Z_{\tau\tau} = -\mathcal{B}o^*(\tau) \ . \tag{4.13}$$

4.4.3 Horizontal kick

The remaining force to be evaluated is the horizontal component of the reaction force, arising due to the slope of the wavefield beneath the drop. It is important to clarify

the somewhat artificial distinction between the reaction and drag forces. By the reaction force, we mean that part of the total force on the drop during contact that is independent (to leading order) of the drop's horizontal velocity. Conversely, the drag component was found to scale linearly with the drop's horizontal speed. Had the drop impact been instantaneous, the tangential component of the reaction force could be obtained from its vertical component simply by calculating the slope of the interface at the position of the drop:

$$\bar{F}_T = -\frac{\partial h(X,\tau)}{\partial X} \cdot F \quad , \tag{4.14}$$

assuming small slope (so that $\sin\theta \approx \theta$ for the slope angle). Such an approximation loses accuracy when the contact time of the drop becomes comparable to the Faraday period, because the slope of the interface changes significantly during contact. The interplay between the interface deformation beneath the drop and its changing slope further away is far from trivial. Unless one can afford to numerically model the whole complex dynamics of this interaction (which would decrease the speed of computation by many orders of magnitude), one can do no better than calculate a weighted average of the slope over the contact time. The average slope weighted by the instantaneous reaction force (4.14) is the most natural and yields the best results; thus, it will adopted in our model. However, the predictions obtained using this model for $\Omega \gtrsim 1$ or for the $(2,1)^1$ walking mode are likely to be skewed, due to the contact time extending over a relatively large fraction of the Faraday period.

4.4.4 Summary of the model

The vertical dynamics of the drop is governed by the logarithmic spring model developed in §3.3.2 in order to capture the dynamics of drop rebound on a liquid bath for Weber numbers ranging from small to moderate ($We \lesssim 3$). It was derived using a variational approach by assuming a quasi-static form for both the drop and interface shape during impact. The dimensional form of the model equations is presented in (4.15) below. When the drop is in flight, it is acted upon only by the effective gravity (gravity plus the fictitious force in the vibrating bath reference frame), with air drag being negligible. During contact the drop also feels a reaction force dependent on the relative position of the drop and bath height $z - h$, as well as a drag dependent on the relative speed of the drop and bath $\dot{z} - \dot{h}$. Unlike for a linear spring model, the dependence of the reaction force on the relative position and of the drag on the relative speed is not linear, as evidenced by the logarithmic correction in

(4.15). This nonlinearity has the effect of reducing dissipation and prolonging contact for smaller impact speeds. There is also a correction to the drop inertia coming from the drop's internal fluid motion. The three coefficients c_i present in the model were fixed by matching the experimentally measured coefficients of restitution and contact times, as described in §3.3. The model was shown to accurately predict the regime diagrams of the drop's vertical bouncing motion. Writing m for the drop mass, $g^*(t) = g + \gamma \sin(2\pi f t)$ for the gravitational acceleration in the vibrating bath frame of reference, and $F_N = m\ddot{z} + mg^*(t)$ for the normal component of the reaction force acting on the drop, we have

$$m\ddot{z} = -mg^*(t) \quad \text{in flight,} \tag{4.15a}$$

$$\left(1+\frac{c_3}{\ln^2\left|\frac{c_1 R_0}{z-h}\right|}\right) m\ddot{z} + \frac{4}{3}\frac{\pi\mu R_0 c_2(\nu)}{\ln\left|\frac{c_1 R_0}{z-h}\right|}\left(\dot{z}-\dot{h}\right) + \frac{2\pi\sigma(z-h)}{\ln\left|\frac{c_1 R_0}{z-h}\right|} = -mg^*(t) \quad \text{otherwise.} \tag{4.15b}$$

The drop is defined to be in flight when either $z \geq h$ or when F_N, as computed from (4.15b), would return a negative value. The constants used here, as in *MBI*, were $c_1 = 2$, $c_3 = 1.4$, $c_2 = 12.5$ for 20 cS and $c_2 = 7.5$ for 50 cS. These values can be determined either by matching the known normal coefficient of restitution C_R^N and contact time T_C of the drop and their dependence on We, or by fitting the regime diagrams of the vertical bouncing motion, as was done in *MBI*. The total height of the standing waves in the bath frame of reference $h = h(X, \tau)$ can be expressed as the sum of contributions from all previous impacts:

$$h(x,t) = \sum_{n=1}^{N} h_0(x, x_n, t, t_n) \quad . \tag{4.16}$$

The single contribution $h_0(x, x_n, t, t_n)$ resulting from an impact at $(x,t) = (x_n, t_n)$ is given by the long-time approximation (C.52):

$$h_0(x, x_n, t, t_n) \approx \sqrt{\frac{2}{\pi}}\frac{k_F R_0}{3k_F^2 R_0^2 + Bo}\frac{R_0 k_C^2 \mu_e^{1/2}}{\sigma}\left[\int F_N(t')\sin(\pi f t')\,\mathrm{d}t'\right] \times$$
$$\times \frac{\bar{H}(t)}{\sqrt{t-t_n}}\exp\left\{(\Gamma/\Gamma_F - 1)\frac{t-t_n}{T_d}\right\} J_0\left(k_C(x-x_n)\right) \quad . \tag{4.17}$$

In order to increase computational speed, the number of previous impacts stored is kept to a manageable size by discarding those whose standing wave amplitude has decayed sufficiently (below 0.1% of its inital value). Since the contact takes place over a finite length of time, x_n and t_n are taken as the weighted averages of x and t over the contact time:

$$x_n = \int_{t_c} F_N(t')x(t')\mathrm{d}t' \Big/ \int_{t_c} F_N(t')\mathrm{d}t' \quad , \quad t_n = \int_{t_c} F_N(t')t'\mathrm{d}t' \Big/ \int_{t_c} F_N(t')\mathrm{d}t' \ . \tag{4.18}$$

Finally, the horizontal dynamics is governed by

$$m\ddot{x} + D(t)\dot{x} = -h_x \cdot F_N \quad , \tag{4.19}$$

where $D(t) = C\sqrt{\rho R_0/\sigma}F_N(t) + 6\pi R_0\mu_a$ is the total instantaneous drag coefficient and C is the proportionality constant for the tangential drag force. If our model is correct, the value of C should be close to 0.3. In fact, we expect it to be slightly less than 0.3, as the tangential coefficient of restitution measured experimentally also includes the contribution from the shearing in the intervening air layer. This contribution is presumably smaller for walking drops, which, after repeated impacts on the bath with associated shear torques, should acquire a rotation which would reduce the relative velocity of the two surfaces during contact.

4.4.5 Analysis for small drops

We now simplify the equations (4.17)-(4.19) by assuming that the drop is in the $(2,1)^2$ mode and $\Omega \ll 1$, which means that the drop is bouncing periodically with the Faraday period $T_F = 2/f$ and the contact time per period is much shorter than T_F. It follows that $\int_t^{t+T_F} F_N(t')\mathrm{d}t' = \int_t^{t+T_F} m\ddot{z}(t) + mg^*(t')\mathrm{d}t' = \dot{z}|_t^{t+T_F} + mgT_F = mgT_F$. We can define the phases Φ_i^1 and Φ_i^2 as follows:

$$\int F_N(t')\sin(\pi f t')\,\mathrm{d}t' = \left[\int F_N(t')\mathrm{d}t'\right]\sin\frac{\Phi_i^1}{2} = mgT_F\sin\frac{\Phi_i^1}{2} \quad , \tag{4.20a}$$

$$\int F_N(t')\cos(\pi f t')\,\mathrm{d}t' = \left[\int F_N(t')\mathrm{d}t'\right]\cos\frac{\Phi_i^2}{2} = mgT_F\cos\frac{\Phi_i^2}{2} \ . \tag{4.20b}$$

Thus, $\sin(\Phi_i^1/2)$ is the weighted average of $\sin(\pi f t)$ over the duration of the contact and similarly $\cos(\Phi_i^2/2)$ the weighted average of $\cos(\pi f t)$. For small Ω, the contact time is sufficiently short that we have $\Phi_i^1 \approx \Phi_i^2$. We then define the phase of impact

Φ_i by the following relation:

$$\sin\Phi_i = 2\sin\frac{\Phi_i^1}{2}\cos\frac{\Phi_i^2}{2} \tag{4.21}$$

Approximating k_C by k_F and $\bar{H}(t)$ by $\cos(\pi f t)$ as in (C.49), we can write (4.17) as

$$h_0(x,x_n,t,t_n) \approx A\sin\frac{\Phi_i^1}{2}\frac{\cos(\pi f t)}{\sqrt{t-t_n}}\exp\left\{(\Gamma/\Gamma_F-1)\frac{t-t_n}{T_d}\right\}J_0\left(k_F(x-x_n)\right) \quad ,$$

$$\text{where} \qquad A = \sqrt{\frac{2}{\pi}}\frac{k_F R_0}{3k_F^2R_0^2+\mathcal{B}o}\frac{R_0 k_F^2\mu_e^{1/2}}{\sigma\rho^{1/2}}mgT_F \; . \tag{4.22}$$

Following Eddi *et al.* [32] we introduce the dimensionless "memory" parameter

$$\mathcal{M}_e = \frac{T_d}{T_F(1-\Gamma/\Gamma_F)} \quad , \tag{4.23}$$

that prescribes the inverse of the decay rate of the waves and so the number of the previous impacts that significantly contribute to the overall surface deformation. Assuming that the drop's horizontal speed varies on a timescale that is much longer than the bouncing period, we can integrate (4.19) over one period to obtain

$$m\ddot{x}+\bar{D}\dot{x} = -mg\frac{\partial h}{\partial x} = -\tfrac{1}{2}Amg\sin\Phi_i\frac{\partial}{\partial x}\sum_{n=1}^{N}\frac{e^{-n/\mathcal{M}_e}}{\sqrt{nT_F}}J_0\left(k_F\left(x-x_n\right)\right) , \tag{4.24}$$

where $\bar{D} = C\sqrt{\rho R_0/\sigma}mg + 6\pi R_0\mu_a$ is the average horizontal drag coefficient. We have used (4.21) and the assumption that the contact time is much smaller than T_F, approximating $t'-t_n$ by $t_{N+1}-t_n$. We have also reversed the sequences $\{x_n\}$ and $\{t_n\}$, so that (x_1,t_1) now corresponds to the most recent impact. We can easily generalize (4.24) to the case of drop walking in a plane rather than a line, by replacing $\partial/\partial x$ with $\boldsymbol{\nabla}$:

$$m\ddot{\boldsymbol{x}}+\bar{D}\dot{\boldsymbol{x}} = -mg\boldsymbol{\nabla}h = -\tfrac{1}{2}Amg\sin\Phi_i\boldsymbol{\nabla}\sum_{n=1}^{N}\frac{e^{-n/\mathcal{M}_e}}{\sqrt{nT_F}}J_0\left(k_F\left(\boldsymbol{x}-\boldsymbol{x}_n\right)\right) , \tag{4.25}$$

which represents the walker's horizontal trajectory equation.

Now we assume that the drop is walking horizontally with steady average speed v, so that $x(t+T_F)-x(t) = v\cdot T_F$. We can then rewrite (4.24) as

$$\bar{D}v = \tfrac{1}{2}Amg\cdot k_F\sin\Phi_i\sum_{n=1}^{N}\frac{e^{-n/\mathcal{M}_e}}{\sqrt{nT_F}}J_1\left(nk_FT_Fv\right) . \tag{4.26}$$

In order to simplify the subsequent equations, we here neglect the contribution of the air drag to the total average drag $\bar{D}$, and derive

$$v = \sqrt{\frac{\sigma}{\rho R_0}} \frac{A k_F \sin\Phi_i}{2C T_F^{1/2}} \sum_{n=1}^{\infty} e^{-n/\mathcal{M}_e} n^{-1/2} J_1\left(n k_F T_F v\right) \ . \tag{4.27}$$

In (4.27), only $\mathcal{M}_e$ and Φ_i depend on the bath acceleration. While $\mathcal{M}_e$ depends strongly on the distance from threshold, Φ_i changes more gradually, with values generally in the range $0.25 < \sin\Phi_i < 0.65$. For the sake of simplicity, at this stage we set $\sin\Phi_i$ to be a constant. Finally, we use $C = 0.2$, a value that is found to best fit the data (see §4.5). After all the aforementioned simplifications, we are left with a relatively simple expression for the horizontal particle speed:

$$v = \frac{5}{2}\sqrt{\frac{\sigma}{\rho R_0}} A \sin\Phi_i k_F T_F^{-1/2} \sum_{n=1}^{\infty} e^{-n/\mathcal{M}_e} n^{-1/2} J_1\left(n k_F T_F v\right) \ . \tag{4.28}$$

For small values of $\mathcal{M}_e$ (far from the Faraday threshold), (4.28) has only one solution, $v = 0$, i.e. a droplet bouncing with no lateral motion. When the memory increases above a critical value $\mathcal{M}_e^c$, however, the zero solution becomes unstable and a pair of nonzero solutions appear (one negative, one positive). It is possible to obtain an approximation to $\mathcal{M}_e^c$ by taking the limit $v \to 0$ (i.e. approaching the critical value from above), or equivalently $J_1\left(n k_F T_F v\right) \to n k_F T_F v/2$ for each n, which means that (4.28) is satisfied for

$$v = 0 \quad \text{or} \quad 1 = \frac{5}{4}\sqrt{\frac{\sigma}{\rho R_0}} A \sin\Phi_i k_F^2 T_F^{1/2} \sum_{n=1}^{\infty} e^{-n/\mathcal{M}_e} n^{1/2} \ . \tag{4.29}$$

$\mathcal{M}_e^c$ is then the value of $\mathcal{M}_e$ for which the latter equality is satisfied. We approximate the infinite sum

$$\sum_{n=1}^{\infty} e^{-n/\mathcal{M}_e} n^{1/2} = \int_0^{\infty} e^{-x/\mathcal{M}_e} x^{1/2} \mathrm{d}x \left(1 + \mathrm{O}\left(\mathcal{M}_e^{-1}\right)\right) \approx \Gamma\left(\tfrac{3}{2}\right) \mathcal{M}_e^{3/2} \ , \tag{4.30}$$

and so deduce

$$\mathcal{M}_e^c \approx \left[\frac{\sqrt{\pi}}{2}\frac{5}{4} A \sin\Phi_i k_F^2 \sqrt{\frac{\sigma T_F}{\rho R_0}}\right]^{-2/3} = \left[\frac{5\sqrt{2}\pi \sin\Phi_i \left(k_F R_0\right)^5}{6\left(3k_F^2 R_0^2 + \mathcal{B}o\right)} \sqrt{\frac{\mu_e g^2 T_F^3}{\sigma R_0}}\right]^{-2/3} . \tag{4.31}$$

By combining (4.31) with (4.23), we can derive an approximation to the walking

threshold Γ_W, while (4.28) enables us to calculate the dependence of the walking speed v on the driving acceleration. The comparison of the predictions for this small drop regime with experimental results is shown in Figs. 4-8-4-9. We note that without the detailed knowledge of $\sin\Phi_i$ (we used a constant value), the predictions are not entirely satisfactory. Although in Fig. 4-8 we see that the predicted walking threshold does shift to higher Ω with increasing frequency, the change is not sufficiently large. Moreover, we cannot capture the finite size of the walking regime, specifically, its confinement to $\Omega \lesssim 1$, without considering the switching of vertical bouncing modes.

In Fig. 4-9, we compare the predicted walking speed dependence on driving acceleration with the experimental data. By choosing the phase Φ_i appropriately, we can match the data for at least one drop size. However, the match for the other drop sizes is then rather poor, with the model being too insensitive to drop size for 20cS (Fig. 4-9a) and too sensitive for 50cS (Fig. 4-9b). Additionally, the slopes of the experimentally measured curves decrease for larger driving accelerations, while the theoretical curves show no such trend. This discrepancy can largely be attributed to the gradual change of phase with increasing driving acceleration, a necessary implication of the periodicity condition. Furthermore, in Fig. 4-9b the phase changes discontinuously around $\Gamma \approx 0.92\Gamma_F$ due to a transition between the $(2,1)^1$ and $(2,1)^2$ walking modes (see §5).

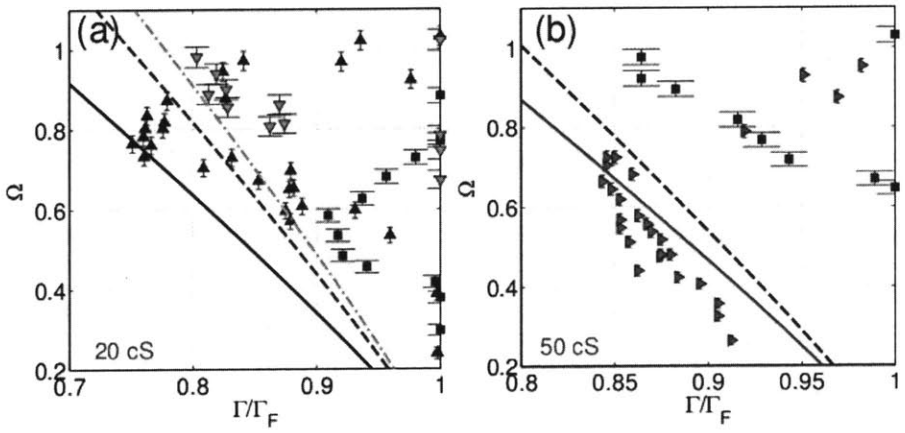

Figure 4-8: The walking thresholds as predicted by (4.31) for **(a)** 20 cS droplets at driving frequency $f = 60$ Hz (*solid line*), $f = 80$ Hz (*dashed line*), $f = 90$Hz (*dash-dot line*) and **(b)** 50 cS droplets at $f = 50$ Hz (*solid line*) and $f = 60$ Hz (*dashed line*). These should be compared to the corresponding experimental data at driving frequency $f = 50$ Hz (►), $f = 60$ Hz (■), $f = 80$ Hz (▲) and $f = 90$ Hz (▼).

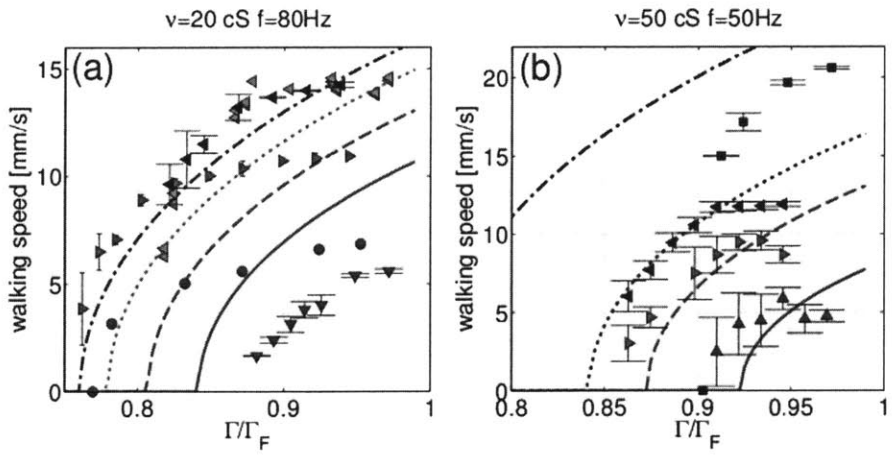

Figure 4-9: The walking speeds of silicone oil droplets for **(a)** $\nu = 20$ cS, $f = 80$Hz and **(b)** $\nu = 50$ cS and $f = 50$ Hz, as a function of the driving acceleration relative to the Faraday threshold Γ/Γ_F. In **(a)**, the experimental data for $R_0 = 0.31$ mm (▼), 0.35 mm (•), 0.38 mm (►) and 0.40 mm (◄) are compared to the speeds obtained using (4.28) with $\sin\Phi_i = 0.5$. In **(b)**, the experimental data for $R_0 = 0.25$ mm (▲), 0.34 mm (►), 0.39 mm (◄) and 0.51 mm (■) are compared to the predictions of (4.28) with $\sin\Phi_i = 0.7$.

ν [cS]	f [Hz]	coefficient C	ν [cS]	f [Hz]	coefficient C
20	60	0.21	50	40	0.21
20	80	0.17	50	50	0.17
20	90	0.21	50	60	0.33

Table 4.2: The values of the tangential drag coefficient C used for the different combinations of oil viscosity ν and driving frequency f in our simulations.

4.5 Results

The results of our theoretical model from §4.4.4 are shown in Figs. 4-10-4-15. In Figs. 4-10-4-13, the value of the tangential drag coefficient C in (4.19) was fit for each combination of frequency and viscosity in order to obtain the best match with experimental data, as shown in Table 4.2. The coefficient C remained in the interval $[0.17, 0.33]$, which is roughly consistent with the experimentally obtained upper bound of 0.3. The value for $\nu = 50$ cS and $f = 60$ Hz is slightly higher than the rest, presumably because it lies close to the limits of validity (see eqn. (C.51)) of our long-time approximation of the standing wavefield (C.52).

In Fig. 4-10, we show the predicted walking regimes for the two viscosities and several driving frequencies. The solid lines indicate the outer limits of the walking

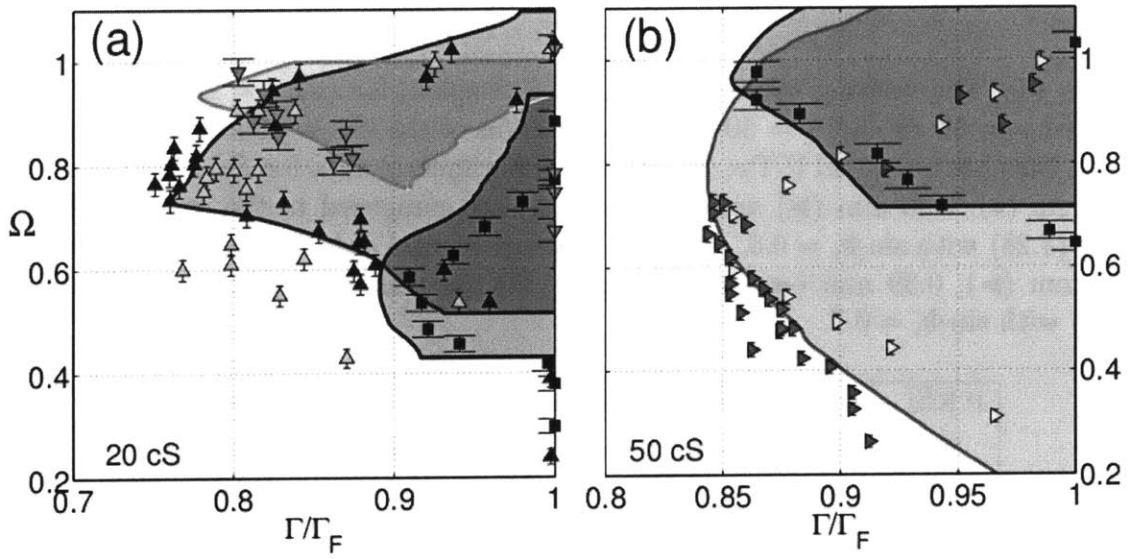

Figure 4-10: The walking thresholds for silicone oil droplets of viscosity **(a)** 20 cS and **(b)** 50 cS on a vibrating bath of the same oil. Our model predictions (*lines*) are compared to the existing data in the $\Gamma/\Gamma_F - \Omega$ plane, where Γ/Γ_F is the ratio of the peak driving acceleration to the Faraday threshold and $\Omega = \omega/\omega_D$ the vibration number. Experimental data is shown for several driving frequencies f: 50 Hz ((►) and (▷) for data from Protière *et al.* [98]), 60 Hz (■), 80 Hz ((▲) and (△) for data from Eddi *et al.* [33]) and 90 Hz (▼).

regimes, which for lower frequencies extend as far as the Faraday threshold. For higher frequencies (e.g. $f = 90$ Hz, $\nu = 20$ cS) such is not the case, as the vertical dynamics becomes chaotic for $\Gamma < \Gamma_F$. We note that while it is possible to have drops walking above the Faraday threshold, the motion is highly irregular, since the wavefield is no longer prescribed by the impacts of the drop alone, with Faraday waves arising throughout the container.

In Fig. 4-11, we show the regime diagram of the drop's horizontal and vertical motion for $\nu = 20$ cS silicone oil and several values of frequencies for which walking occurs. The walking regime, denoted **W**, is located in the region where one of the $(2,1)$ modes is stable sufficiently close to the Faraday threshold to create long-lived standing waves. As the driving frequency is increased, the walking regime moves to higher Ω and decreases in size until it disappears completely. Conversely, as the driving frequency is reduced, the Faraday threshold decreases and penetrates further into the region of steady $(2,1)$ bouncing. For sufficiently low frequency, the Faraday threshold is lower than the minimum driving acceleration required to sustain a period-doubled mode and the walking region disappears entirely. Therefore, walking occurs only in a finite interval of driving frequencies.

Our model predicts that in most walking regions, the droplet is in the higher energy $(2,1)^2$ bouncing mode (see Fig. 4-3b and 4-16b), especially for higher frequencies, smaller drops and lower viscosities. However, there are cases (e.g. when $\nu = 50$ cS and $f = 50$ Hz) when the model predicts that drops can walk even in the lower energy $(2,1)^1$ mode (see Fig. 4-3a and 4-16a). We note that our model is less accurate for the lower energy mode, due to its longer average contact time, which leads to an overestimation of the walking regime for $\nu = 50$ cS and $f = 50$ Hz.

In Fig. 4-12, we compare our model predictions of the walking speeds with the existing and new experimental data. As with the walking thresholds, the match is better for fluids with smaller viscosity. Compared to the previous predictions for the walking speeds [98] which were significantly too high, our model achieves a satisfactory match. We note that a slight overestimate for larger drops (see Fig. 4-12b, $R_0 = 0.51$mm) arises as a result of the point force approximation (eqn. (C.27)). The walking speed generally increases with increasing driving acceleration and drop size. However, this trend can be violated when the drop switches from one bouncing mode to another. Most striking is the switch from the $(2,1)^1$ mode to $(2,1)^2$, as is evidenced by the discontinuities in the theoretical curves in Fig. 4-12b in the region $0.9 < \Gamma/\Gamma_F < 0.95$ for the smallest three drops examined. When walking occurs in the region of chaotic vertical motion, the walking speed varies between each contact

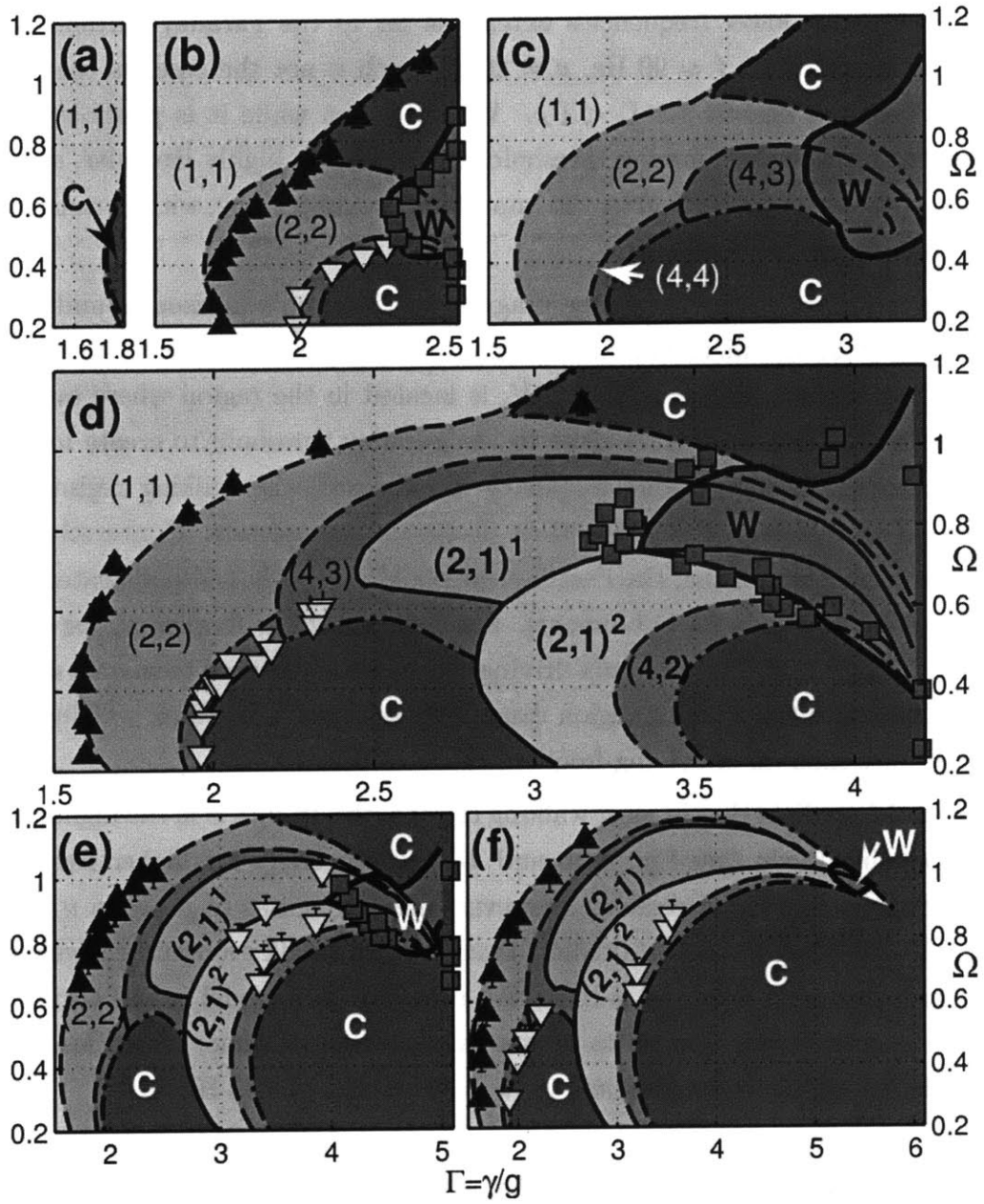

Figure 4-11: Regime diagrams delineating the dependence of the form of the drop's vertical and horizontal motion on the forcing acceleration $\Gamma = \gamma/g$ and the vibration number Ω. Silicone oil of viscosity 20 cS is considered and several values of the driving frequency: **(a)** $f = 50$ Hz, **(b)** 60 Hz, **(c)** 70 Hz, **(d)** 80 Hz, **(e)** 90 Hz and **(f)** 100 Hz. The walking regime (**W**) occurs primarily within the $(2, 1)$ bouncing mode regimes, and a sharp change in the slope of its boundary is evident across the border between the $(2,1)^1$ and $(2,1)^2$ modes. The walking regime, whose extent is seen to depend strongly on f, generally borders on chaotic bouncing regions (**C**) both above and below. Where available, experimental data on the first (▲) and second (▼) period doubling and on the walking thresholds (■) are also shown. The rightmost boundary corresponds to the Faraday threshold Γ_F. Characteristic error bars are shown.

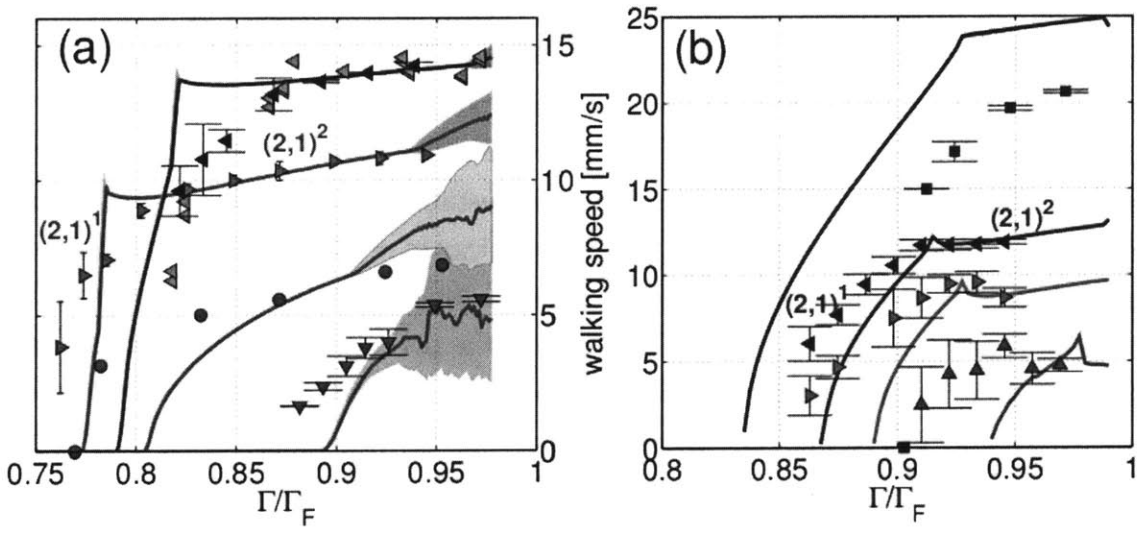

Figure 4-12: The walking speeds of silicone oil droplets for **(a)** $\nu = 20$ cS, $f = 80$ Hz and **(b)** $\nu = 50$ cS, $f = 50$ Hz, as a function of the dimensionless driving acceleration. Our model predictions (*lines*) are compared to the existing data for selected drop radii. These are: **(a)** $R_0 = 0.31$ mm (▼), 0.35 mm (◯), 0.38 mm (►) and 0.40 mm (◄, ◁); **(b)** $R_0 = 0.25$ mm (▲), 0.34 mm (►), 0.39 mm (◄) and 0.51 mm (■). In **(a)**, the predicted range of instantaneous walking speeds in the chaotic bouncing regime is indicated by the shaded regions. Discontinuities in slope of the theoretical curves indicate a switching of vertical bouncing modes from $(2,1)^1$ to $(2,1)^2$ with increasing Γ. Characteristic error bars are shown.

depending on the phase and depth of the previous impact. This is indicated in Fig. 4-12a for the smallest three drops by the shaded regions, which mark the possible range of the instantaneous walking speeds. The solid curves within these shaded regions were obtained by averaging the horizontal speed over many impacts.

In order to verify that the switching between the two different $(2,1)$ modes is not a peculiarity of our theoretical model, we measured the contact time of drops in or near the walking regime. The ratio of the contact time to the period of vertical motion, t_c/T, is shown as a function of drop radius in Fig. 4-13. The experimental results are shown in Fig. 4-13a, while the theoretical predictions are shown in Fig. 4-13b. Both plots indicate the appearance of the $(2,1)^2$ mode at $\Gamma = 3.9$, which is characterized by $t_c/T < 0.3$. Also evident is the increased range of drops in the $(2,1)^2$ mode with increased driving acceleration. We observe a satisfactory match between theory and experiments. The model consistently underestimates the relative contact times relative to the experiments owing to the different way of defining contact in each case. Experimentally, we measured the interval between the first contact and detachment of the drop. This interval is in general longer than the period of positive reaction force, our theoretical definition of contact time, due to the effects of the intervening air layer dynamics. Fig. 4-14 shows the dependence of the walking speed on the driving acceleration and drop size, as predicted by our model. The maximum walking speeds arise at the Faraday threshold for drops near the upper limit of the walking regime. In Fig. 4-14a, the region of chaotic vertical motion ($0.4 < \Omega < 0.7$, $0.9 < \Gamma/\Gamma_F < 1$) is marked by oscillations in the walking speeds. In Fig. 4-14b, the transition from the $(2,1)^1$ mode to the $(2,1)^2$ mode can be discerned from the sharp change in orientation of the velocity isoclines. In Fig. 4-15(a,c), we show the extent and depth $1-\Gamma_W/\Gamma_F$ of the walking region across a range of driving frequencies, as predicted using a single value for the proportionality constant $C = 0.2$. Our model predicts that walking only occurs for 52 Hz $\leq f \leq$ 103 Hz when $\nu = 20$ cS and for 39 Hz $\leq f \leq$ 80 Hz when $\nu = 50$ cS, which is in agreement with the range found experimentally by Protière *et al.* [100] (see Table 4.1). In Fig. 4-15(b,d) we show the different vertical bouncing modes of drops at the walking threshold. Besides the familiar $(2,1)$ modes and their period-doubled variants (arising for $f \geq 70$ Hz for $\nu = 20$ cS, $f \geq 50$ Hz for $\nu = 50$ cS), we also note the existence of "limping" drops at smaller frequencies, for which two strong impacts of the drop, roughly one Faraday period apart, are separated by a relatively weak impact. A few of the simplest limping modes are shown in Fig. 4-16d-f, together with chaotic limping (Fig. 4-16g) and non-limping modes (Fig. 4-16a-c). Finally, we note that the lower boundary of the walking region consists predominantly

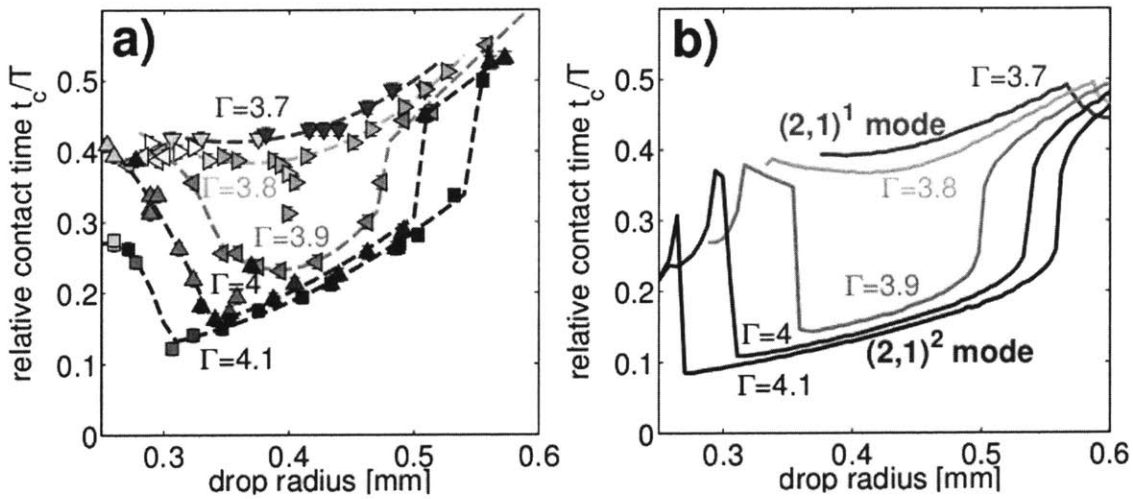

Figure 4-13: The fraction of the drop's bouncing period T spent in contact with the bath, as a function of the drop radius. Experimental results **(a)** for dimensionless driving $\Gamma = 3.7$ (▼), $\Gamma = 3.8$ (►), $\Gamma = 3.9$ (◄), $\Gamma = 4.0$ (▲) and $\Gamma = 4.1$ (■) are compared to the theoretical predictions **(b)** for the same set of Γ. The appearance of the higher energy $(2,1)^2$ mode (see Fig. 4-3a,b) at $\Gamma = 3.9$ is marked by a discrete decrease of contact time.

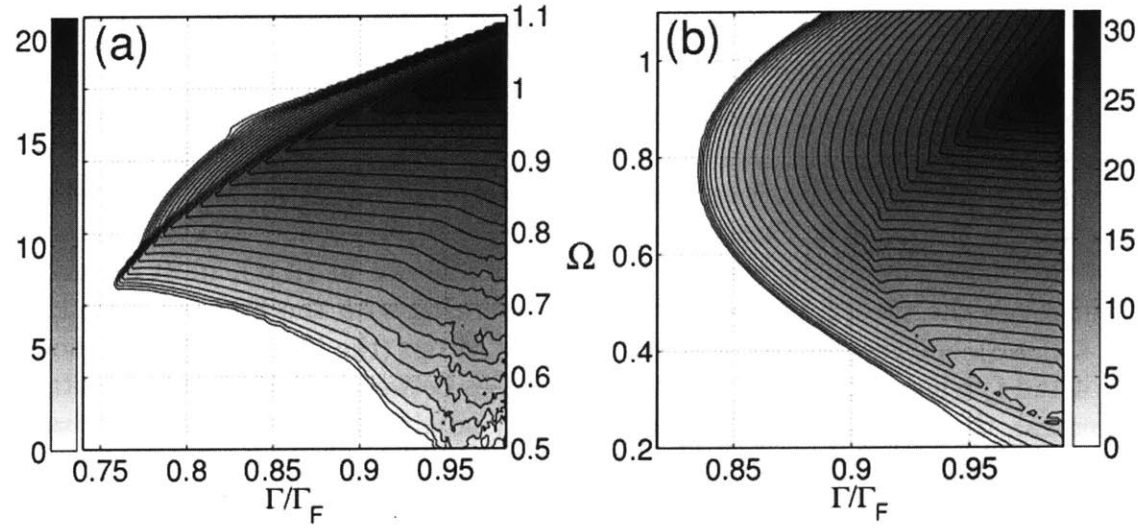

Figure 4-14: The walking speeds [mm/s] obtained with our model for **(a)** $\nu = 20$ cS, $f = 80$ Hz and **(b)** $\nu = 50$ cS, $f = 50$ Hz. The horizontal axis indicates the ratio of the peak driving acceleration to the Faraday threshold, while the vertical axis indicates the vibration number $\Omega = \omega/\omega_D$.

of chaotic walkers, for which the vertical motion is aperiodic. This makes it difficult to experimentally determine the walking threshold for small drops, for which random horizontal motion might also be attributable to weak air currents above the bath.

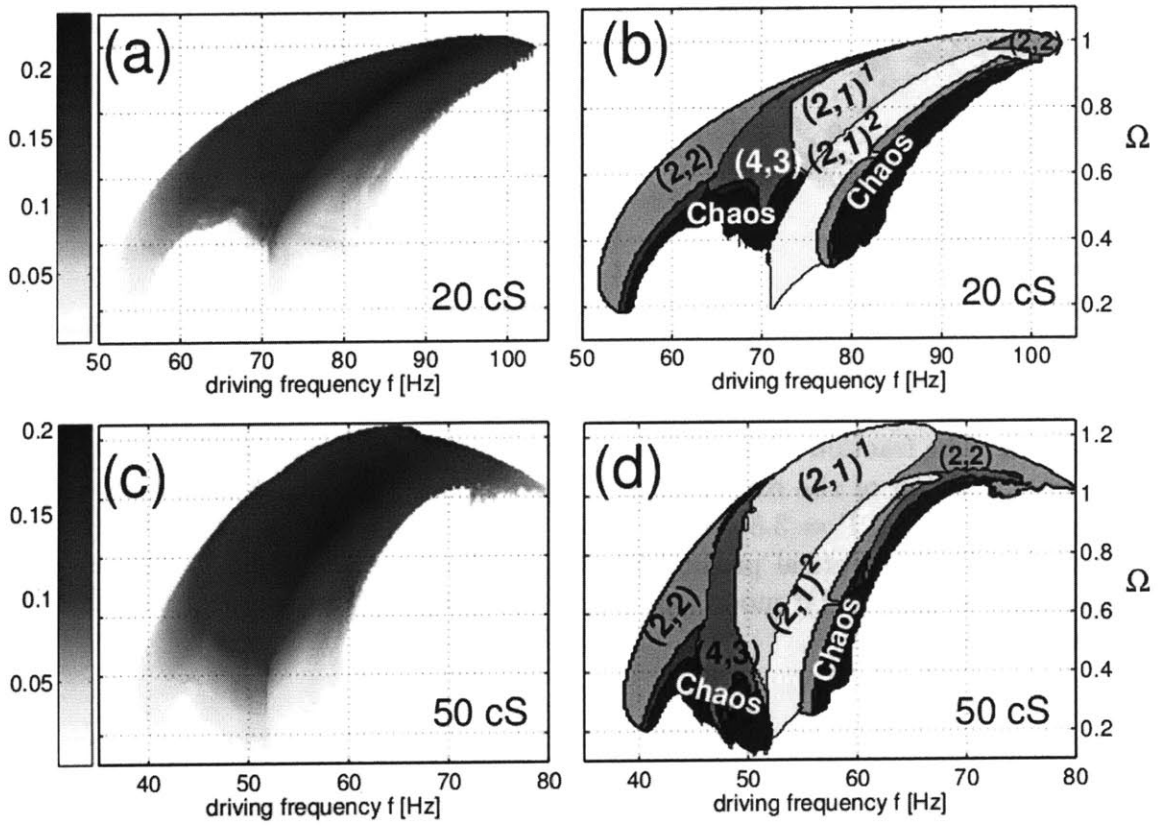

Figure 4-15: The walking region for **(a-b)** 20 cS and **(c-d)** 50 cS silicon oil drops, as predicted by our model (eqns.(4.15-4.19)). Horizontal axes indicate the driving frequency f, while the vertical axes indicate $\Omega = \omega/\omega_D$. In **(a,c)**, the relative distance from walking threshold to Faraday threshold $1 - \Gamma_W/\Gamma_F$ is shown. The various modes of vertical bouncing at the walking threshold are shown in **(b,d)**, most significant of which are the two $(2,1)$ modes (resonant bouncing with the Faraday period, see Fig. 4-16a-b), and the different kinds of "limping" drops (the $(2,2)$,$(4,3)$,$(4,4)$ modes, Fig. 4-16d-f) where a relatively weak contact arises between a pair of strong contacts. In general, the walking regime's lower boundary adjoins a region marked by chaotic bouncing (Fig. 4-16(c,g)).

4.6 Conclusion

Several new phenomena have been observed experimentally and rationalized theoretically, most notably the coexistence of different vertical bouncing modes in the walking

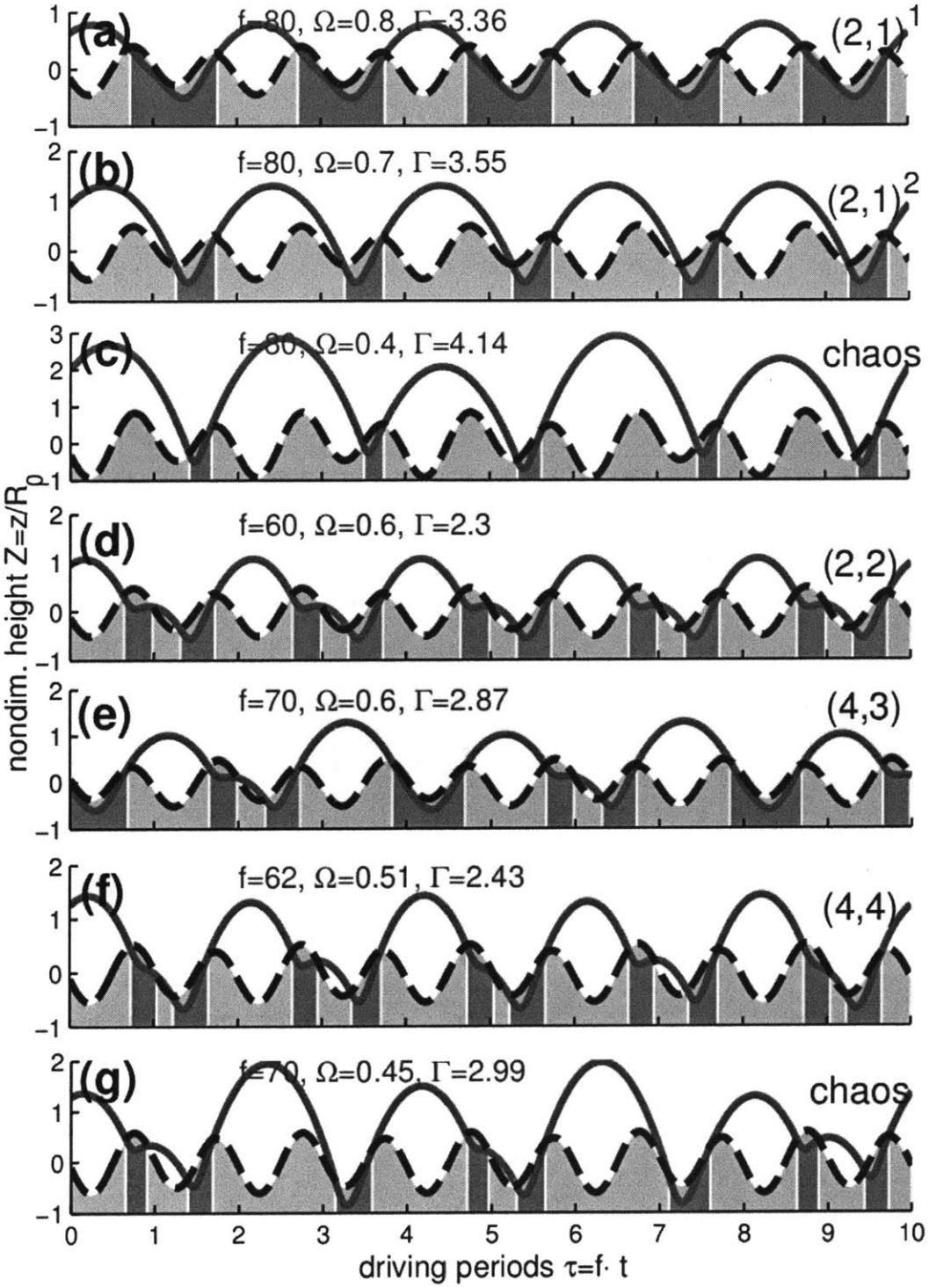

Figure 4-16: The most common bouncing modes of 20 cS drops near the walking threshold. These are **(a)** the $(2,1)^1$ mode, **(b)** the $(2,1)^2$ mode, **(c)** chaotic bouncing, **(d)** the $(2,2)$ mode, **(e)** the $(4,3)$ mode, **(f)** the $(4,4)$ mode and **(g)** chaotic limping. Modes **(d)-(g)** are referred to as "limping" modes, due to the short steps alternating with long ones.

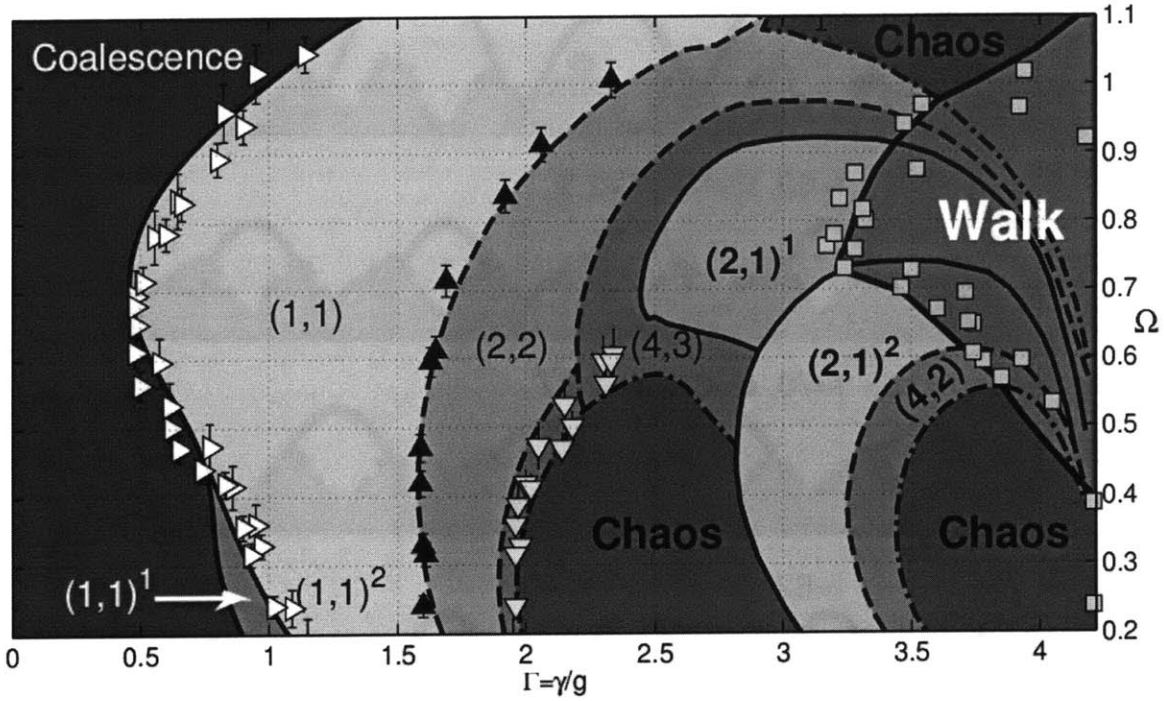

Figure 4-17: Comparison of the regime diagram for 20 cS silicone oil and $f = 80$ Hz, as predicted by our model, to the experimental data. The data on the bouncing threshold (►), first (▲) and second (▼) period doubling and on the walking threshold (■) are shown. The rightmost boundary corresponds to the Faraday threshold Γ_F.

regime for identical system parameters. Switching between the different modes can lead to discontinuous or non-monotonic dependence of the walking speed and contact time on the driving acceleration. Our model also predicts that for higher frequencies, the walking regime does not necessarily extend to the Faraday threshold, and may instead give way to a chaotic walking state.

We have combined models for the vertical and horizontal dynamics of bouncing drops in order to rationalize the extent of the walking regimes and the dependence of walking speeds on the forcing acceleration. We have reduced the number of free parameters from as many as 5 in some of the previous models to one with tight bounds. Our remaining fitting parameter is the constant of proportionality C, defined in (4.10), which can be rewritten

$$C = \frac{\int F^T(\tau)\mathrm{d}\tau}{\int F^N(\tau)X_\tau \mathrm{d}\tau} = \frac{\int X_{\tau\tau}\mathrm{d}\tau}{\int X_\tau \left(Z_{\tau\tau} + \mathcal{B}o^*(\tau)\right)\mathrm{d}\tau} \approx \frac{1 - C_R^T}{(1 + C_R^N)\mathcal{W}e_{in}^{1/2}} \quad , \tag{4.32}$$

where F^N, F^T are the normal and tangential components of the dimensionless reaction force acting on the drop during contact, and C_R^N, C_R^T are the normal and tangential coefficients of restitution, respectively. The values of C used in our model were between 0.17 and 0.33, while experimentally it was found to be near 0.3. The match with experiments is improved significantly relative to existing models [19, 98] due to a more thorough analysis of the standing waves created by the drop impacts and the forces acting on the drop during impact.

Our model, summarized in §4.4.4, combines the description of the vertical dynamics (4.15) developed in *MBI* and the horizontal dynamics (4.19) via an approximate description of the Faraday wavefield (4.16-4.18). The approximation, derived analytically in Appendix C, is valid for a finite range of oil viscosities defined in (C.51) that includes those examined experimentally. Assuming that the drop is a resonant walker in the $(2,1)^2$ bouncing mode and that its horizontal speed changes slowly relative to its bouncing period, one can average out the vertical motion and derive a trajectory equation (4.25) for the drop's horizontal motion. The more exotic walking states, such as limping or chaotic walking, will be the subject of a future study of gait changes in walking droplets.

The model was kept relatively simple for the sake of tractability. As a result, there are cases where the simplifying assumptions are being pushed to their limits; nevertheless, it should be straightforward to extend the validity of our model starting from the same equations and include higher order corrections. First of the simplifications made was the approximation of the underlying standing wave field by the formula

(4.7), which works well for the oil viscosities used in our experiments, as shown in Fig. 4-6. However, if the model is to be extended to smaller or higher viscosities, it might be necessary to including higher order terms in evaluating the integral (C.47) using Laplace's method, in order to achieve sufficient accuracy within the first few Faraday periods. The heuristic formula for the tangential force during impact is another major simplification of the model, which ties the tangential and normal components of the reaction force. The actual temporal profile of the tangential force is likely to be slightly different than that given by (C.46), leading to increased error for long contact time. On the other hand, when the contact time is much shorter than the Faraday period, the temporal profile is inconsequential, as only the overall loss of tangential momentum will affect the walking dynamics.

More important, and likely the major source of error of our model, is the approximation of the horizontal kick received by the drop during impact, as summarised in equation (4.14). This result was deduced by assuming that the impact is much shorter than the Faraday period and that the bath disturbance radius is much shorter than the Faraday wavelength. For larger drops or drops in lower energy modes these assumptions are no longer strictly valid. Nevertheless, the model predictions still fare rather well. In order to improve upon this approximation, terms involving higher spatial and temporal derivatives of the surface profile could be added to (4.14). On its own [88], or combined with a numerical model that captures the outgoing transient surface wave created at each impact [75], our model represents the first rational hydrodynamic pilot-wave theory, and provides a solid foundation for modeling the quantum-like behaviour of walking droplets.

Chapter 5

Exotic states of bouncing and walking droplets

5.1 Background

Drops bouncing on a vibrating fluid bath [124, 18] have recently received considerable attention for two principal reasons. First, they represent a rich dynamical system, exhibiting many features of low-dimensional chaotic oscillators [48, 46, 45]. Second, in certain parameter regimes, the bouncers walk horizontally through resonant interaction with their wave field [19, 98, 33, 32, 78]. The resulting walkers represent the first known example of a macroscopic pilot-wave system [23, 79, 88, 17], and exhibit many features thought to be exclusive to the microscopic quantum realm [6], including self-organising lattice structures [29, 28], single particle diffraction [16], quantized orbits [43], orbital level splitting [31], tunneling effects [30] and wave-like statistics in confined geometries [59].

Consider a fluid of density ρ, kinematic viscosity ν and surface tension σ in a horizontal bath of depth H driven by a vertical vibration of amplitude A and frequency $f = \omega/(2\pi)$. The effective gravity in the vibrating bath frame of reference is $g^*(t) = g + \gamma \sin(2\pi f t)$ where g is the gravitational acceleration and $\gamma = A\omega^2$. At low forcing acceleration, the fluid remains quiescent in the vibrating frame; however, above a critical acceleration amplitude γ_F corresponding to the Faraday threshold, the layer becomes unstable to a field of standing Faraday waves [4, 27]. The waves are subharmonic, with half the frequency of the vibrational forcing, $\omega_F = \omega/2$, and with

wavelength $\lambda_F = 2\pi/k_F$ prescribed by the standard surface wave dispersion relation:

$$\omega_F^2 = \tanh(k_F H)\left(gk_F + \frac{\sigma k_F^3}{\rho}\right). \tag{5.1}$$

In the experiments of interest, the vibrational forcing is less than the Faraday threshold, $\gamma < \gamma_F$; consequently, the interface would remain flat if not for the presence of a droplet.

When a fluid drop is placed on a vibrating bath (Fig. 5-1), there are three basic outcomes: the droplet may either coalesce, bounce in place or walk across the fluid surface [98, 32, 124]. For $\gamma < \gamma_B \approx g$, where γ_B is the bouncing threshold, the applied forcing is insufficient to levitate the drop, which then settles towards the bath. The intervening air layer thins until reaching a critical thickness at which Van der Waals forces between drop and bath initiate coalescence. For sufficiently large $\gamma > \gamma_B$, this air layer is sustained during impact, precluding coalescence and enabling a stable bouncing state. Beyond a critical forcing threshold, $\gamma > \gamma_w$, where γ_w is the walking threshold, the stationary bouncing state is destabilised by the underlying wave field, giving way to a dynamical state in which the drops walk across the fluid bath. The walking regime arises only for a limited range of drop sizes and forcing conditions.

Figure 5-1: Walking drop of 20 cS silicone oil of radius 0.48 mm (a) before, (b) during, and (c) after an impact with a bath of the same liquid vibrating at 70 Hz.

Couder's group has characterised the behaviour of drops bouncing on a fluid bath in terms of the drop diameter $D = 2r_0$ and dimensionless forcing acceleration $\Gamma = \gamma/g$. Protiere *et al.* [98] conducted experiments with a viscosity-frequency combination of 50 cS-50 Hz and summarised their results in a regime diagram illustrating the droplet behaviour in the D-Γ plane. For low forcing accelerations, simple bouncing arises: the drop hits the bath once every driving period. Increasing the acceleration leads to a period-doubled bouncing state for medium-sized drops. For relatively small and large drops, a period doubling cascade may occur, culminating in temporally chaotic behaviour. For the larger drops, an intermittent regime can also arise in which the drop changes from one bouncing state to another in an irregular fashion. For drops within a limited size range, there is a critical $\Gamma_w = \gamma_w/g$ above which they walk along

the surface of the bath. The walking regime was assumed to be associated with a fully period doubled bouncing state; more complex walking modes will be highlighted herein. A similar regime diagram was obtained for a 20 cS-80 Hz combination, yielding the same four characteristic modes [33, 32]. The theoretical rationale for the form of the regime diagrams was only recently developed [78, 79], and will be built upon herein.

Gilet & Bush [48] considered the motion of a drop on a vibrating soap film, and demonstrated that the film behaves like a linear spring with a spring constant proportional to the surface tension. They observed and rationalised a number of complex bouncing states, multiperiodicity (the existence of different bouncing states at identical system parameters), and period doubling transitions to chaos. Different bouncing states were denoted by (m, n), where m/f represents the period of the mode, during which the drop contacts the surface n times. The dynamics of interest here, of droplets bouncing on a vibrating fluid bath, are significantly complicated by the influence of the fluid bath's inertia.

Molacek & Bush [78] (henceforth MB1) examined droplets bouncing on a vibrating fluid bath, and detailed both experimentally and theoretically the dependence of the bouncing mode on the system parameters. They introduce the vibration number, $\Omega = 2\pi f\sqrt{\rho r_0^3/\sigma}$, the relative magnitude of the forcing frequency and the drop's natural oscillation frequency, and summarised their results in regime diagrams that indicate the droplet behaviour in the Ω-Γ plane. They demonstrate that droplets of a given size can bounce at the lowest forcing amplitude when $\Omega \approx 0.65$, that is, when the drop is forced at its natural frequency. They noted different bouncing states with the same periodicity, which they denote by $(m, n)^i$, where the integer superscript i increases with the states's mean mechanical energy. In addition to identifying a number of new bouncing states previously unreported, MB1 developed a theoretical model that rationalises the observed dynamics. The vertical interaction between the bouncing drop and the liquid bath during drop contact was described using a logarithmic spring model, which built upon their model of drop impact on a rigid substrate [77].

Molacek & Bush [79] (henceforth MB2) extended their theoretical model in order to capture the dynamics of walking droplets. Specifically, their logarithmic spring model was supplemented by consideration of the wave field of the bath, which may destabilise the stationary bouncing states. While they rationalised the limited extent of the walking regime, they did not characterise the dependence of the walking style on the system parameters. Their model successfully rationalised the experimentally

reported transitions from bouncing to walking states, as well as the dependence of the walking speed on the system parameters. They also noted the coexistence of different walking states at the same system parameters, and highlighted the predominance of the $(2,1)^1$ and $(2,1)^2$ modes. Finally, they reported a number of exotic walking states, including chaotic walkers and "limping" drops that walk with unequal steps, the subject of the present study.

The goal of the current study is to extend our knowledge of the bouncing drop dynamics by presenting the most detailed regime diagrams to date. In addition to reporting a number of new exotic bouncing and walking states, we extend the predictions of our theoretical model [78, 79] in order to rationalise our observations. In section 5.2, we describe our experimental set-up. In section 5.3, we present the experimentally obtained regimes diagrams in which we identify the different walking and bouncing modes. We also examine the dependence of the walking speed on the bouncing mode. In section 5.4, we review our theoretical model and compare its predictions with our new experimental observations. Our results are summarised in section .

5.2 Experimental set-up

In Figure 5-2 we present a schematic illustration of our experimental set-up. A circular fluid tray of diameter 76 mm and depth 16 mm is oscillated vertically in a sinusoidal manner with frequency f, amplitude A and peak acceleration $\gamma = (2\pi f)^2 A$. The tray is vibrated by an industrial shaker mounted on a massive levelling platform, which rests beneath an optical table. The shaker is driven by a power amplifier controlled using a data acquisition system and custom software. We measure the acceleration using two piezoelectric accelerometers, and use a feedback loop to maintain a constant vibration amplitude, corresponding to a tolerance of 0.01 g in vibrational acceleration amplitude. An air bearing carriage with a square cross section is mounted to a levelling platform to ensure that the vibratory motion lies strictly along a single vertical axis. The air bearing minimises lateral vibration introduced by the shaker, a technique developed for careful studies of vibrated granular layers [107, 51, 24]. A thin coupling rod connects the shaker to the slider bar of the air bearing.

We use two different silicone oils, the first with kinematic viscosity $\nu = 20$ cS, density $\rho = 949$ kg/m^3 and surface tension $\sigma = 20.6$ mN/m, the second with $\nu = 50$ cS, $\rho = 965$ kg/m^3 and $\sigma = 20.8$ mN/m. We identify the Faraday threshold γ_F for each combination of experimental parameters by gradually increasing the acceleration

amplitude γ until standing waves with frequency $f/2$ spontaneously form at the free surface. The precise value of γ_F depends on the vibration frequency, the depth and viscosity of the oil. The dimensionless Faraday threshold is denoted by $\Gamma_F = \gamma_F/g$.

Oil drops are created by rapidly extracting a submerged needle from the fluid bulk [98]. Of the droplets formed, we select those of radius r_0 between 0.20 mm to 0.51 mm. The undeformed drop radius r_0 is measured optically with a high-speed camera, recording at 4000 frames per second. The optical set-up results in a pixel density of $71 - 88$ pixels per mm, leading to an uncertainty in drop radius of $\pm 1.5\%$. The horizontal motion of the drop is captured from above with a Machine Vision CCD camera and is tracked using particle-tracking software. We performed measurements

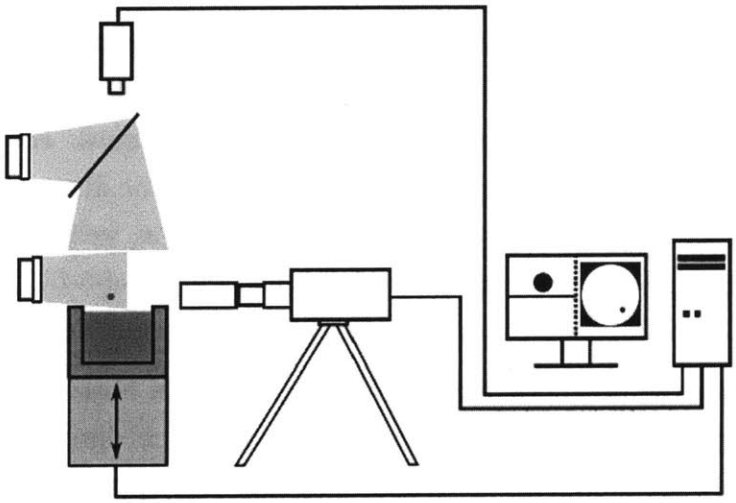

Figure 5-2: Schematic illustration of the experimental set-up. The vibrating bath is illuminated by two LED lamps, and the drop motion recorded by two digital video cameras. The top view camera captures images at $17.5 - 20$ frames per second, while the side view camera records at 4000 frames per second. The video processing is done on a computer.

for a single drop size by either increasing or decreasing the driving acceleration in a stepwise manner from some initial value of Γ, with typical step size $d\Gamma = 0.1\Gamma$. The entirety of the bouncing and walking regimes could thus be explored by varying γ between γ_B and γ_F.

5.3 Experimental results

Three different combinations of fluid viscosity and forcing frequency were investigated. A 20 cS silicone oil bath was forced at 70 and 80 Hz, and a 50 cS oil bath at 50

Fluid viscosity	Driving frequency	Regime diagram	Bouncing and walking modes
20 cS	80 Hz	Fig. 5-3(a)	$(2,1)^1$, $(2,1)^2$, (2,2), **(4,2), (4,3), (4,4)**, chaotic. Fig. 5-4
50 cS	50 Hz	Fig. 5-3(b)	$\mathbf{(2,1)^1}$, $\mathbf{(2,1)^2}$, **chaotic**. Fig. 5-5
20 cS	70 Hz	Fig. 5-3(c)	**(2,2)**, (4,3), **(13,10)**, $(2,1)^1$, $(2,1)^2$, **mixed mode**, chaotic. Fig. 5-6

Table 5.1: The observed walking and bouncing modes for the three viscosity/frequency combinations examined. Modes in bold typeface are those for which an associated spatio-temporal diagram is included (see Figs. 5-4 to 5-6).

Hz. A full exploration of both walking and bouncing region was conducted for the 20 cS-80 Hz combination, since this exhibited the richest behaviour. For the other two combinations, we focused on characterising the walking regimes. For each combination of oil viscosity and driving frequency we present a regime diagram indicating the droplet bouncing behaviour in the Γ-Ω plane (Fig. 5-3), as well as spatio-temporal diagrams of selected bouncing and walking modes (Figs. 5-4-5-6). In Table 5.1, a summary of the observed bouncing and walking modes is provided.

In the three regime diagrams reported in Fig. 5-3, the horizontal axis is the dimensionless forcing $\Gamma = \gamma/g$, and the vertical axis is the dimensionless vibration number Ω, a proxy for drop size. Individual markers correspond to experimental observations, with square and round markers denoting stationary bouncing and walking states, respectively. The colour of the marker denotes the observed bouncing or walking mode. We first describe the experimental results, and reserve the comparison with theoretical predictions for section 5.4.

A full exploration of both the bouncing and walking regime for the 20 cS-80 Hz combination is shown in Fig. 5-3(a). For relatively weak forcing, $1.5 < \Gamma < 2.3$, the $(2,2)$ bouncing mode is dominant; however, a band of the $(4,4)$ mode (Fig. 5-4(a)) is also observed for vibration numbers $\Omega \lesssim 0.5$. As Γ is increased, additional $m = 4$ modes are observed. Specifically the $(4,3)$ mode (Fig. 5-4(b)) arises in a region around $\Gamma \approx 2.6$ and $\Omega \approx 0.5$, and the $(4,2)$ mode (Fig. 5-4(c)) appears for almost all vibration numbers investigated, for $\Gamma > 3.3$, spanning both the bouncing and walking regimes. A region of $(2,1)$ bouncing modes extends from $\Gamma = 2.5$ up to Γ_F for vibration numbers between 0.6 and 1. This region crosses into the walking region; it starts out in the low energy $(2,1)^1$ mode, and then transitions into the high energy $(2,1)^2$ mode as Γ is increased. This $(2,1)$ region also arises for smaller drops,

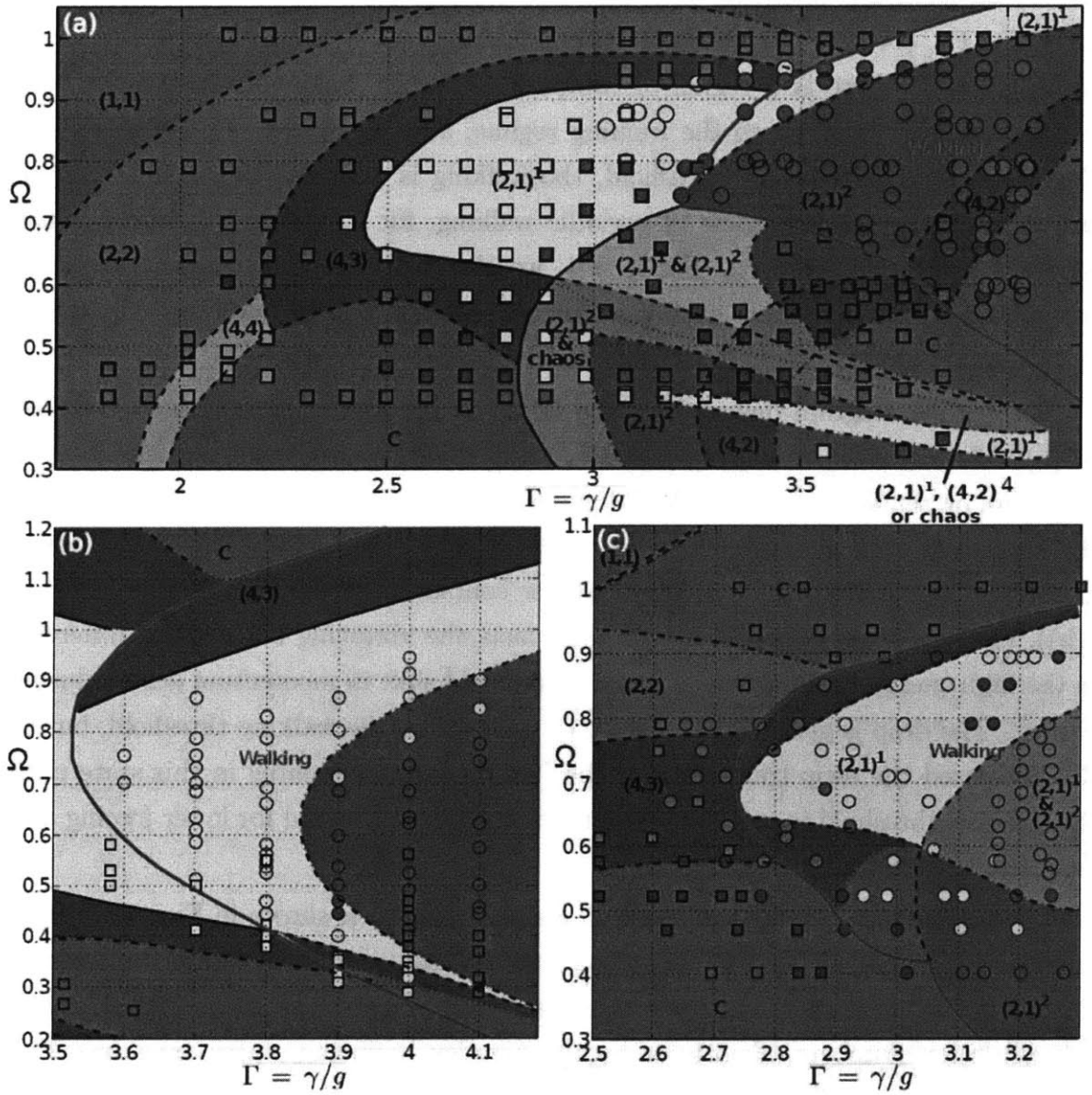

Figure 5-3: Regime diagrams indicating the dependence of the droplet behaviour on the dimensionless driving acceleration, $\Gamma = \gamma/g$, and the vibration number, $\Omega = 2\pi f\sqrt{\rho r_0^3/\sigma}$. (a) The 20 cS-80 Hz combination for which $\Gamma_F = 4.22 \pm 0.05$. (b) 50 cS-50 Hz for which $\Gamma_F = 4.23 \pm 0.05$. (c) 20 cS-70 Hz for which $\Gamma_F = 3.33 \pm 0.05$. Filled areas correspond to theoretical predictions, the solid red line denoting the theoretically predicted walking threshold. Square markers denote stationary bouncing drops; round markers indicate observed walking drops. The colour of the markers indicate the observed bouncing mode.

$\Omega \approx 0.4 - 0.5$, along a band with Γ ranging from 2.9 to 4, stretching into a seemingly chaotic region. Three distinct regions of complex or chaotic motion are observed. One exists for drops bouncing with $2.3 < \Gamma < 3$ and $\Omega \approx 0.4$. Another arises near $3.5 < \Gamma < \Gamma_F$, $0.4 < \Omega < 0.8$ and spans the bouncing and walking regimes. For larger drops ($\Omega \approx 1$) there is a region of complex or chaotic behaviour stretching from the bouncing ($\Gamma \approx 3.1$) into the walking regime, and up to the Faraday threshold. Generally, near the Faraday threshold, the walking is observed to be chaotic, with only a relatively small window of periodic walking, for $0.8 < \Omega < 1$, above which chaotic bouncing is observed. For $\Omega \approx 1$, we observed stationary chaotic bouncing drops that, when perturbed with a submerged needle, transitioned into the stable $(2,1)$ walking mode.

The regime diagram deduced for the 50 cS-50 Hz combination is shown in Fig. 5-3(b). The observed modes were $(2,1)^1$, $(2,1)^2$, and chaotic bouncing, the form of which are presented in Fig. 5-5. Walking occurs only in the $(2,1)^1$ and $(2,1)^2$ modes; the horizontal drop speed being significantly larger in the former than in the latter. The $(2,1)^1$ mode (Fig. 5-5(a)) has a longer contact time than the $(2,1)^2$ (Fig. 5-5(b)), and the phase at which the drop impacts the vibrating bath is also different. In the high energy $(2,1)^2$ mode, a much more rapid shift in momentum occurs during impact. The drop is generally in the $(2,1)^1$ mode near the walking threshold, but as Γ is increased the drop transitions to the $(2,1)^2$ mode, remaining in this state until the Faraday threshold is reached. Chaotic bouncing is observed for lower forcing and drop size (Fig. 5-5(c)).

The regime diagram for the 20 cS-70 Hz combination is shown in Fig. 5-3(c) and includes a number of "exotic" bouncing and walking modes. Outside the walking region, three bouncing modes are observed. For large ($\Omega \approx 1$) and small ($\Omega \approx 0.4$) vibration numbers, chaotic or highly complex bouncing states are seen. Fig. 5-6(a) shows a spatio-temporal evolution of a highly complex $(13,10)$ mode. For intermediate Ω, (4,3) and (2,2) bouncing modes arise, the former being observed for drops with $\Omega \approx 0.4 - 0.6$, and the latter for $\Omega \approx 0.6 - 0.8$. Fig. 5-6(b) shows the spatio-temporal diagram of a drop in the (2,2) mode. We refer to these as limping drops, owing to their unequal step sizes. The (4,3) and (2,2) modes stretch into the walking region, where the $(2,1)$ modes are dominant. Generally the $(2,1)^2$ mode is observed at lower Ω than the $(2,1)^1$ mode.

Of particular interest is the region of "mixed states" for $\Gamma > 3.1$ and $0.55 < \Omega < 0.8$. Here the drops alternate between the low and high energy $(2,1)$ modes, as shown in Fig. 5-6(c), where the evolution is from $(2,1)^1$ to $(2,1)^2$ to $(2,1)^1$ to $(2,1)^2$. While

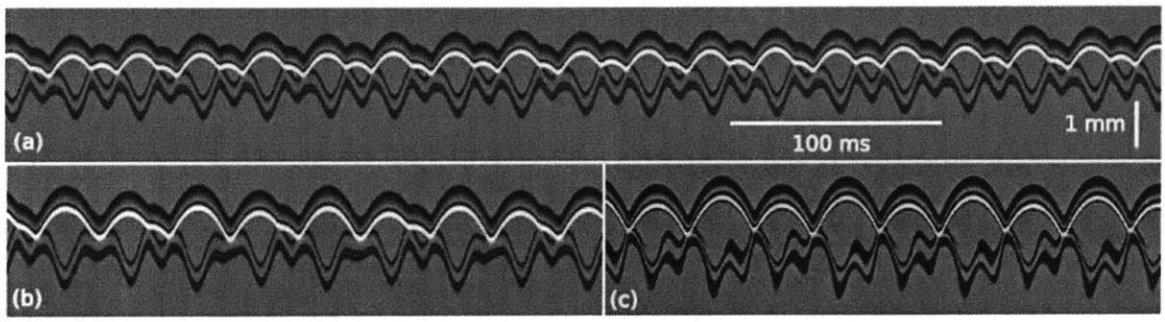

Figure 5-4: Some of the bouncing modes observed for the 20 cS-80 Hz combination. (a) Bouncing (4,4) mode. $\Gamma = 2.3$, $\Omega = 0.45$. (b) Bouncing (4,3) mode. $\Gamma = 2.7$, $\Omega = 0.45$. (c) Bouncing (4,2) mode. $\Gamma = 3.5$, $\Omega = 0.42$.

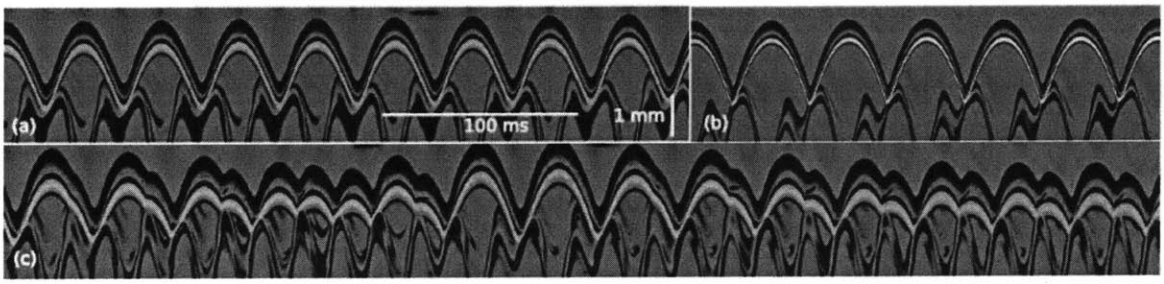

Figure 5-5: Some of the modes observed for the 50 cS-50 Hz combination. (a) Walking $(2,1)^1$ mode. $\Gamma = 3.7$, $\Omega = 0.59$. (b) Walking $(2,1)^2$ mode. $\Gamma = 4.0$, $\Omega = 0.44$. (c) Chaotic bouncing with no apparent periodicity. $\Gamma = 4$, $\Omega = 0.94$.

the height of the jumps are roughly equal, the phase of impact shifts rapidly. In Fig. 5-7(a), the horizontal trajectory of a drop in the mixed state is shown. The shading of the trajectory reflects its local horizontal speed which fluctuates by a factor of 4 as it switches between the fast $(2,1)^1$ mode and the slow $(2,1)^2$ mode. Fig. 5-7(b) shows the velocity of the mixed mode as a function of arc-length. The variation of the velocity occurs over a distance of approximately one Faraday wavelength, resulting in a highly peaked power spectrum (Fig. 5-7(c)). We note that the mixed mode is generally stable to the perturbation arising when the drop interacts with the boundary of the fluid tray. However, by redirecting the drop with the meniscus of a submerged pin or interaction with a boundary, the mixed mode can be destabilised, causing the drop to shift into either the $(2,1)^1$ or $(2,1)^2$ walking modes. Fig. 5-7(d) shows the trajectory of a mode switcher settling into the high energy $(2,1)^2$ mode after being perturbed by an approach to the boundary at nearly normal incidence. We note that we might alternatively have denoted the mixed state by a purely periodic mode, (24,12); however, we find it useful to distinguish between the two phases of its motion ($(2,1)^1$ and $(2,1)^2$), in which its speed is markedly different.

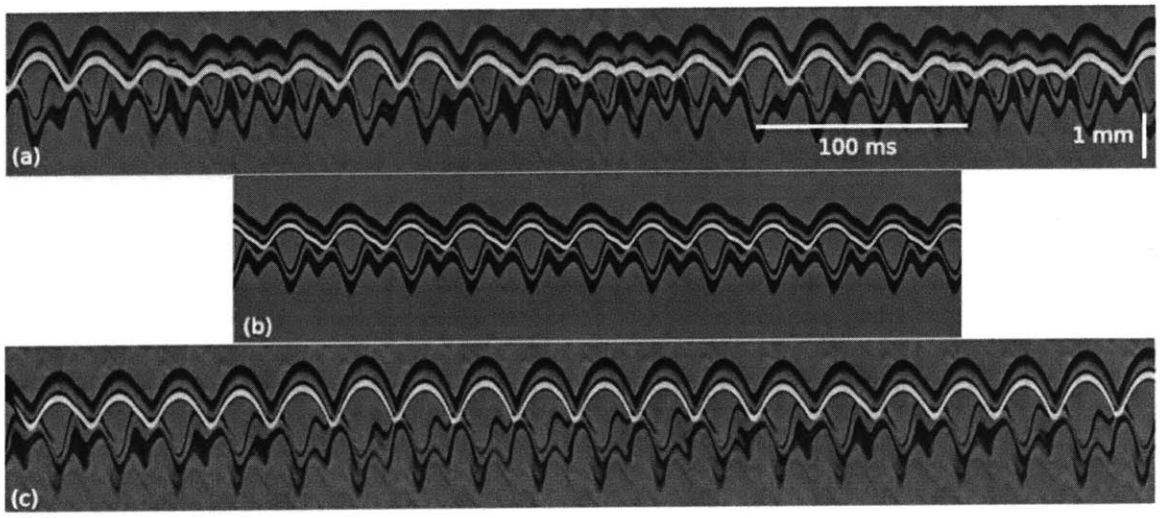

Figure 5-6: Some of the modes observed for the 20 cS-70 Hz combination. (a) Exotic bouncing mode (13,10): highly complex periodic motion. $\Gamma = 3.3$, $\Omega = 0.97$. (b) The limping drop, a (2,2) walking mode. $\Gamma = 2$, $\Omega = 0.42$. (c) The mixed walking state, shown here evolving from $(2,1)^1 \rightarrow (2,1)^2 \rightarrow (2,1)^1 \rightarrow (2,1)^2$. $\Gamma = 3.4$, $\Omega = 0.72$.

5.4 Theoretical predictions

In order to obtain theoretical predictions for the dependence of the bouncing behaviour on the system parameters, we adopted the model presented in MB1 and MB2. There, it was shown that the vertical drop motion is governed by

$$\begin{aligned} -mg^*(t) &= m\ddot{z} \quad \text{in free flight } (\mathcal{Z} \geq 0 \text{ or } F_N \leq 0)\ , \\ -mg^*(t) &= \left(1 + \frac{c_3}{\ln^2 |\frac{c_1 r_0}{\mathcal{Z}}|}\right) m\ddot{z} + \frac{4}{3}\frac{\pi \mu r_0 c_2(\nu)}{\ln |\frac{c_1 r_0}{\mathcal{Z}}|}\dot{\mathcal{Z}} + \frac{2\pi\sigma\mathcal{Z}}{\ln |\frac{c_1 r_0}{\mathcal{Z}}|} \quad \text{during contact}\ , \end{aligned} \tag{5.2}$$

where m is the drop mass, z its centre of mass, $\mathcal{Z} = z - h$ is the height of the drop above the bath surface. During free flight, the drop responds only to gravity. During impact, $F_N(t) = m\ddot{z} + mg^*(t)$ is the normal component of the reaction force acting on the drop. The constants used here, $c_1 = 2$, $c_3 = 1.4$, $c_2 = 12.5$ for 20 cS oil and $c_2 = 7.5$ for 50 cS oil, were deduced in MB1 by matching with experimental measurements of the normal and tangential coefficient of restitution. To consider 1-dimensional horizontal drop motion, we write $h = h(x,t)$ as the total height of the standing waves in the bath frame of reference. $h(x,t)$ can be expressed as the sum of

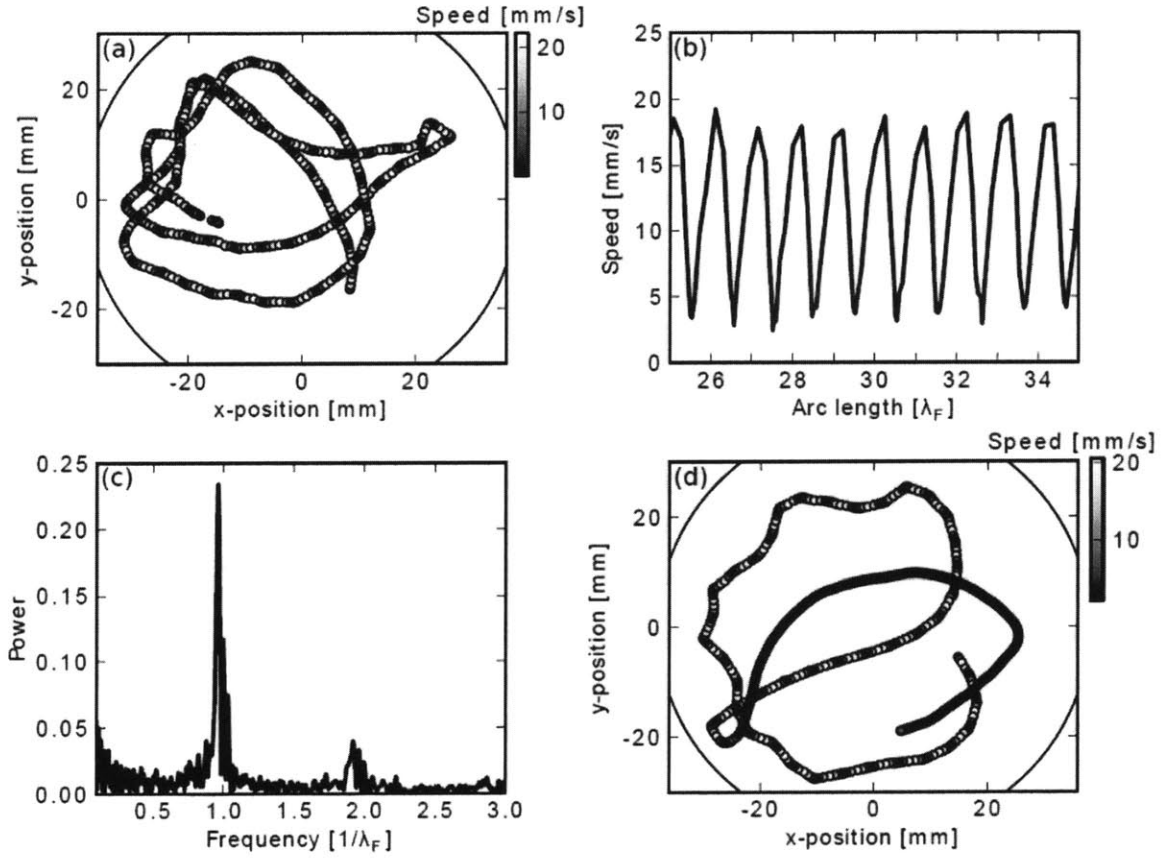

Figure 5-7: Mixed state walkers observed with the 20 cS-70 Hz combination, $\Gamma = 3.4$, $\Omega = 0.72$. (a) The trajectory for a drop in the mixed state, shaded according to the speed. The circular bath domain is indicated. (b) The observed variation of walking speed with arc-length, as normalised by the Faraday wavelength. (c) A Fourier power spectrum of the normalised velocity fluctuations. (d) Trajectory of a mixed mode, shaded according to speed, that destabilises into a $(2,1)^2$ walker after collision with the boundary near $(x, y) = (-25, -20)$ mm.

contributions from all previous impacts:

$$h(x,t) = \sum_{n=1}^{N} h_0(x, x_n, t, t_n) \quad . \tag{5.3}$$

The contribution $h_0(x, x_n, t, t_n)$, resulting from a single drop impact at $(x,t) = (x_n, t_n)$, can be approximated, in the long-time limit, by a standing wave decaying exponentially in time with a spatial profile prescribed by a zeroth order Bessel function of the first kind, $J_0(x)$:

$$h_0(x, x_n, t, t_n) \approx J_0\left(k_F(x - x_n)\right) \sqrt{\frac{2}{\pi}} \frac{k_F r_0}{3k_F^2 r_0^2 + \mathcal{B}o} \frac{r_0 k_F^2 \mu_{eff}^{1/2}}{\sigma} \frac{\cos(\pi f t)}{\sqrt{t - t_n}} \times$$
$$\times \exp\left\{(\Gamma/\Gamma_F - 1)\frac{t - t_n}{T_d}\right\} \int F_N(t') \sin(\pi f t')\, \mathrm{d}t' \; . \tag{5.4}$$

Here $\mathcal{B}o = \rho g r_0^2/\sigma$ is the Bond number, and T_d is the characteristic decay time of the unforced waves, which depends on the fluid viscosity and the critical wavenumber. μ_{eff} is a phenomenological viscosity required to ensure that the decay rate of the waves matches that in a fully analytical model (MB2, Appendix A.1). The integral of the reaction force, $F_N(t)$ is carried out over the duration of contact.

In order to increase computational speed, the number of previous impacts stored is kept to a manageable size by discarding those whose standing wave amplitude has decayed sufficiently (below 0.1% of its initial value). Since the contact takes place over a finite length of time, x_n and t_n are taken as the weighted averages of x and t over the contact time t_c, defined as the interval during which the vertical reaction force $F_N(t)$ on the drop is positive:

$$x_n = \frac{\int_{t_c} F_N(t') x(t') \mathrm{d}t'}{\int_{t_c} F_N(t') \mathrm{d}t'}, \quad t_n = \frac{\int_{t_c} F_N(t') t' \mathrm{d}t'}{\int_{t_c} F_N(t') \mathrm{d}t'}. \tag{5.5}$$

The horizontal dynamics is governed by

$$m\ddot{x} + D(t)\dot{x} = -\frac{\partial h(x,t)}{\partial x} \cdot F_N(t) \quad , \tag{5.6}$$

where

$$D(t) = 0.17\frac{\sqrt{\rho r_0}}{\sigma} F_N(t) + 6\pi r_0 \mu_a \left(1 + \frac{g r_0}{12} \nu_a f\right) \tag{5.7}$$

is the total instantaneous drag coefficient. The subscript a denotes air. The first term represents the momentum drag induced during impact, the second term the

aerodynamic drag induced during flight. The term on the right hand side of Eq. (5.6) is the propulsive wave force applied during contact, which is well-approximated by the tangential component of the total reaction force.

The system of equations (5.2)-(5.6) was solved numerically, with time step $0.05\sqrt{\rho r_0^3/\sigma}$ during contact, the duration of which was typically at least $4\sqrt{\rho r_0^3/\sigma}$. We followed a procedure akin to that adopted to obtain the experimental data reported in Fig. 5-3; specifically, we scan a wide range of Ω ($0.2 \leq \Omega \leq 1.2$), with increments of $d\Omega = 0.005$. For each Ω value, we start at a value of Γ close to the Faraday threshold, specifically $\Gamma = 0.99\Gamma_F$, then decrease Γ in small increments until reaching some pre-defined lower limit. We shall refer to one such sweep of Γ as a *run*. The bath is taken to be initially quiescent, $h(x,0) = 0$. We performed several runs, starting each with different initial conditions on the drop position $z(0)$ and speed $\dot{z}(0)$, so as to increase the likelihood of discovering all the possible bouncing modes in case of the coexistence of multiple modes. Usually, this meant setting $z(0) = 0$ and varying $\dot{z}(0)$ between -0.3 and 0.3.

For relatively large drops close to the Faraday threshold, as in our experiments, both walking and bouncing states may arise at identical system parameters. To ensure resolution of the walking solution, the initial horizontal speed was set to a value higher than the equilibrium speed. Then, for each run, we slowly decreased Γ in steps $d\Gamma = 0.001\Gamma_F$, at each step waiting for the walking speed to converge, specifically until the difference between the average walking speed at successive impacts drops below 0.1% :

$$0.999 < \left|\frac{\bar{v}_t}{\bar{v}}\right| < 1.001, \tag{5.8}$$

where $\bar{v}$ and $\bar{v}_t$ are the average horizontal drop speed up to the time of the penultimate and last impacts, respectively.

At each Γ value, we recorded the period of vertical motion and number of contacts per period, which yielded the (m,n) mode number. We also recorded the average contact time $\bar{T}_C$, the total contact time per period of vertical motion divided by the number of contacts n. This allowed us to differentiate between different energy levels, as the high energy modes had $\bar{T}_C < 5\sqrt{\rho r_0^3/\sigma}$ (typically, $\bar{T}_C \approx 3.5\sqrt{\rho r_0^3/\sigma}$), while the low energy modes had $\bar{T}_C > 5\sqrt{\rho r_0^3/\sigma}$ (typically, $\bar{T}_C \approx 8\sqrt{\rho r_0^3/\sigma}$). When the forcing is decreased below a critical value Γ_W, the walking speed drops to 0. The equations of motion can then be simplified somewhat, as (5.6) is identically 0, and $J_0\left(k_C(x - x_n)\right) = 1$ in (5.4). Asimilation of the data obtained by this procedure yielded our theoretical regime diagrams (Fig. 5-3).

The solid coloured regions of Fig. 5-3(a)-5-3(c) indicate the theoretically pre-

dicted bouncing modes. The red line indicates the predicted walking threshold. For the 20 cS-80 Hz combination (Fig. 5-3(a)) several modes are found to exist where predicted, including the observed (2,1), (2,2), (4,4), (4,2), and chaotic modes. The experimental walking threshold for large and small vibration numbers ($\Omega < 0.7$ and $\Omega > 0.9$) coincide with the theoretical predictions; however, for drops of intermediate size, the agreement is less convincing. The (4,3) bouncing mode is experimentally observed for smaller drop sizes than predicted, and the experimental $(2,1)^1$ bouncing region extends further into the theoretical (4,3), $(2,1)^2$ and chaotic regions than predicted. The model does capture the observed $(2,1)^1$-branch cutting across several other regions near $\Gamma \approx 3-4$ and $\Omega < 0.6$.

For the 50 cS-50 Hz combination (Fig. 5-3(b)), the observed and predicted $(2,1)^1$ and $(2,1)^2$ modes coincide convincingly, and the theoretical and experimental walking threshold also match. Furthermore, chaotic bouncers were observed inside the theoretically predicted chaotic region. The (4,3) walking regime was not observed experimentally, but might have been, had larger drops been examined.

For the 20 cS-70 Hz regime diagram (Fig. 5-3(c)), the observed chaotic region for large drops ($\Omega \approx 1$) coincides with that predicted. For smaller drops ($\Omega \approx 0.4-0.6$), the observed (4,3) mode is offset relative to that predicted, as was the case in the experiments at 20 cS-80 Hz (Fig. 5-3(a)). The (2,2) bouncing mode is also observed at slightly lower vibration numbers than predicted. The observed high and low energy (2,1) modes do not coincide with the theory within the walking region, but the walking threshold is generally well-predicted. The mixed mode region found experimentally corresponds closely to the theoretically predicted region of coexistence of the $(2,1)^1$ and $(2,1)^2$ modes. We note that a true mixed mode, characterised by a stable periodic shift between the low and high energy (2,1) modes, has not yet been observed theoretically.

Finally we note that, in our experiments the threshold between bouncing states generally depends on whether it was approached from above or below. Specifically, by increasing and decreasing Γ across a regime boundary, the Γ threshold between states has a characteristic uncertainty of $\Delta\Gamma \approx 0.1$. This hysteresis, which may reflect the existence of prolonged transient behaviour, provides some rationale for the relatively small discrepancy between theory and experiment. We note that significantly less hysteresis was apparent in the simulations, which could be simply extended beyond the transient.

5.5 Conclusion

5.1 We have conducted a combined experimental and theoretical study of drops bouncing on a vibrating fluid bath, and focused on the parameter regime of interest to those studying hydrodynamic quantum analogs. By comparing our experimental results with the theory developed in MB1 and MB2, we have extended the current knowledge of the bouncing droplet system. We have enumerated the myriad styles in which drops can bounce and walk, and presented, in Fig. 5-3, the most detailed experimental and theoretical regime diagrams to date. We have highlighted a mixed state, in which the walking drop shifts between two distinct modes, a state that may serve as an analog of a superposed state in quantum mechanics. Particular interest has been given to elucidating the rich and varied dynamics within the walking regime, an understanding of which will assist in rationalising the quantum mechanical behaviour of walking drops.

Chapter 6

Concluding Remarks

For a drop walking on a vibrating bath, three timescales are important. The shortest of them is the *bouncing timescale*, given by the interval between the successive drop impacts, typically the Faraday period. The intermediate *walking timescale* is prescribed by the drop's horizontal motion, given by the time required to walk one Faraday wavelength. The longest *statistical timescale* emerges when the drop is confined to a finite region of space, and is given by the typical time required for a coherent statistical behaviour to emerge. To discern the spatial profile of the probability distribution function of the drop, the drop's position needs to be recorded over time longer than the statistical timescale. In this thesis, we have developed models to describe the drop's motion on the first two of these three timescales, with a simple model for the statistical timescale treated in Appendix E.

In Chapters 2 and 3 we developed a model that describes the drop motion on the bouncing timescale. In the parameter regime of interest to hydrodynamic quantum analogues, the Weber number varies from 0.01 to 10, necessitating a model that captures the dynamics in both the high and low We regimes. This was achieved with the logarithmic spring model, which captures the increasing ability of the drop and bath for increasingly small We to store the initial kinetic energy of the drop in the surface energy associated with the deformed surface. At the same time, the model captures the increased energy loss to dissipation and outgoing waves with increasingly large We, and the heavier role of fluid inertia.

We first demonstrated the accuracy of the model by comparison with the existing numerical results and experimental data describing drop impact on rigid substrates. We observed a satisfactory match and were able to derive analytical results for the contact time and coefficient of restitution. The model was derived for a substrate of arbitrary radius of curvature, and demonstrated that for small Weber numbers,

the effects of inertia and substrate curvature are captured with a single dimensionless parameter, which we called the rescaled Weber number. Experimental data only exists for impacts on flat boundaries. It would thus be interesting to study experimentally the effects of substrate curvature in order to test the model predictions, specifically to observe what happens when the substrate curvature approaches that of the drop.

In Chapter 3, we extended the model to consider drop impact on a fluid bath, assumed to be initially quiescent. We validated the model by rationalizing existing and new regime diagrams that characterize the behaviour of drops bouncing on a vibrating bath. Using the dimensionless *vibration number*, we were able to collapse our experimental data for different frequencies. We demonstrated that the minima of the bouncing and period-doubling threshold curves correspond to drops for which the resonant frequency of the drop-bath system matches the driving frequency. We showed that the bouncing threshold, the minimum driving acceleration required to prevent drop coalescence, can be accurately predicted using the model without any detailed knowledge of the intervening air layer dynamics. Furthermore, we highlighted the existence and possible overlap of two energy levels of the bouncing modes $(1,1)$ and $(2,1)$. The threshold between the $(1,1)^1$ and $(1,1)^2$ modes sets the lower branch of the bouncing threshold curve, while the $(2,1)^1 - (2,1)^2$ threshold causes an abrupt reversal in the slope of the walking threshold curve (Fig. 4-11).

In Chapter 4, we developed a quantitative model of the walking drops by supplementing the model of the bouncing dynamics with a theoretical description of the evolution of the standing waves on the bath surface. The wave formula derived, obtained via a long-time analysis of the Hankel-transformed fluid equations, was shown to be sufficiently accurate even for times as short as one Faraday period after impact, thanks to the fortuitous combination of the fluid viscosity and driving frequency in the parameter range of interest. A heuristic formula for the tangential drag on the drop during impact was used to complete the physical picture. In the process, we corrected an error in the literature, the misattribution of the origins of this drag to shear in the intervening air layer. A more comprehensive experimental study of the tangential force balance during an oblique drop impact would be of benefit in the future, along with further theoretical developments to describe a wider range of system parameters.

Using our model, we successfully rationalized the extent of the walking region and the dependence of the walking speed on the system parameters. We also gained an intuition into why walking occurs only for a small window of driving frequencies: this is due to the relative locations of the regions of stability of the two $(2,1)$ modes

and the Faraday threshold. By integrating over the vertical dynamics, we obtained the trajectory equation describing the drop's horizontal movement on the walking timescale. This trajectory equation represents an important contribution to the first rational theory for a pilot-wave system and has already proven useful in more complex contexts such as walkers on a rotating bath [88, 87].

In Chapter 5 we further investigated the walking region, using new combinations of driving frequency and oil viscosity We discovered new walking states, the most interesting one being the mixed state where the drop switches periodically between the $(2,1)^1$ and the $(2,1)^2$ bouncing modes. This state may serve as an analogue of a superposed state in quantum mechanics. The experimental results were compared to the theory developed in the previous chapter and further validated our model.

We believe that the work presented in this thesis will serve as a useful reference for future theoretical, numerical and experimental investigation of this walking droplet system. In particular, we hope that the logarithmic spring model and the trajectory equation derived herein will enable more sophisticated numerical modeling of the system [75] and guide the experimental search for new hydrodynamic quantum analogues.

Appendix A

Silicone oil properties

The dependence the density and surface tension on viscosity can be captured by the following fit functions:

$$\frac{\rho}{\mathrm{kg}\cdot\mathrm{m}^{-3}} = 975 - 157\left(\frac{\nu}{\mathrm{cS}}\right)^{-0.6} \qquad \frac{\sigma}{\mathrm{mN/m}} = 21.2 - 3.9\left(\frac{\nu}{\mathrm{cS}}\right)^{-0.6} \tag{A.1}$$

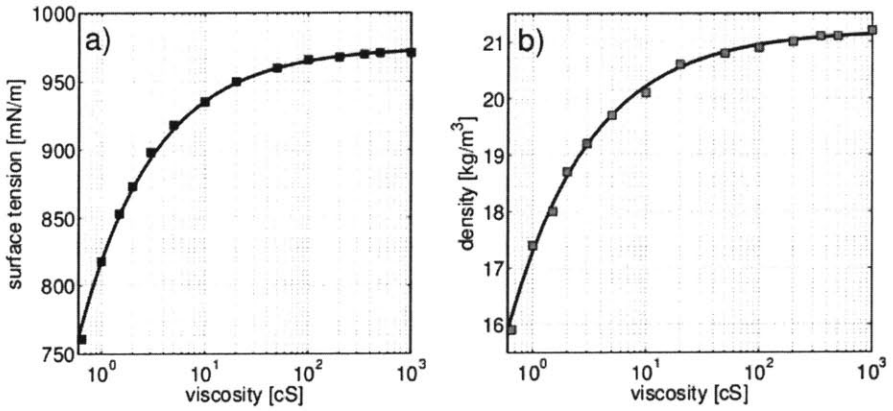

Figure A-1: The surface tension **(a)** and density **(b)** of silicone oil as a function of the viscosity ν. Squares indicate the values for the standard set of industrial oils with $0.65\mathrm{cS} \leq \nu \leq 1000\mathrm{cS}$, while the lines indicate the fitted curves (A.1).

ν [cS]	ρ [kg/m^3]	σ [mN/m]	ν_{99}/ν_{38} [4pt]
0.65	761	15.9	0.31
1.0	818	17.4	0.37
1.5	853	18.0	0.46
2.0	873	18.7	0.48
3.0	898	19.2	0.51
5.0	918	19.7	0.54
10	935	20.1	0.56
20	950	20.6	0.59
50	960	20.8	0.59
100	966	20.9	0.60
200	968	21.0	0.60
350	970	21.1	0.60
500	971	21.1	0.60
1000	971	21.2	0.61

Table A.1: The physical properties of the standard set of industrial silicone oils (polydimethylsiloxanes) at $T = 25°C$. The density ρ, surface tension σ and the viscosity-temperature coefficient $\nu(99°)/\nu(38°)$ are all monotonically increasing functions of the viscosity.

Appendix B

Derivation of the Logarithmic Spring Equation

We consider the regime $We \ll 1$ and build a quasi-static model similar to that developed for drop impact on a rigid substrate [77]. The actual instantaneous shape of the drop and the bath are approximated by relatively simple shapes characterized by a small number of variables. The family of shapes we choose is one consisting of sessile shapes of liquid drops resting on a liquid bath (now not necessarily made of the same liquid as the drop). The reason for this choice is that in the $We \ll 1$ regime, when the overall rebound dynamics is slow relative to the dynamics of the typical surface waves created, one expects the surface shapes to equilibrate to some quasi-static form [1]. If the drop has surface tension σ_D and density ρ_D, and the bath σ_B and ρ_B, the sessile shape family has dimensionality 3 by Buckingham's theorem; it can be parametrized by two Bond numbers $A = \mathcal{B}o_D = \rho_D g R_0^2/\sigma_D$, $C = \mathcal{B}o_B = \rho_B g R_0^2/\sigma_B$ and the parameter $B = \sigma_D \mathcal{B}o_D/\sigma_B$. Although in our system we have $\sigma = \sigma_B$ and $\rho = \rho_B$, initially we keep these variables separate in order to describe the deformation of the drop and bath independently. Parameter A prescribes the magnitude of the drop's deformation, B the vertical bath deformation and C the horizontal extent of bath deformation. Minimizing the total potential energy of the drop and bath allows one to obtain the sessile profile of the drop-bath system and the corresponding values of the total surface and gravitational potential energy. Keeping A, B and C independent for the time being, while setting $\sigma_D = \sigma_B = \sigma$ and $\rho_D = \rho_B = \rho$ for the

sake of simplicity, we obtain

$$\frac{\mathcal{S}.\mathcal{E}._{TOT}}{\pi\sigma R_0^2} \approx \frac{2}{9}A^2\left(\ln\frac{6}{(A+B)C} - 2\gamma - \frac{1}{2}\right) + \frac{2}{9}B^2\left(\ln\frac{6}{A+B} - \frac{4}{3}\right) \quad ,$$
$$\frac{\mathcal{P}.\mathcal{E}._{TOT}}{\pi\sigma R_0^2 \mathcal{B}o} \approx -\frac{4}{9}A\left(\ln\frac{6}{(A+B)C} - 2\gamma + 1\right) - \frac{4}{9}B\left(\ln\frac{6}{A+B} - \frac{5}{6}\right) + \frac{2}{9}\frac{A^2}{C} \quad . \quad \text{(B.1)}$$

Here $\gamma = 0.577216\ldots$ is the Euler-Mascheroni constant, arising via a small-argument approximation of the Bessel function $K_0(x)$. When the fluid viscosity is sufficiently low ($\mathcal{O}h \ll 1$), the flow inside the drop and bath can be approximated by a potential flow. Note that in our experiments, $0.1 < \mathcal{O}h < 1$. Expressing the drop deformation as a sum of spherical harmonic modes, one can then evaluate the kinetic energy associated with a continuous change of drop shape within the sessile shape family (i.e. when $A = A(t)$). The kinetic energy of the bath, moving as a result of time-dependent parameters B and C, can be similarly obtained using the Hankel transform of the bath surface deformation. The total kinetic energy of the system is then given by

$$\frac{\mathcal{K}.\mathcal{E}._{TOT}}{\pi\rho R_0^5} \approx \frac{\pi A^2}{C^{3/2}}\left[\frac{1}{9}\left(\frac{\dot{A}}{A}\right)^2 - \frac{1}{6}\left(\frac{\dot{A}}{A}\right)\left(\frac{\dot{C}}{C}\right) + \frac{5}{72}\left(\frac{\dot{C}}{C}\right)^2\right] + \frac{2}{9}C_{K0}\dot{B}^2 + \frac{2}{3}\dot{Z}^2 \quad , \quad \text{(B.2)}$$

where

$$Z = -\frac{A}{3}\left(\ln\frac{6}{(A+B)C} - 2\gamma\right) - \frac{B}{3}\left(\ln\frac{6}{A+B} - \frac{5}{6}\right) \leq 0 \quad \text{(B.3)}$$

is the dimensionless height of the drop's center of mass ($Z = z/R_0$) and $C_{K0} = \pi^2/12 - 17/27 \approx 0.193$. The coordinates are chosen such that $Z = 0$ when the drop is spherical and the bath flat ($A = B = 0$, corresponding to the initiation of impact). The viscous dissipation inside the drop and bath can also be calculated using the potential flow approximation, provided the condition $\mathcal{O}h \ll 1$ is satisfied. Doing so yields

$$\frac{\mathcal{D}_{TOT}}{\pi\mu R_0^3} = \frac{2\pi A^2}{C^{1/2}}\left[\frac{4}{9}\left(\frac{\dot{A}}{A}\right)^2 - \frac{2}{9}\left(\frac{\dot{A}}{A}\right)\left(\frac{\dot{C}}{C}\right) + \frac{1}{18}\left(\frac{\dot{C}}{C}\right)^2\right] + \frac{8}{9}C_{D0}\dot{B}^2 \quad , \quad \text{(B.4)}$$

where $C_{D0} = \pi^2/4 - 5/12 \approx 2.051$. For a more detailed derivation of equations (B.3-B.4), see the previous chapter. Using expressions (B.1)-(B.4), the equations of

motion can be derived using the Euler-Langrange equation with dissipation [see 122]:

$$\frac{d}{dt}\left[\frac{\partial \mathfrak{L}}{\partial \dot{X}}\right] + \frac{1}{2}\frac{\partial \mathcal{D}_{TOT}}{\partial \dot{X}} = \frac{\partial \mathfrak{L}}{\partial X} \quad , \tag{B.5}$$

where the Lagrangian $\mathfrak{L} = \mathcal{K}.\mathcal{E}_{.TOT} - \mathcal{S}.\mathcal{E}_{.TOT} - \mathcal{P}.\mathcal{E}_{.TOT}$. It should be stressed that the expressions (B.1)-(B.4) are only leading order approximations valid in the limit of small deformations (i.e. when $A, B, C \ll 1$), which arises for impacts at small We.

In order to avoid dealing with a system of 3 differential equations with 3 variables, we need to further simplify the model. Since the drop and bath consist of the same liquid, we expect their deformation to be similar in magnitude (i.e. $A(t) \approx B(t)$), which can be verified either experimentally or by solving the full 3×3 system. Therefore, we set $A = B$. In the moderate Weber number regime ($0.01 < We \lesssim 1$), deformation of the bath occurs predominantly in the region near the drop. The horizontal lengthscale of significant bath deformation, though increasing in time, then remains comparable to the drop radius R_0 throughout the impact, suggesting that we approximate C by a constant. Doing so, we are left with a single independent variable $A(t)$. Thus (B.1)-(B.4) simplify to

$$\frac{\mathcal{S}.\mathcal{E}_{.TOT}}{\pi\sigma R_0^2} \approx \frac{2}{9}A^2\left(2\ln\frac{3}{A} - \ln C - 2\gamma - \frac{11}{6}\right) \quad \frac{\mathcal{P}.\mathcal{E}_{.TOT}}{\pi\sigma R_0^2 Bo} \approx \frac{4}{3}Z + \frac{2}{9}\frac{A^2}{C} \quad , \tag{B.6}$$

$$\frac{\mathcal{K}.\mathcal{E}_{.TOT}}{\pi\rho R_0^5} \approx \frac{2}{3}\dot{Z}^2 + \frac{2}{9}C_{K0}\dot{A}^2 + \frac{\pi}{9}\frac{\dot{A}^2}{C^{3/2}} \qquad \frac{\mathcal{D}_{TOT}}{\pi\mu R_0^3} \approx \frac{8}{9}\frac{\pi\dot{A}^2}{C^{1/2}} + \frac{16}{9}C_{D0}\dot{A}^2 \quad , \tag{B.7}$$

with

$$Z = -\frac{A}{3}\left(2\ln\frac{3}{A} - \ln C - 2\gamma - \frac{5}{6}\right) \quad . \tag{B.8}$$

We now express (B.6) and (B.7) in terms of Z instead of A, employing the fact that for small A, (B.8) can be rewritten as

$$A = -\frac{3Z}{2\ln(-1/Z) + \ldots} \tag{B.9}$$

Assuming $|Z| \ll 1$ and keeping only the leading order contributions in each expression, we obtain

$$\frac{\mathcal{S}.\mathcal{E}_{.TOT}}{\pi\sigma R_0^2} \approx \frac{Z^2}{\ln(\alpha/|Z|)} \qquad \frac{\mathcal{P}.\mathcal{E}_{.TOT}}{\pi\sigma R_0^2 Bo} \approx \frac{4}{3}Z \quad , \tag{B.10}$$

$$\frac{\mathcal{K}.\mathcal{E}_{.TOT}}{\pi\rho R_0^5} \approx \frac{2}{3}\dot{Z}^2 + \frac{(2C_{K0} + \pi C^{-3/2})\dot{Z}^2}{\ln^2(\alpha/|Z|)} \quad \frac{\mathcal{D}_{TOT}}{\pi\mu R_0^3} \approx \frac{\left(16C_{D0} + 8\pi C^{-1/2}\right)\dot{Z}^2}{\ln^2(\alpha/|Z|)} \quad . \tag{B.11}$$

Switching to the dimensionless time $\tau = t/(\rho R_0^3/\sigma)^{1/2}$ and using (B.5), we derive the following equation of motion, keeping the leading order terms only:

$$\frac{d^2Z}{d\tau^2}\left[1+\frac{3C_{K0}+1.5\pi C^{-3/2}}{\ln^2(\alpha/|Z|)}\right]+\mathcal{O}h\frac{6\pi C^{-1/2}+12C_{D0}}{\ln^2(\alpha/|Z|)}\frac{dZ}{d\tau}+\frac{3/2}{\ln(\alpha/|Z|)}Z=-\mathcal{B}o\ . \tag{B.12}$$

Equation (B.12) suggests that the impact of a drop on a quiescent bath can be approximated by a "logarithmic spring" model of the form

$$\frac{d^2Z}{d\tau^2}\left(1+\frac{c_3}{\ln^2(c_1/|Z|)}\right)+\mathcal{O}h\frac{c_2(\mathcal{O}h)}{\ln^2(c_1/|Z|)}\frac{dZ}{d\tau}+\frac{3/2}{\ln(c_1/|Z|)}Z=-\mathcal{B}o\ , \tag{B.13}$$

where c_1, c_2 and c_3 are constants to be determined. Replacing $\mathcal{B}o$ in (B.13) by the effective Bond number $\mathcal{B}o^*(\tau) = \mathcal{B}o\cdot(1+\Gamma\sin\Omega\tau)$, we obtain the logarithmic spring model for a drop bouncing on a vibrating bath:

$$\frac{d^2Z}{d\tau^2}\left(1+\frac{c_3}{Q^2(Z)}\right)+\mathcal{O}h\frac{c_2(\nu)}{Q(Z)}\frac{dZ}{d\tau}+\frac{3/2}{Q(Z)}Z=-\mathcal{B}o^*(\tau)\ , \tag{B.14}$$

where $Q(Z)=\ln(c_1/|Z|)$.

Appendix C

Derivation of the equations for the bath interface shape

We here derive the equations governing the evolution of the radially symmetric disturbance on a liquid bath caused by the rebound of a liquid drop. Besides the assumption of radial symmetry, we approximate the excess pressure distribution (the difference between the local pressure and the atmospheric pressure) over the contact area between the drop and the bath (i.e. the area where the intervening air layer thickness is much smaller than the drop radius and the two liquid-air surfaces have almost the same profile) by a constant: $p(r,t) = p(t)$. Nondimensionalizing using the drop radius R_0 and the characteristic drop oscillation frequency $\omega_D = (\sigma/\rho R_0^3)^{1/2}$, we have

$$h = h'/R_0, r = r'/R_0, \tau = t\omega_D, Z = z/R_0, k = k'R_0 \quad , \tag{C.1}$$

where $h = h(r,\tau)$ is the bath surface height, r the distance from the axis of symmetry, τ the dimensionless time, Z the drop vertical height and k the dimensionless wavenumber. Then the extra surface potential energy is given by

$$\Delta\mathcal{S}.\mathcal{E}. = \sigma R_0^2 \int_0^\infty 2\pi r \left[\sqrt{1+h'^2(r)} - 1\right] \mathrm{d}r \approx \pi\sigma R_0^2 \int_0^\infty r h'^2(r) \mathrm{d}r \quad , \tag{C.2}$$

provided that $h'(r) \ll 1$, where σ is the liquid surface tension. Similarly, the extra gravitational energy is given by

$$\Delta\mathcal{P}.\mathcal{E}. = \rho g R_0^4 \int_0^\infty 2\pi r \frac{1}{2} h^2(r) \mathrm{d}r = \pi\rho g R_0^4 \int_0^\infty r h^2(r) \mathrm{d}r \quad , \tag{C.3}$$

where ρ is the liquid density and g the gravitational acceleration. Finally, the presence of the excess pressure above the contact area gives rise to a pressure potential energy

$$\Delta\mathcal{P}.\mathcal{E}._P = p(\tau)R_0^3\int_0^w 2\pi r h(r)\mathrm{d}r = 2\pi R_0^3 p(\tau)\int_0^w rh(r)\mathrm{d}r \quad , \tag{C.4}$$

where w is the dimensionless radius of the contact area. In order to proceed further, we need to convert the equations derived so far into ones involving the Hankel transform of the surface height. The Hankel transform $H(k)$ of the surface height $h(r)$ is defined as

$$H(k) = \int_0^\infty h(r)J_0(kr)r\mathrm{d}r \quad \text{so that} \quad h(r) = \int_0^\infty H(k)J_0(kr)k\mathrm{d}k \quad , \tag{C.5}$$

where $J_0(x)$ is the Bessel function of the first kind of order 0. The *Plancherel theorem* states that for two functions $f(r)$, $g(r)$ and their Hankel transforms $F(k)$, $G(k)$, the following relationship holds:

$$\int_0^\infty f(r)g(r)r\mathrm{d}r = \int_0^\infty F(k)G(k)k\mathrm{d}k \quad . \tag{C.6}$$

Using the Plancherel theorem, we can easily convert the equation (C.3) to

$$\Delta\mathcal{P}.\mathcal{E}. = \pi g R_0^4\int_0^\infty H^2(k)k\mathrm{d}k \quad . \tag{C.7}$$

Substituting for $h'(r) = -\int k^2 J_1(kr)H(k)\mathrm{d}k$ into (C.2) and using the closure equation $\int_0^\infty xJ_i(ux)J_i(vx)\mathrm{d}x = \delta(u-v)/u$, where $\delta(x)$ is the Dirac delta function, we obtain

$$\Delta\mathcal{S}.\mathcal{E}. = \pi\sigma R_0^2\int_0^\infty H^2(k)k^3\mathrm{d}k \quad . \tag{C.8}$$

Finally, (C.4) can be rewritten as

$$\Delta\mathcal{P}.\mathcal{E}._P = 2\pi R_0^3 p(\tau)\int_0^\infty H(k)k\int_0^w J_0(kr)r\mathrm{d}r\mathrm{d}k = 2\pi R_0^3 p(\tau)\int_0^\infty H(k)J_1(kw)w\mathrm{d}k \quad . \tag{C.9}$$

C.0.1 Small viscosity

When the viscosity of the liquid is small, we can approximate the flow inside the bath by potential flow. The general axisymmetric solution to $\nabla^2\Phi = 0$ in cylindrical

coordinates, which decays as $r \to \infty$, can be written as

$$\Phi(r,z,t) = \int_0^\infty \varphi(k,\tau) J_0(kr) e^{kz} k \mathrm{d}k \quad . \tag{C.10}$$

The linearized kinematic boundary condition at the surface $R_0 \frac{\partial h(r,t)}{\partial t} = u_z(x,0,t) = \frac{1}{R_0}\frac{\partial \Phi}{\partial z}|_{z=0}$ implies

$$R_0^2 \int_0^\infty \dot{H}(k,t) J_0(kx) k \mathrm{d}k = \int_0^\infty \varphi(k,t) J_0(kx) k^2 \mathrm{d}k \quad , \tag{C.11}$$

and therefore $\varphi(k,t) = R_0^2 \dot{H}(k,t)/k$. Equation (C.10) can therefore be written

$$\Phi(r,z,\tau) = R_0^2 \int_0^\infty \dot{H}(k,\tau) J_0(kx) e^{kz} \mathrm{d}k \quad . \tag{C.12}$$

The kinetic energy of the bath is given by

$$\begin{aligned} \frac{\mathcal{K}.\mathcal{E}.}{\rho} &= \frac{1}{2}\int_V \boldsymbol{\nabla}\Phi \cdot \boldsymbol{\nabla}\Phi \mathrm{d}V = \frac{1}{2}\int_V \boldsymbol{\nabla}\cdot(\Phi\boldsymbol{\nabla}\Phi)\,\mathrm{d}V = \\ &= \frac{1}{2}\int_S \Phi\boldsymbol{\nabla}\Phi\cdot\mathrm{d}\boldsymbol{S} = \frac{R_0}{2}\int_0^\infty \Phi\frac{\partial\Phi}{\partial z} 2\pi x \mathrm{d}x = \pi R_0^5 \int_0^\infty \dot{H}^2(k,t)\mathrm{d}k \quad , \end{aligned} \tag{C.13}$$

where we have used the Plancherel theorem again and approximated the direction of the surface normal vector as vertical. It can similarly be shown that the viscous dissipation in the bath is given by

$$\mathcal{D} = 8\pi\mu R_0^3 \int_0^\infty \dot{H}^2(k,t) k^2 \mathrm{d}k \quad . \tag{C.14}$$

Then the equations of motion can be derived via the Euler-Lagrange equation with dissipation [41, 122, p.271]

$$\frac{\mathrm{d}}{\mathrm{d}t}\frac{\partial \mathfrak{L}}{\partial \dot{H}} + \frac{1}{2}\frac{\partial \mathcal{D}}{\partial \dot{H}} = \frac{\partial \mathfrak{L}}{\partial H} \quad , \tag{C.15}$$

where $\mathfrak{L}$ is the Lagrangian, defined as

$$\mathfrak{L} = \mathcal{K}.\mathcal{E}. - \Delta\mathcal{S}.\mathcal{E}. - \Delta\mathcal{P}.\mathcal{E}. - \mathcal{P}.\mathcal{E}._P \quad . \tag{C.16}$$

Substituting for $\mathfrak{L}$ from (C.16) into (C.15), and using the expressions (C.7)-(C.9),(C.13)-(C.14) yields

$$\ddot{H} + 2\frac{\mu k^2}{\rho R_0^2}\dot{H} + \frac{\sigma}{\rho R_0^3}\left[k^3 + k\mathcal{B}o\right] H + \frac{pw}{\sigma R_0^2} J_1(kw) = 0 \ , \qquad \text{(C.17)}$$

where $\mathcal{B}o = \rho g R_0^2/\sigma$ is the Bond number. Going back to the dimensionless time $\tau = t\omega_D$, we obtain

$$H_{\tau\tau} + 2\mathcal{O}h \cdot k^2 H_\tau + \left[k^3 + k\mathcal{B}o\right] H + \frac{R_0 pw}{\sigma} J_1(kw) = 0 \ , \qquad \text{(C.18)}$$

with $\mathcal{O}h = \mu/(\sigma\rho R_0)^{1/2}$ being the Ohnesorge number. The total reaction force F_R acting on the bath, given by $F_R = R_0^2 \int_0^w 2\pi r p dr = \pi w^2 R_0^2 p$, is the same force acting on the drop, so that $m\ddot{z} = F_R - mg$. Rewriting the last expression in terms of the dimensionless coordinates, we get $Z_{\tau\tau} = \frac{3}{4} R_0 w^2 p/\sigma - \mathcal{B}o \equiv F - \mathcal{B}o$, and so (C.18) can be rewritten as

$$H_{\tau\tau} + 2\mathcal{O}h \cdot k^2 H_\tau + \left[k^3 + k\mathcal{B}o\right] H + \frac{4}{3} F \frac{J_1(kw)}{w} = 0 \ , \text{ with } F = Z_{\tau\tau} + \mathcal{B}o \ . \qquad \text{(C.19)}$$

C.0.2 Appreciable viscosity

For appreciable viscosity, the fluid motion diverges significantly from potential flow near the surface and the method described above can no longer be applied. However, considerable accuracy can be maintained without sacrificing the simplicity of (C.19) by replacing $\mathcal{O}h$ by a phenomenological or "effective" Ohnesorge number $\mathcal{O}h_e$, so that the rates of decay predicted by this pseudo-linear model and the full analytic model coincide. Alternatively, one can try to match the experimentally observed decay rates, as was done by Eddi *et al.*[32]. To determine the value of $\mathcal{O}h_e$ analytically, we follow Prosperetti[93] and match the principal decay rates of the surface waves with wavelength k by replacing equation (C.19) with

$$A\left(k, \mathcal{O}h, \mathcal{B}o\right) H_{\tau\tau} + 2\mathcal{O}h \cdot D\left(k, \mathcal{O}h, \mathcal{B}o\right) k^2 H_\tau + \left[k^3 + k\mathcal{B}o\right] H + \frac{4}{3} F \frac{J_1(kw)}{w} = 0 \ , \qquad \text{(C.20)}$$

where the coefficients A, D are chosen so that the roots of the equation

$$Ax^2 + 2aDx + 1 = 0 \ , \quad \text{where} \quad a = \frac{\mathcal{O}h \cdot k^{3/2}}{(\mathcal{B}o + k^2)^{1/2}} \ , \qquad \text{(C.21)}$$

are the two roots with the largest real part of the polynomial equation

$$\left[(x+2a)^2+1\right]^2 = 16a^3(x+a) \quad . \tag{C.22}$$

Then

$$\mathcal{O}h_e = \mathcal{O}h \cdot D \quad . \tag{C.23}$$

It can be shown that $D \to 2$ as $\mu \to 0$, while $D \to 1$ as $\mu \to \infty$ [71]. On the other hand, $A \to 1$ as $\mu \to 0$ and remains close to 1 for $\mathcal{O}h \cdot k^{1/2} < 0.3$. From now on we will thus approximate A by 1 and write $\mathcal{O}h_e$ instead of $\mathcal{O}h$.

When the bath is shaken vertically with frequency f and peak acceleration Γg, we need only replace $\mathcal{B}o$ by an effective Bond number $\mathcal{B}o^*$ which is now a function of time:

$$\mathcal{B}o^*(\tau) = \mathcal{B}o\,(1+\Gamma \sin \Omega\tau) \quad , \tag{C.24}$$

and represents the sum of gravity and fictitious forces in the non-inertial frame of reference fixed with the oscillating bath. Here $\Omega = \omega/\omega_D = 2\pi f/\omega_D$ is the vibration number. Thus we arrive at the equation

$$H_{\tau\tau} + 2\mathcal{O}h_e k^2 H_\tau + \left[k^3 + k\mathcal{B}o^*(\tau)\right] H = -\frac{4}{3}F\frac{J_1(wk)}{w} \quad , \tag{C.25}$$

We are interested in the behaviour of the model for k near k_F, the Faraday wavelength, which is defined by the dimensionless dispersion relation [see 69, p. 1121]

$$k_F^3 + \mathcal{B}o \cdot k_F = \frac{1}{4}\Omega^2 \quad , \tag{C.26}$$

particularly in the regime $\Omega \lesssim 1$ where we observe walking. Since $\mathcal{B}o \cdot k_F$ is positive, we have $k_F \leq \left(\frac{\Omega}{2}\right)^{2/3}$.

C.0.3 Point force approximation

We seek to show that for the range of parameters explored in our experiments, wk_F is always small, so we can approximate the impact forcing by a point forcing. During rebound, the extra pressure in the intervening air layer beneath the contact area can be bounded below by half the capillary pressure σ/R_0 [63]. The drop's change of momentum during impact is at most $\Delta P \approx \frac{4}{3}\pi\rho R_0^3 2v$, where v is the drop speed at impact. The rebound time is roughly $t_C \approx 4\left(\rho R_0^3/\sigma\right)^{1/2}$ (see *MBI*, Fig. 8); thus, the typical force on the drop during rebound is $F_R \approx \Delta P/t_C \approx \left(\rho R_0^3\sigma\right)^{1/2} 2v$. Dividing

the typical reaction force by the lower bound on the pressure yields an upper bound on the typical contact area: $\pi R_0^2 w^2 \leq 2R_0^2 We^{1/2}$, where $We = \rho R_0 v^2/\sigma$ is the Weber number. Hence $w^2 \leq 2We^{1/2}/\pi$. For droplets bouncing periodically with the Faraday period (twice the driving period) we have $Z\left(\tau + \frac{4\pi}{\Omega}\right) = Z(\tau)$. The acceleration of the drop in flight is Bo so the maximum dimensionless relative velocity is $We_{max}^{1/2} = Bo\frac{2\pi}{\Omega}$. Therefore, $wk_F \leq \left[Bo\frac{2\pi}{\Omega}\frac{2}{\pi}\right]^{1/2}\left(\frac{\Omega}{2}\right)^{2/3} = (Bo)^{1/2}\left(\frac{\Omega}{2}\right)^{1/6}$.

Since $J_1(x) = \frac{x}{2} - \frac{x^3}{16} + O(x^5)$, for $\frac{x^2}{8} \ll 1$ we can approximate $J_1(x)$ by $\frac{x}{2}$. Thus we can write $J_1(wk)/w = k/2$, provided $w^2k_F^2/8 \leq 2Bo\left(\frac{\Omega}{2}\right)^{1/3} \ll 1$. Restricting ourselves to the region $\Omega \leq 1$, it follows that by using the point force approximation we commit a relative error of at most $2Bo$ in estimating the forcing for each wavenumber. Typically, $R_0 \approx 0.3 - 0.4$ mm ($Bo = 0.04 - 0.08$) leading to a relative error of at most $10 - 15\%$. We note that this is likely an overestimate of the relative error, as the actual contact area and relative velocity of impact will both be significantly smaller than the upper bounds used.

C.0.4 Analysis of the standing waves for small viscosity

We shall henceforth use the point force approximation, bearing in mind that it might lead to an overestimate of the bath deformation for larger drops ($R_0 > 0.4$ mm). Thus (C.26) simplifies to

$$H_{\tau\tau} + 2Oh_e k^2 H_\tau + H\left(k^3 + kBo^*(\tau)\right) = -\frac{2}{3}kF(\tau)\ . \tag{C.27}$$

We shall write $\Upsilon(k) = Oh_e(k)\cdot k^2$ for simplicity and consider presently the case of no forcing (right-hand side of (C.27) equals zero), assuming $Oh_e \ll 1$:

$$H_{\tau\tau} + 2\Upsilon H_\tau + H\left(k^3 + kBo^*(\tau)\right) = 0\ . \tag{C.28}$$

Making the substitution $H(\tau) = \exp(-\Upsilon\tau)\mathcal{H}(\tau)$, we can convert (C.28) into the Mathieu equation and by applying Floquet's theorem we obtain the form of general solution of (C.28):

$$H(\tau) = c_1 H_1(\tau) + c_2 H_2(\tau) = c_1 \exp(\beta\tau)\,\bar{H}(\tau) + c_2 \exp\left[(\beta - 2\Upsilon)\tau\right]\bar{H}\left(\pi/\Omega - \tau\right)\ , \tag{C.29}$$

where $\bar{H}(\tau)$ is a periodic function with period $4\pi/\Omega$. Below the Faraday threshold, we may assume without loss of generality that $\beta < \Upsilon < 0$, so that $H_2(\tau)$ decays faster than $H_1(\tau)$. Thus, for large times, $H_1(\tau)$ will dominate the behaviour of $H(\tau)$. Now

we return to (C.27) and consider the Green's function $G(\tau, \tau_0)$ for the forcing, defined as the solution of

$$G_{\tau\tau} + 2\Upsilon G_\tau + G\left(k^3 + k\mathcal{B}o\left(1 + \Gamma \sin \Omega\tau\right)\right) = \delta(\tau - \tau_0) \quad . \tag{C.30}$$

We can write $G(\tau, \tau_0)$ as a linear combination of the two solutions of the homogeneous problem (C.28). Equation (C.30) implies that $G(\tau_0, \tau_0) = 0$ and $G_\tau(\tau_0^+, \tau_0) = 1$, from which we derive

$$G(\tau, \tau_0) = \frac{H_1(\tau)H_2(\tau_0) - H_2(\tau)H_1(\tau_0)}{H_{1\tau}(\tau_0)H_2(\tau_0) - H_1(\tau_0)H_{2\tau}(\tau_0)} \quad . \tag{C.31}$$

The denominator in (C.31) is the Wronskian $W(H_2, H_1)(\tau_0)$, which satisfies $W_\tau = -\Upsilon W$, implying $W(\tau_0) = \exp\left(-\Upsilon\tau_0\right) W(0)$. Using this identity and the forms of H_1 and H_2, we can express (C.31) as

$$G(\tau, \tau_0) = \frac{e^{-\beta(\tau-\tau_0)}\bar{H}(\tau)\bar{H}\left(\frac{\pi}{\Omega} - \tau_0\right) - e^{(\beta-2\Upsilon)(\tau-\tau_0)}\bar{H}(\tau_0)\bar{H}\left(\frac{\pi}{\Omega} - \tau\right)}{\bar{H}_\tau(0)\bar{H}\left(\frac{\pi}{\Omega}\right) + \bar{H}(0)\bar{H}_\tau\left(\frac{\pi}{\Omega}\right) - 2\bar{H}(0)\bar{H}\left(\frac{\pi}{\Omega}\right)(\beta - \Upsilon)} \quad . \tag{C.32}$$

By neglecting the H_2 component of $G(\tau, \tau_0)$ for large times, when it has decayed sufficiently relative to H_1, we can approximate the solution to (C.27) as follows:

$$\begin{aligned} H(\tau) &\approx \left[\int -\frac{2}{3}kF(\tau')G_1(\tau')\mathrm{d}\tau'\right] e^{-\beta\tau}\bar{H}(\tau), \\ \text{where } G_1(u) &= \frac{\exp(\beta u)\bar{H}\left(\frac{\pi}{\Omega} - u\right)}{\bar{H}_\tau(0)\bar{H}\left(\frac{\pi}{\Omega}\right) + \bar{H}(0)\bar{H}_\tau\left(\frac{\pi}{\Omega}\right) + 2\left(\Upsilon - \beta\right)\bar{H}(0)\bar{H}\left(\frac{\pi}{\Omega}\right)} \quad . \end{aligned} \tag{C.33}$$

In order to proceed, we need to determine the periodic function $\bar{H}(\tau)$. We decompose $\bar{H}(\tau)$ into its Fourier components, starting with the sub-harmonic component with angular frequency $\Omega/2$:

$$H(\tau) = e^{\beta\tau} \sum_{n=-\infty}^{\infty} \hat{H}_n \cdot e^{i\Omega\frac{n}{2}\tau} \quad . \tag{C.34}$$

Substituting this form into (C.28) yields

$$\hat{H}_n\left[k^3 + k\mathcal{B}o - \frac{n^2}{4}\Omega^2 + 2\Upsilon\beta + \beta^2 + i\left(\beta\Omega n + \Upsilon\Omega n\right)\right] - \frac{i}{2}k\mathcal{B}o\Gamma\left[\hat{H}_{n-2} - \hat{H}_{n+2}\right] = 0 \quad . \tag{C.35}$$

This recurrence relation along with the reality condition $\hat{H}_n = \hat{H}_{-n}^*$ and smoothness of $H(t)$, $\lim_{|n|\to\infty} |n\hat{H}_n| = 0$, allows one to obtain the complete Fourier series of $\bar{H}(\tau)$,

involving two multiplicative constants (one for the odd terms, the other for the even terms), which are determined from the initial conditions. The growth rate β depends on Γ, corresponding to the amplitude of the bath oscillation; for $\Gamma < \Gamma_F$, $\beta < 0$ and $H(\tau)$ decays exponentially in time, while for $\Gamma > \Gamma_F$, $\beta > 0$ and $H(\tau)$ grows exponentially. Γ_F denotes the Faraday threshold, and we will be interested in the behaviour of $H(\tau)$ for Γ near Γ_F. Since $\beta = 0$ for $\Gamma = \Gamma_F$, β must be small for Γ near Γ_F . Finally, the value of the Faraday threshold depends strongly on the wavenumber k. We are interested in the wavenumbers k near k_C, the critical wavenumber where $\Gamma_F(k)$ achieves a global minimum. Assuming that for small damping ($\mathcal{O}h_e \ll 1$) the function $H(\tau)$ is nearly sinusoidal, so that the terms $\hat{H}_{\pm 1}$ dominate all others, we obtain

$$\hat{H}_1 \left[k^3 + k\mathcal{B}o - \frac{\Omega^2}{4} + 2\Upsilon\beta + i\left(\beta\Omega + \Upsilon\Omega\right) \right] - \frac{i}{2} k\mathcal{B}o\Gamma \hat{H}_1^* = 0 \ . \tag{C.36}$$

Writing $\hat{H}_1 = |\hat{H}_1| \cdot e^{i\theta}$ and considering the real and imaginary parts separately, we obtain

$$k^3 + k\mathcal{B}o - \frac{\Omega^2}{4} + 2\Upsilon\beta = \frac{1}{2} k\mathcal{B}o\Gamma \sin(2\theta) \ , \qquad \beta\Omega + \Upsilon\Omega = \frac{1}{2} k\mathcal{B}o\Gamma \cos(2\theta) \ . \tag{C.37}$$

When $\mathcal{O}h_e = 0$, $\Gamma_F = 0$, and $k_C = k_F$; therefore, we expect $k_C \approx k_F$ when $\mathcal{O}h_e$ is small. Then, we assume $|\beta| \ll 1$, write $k = k_F(1 + \delta k)$ with $\delta k \ll 1$, and expand in powers of δk to obtain

$$\frac{\sin 2\theta}{2} = \frac{3k_F^2 + \mathcal{B}o}{\mathcal{B}o\Gamma} \delta k + O\left((\delta k)^2\right) + O(\beta) \ , \qquad \beta = -\Upsilon + \frac{k\mathcal{B}o\Gamma}{2\Omega} \cos 2\theta \ . \tag{C.38}$$

Assuming $\theta \ll 1$ so that $\frac{1}{2}\sin 2\theta \approx \theta$, we can write $\cos 2\theta = 1 - 2\theta^2$ and substitute for θ from (C.38) to deduce

$$\beta = -\Upsilon + \frac{\mathcal{B}o\Gamma k}{2\Omega} \left(1 - \frac{2(3k_F^2 + \mathcal{B}o)^2 (k - k_F)^2}{\Gamma^2 \mathcal{B}o^2 k_F^2} \right) \ . \tag{C.39}$$

Setting $\beta = 0$, solving for Γ_F and minimizing with respect to k yields

$$k_C \approx k_F \left(1 - \epsilon^2\right) \quad \text{and} \quad \Gamma_F \approx \frac{2\mathcal{O}h_e \Omega k_F}{\mathcal{B}o} \left(1 - \frac{1}{2}\epsilon^2\right) = 2\epsilon \left(1 + \frac{3k_F^2}{\mathcal{B}o}\right) \left(1 - \frac{1}{2}\epsilon^2\right) \ , \tag{C.40}$$

$$\text{where} \quad \epsilon = \frac{\mathcal{O}h_e \Omega k_F}{3k_F^2 + \mathcal{B}o} \ , \tag{C.41}$$

so that

$$\beta \approx \mathcal{O}h_e k_C^2 \left(\frac{\Gamma}{\Gamma_F} - 1\right) - \frac{\mathcal{O}h_e}{2\epsilon^2}\left(1 + 2\epsilon^2\right)(k - k_C)^2 \tag{C.42}$$

and

$$\theta \approx -\frac{\epsilon}{2} + \frac{k - k_C}{2\epsilon k_F} \quad . \tag{C.43}$$

The long-term behaviour of $H(k,\tau)$ is thus given by

$$H(k,\tau) \approx A(k) e^{\beta(k)\tau} \cos\left(\frac{\Omega}{2}\tau - \frac{\epsilon}{2} + \frac{k - k_C}{2\epsilon k_F}\right) \quad . \tag{C.44}$$

In order to simplify the subsequent formulae, we introduce the decay time τ_D by writing

$$\beta(k) = \left(\Gamma/\Gamma_F - 1\right)\frac{1}{\tau_D} - \beta_1 (k - k_C)^2 \quad . \tag{C.45}$$

By comparison with (C.42) we have

$$\tau_D \approx \left(\mathcal{O}h_e k_C^2\right)^{-1} \quad , \quad \beta_1 \approx \frac{\mathcal{O}h_e}{2\epsilon^2}\left(1 + 2\epsilon^2\right) \quad . \tag{C.46}$$

We henceforth assume that $\Gamma < \Gamma_F$, so $\beta(k) < 0$. When $\beta_1 \tau k_C^2 \gg 1$, $\beta(k)$ has a sharp maximum at k_C and we can use Laplace's method:

$$\begin{aligned} h(r,\tau) &= \int_0^\infty H(k,\tau) J_0(kr) k \mathrm{d}k \approx \\ &\approx \cos\frac{\Omega\tau}{2} \exp\left\{\left(\frac{\Gamma}{\Gamma_F} - 1\right)\frac{\tau}{\tau_D}\right\} \int_0^\infty A(k) e^{-\beta_1 \tau (k - k_C)^2} \cos\frac{k - k_C}{2\epsilon k_F} J_0(kr) k \mathrm{d}k \approx \\ &\approx \cos\frac{\Omega\tau}{2} A(k_C) \frac{\exp\left\{\left(\Gamma/\Gamma_F - 1\right)\tau/\tau_D\right\}}{\exp\left\{1/16\epsilon^2 k_F^2 \beta_1 \tau\right\}} \sqrt{\frac{\pi}{\beta_1 \tau}} J_0(k_C r) k_C \left[1 + O\left(\frac{r^2}{4\beta_1\tau}\right)\right] \quad . \end{aligned} \tag{C.47}$$

Here we have used the identity $\int_0^\infty \exp\left(-ax^2\right)\cos bx \mathrm{d}x = \exp\left(-b^2/4a\right)\sqrt{\pi/a}$. Therefore, within a certain radius $r(\tau) \sim \sqrt{\beta_1 \tau}$, the surface height can be approximated by a standing wave with a radial profile prescribed by a Bessel function. We assume that the drop is within this radius as measured from all the previous impacts for which the corresponding standing wave has not yet decayed sufficiently to be negligible. This condition sets an upper bound on the allowable horizontal speed $|dx/d\tau|^2 < 2\beta_1\left(1 - \Gamma/\Gamma_F\right)/\tau_D$. In order to approximate the wave amplitude $A(k_C)$, we use $\bar{H}(\tau) \approx \cos\left(\Omega\tau/2\right)$ in (C.33) to obtain

$$G_1(u) \approx -\frac{2}{\Omega}\sin\frac{\Omega u}{2} \quad . \tag{C.48}$$

Substitution of (C.48) into (C.33) and (C.47) yields

$$h(r,\tau) \approx \frac{4k_C^2}{3\Omega}\sqrt{\frac{\pi}{\beta_1\tau}}\cos\frac{\Omega\tau}{2}\left[\int F(u)\sin\frac{\Omega u}{2}\mathrm{d}u\right]\frac{\exp\left\{(\Gamma/\Gamma_F-1)\,\tau/\tau_D\right\}}{\exp\left\{1/16\epsilon^2k_F^2\beta_1\tau\right\}}J_0(k_C r)\ . \tag{C.49}$$

When $16\epsilon^2k_F^2\beta_1\tau \gg 1$, $\exp\left\{1/16\epsilon^2k_F^2\beta_1\tau\right\} \approx 1$ and by using (C.46) we can approximate (C.49) as

$$h(r,\tau) \approx A\cos\frac{\Omega\tau}{2}\exp\left\{(\Gamma/\Gamma_F-1)\,\tau/\tau_D\right\}\tau^{-1/2}J_0(k_C r)\ , \tag{C.50}$$

$$\text{where}\quad A=\frac{4\sqrt{2\pi}}{3}\frac{k_C^2k_F\mathcal{O}h_e^{1/2}}{3k_F^2+\mathcal{B}o}\left[\int F(u)\sin\frac{\Omega u}{2}\mathrm{d}u\right]\ .$$

The approximation (C.50) is valid when $16\epsilon^2\beta_1\tau k_F^2 \gg 1$ and $\beta_1\tau k_F^2 \gg 1$. We are interested in the bath distortion only insofar as it affects the drop dynamics; therefore, the earliest time after the initial disturbance at which we need use the approximation is on the next impact, a Faraday period later (assuming the drop is in the $(2,1)^2$ mode). We thus require that $16\epsilon^2\beta_1\tau_F k_F^2 \gg 1$ and $\beta_1\tau_F k_F^2 \gg 1$. Employing the lower bound $k_F > (\Omega/2)^{2/3}$ following from the definition of k_F (C.26), together with (C.46), the two conditions are met provided

$$0.014 \approx \left(2\pi^{1/3}\right)^{-4} \ll \left(\frac{\mu^3 f}{\rho\sigma^2}\right)^{1/3} \ll \frac{9}{8}\pi^{2/3} \approx 2.4\ . \tag{C.51}$$

For $\nu = 20$ cS and 50 Hz $\leq f \leq$ 100 Hz, we obtain values between 0.09 and 0.12, while for $\nu = 50$ cS and 40 Hz $\leq f \leq$ 80 Hz, we obtain values between 0.22 and 0.28. For lower viscosities, the lower bound is violated, while for higher viscosities, the upper bound is violated. In those cases, the approximation (C.50) becomes accurate only after multiple Faraday periods have elapsed since impact and higher order terms in the Laplace approximation (C.47) need to be included to achieve sufficient accuracy for all drop impacts. Nevertheless, for our purposes, the leading-order approximation (C.50) will suffice.

C.0.5 Numerical simulation

The approximations to the critical wavenumber k_C, Faraday threshold Γ_F and the decay time τ_D, given by the formulae (C.40) (C.41) and (C.46), respectively, are only valid in the limit $\epsilon \ll 1$, where $\epsilon = \mathcal{O}h_e\Omega k_F/(3k_F^2+\mathcal{B}o)$. As the values of these parameters play a crucial role in the evolution of the standing waves near the Faraday

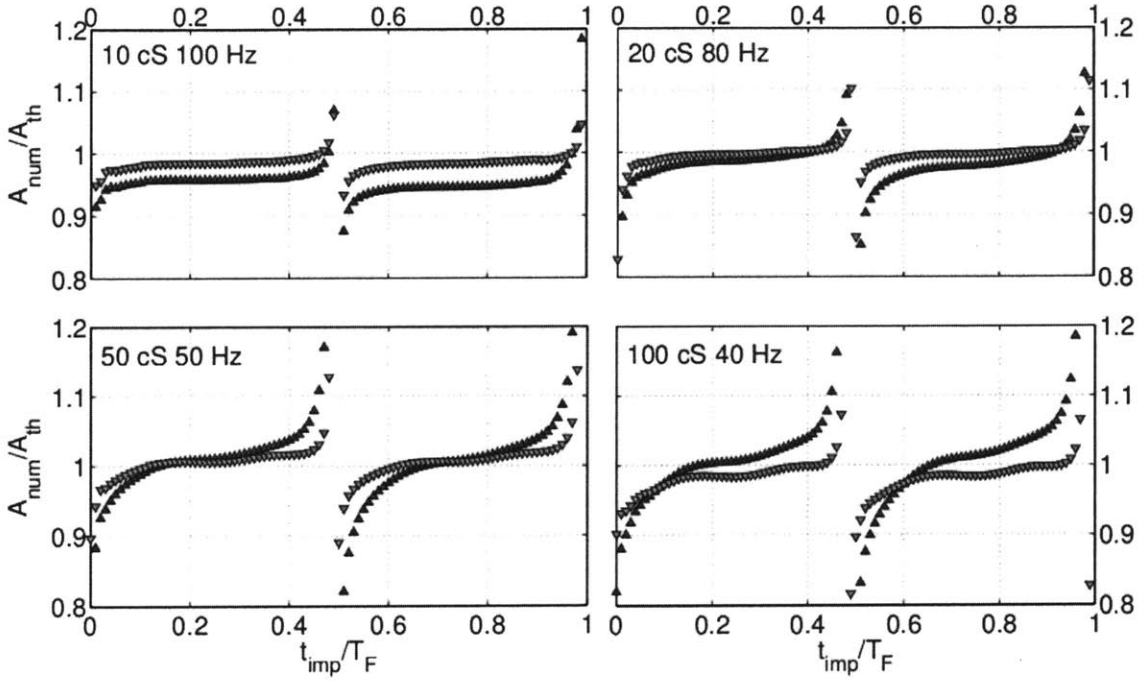

Figure C-1: Comparison between the full numerical model and the long-term approximation (C.52). The bath surface is forced at time $t = t_{imp}$ and then evolved freely, and the amplitude of the standing wave $A(t) = h(0,t)$ is recorded, as computed by a full numerical scheme solving (C.27) (A_{num}) and as given by (C.52) (A_{th}). The average ratio A_{num}/A_{th} over $T_F \leq t \leq 6T_F$ (▲) and over $T_F \leq t \leq 10T_F$ (▼) is shown as a function of t_{imp}, for different combinations of oil viscosity and driving frequency: **(a)** $\nu = 10$ cS and $f = 100$ Hz, **(b)** $\nu = 20$ cS and $f = 80$ Hz, **(c)** $\nu = 20$ cS and $f = 50$ cS and **(d)** $\nu = 100$ cS and $f = 40$ Hz. The ratio tends to 1 for large times, except near $t_{imp} \approx \frac{n}{2}T_F$, when $G_1(t_{imp}) \approx 0$ and other wavenumbers contribute to the overall amplitude beside the region near k_F.

ν	f		Γ_F		k_C/k_F		τ_F/τ_D		$\beta_1 k_F^2 \tau_F$	
[cS]	[Hz]	ϵ	theor.	num.	theor.	num.	theor.	num.	theor.	num.
10	100	0.097	3.324	3.326	0.991	0.988	0.804	0.816	44.35	44.69
10	120	0.102	4.526	4.530	0.990	0.987	0.868	0.883	43.07	43.41
20	60	0.156	2.562	2.566	0.976	0.971	1.126	1.173	25.60	26.26
20	80	0.170	4.220	4.228	0.971	0.965	1.303	1.369	25.32	25.99
20	90	0.176	5.159	5.170	0.969	0.962	1.373	1.447	25.08	25.76
50	40	0.311	2.707	2.731	0.903	0.904	1.664	1.967	12.59	14.38
50	50	0.335	4.028	4.073	0.888	0.888	1.893	2.311	13.12	15.03
50	60	0.353	5.514	5.586	0.875	0.874	2.056	2.577	13.45	15.47
100	40	0.563	4.334	4.646	0.683	0.772	1.721	3.295	9.51	13.47
100	50	0.597	6.251	6.789	0.644	0.746	1.775	3.779	10.29	14.65

Table C.1: Comparison of some of the critical parameters describing the standing wave evolution, as calculated numerically and given by the theoretical approximations (C.40), (C.46), for the combinations of oil viscosity ν and driving frequency f at which walking occurs. These are the Faraday threshold $\Gamma_F = \gamma_F/g$, the ratio of the most unstable wavenumber k_C to the Faraday wavenumber k_F, the ratio of the Faraday period τ_F to the decay time τ_D and the parameter $\beta_1 k_F^2 \tau_F$, which describes the increase of the decay rate of $H(k)$ as k moves away from k_C. The parameter ϵ, defined in (C.41), was assumed small in our theoretical analysis. We observe a good match for small ν, which gradually worsens as ν (and thus also ϵ) increases. The error is of order ϵ^2.

threshold, in order to achieve a better match with experiments for larger values of ϵ (e.g. when $\nu = 50$ cS), we calculate them numerically. Starting from the recurrence relation (C.35), the conditions $\hat{H}_n = \hat{H}^*_{-n}$ and $\lim_{n\to\infty} |n\hat{H}_n| = 0$ yield a unique solution for Γ, given β. The solution can be found by choosing arbitrary values of $\hat{H}_N$ and $\hat{H}_{N-2}$ for some large odd N, then working backwards using the recurrence relation and finally rescaling all terms in order to satisfy the reality condition $\hat{H}_n = \hat{H}^*_{-n}$. Choosing $N > 15$ usually suffices to achieve 10-digit accuracy in Γ. Thus, given k and β, we can find the corresponding Γ. Setting $\beta = 0$ gives us $\Gamma_F(k)$, and minimizing with respect to k yields k_C and Γ_F. In order to obtain τ_D, we need only calculate Γ' corresponding to some small β and then use the relation $\tau_D = (\Gamma'/\Gamma_F - 1)/\beta$. Table C.1 compares the values obtained analytically and numerically.

In our analytic treatment of the standing wave evolution, we have approximated the time-periodic part $\bar{H}(\tau) = \sum_{-\infty}^{\infty} \hat{H}_n \exp(i\Omega n\tau/2)$ of the Hankel transform of the surface height by its first Fourier component: $\bar{H}(\tau) \approx \sum_{-1}^{1} \hat{H}_n \exp(i\Omega n\tau/2) = \cos\left(\frac{\Omega\tau}{2} + \theta\right)$ ($\hat{H}_{2m} = 0$ for the sub-harmonic mode). When the viscosity is appreciable, accurate representation of the time-periodicity requires inclusion of the next Fourier

modes $\hat{H}_{\pm 3}$. Therefore, the approximation to the standing wave evolution, which will be used in the numerical model, is given by (compare with (C.50)):

$$h(r,\tau) \approx \frac{4\sqrt{2\pi}}{3} \frac{k_C^2 k_F \mathcal{O}h_e^{1/2}}{3k_F^2 + \mathcal{B}o} \left[\int F(u) G_1(u) \mathrm{d}u \right] \frac{\bar{H}(\tau)}{\sqrt{\tau}} \exp\left\{ (\Gamma/\Gamma_F - 1) \frac{\tau}{\tau_D} \right\} J_0(k_C r) \ , \tag{C.52}$$

where

$$\bar{H}(\tau) = \sum_{n=-2}^{1} \hat{H}_{2n+1} \exp\left\{ i\Omega(n + 1/2)\tau \right\} \ , \tag{C.53}$$

and $G_1(u)$ is given by (C.33) with $\beta = 0$. The values of $\hat{H}_{2n+1}$ are obtained by solving the recurrence relation (C.35) with $\beta = 0$, $k = k_C$ and subject to the conditions $\hat{H}_n = \hat{H}^*_{-n}$, $\lim_{|n|\to\infty} |n\hat{H}_n| = 0$ and $|\hat{H}_1| = 1$. We illustrate the accuracy of the approximation (C.52) in Fig. 4-6, where it is compared to a full numerical simulation of the bath deformation. The full numerical solution was obtained by solving (C.27) for $k_n = n\delta k$ with $\delta k = 0.001$ and $1 \leq n \leq 2000$ and approximating $h(r,t) \approx \sum_{n=1}^{2000} H(k_n,\tau) J_0(k_n r) k_n \delta k$. We observe a good match between the full numerical solution and the approximation (C.52) for both viscosities.

Appendix D

Shearing in the Intervening Air Layer

When the thickness of the air layer separating the drop and the bath decreases to a value much smaller than the drop radius, the infinite space assumption used to calculate the air drag acting on the drop breaks down and we describe this part of the droplet motion as **contact**. However, due to the air viscosity resisting the drainage of the intervening air layer, the two liquid-gas surfaces never join. The film drainage problem is an interesting one and has been studied, among others, by Hartland [60, 61, 64, 62, 63, 66, 65], Jones & Wilson [68], or more recently by Gopinath & Koch [53]. The scenario most accesible to theoretical analysis is the limit $We \ll 1$, i.e. slowly approaching or settling drops, when the pressure distribution in the drop over the contact area can be assumed constant. Even then the intervening layer thickness, as a function of the distance from the axis of symmetry, is given by a complicated system of differential equations and has to be solved numerically; in the case of $We \sim O(1)$ any fast numerical solution for the air layer profile is unlikely to exist. At the same time, knowledge of the profile is crucial to calculating the drag on the drop as the tangential stress in the air layer is inversely proportional to its thickness. In general, the intervening air layer thickness is almost constant over the "contact area", being thickest in the center and then slowly thinning with increasing radial distance from the axis of symmetry. At the edge of the contact area the air layer thickness sharply decreases to its minimal value before rapidly increasing outside of the contact area [68].

We shall use the simplest possible model of the air layer, in order to obtain an order of magnitude value for the total drag on the sphere. We will assume constant thickness over the entire contact area and use no-slip boundary condition on each

surface. Moreover, we assume that the horizontal drop speed is small enough that the distortion of the drop and bath can be assumed radially symmetric at the leading order and that the vertical speed of impact is small enough that the contact area can be assumed horizontal. While the first assumption is generally satisfied for walking drops, the second is violated when $We \gtrsim 1$, as is the case for $f \leq 60$ Hz and $\Omega \approx 1$. The significant distortion of the bath then results in a more efficient transfer of the momentum from the drop to the bath and thus a higher total drag.

Let us assume that the drop is separated from the bath by a thin air layer of constant thickness s over a circular contact area with radius L. When the drop is moving vertically, the situation is radially symmetric. Morever, assuming $s \ll L$, the lubrication approximation results in the air pressure being independent of the vertical position inside the gap to leading order, and the air velocity being horizontal. On the other hand, if the drop was moving horizontally with speed V, no-slip boundary conditions for the air velocity in the gap, with $u(\boldsymbol{x}) = 0$ at the lower boundary and $u(\boldsymbol{x}) = V\hat{\boldsymbol{e}}_x$ at the upper boundary, would result in the air speed increasing linearly in the vertical direction from 0 to V. Then the total tangential drag force on the drop would be simply

$$F_D = \int \mu_a \frac{V}{s} \mathrm{d}S = \pi L^2 \mu_A \frac{V}{s} \quad , \tag{D.1}$$

where μ_a is the viscosity of air. Since during the impact of a walking drop the drop velocity is nearly vertical, we will assume that its small horizontal component V has a negligible impact on the intervening layer drainage and thus the thickness s can be calculated by assuming purely vertical drop motion. Once we obtain the thickness s we calculate the drag F_D from (D.1).

Therefore we now consider a vertical drop impact, use cylindrical coordinate system such that the bath surface is at $z = 0$, while the lower drop boundary is at $z = s(t)$ for $0 \leq r \leq L(t)$. From the radial symmetry of the situation and the lubrication approximation, the air velocity inside the gap is purely radial: $\boldsymbol{u}(\boldsymbol{x}) = u_r(r, z)\boldsymbol{e}_r$. Neglecting any circulation in either of the liquids, we impose no-slip boundary conditions $u_r(r, 0) = 0$, $u_r(r, s(t)) = 0$. Neglecting the air inertia, we have

$$-\frac{\partial p}{\partial r} + \mu_a \frac{\partial^2 u_r}{\partial z^2} = 0 \quad . \tag{D.2}$$

Solving (D.2) subject to the boundary conditions given above yields

$$u_r(r, t) = \frac{1}{2\mu_a} \frac{\partial p(r, t)}{\partial r} z(z - s(t)) \quad . \tag{D.3}$$

Conservation of mass requires

$$2\pi r \int_0^s u_r(z)\mathrm{d}z = \int_0^r 2\pi r' \frac{\partial s}{\partial t}\mathrm{d}r' \quad . \tag{D.4}$$

Substituting for $u_r(z)$ from (D.3) we obtain

$$\frac{\partial p(r,t)}{\partial r} = 6\mu_a r \frac{\dot{s}}{s^3} \tag{D.5}$$

Solving (D.5) subject to the normalizing condition $p(L,t) = 0$ we obtain

$$p(r,t) = 3\mu_a \frac{\dot{s}}{s^3}\left(r^2 - L^2\right) \tag{D.6}$$

The total normal reaction force on the drop is then obtained by integrating (D.6) over the contact area. We obtain

$$F_R = -\frac{3}{2}\pi\mu_a L^4 \frac{\mathrm{d}s/\mathrm{d}t}{s^3} \quad . \tag{D.7}$$

A more detailed calculation, taking into account also the air flow just outside the contact area, would yield

$$F_R = -\frac{3}{2}\pi\mu_a L^4 \frac{\mathrm{d}s/\mathrm{d}t}{s^3}\left[1 + \frac{3\pi}{4}\epsilon + 3\epsilon^2 + \frac{3\pi}{4}\epsilon^3 + \epsilon^4\right] \quad \text{where } \epsilon = \sqrt{2R_0 s}/L \quad . \tag{D.8}$$

Once we determine the evolution of contact area size $L(t)$, we can then calculate $s(t)$ by solving (D.7) or (D.8) with appropriate initial conditions and using the reaction force $F_R(t)$ obtained from our model of vertical dynamics. There are two ways in which one get eliminate $L(t)$ from the differential equations above:

(A) We can use the low We approximation to the contact area, assuming that the pressure inside the drop is roughly $2\sigma/R_0$ (capillary pressure), while the pressure in the bath just below the contact area is roughly zero (discounting atmospheric pressure contribution from both terms), so the pressure inside the intervening air layer will be roughly σ/R_0. Then the reaction force can be obtained by integrating this pressure over the contact area:

$$F_R = \pi L^2 \sigma/R_0 \quad , \tag{D.9}$$

from which we can deduce L once F_R is known. We will further approximate the equation (D.8) to

$$F_R = -\frac{3}{2}\pi\mu_a L^4 \frac{\mathrm{d}s/\mathrm{d}t}{s^3}\left[1 + \frac{4R_0^2 s^2}{L^4}\right] \quad , \tag{D.10}$$

which is a good approximation to (D.8) both in the limit $\epsilon \ll 1$ and $\epsilon \gg 1$, where $\epsilon = \sqrt{2R_0 s}/L$. Substituting for L from (D.9) into (D.10) and reverting to our dimensionless coordinates, we obtain

$$\frac{\mathrm{d}S/\mathrm{d}\tau}{S^3} = -\frac{2F}{\mathbb{O}h_a\left(4F^2+9S^2\right)} \quad , \tag{D.11}$$

where $S = s/R_0$ is the dimensionless air layer thickness, $\mathbb{O}h_a = \mu_a/\left(\rho\sigma R_0\right)^{1/2}$ the air Ohnesorge number and $F(\tau) = Z_{\tau\tau}(\tau) + \mathbb{B}o^*(\tau)$ is the dimensionless reaction force acting on the drop. The dimensionless form of (D.1) then reads, after substituting for L from (D.9):

$$\bar{F}_D = \frac{\mathbb{O}h_a F X_\tau}{S} \quad . \tag{D.12}$$

(B) A cruder approximation, leading to somewhat simpler model, is given by assuming L constant in (D.7). We integrate (D.7) assuming the beginning of impact at $t = 0$ and $s(0) = \infty$, giving

$$-\frac{1}{2s^2(t)} = -\frac{2}{3\pi\mu_a L^4}\int_0^t F_R(t')\mathrm{d}t' \quad . \tag{D.13}$$

Substituting for $1/s(t)$ from (D.13) into (D.1), we obtain

$$F_D = \left(\frac{4}{3}\pi\mu_a\right)^{1/2}\left[\int_0^t F_R(t')\mathrm{d}t'\right]^{1/2} V \quad , \tag{D.14}$$

which in the dimensionless form reads

$$\bar{F}_D = -\mathbb{O}h_a^{1/2}\left[\int_0^\tau F(\tau')\mathrm{d}\tau'\right]^{1/2} X_\tau \quad . \tag{D.15}$$

Assuming a sinusoidal dependence of F on time $F(\tau) = F_{max}\sin\left(\pi\tau/\tau_C\right)$, where τ_C is the contact time, we have $\int_0^\tau F(\tau')\mathrm{d}\tau' = F_{max}\frac{\tau_C}{\pi}\left(1-\cos\frac{\pi\tau}{\tau_C}\right) = F_{max}\frac{2\tau_C}{\pi}\sin^2\frac{\pi\tau}{2\tau_C}$. Therefore the total loss of horizontal momentum (assuming it is small relative to the total horizontal momentum, so that X_τ stays roughly the same during contact) is $\int_0^{\tau_C}\bar{F}_D(\tau')\mathrm{d}\tau' = \left[\frac{2}{\pi}F_{max}\tau_C\mathbb{O}h_a\right]^{1/2}X_\tau\int_0^{\tau_C}\sin\frac{\pi\tau^0}{2\tau_C}\mathrm{d}\tau'$. When the droplet is bouncing with the Faraday period, we must have $\int_0^{\tau_C}F(\tau')\mathrm{d}\tau' = \mathbb{B}o\tau_F = \mathbb{B}o\frac{4\pi}{\Omega}$, from which we get $\frac{2}{\pi}\tau_C F_{max} = \mathbb{B}o\frac{4\pi}{\Omega}$. Thus

$$\int_0^{\tau_C}\bar{F}_D(\tau')\mathrm{d}\tau' = \frac{2}{\pi}\left[\frac{4\pi\mathbb{O}h_a\mathbb{B}o}{\Omega}\right]^{1/2}\tau_C X_\tau = \left[\frac{2\mu_a g}{\sigma f}\right]^{1/2}\frac{2}{\pi}\tau_C X_\tau \quad . \tag{D.16}$$

Therefore, under this approximation, the loss of horizontal momentum grows linearly with the contact time and we can therefore achieve the same effect by having a dimensionless force $\bar{F}_D = \left[\frac{2\mu_a g}{\sigma f}\right]^{1/2} \frac{2}{\pi} X_\tau$ act on the drop whenever it is in contact with the bath.

Appendix E

Walker Motion along a Line in a Central Force: the 1-dimensional Simple Harmonic Oscillator

E.1 Background

We here consider the motion of a walker along a line in a linear central force, which provides the simplest way to confine the drop's motion. We proceed by simplifying the trajectory equation (4.25), in order to describe motion in 1 dimension, and investigate the regime diagram of the drop's motion in the high memory limit. We observe several types of qualitatively different behaviour depending on the two remaining free parameters. The most prevalent of these is the *ground state*, where the drop executes a periodic motion with amplitude equal to a quarter of the Faraday wavelength, and the *unbounded solution*, where despite the action of the central force the drop's position diverges to infinity with increasing time. In between these two extreme dynamical limits, the drop movement is typically chaotic, with occasional windows of periodicity. We investigate the dependence of the distribution function on the system parameters. Surprisingly, the average kinetic energy of the drop is independent of the central force strength and is found to be exactly equal to its free space value. We examine analytically the threshold above which the unbounded solutions exist, showing that it too is independent of the strength of the central force. Finally, we discuss the variety of new questions that this introductory examination has posed and outline the directions of future research in this area.

E.2 Equations of Motion and Walking Threshold

Consider a walker constrained to move along a line in the presence of a central force of the form $\boldsymbol{F}(\boldsymbol{x}) = -k\boldsymbol{x}$. The trajectory equation (4.25) is readily generalizable to this case:

$$m\ddot{\boldsymbol{x}} + \bar{D}\dot{\boldsymbol{x}} + k\boldsymbol{x} = -mg\nabla\bar{h}(\boldsymbol{x}, t) \quad , \tag{E.1}$$

where m is the mass of the drop, $\bar{D}$ the effective drag on the drop, g the gravitational acceleration and $\bar{h}$ is the effective height of the surface waves created by all the previous drop impacts:

$$\bar{h}(\boldsymbol{x}, t) = A\sum_{i=0}^{n-1} \frac{e^{(i-n)/\mathcal{M}e}}{n-i} J_0\left(k_F|\boldsymbol{x}(t) - \boldsymbol{x}_i|\right) \quad . \tag{E.2}$$

Here, as before, $J_0(x)$ is the Bessel function of the first kind and zero order. We now consider a similar scenario in 1-dimensional space, where the standing wave created by the drop impact has the spatial form of a sinusoid rather than a Bessel function. For the sake of simplicity, we approximate the temporal damping of the waves as being purely exponential. Then the equations (E.1-E.2) take the form

$$\begin{aligned} m\ddot{x} + \bar{D}\dot{x} + kx &= -mgA\frac{\mathrm{d}}{\mathrm{d}x}\sum_{i=0}^{n-1} e^{(i-n)/\mathcal{M}e}\cos\left[k_F(x(t) - x_i)\right] \\ &\approx \frac{mgAk_F}{T_F}\int_0^t e^{(s-t)/\mathcal{M}e}\sin\left[k_F(x(t) - x(s))\right]\mathrm{d}s \ . \end{aligned} \tag{E.3}$$

Here, as before, the memory parameter $\mathcal{M}e$, as defined in (4.23), denotes the number of previous drop impacts that significantly contribute to the total wavefield. Now by rescaling x and t such that $x = x'/k_F$, $t = mt'/\bar{D}$, $k' = km/\bar{D}^2$, $A' = Agk_F^2m^3/\bar{D}^3T_F$ and then dropping the primes, we can transform (E.3) into the form

$$\ddot{x} + \dot{x} + kx = A\int_0^t e^{(s-t)/\mathcal{M}e}\sin\left(x(t) - x(s)\right)\mathrm{d}s \quad . \tag{E.4}$$

By splitting $\sin\left(x(t) - x(s)\right) = \sin x(t)\cos x(s) - \sin x(s)\cos x(t)$, and writing

$$I_1(t) := \int_0^t e^{(s-t)/\mathcal{M}e}\cos x(s)\mathrm{d}s \tag{E.5a}$$

$$I_2(t) := \int_0^t e^{(s-t)/\mathcal{M}e}\sin x(s)\mathrm{d}s \ , \tag{E.5b}$$

we arrive at the equivalent description of the motion in terms of a system of ODEs:

$$\ddot{x} + \dot{x} + kx = A\left[I_1 \sin x - I_2 \cos x\right] \tag{E.6a}$$

$$\dot{I}_1 = -\tfrac{1}{\mathcal{M}e} I_1 + \cos x \tag{E.6b}$$

$$\dot{I}_2 = -\tfrac{1}{\mathcal{M}e} I_2 + \sin x \tag{E.6c}$$

There are thus 3 parameters we can vary, the memory $\mathcal{M}e$, force strength k and wave amplitude A. We will be particularly interested in the limit of $\mathcal{M}e \to \infty$.

The principal advantage of writing the trajectory equation (E.4) as the system (E.6) is that instead of needing to know the entire history of the drop position $x(t)$ in order to calculate the integral on the right-hand side of (E.4), we need only keep track of four variables $x, \dot{x}, I_1, I_2$. This provides an enormous computational benefit which will enable us to track the drop motion over very long times. Unfortunately, this way of rewriting the trajectory equation is unique to one dimension, where any linear combination of monochromatic waves can be rewritten as a combination of a sine and a cosine.

E.2.1 Walking Threshold

We proceed by deriving the minimum memory necessary for walking to occur, which we denote $\mathcal{M}e^W = \mathcal{M}e^W(A,k)$.

Negligible central force. In the limit $k \to 0$, we get a motion in free space. Besides the usual stationary solution $x(t) = x_0$, there exists a steady walking solution $x(t) = x_0 + v_W t$ for $\mathcal{M}_e > \mathcal{M}_e^W$. Substituting for $x(t)$ into (E.4), we obtain $v_W = A\int_0^\infty e^{-s/\mathcal{M}e} \sin(v_W s)\, ds = A\frac{\mathcal{M}_e^2 v_W}{1+\mathcal{M}e^2 v_W^2}$ from which

$$v_W = \left[A - \mathcal{M}e^{-2}\right]^{1/2} \qquad \mathcal{M}e^W = A^{-1/2} \tag{E.7}$$

General central force. Now we assume that $k > 0$ and that we are just above the walking threshold. Assuming the motion to be sinusoidal with an infinitesimal amplitude, we write $x(t) = \delta e^{i\omega t}$ with $\delta \ll 1$ and substitute into (E.4) to obtain, after neglecting terms of higher order in δ:

$$k - \omega^2 + i\omega = A\mathcal{M}e\frac{\omega^2\mathcal{M}e^2 + i\omega\mathcal{M}e}{1+\omega^2\mathcal{M}e} \quad . \tag{E.8}$$

Comparing the imaginary parts of (E.8) we obtain $1 + \omega^2 \mathcal{M}e^2 = A\mathcal{M}e^2$, or equivalently $\mathcal{M}e = (A - \omega^2)^{-1/2}$. Substituting this result into the real part of (E.8) gives $k - \omega^2 = \omega^2 (A - \omega^2)^{-1/2}$ which can be written as

$$p(\omega^2) := \omega^4 + (\omega^2 - A)(\omega^2 - k)^2 = 0 \tag{E.9}$$

The cubic $p(z)$ can be shown to have a single real root for $A, k > 0$, and since $p(0) = -Ak^2 < 0$ while $p(A) = A^2 > 0$ and $p(k) = k^2 > 0$, the root must lie between 0 and $\min\{k, A\}$. It is straightforward to show that $\mathcal{M}e^W \approx A^{-1/2}$ when $k \ll A$ and $\mathcal{M}e^W \sim k/A$ when $k \gg A$, as is shown in Fig. E-1.

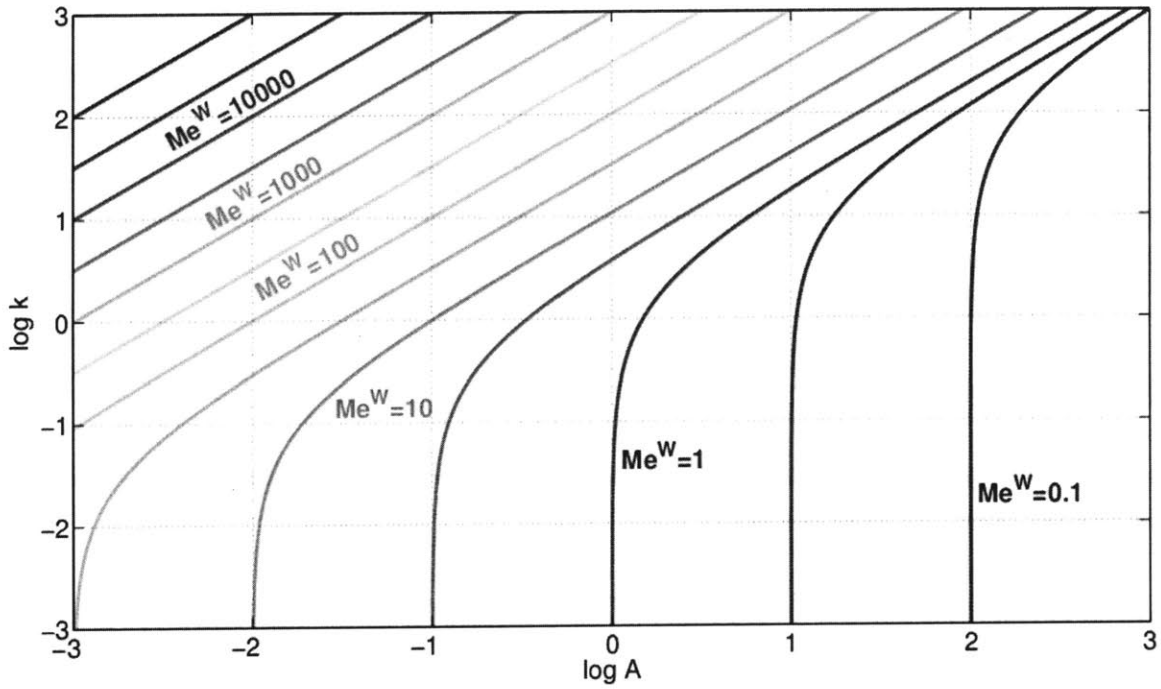

Figure E-1: The dependence of the threshold value of memory $\mathcal{M}e^W$ at which walking occurs, on the wave amplitude A and force strength k. The level sets of $\mathcal{M}e^W$ are plotted on a $\log A - \log k$ plane.

From now on we shall consider only $\mathcal{M}e \gg \mathcal{M}e^W$.

E.3 Regime Diagram of the Walking Motion

We solved the system (E.6) numerically spanning the entirety of the region $10^{-3} \leq A \leq 10^3$, $10^{-3} \leq k \leq 10^2$, for $\mathcal{M}e = 10^9$. Depending on the required level of accuracy, we used either a second-order implicit method with time step $\Delta t = 0.005$ or a third-order implicit method with $\Delta t = 10^{-4}$. The probability distribution function of

$x(t)$ and $\dot{x}(t)$ was recorded by storing the values of x and $\dot{x}$ at each timestep, which also allowed for subsequent evaluation of the average potential and kinetic energy. The length of time over which the system was recorded was varied depending on the rate of convergence of the probability density function, varying between $5 \cdot 10^5$ and $30 \cdot 10^5$. The initial conditions were kept the same throughout, specifically, $x(0) = I_1(0) = I_2(0) = 0$ and $\dot{x}(0) = 0.01$, corresponding to a small initial disturbance at time $t = 0$.

In Fig. E-2 we show the various types of motion observed. We summarize our results in a regime diagram (Fig. E-3). When $A < 0.04$ or $k \gg A$ (see Fig. E-2ab), the drop is strongly confined by the central force and its position switches periodically between $+\pi/2$ and $-\pi/2$. The switching occurs over a short period of time relative to the period of the motion, which can be shown analytically to be approximately $4k/A$ when $k \gg A$. We call this motion the *ground state*, since it corresponds to the lowest possible drop potential energy, the zero solution being unstable in the high memory limit. When $k \sim A$ (see Fig. E-2eh), the drop is still strongly bound by the central force, but its motion is no longer periodic: small variations arise in the position at which the drop seems to settle (for $A \lesssim 1$), or around which it oscillates (for $A \gtrsim 1$) before switching to the opposite side of the origin. We call these kinds of motion the *chaotic ground state*. As the force strength k is reduced further below the value of A, the motion becomes increasingly chaotic, its amplitude increases and we characterize it as fully chaotic.

Note that although the transition from chaotic ground state to chaotic motion is often discrete, it can also happen gradually. For the purposes of quantitative determination of the threshold in the regime diagram, we use the following criterion: We calculate the ratio β between the fourth moment and the square of the second moment of the drop's position:

$$\beta = \frac{M_4}{(M_2)^2} \text{ where } M_n = \lim_{T\to\infty} \int_0^T |x(t)|^n dt \tag{E.10}$$

The value of β approaches one when the amplitude $|x(t)|$ is strongly confined to a single value, $\beta = 1.8$ when the position is uniformly distributed over an interval symmetric around the origin, and finally $\beta = 3$ when the position distribution is gaussian. Therefore, for the ground state we have $\beta \approx 1$ while for chaotic motion $\beta \approx 3$; we shall set the threshold between the chaotic ground state and fully chaotic motion at $\beta = 1.8$, i.e. the value for a uniform probability density of $x(t)$.

In Fig. E-2cdf we show the various instances of fully chaotic motion. The motion is

composed of a fast oscillation, with period on the order of $A^{-1/2}$, around a mean that slowly and chaotically varies in time. Generally speaking, the amplitude of the motion is larger for smaller k and larger A, but the relationship is in not straightforward. While the probability distribution function is typically symmetric around the origin in the chaotic regime, when the parameter k is sufficiently small this no longer holds and we observe motions which lie on one side of the origin only, as is shown in Fig. E-12. The boundary of the region where these non-axisymmetric solutions may arise is outlined in the regime diagram (E-2), but further investigation is needed as the initial conditions presumably play a significant role in the establishment of this kind of motion.

Finally, when A is larger than some critical value A_C, the drop's position can destabilize into a motion that diverges to infinity for large times (see Fig. E-5). In this type of motion, the two timescales of the drop's motion are clearly visible, with a fast oscillation superposed on a slower monotonic mean motion. This motion, which we call the *unbounded solution* will be the subject of the next section, where we deduce that the critical value A_C is equal to 86.641 independently of k. Note that this statement is not in contradiction with the earlier statements of the existence of the ground state - both solutions are possible when $k \gg A > A_C$, depending on the initial conditions. For A below but relatively near A_C, the motion is marked by rapid oscillations around a slowly increasing mean, followed by a rapid return to the origin, as is shown in Fig. E-2g and Fig. E-6. The maximum amplitude of the motion gets progressively larger as one approaches A_C from below, as documented in Table E.1.

E.4 Energetics

The total energy of the walking drop can be defined as

$$\mathcal{E}_{TOT} := \frac{1}{2}\dot{x}^2 + \frac{1}{2}kx^2 + h(x) \quad \text{where}$$
$$h(x,t) = A\int_{-\infty}^{t} e^{(s-t)/Me}\cos\left(x(t)-x(s)\right)\mathrm{d}s = A\left(I_1\cos x + I_2\sin x\right)\ . \qquad \text{(E.11)}$$

The three components of the total energy are, in turn, the kinetic energy $\frac{1}{2}\dot{x}^2$, the potential energy $\frac{1}{2}kx^2$, and the energy stored in the wavefield, given by its height $h(x)$ at the drop's location. We also define the mean kinetic and mean potential energy

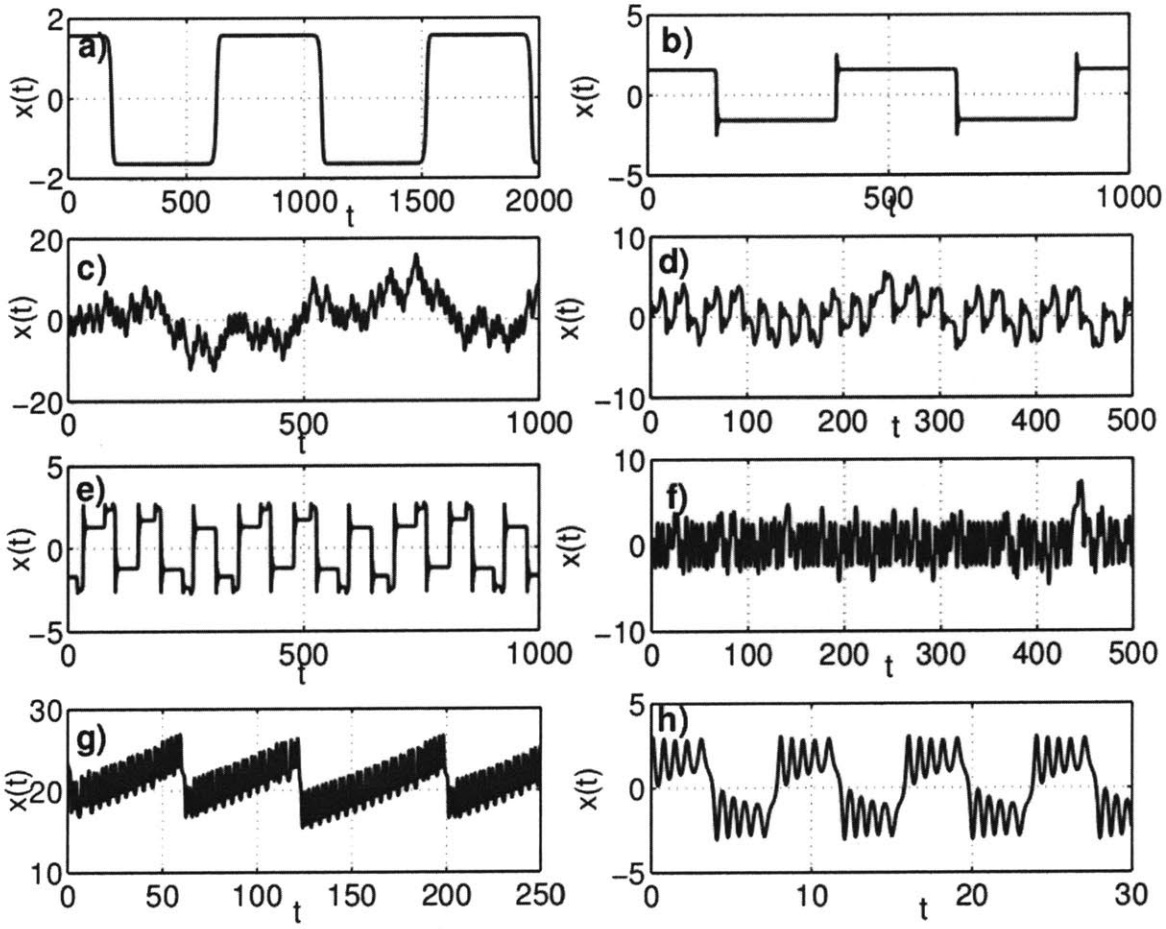

Figure E-2: The position $x(t)$ of the drop as a function of time for various combinations of the wave amplitude A and the central force strength k: **(a)** $A = 0.001$ and $k = 0.001$, **(b)** $A = 0.1$ and $k = 10$, **(c)** $A = 1$ and $k = 0.1$, **(d)** $A = 1$ and $k = 1$, **(e)** $A = 1$ and $k = 10$, **(f)** $A = 5$ and $k = 2$, **(g)** $A = 20$ and $k = 0.05$, **(h)** $A = 50$ and $k = 50$.

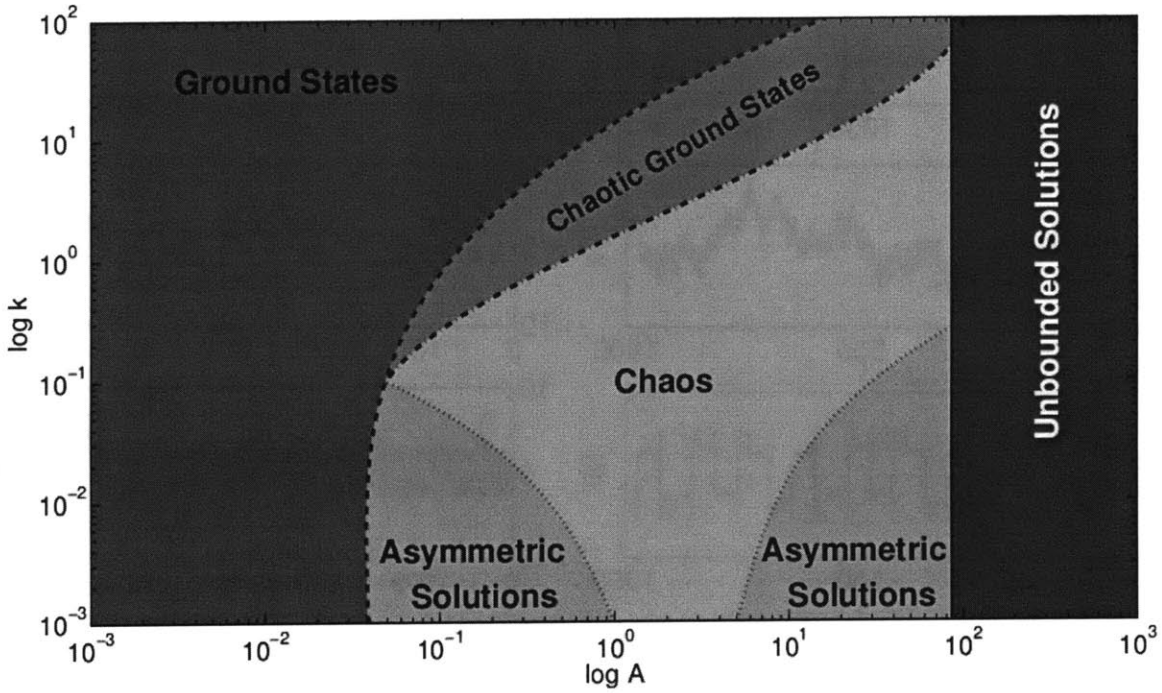

Figure E-3: The regime diagram deduced from solution of the system (E.6), describing the behaviour of a drop walking in 1 dimension subject to central force, for $\mathcal{M}e = 10^9$. Four different dynamical states are observed according to the value of the wave amplitude A (horizontal axis) and central force strength k (vertical axis): a ground state ($A < 0.03$ or $k > A$), a chaotic ground state ($k \sim A$), chaotic motion $k < A$ and unbounded solutions $A > A_C \approx 86.6$. The regions where an asymmetric probability density was observed (for small k) are also indicated.

by taking a long-term average:

$$\mathcal{K}.\mathcal{E}_{.avg} = \tfrac{1}{2}\left\langle \dot{x}^2 \right\rangle := \lim_{T\to\infty} \int_0^T \tfrac{1}{2}\dot{x}^2(t)\mathrm{d}t \quad , \quad \mathcal{P}.\mathcal{E}_{.avg} = \tfrac{1}{2}k\left\langle x^2 \right\rangle := \lim_{T\to\infty} \int_0^T \tfrac{1}{2}kx^2(t)\mathrm{d}t \ . \tag{E.12}$$

Despite the different kinds of behaviour observed, one statistical feature of the system shows remarkable regularity: In the limit of $\mathcal{M}e \to \infty$, the mean kinetic energy is equal to $A/2$, i.e. its value for rectilinear walking without any central force, or it is equal to 0 (for the unbounded solution or for the unstable zero solution $x(t) = 0$). This can be shown by differentiating (E.11) with respect to time:

$$\begin{aligned} \frac{\mathrm{d}}{\mathrm{d}t}\mathcal{E}_{TOT} &= \dot{x}\ddot{x} + kx\dot{x} + A\dot{x}\left(-I_1 \sin x + I_2 \cos x\right) + A\left(\dot{I}_1 \cos x + \dot{I}_2 \sin x\right) = \\ &= \dot{x}\left[\ddot{x} + kx + A\left(I_2 \cos x - I_1 \sin x\right)\right] + A\left[1 - \tfrac{1}{\mathcal{M}e}\left(I_1 \cos x + I_2 \sin x\right)\right] = \\ &= A - \dot{x}^2 - \frac{h(x)}{\mathcal{M}e} \end{aligned} \tag{E.13}$$

Integrating (E.13) from 0 to T for large T, we find

$$\left\langle \dot{x}^2 \right\rangle = A - \frac{1}{\mathcal{M}e}\left\langle h(x) \right\rangle - \lim_{T\to\infty} \frac{\mathcal{E}_{TOT}(T) - \mathcal{E}_{TOT}(0)}{T} \ . \tag{E.14}$$

For the zero solution, we have $E_{TOT}(t) = E_{TOT}(0) = h(0) = A\mathcal{M}e$ so $\langle \dot{x}^2 \rangle = A - A = 0$, while for the unbounded solution $E_{TOT}(T) \sim kx^2(T)/2 = AT$ and so again $\langle \dot{x}^2 \rangle = A - A = 0$. For non-zero bounded solution we have $\langle h(x) \rangle = 0$ and E_{TOT} bounded, giving $\langle \dot{x}^2 \rangle = A$.

No such simple result could be found for the mean potential energy, where a set of discrete values was hoped to be observed. The potential energy is bound below by its value for the ground state, which is just $k(\pi/2)^2 \equiv \mathcal{P}.\mathcal{E}_{.0}$. Figure Fig. E-4a shows the dependence of $\mathcal{P}.\mathcal{E}./k$ on A and k, while Fig. E-4b shows the dependence of $\mathcal{P}.\mathcal{E}. - \mathcal{P}.\mathcal{E}_{.0}$; neither exhibits any obvious quantization.

E.5 Unbounded solution

Assume that $x(t)$ is composed of a slowly varying large component and a small correction, whose amplitude also varies slowly:

$$x(t) = X(\epsilon t) + Y(\epsilon t)y(t) + o(Y) \ , \qquad \text{with } X \gg 1 \text{ and } Y, \epsilon \ll 1 \ . \tag{E.15}$$

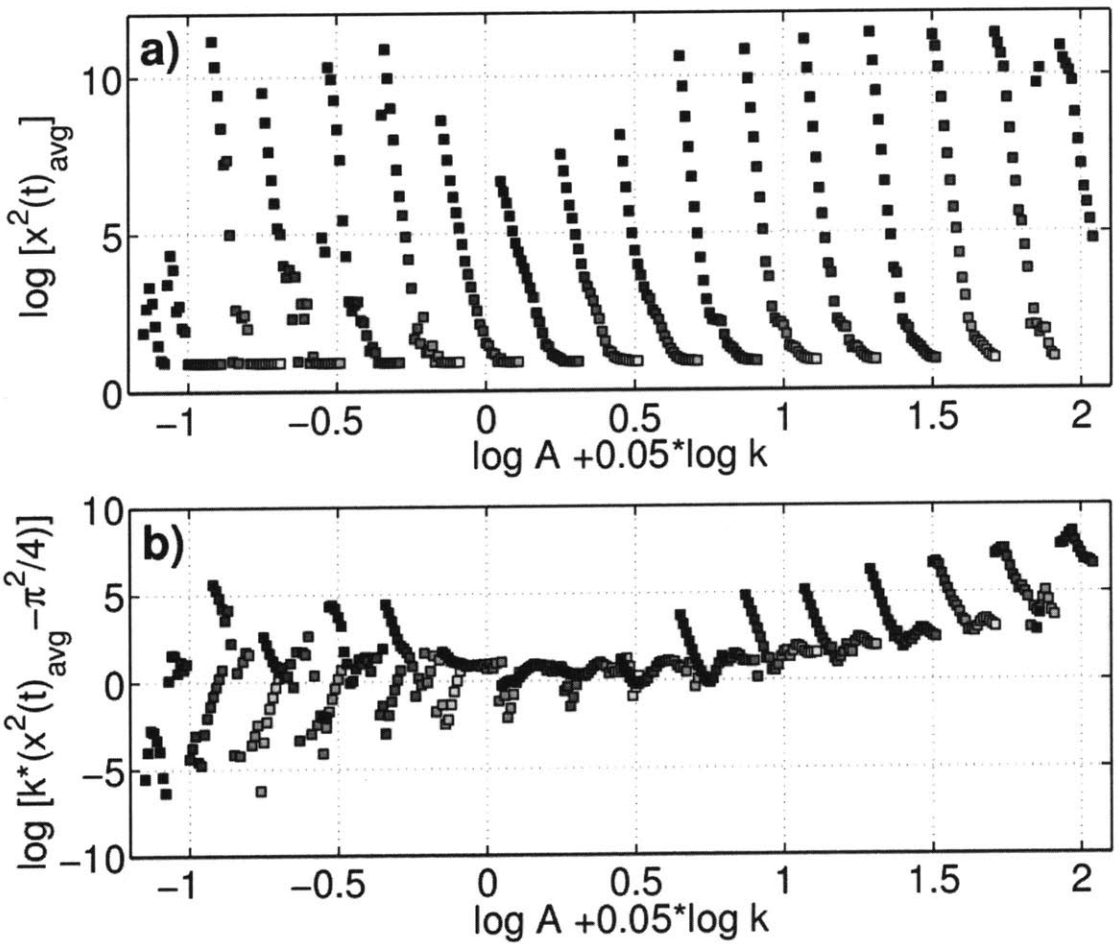

Figure E-4: The dependence of **(a)** $\langle x^2 \rangle$ and **(b)** $\mathcal{P}.\mathcal{E}. - \mathcal{P}.\mathcal{E}._0 = k \langle x^2 \rangle - k\pi^2/4$ on the parameters A and k. By using $\log A + 0.05 \log k$ for the horizontal scale, we obtain clusters of data points, each corresponding to a single value of A.

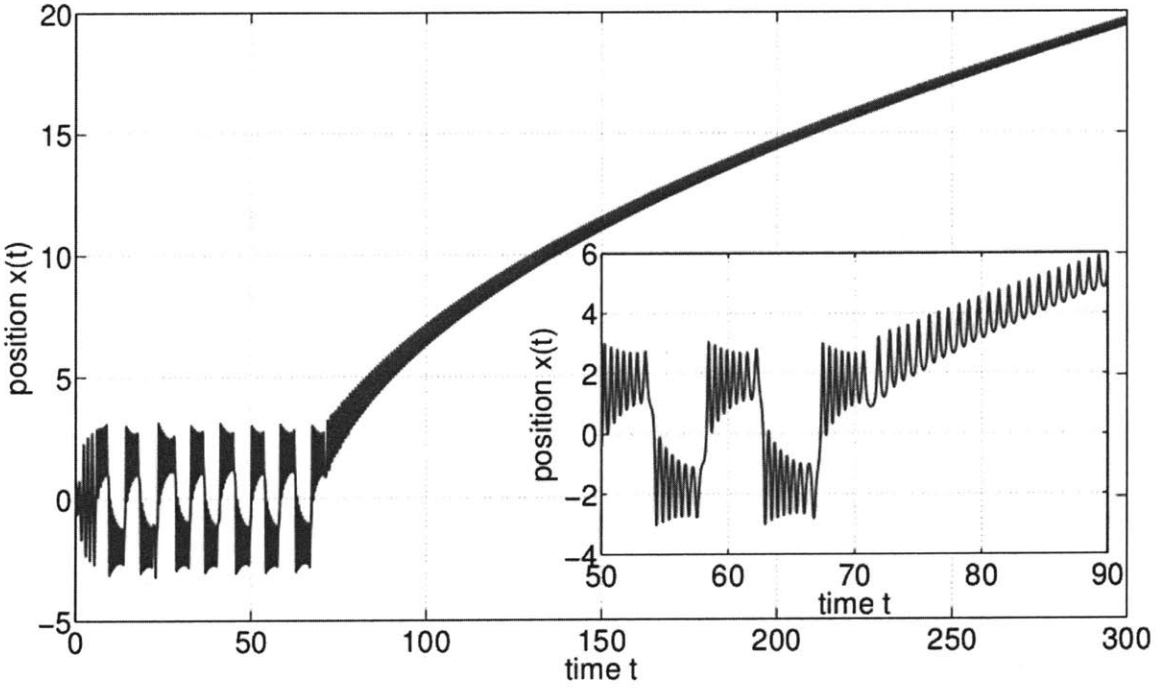

Figure E-5: The position $x(t)$ as a function of time for $A = 87$ and $k = 100$ for initial conditions $x(0) = I_1(0) = I_2(0) = 0$ and $\dot{x}(0) = 5$. The solution diverges from the origin starting from around $t \approx 60$, with the transition shown in more detail in the inset.

Moreover, we assume that $y(t)$ is periodic with period P. Then, without loss of generality, we can assume $\int_t^{t+P} y(s)\mathrm{d}s = 0$, since we can absorb the average value of $y(t)$ into the slowly varying part $X(\epsilon t)$. Now we substitute (E.15) into the governing system of equations (E.6) in the limit $\mathcal{M}e \to \infty$. Then (E.6bc) imply

$$\dot{I}_1 = \cos x = \cos X \left(1 - \tfrac{1}{2}Y^2y^2\right) - Yy \sin X + O\left(Y^3\right) \tag{E.16a}$$

$$\dot{I}_2 = \sin x = \sin X \left(1 - \tfrac{1}{2}Y^2y^2\right) + Yy \cos X + O\left(Y^3\right) \tag{E.16b}$$

Now, using repeated integration by parts, we have

$$\begin{aligned}\int \cos X(\epsilon s)\mathrm{d}s &= \int \frac{1}{\epsilon X'} \cos X(\epsilon s)\epsilon X'\mathrm{d}s = \frac{\sin X}{\epsilon X'} + \int \sin X \frac{X''}{X'^2}\mathrm{d}s = \\ &= \frac{\sin X}{\epsilon X'} - \cos X \frac{X''}{\epsilon X'^3} + \int \cos X \left(\frac{X'''}{X'^3} - \frac{3X''^2}{X'^4}\right)\mathrm{d}s = \\ &= \frac{\sin X}{\epsilon X'} - \cos X \frac{X''}{\epsilon X'^3} + \sin X \left(\frac{X'''}{\epsilon X'^4} - \frac{3X''^2}{\epsilon X'^5}\right) + O\left(\frac{1}{\epsilon X^4}\right)\end{aligned} \tag{E.17}$$

By the same method, we derive

$$\int \sin X(\epsilon s)\mathrm{d}s = -\frac{\cos X}{\epsilon X'} - \sin X \frac{X''}{\epsilon X'^3} - \cos X \left(\frac{X'''}{\epsilon X'^4} - \frac{3X''^2}{\epsilon X'^5}\right) + O\left(\frac{1}{\epsilon X^4}\right) \tag{E.18}$$

Using the fact that $\int_t^{t+P} y(s)\mathrm{d}s = 0$, single integration by parts gives

$$\int Y(\epsilon s)y(s) \sin X(\epsilon s)\mathrm{d}s = Y \sin X \int y(s)\mathrm{d}s + O\left(\epsilon Y\right) , \tag{E.19a}$$

$$\int Y^2(\epsilon s)y^2(s) \sin X(\epsilon s)\mathrm{d}s = Y^2 \sin X \int y^2(s)\mathrm{d}s + O\left(\epsilon t Y^2\right) . \tag{E.19b}$$

Analogous results hold if one replaces $\sin X$ in (E.19) by $\cos X$. Combining (E.17)-(E.19) and substitution of (E.15) into (E.6) yields

$$\begin{aligned}&kX + \epsilon X' + Y\left(\ddot{y} + \dot{y} + ky\right) + O\left(\epsilon^2 X, \epsilon Y\right) = \\ &= A\left[\frac{1}{\epsilon X'} + \left(\frac{X'''}{\epsilon X'^4} - \frac{3X''^2}{\epsilon X'^5}\right) - Y\int y(s)\mathrm{d}s - \frac{X''Yy}{\epsilon X'^3} - \tfrac{1}{2}\frac{Y^2y^2}{\epsilon X'} + O\left(\frac{1}{\epsilon X^4}, \frac{Y}{\epsilon X^3}, \frac{Y^2}{\epsilon X^2}\right)\right] .\end{aligned} \tag{E.20}$$

Provided that $\epsilon X' \cdot Y \ll 1$, the leading order terms in (E.20) give $kX = A/\epsilon X'$, or, equivalently, $\epsilon X X' = A/k$, which can be integrated to yield

$$X(\epsilon t) = \pm \left[\frac{2A(t-t_0)}{k}\right]^{1/2} \quad . \tag{E.21}$$

The condition of slow time dependence of X requires $(t - t_0) \sim \epsilon^{-1}$, which implies $X \sim \epsilon^{-1/2}$, consistent with our assumption that $X \gg 1$. Now for X given by (E.21), the expression $(X'''/\epsilon X'^4 - 3X''^2/\epsilon X'^5)$ on the right-hand side of (E.20) vanishes, and $AX''/\epsilon X'^3 = -k$, which enables us to simplify (E.20), after multiplying through $\epsilon X'$, to

$$(\epsilon X')^2 + (\epsilon X')\, Y \left(\dddot{y} + \ddot{y} + A \int y(s)\mathrm{d}s\right) + Y^2 \tfrac{1}{2} A y^2 = O\left(\epsilon^{3/2}, \epsilon Y, \epsilon^{1/2} Y^2\right) \quad . \tag{E.22}$$

It can now be seen from (E.22) that the natural choice of Y, and indeed the only choice consistent with our assumptions, is $Y = \epsilon X'$, which sets all the terms on the left-hand side of (E.22) at the same order. We thus arrive at

$$1 + \dddot{y} + \ddot{y} + A \int y(s)\mathrm{d}s + \frac{1}{2} A y^2 = O(\epsilon^{1/2}) \ , \text{ and } \ Y = \epsilon X' = \left[\frac{A}{2k(t-t_0)}\right]^{1/2} \quad . \tag{E.23}$$

Differentiating (E.23) with respect to time and neglecting higher order terms, we obtain

$$\ddddot{y} + \dddot{y} + Ay + Ay\ddot{y} = 0 \quad . \tag{E.24}$$

Note that if a solution to (E.24) is periodic with period P, it necessarily satisfies $\int_t^{t+P} y(s)\mathrm{d}s = 0$, as can be immediately obtained by subtracting (E.23) evaluated at $t + P$ and t.

It is the existence and stability of a periodic solution to (E.24) that determines whether an unbounded solution exists for a given A and k: provided such periodic solution exists and is stable, there are initial conditions on $x, \dot{x}, I_1, I_2$ that will ensure that $x(t)$ will have the asymptotic form given by (E.15). From (E.21), it then necessarily follows that $|x(t)| \to \infty$ as $t \to \infty$. Conversely, if the periodic solution to (E.24) is unstable, the unbounded solution will not be observed. Since (E.24) is independent of k, the existence and stability of the periodic solution depends only on A. It will be shown that for $A > A_C \approx 86.64$ stable periodic solution exists, while for $A < A_C$ it does not. As A approaches A_C from below, we see large deviations of x from 0, with $x(t)$ closely following the initial stages of the unbounded solution,

k \ A	10	20	30	40	50	60	70	80	83	85
0.001	589	1165	2869	5524	9252	14354	21146	30396	33668	36135
0.01	67.6	129	304	573	956	1480	2159	3114	3436	3727
0.1	19.5	31.1	44.7	72.7	109	165	232	333	369	404
1	12.0	11.4	15.6	21.3	25.9	30.8	38.6	47.6	52.7	57.9
10	5.46	6.14	6.86	7.60	7.73	11.3	12.9	14.2	16.4	16.7

Table E.1: Maximum value of $|x(t)|$ for selected values of k and A below the critical value A_C. A rapid increase of the foray distance is evident as $A \to A_C$ for all k.

presumably because the higher order terms in the expansion (E.15) have a stabilizing effect. Nevertheless, as $|x|$ increases the higher order terms become progressively less important until the inherent instability of $y(t)$ causes a rapid collapse towards the origin. The typical magnitude of these excursions in x is shown in Table E.1 for various values of A and k.

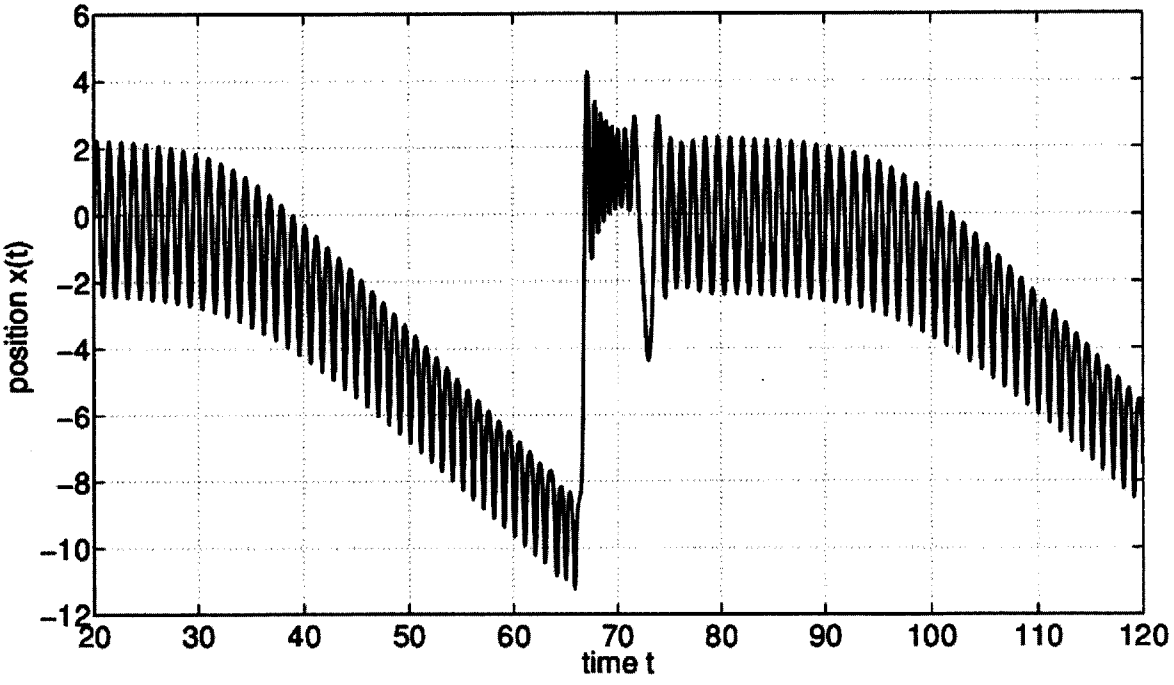

Figure E-6: The position $x(t)$ as a function of time for $A = 80$ and $k = 10$, for initial conditions $x(0) = I_1(0) = I_2(0) = 0$ and $\dot{x}(0) = 5$. The walker slowly drifts away from the origin while oscillating rapidly, before it snaps back to the vicinity of the origin and the process repeats.

We now focus on the case $A \gtrsim A_C$. Since $A_C \approx 86$, we will regard A as a large parameter. Rescaling time by writing $t = T\tau$, we have $T^{-3}y_{\tau\tau\tau} + T^{-2}y_{\tau\tau} + Ay + AT^{-1}yy_\tau = 0$. Considering the leading order balance, the only self-consistent choice

of T is $T = A^{-1/2}$, which gives

$$y_{\tau\tau\tau} + yy_\tau + A^{-1/2}\left(y_{\tau\tau} + y\right) = 0 \quad \text{where} \quad y(\tau) = y\left(tA^{1/2}\right) \tag{E.25}$$

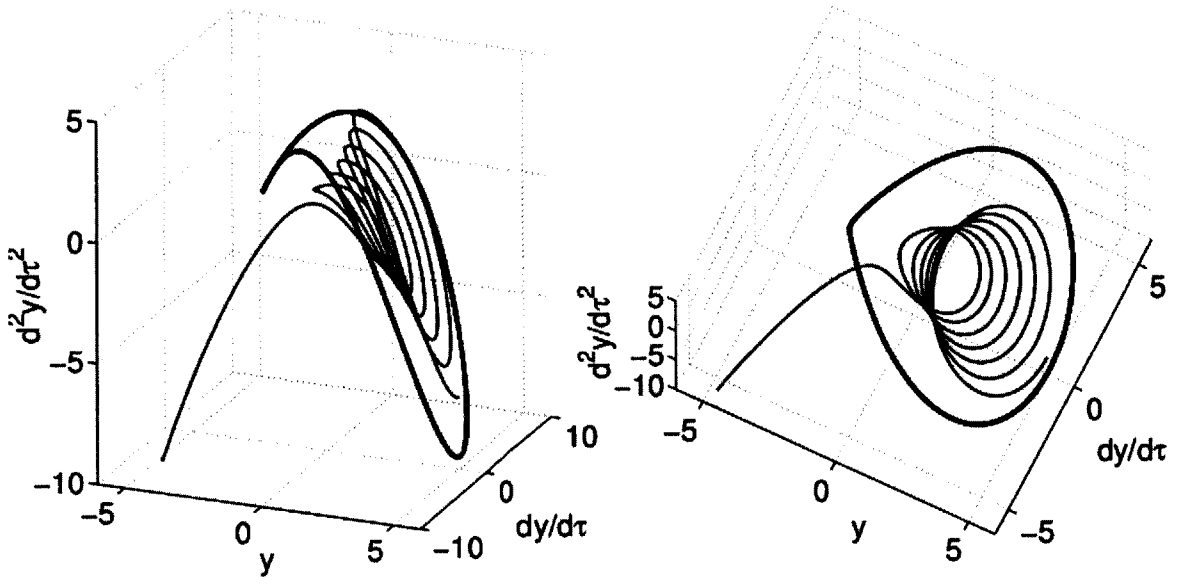

Figure E-7: The limit cycle for the system (E.25) together with a part of an unbounded trajectory starting at $(y, y_\tau, y_{\tau\tau}) = (5, 0, -7)$ in the $(y, y_\tau, y_{\tau\tau})$ space, shown from two different angles.

E.5.1 The large wave amplitude limit $A \to \infty$

For large A, the periodic solution of (E.25) will be close to the periodic solution of

$$y_{\tau\tau\tau} + yy_\tau = 0 \ , \tag{E.26}$$

for which the integral $\int y(s)\mathrm{d}s$ over one period vanishes. The period of $y(\tau)$ will be denoted by $p = PA^{1/2}$. Note that we now have to enforce this vanishing average condition, since by dropping the smaller two terms in going from (E.25) to (E.26), this condition is no longer automatically satisfied by every periodic solution. Equation (E.26) can be integrated once to give

$$y_{\tau\tau} + \tfrac{1}{2}y^2 = \tfrac{1}{2}\lambda \ . \tag{E.27}$$

The constant λ has to be non-negative for a periodic solution to exist, since $0 = \int y_{\tau\tau}(s)\mathrm{d}s = \frac{1}{2}\int \lambda - y^2(s)\mathrm{d}s \leq \frac{1}{2}\int \lambda \mathrm{d}s = \frac{1}{2}p\lambda$, where the integral is taken over one period of z. Therefore we can write $\lambda = F^2$:

$$y_{\tau\tau} + \tfrac{1}{2}\left(y^2 - F^2\right) = 0 \ . \tag{E.28}$$

For each choice of constant F, equation (E.28) describes a conservative system, as can be seen by multiplying (E.28) by $2y_\tau$ and integrating once more to give

$$y_\tau^2 + \tfrac{1}{3}y^3 - F^2 y = E \ . \tag{E.29}$$

Thus E is conserved in time and can be thought of as energy, and the level sets of E coincide with the trajectories of y in the $y - y_\tau$ phase plane. The system has two fixed points at $y = \pm F$, with $y = -F$ being a saddle point and $y = F$ being a center. Therefore $E = -\frac{2}{3}F^3$ corresponds to a constant solution, while $E = \frac{2}{3}F^3$ corresponds to a homoclinic orbit; periodic solutions thus occur for $-\frac{2}{3}F^3 < E < \frac{2}{3}F^3$. The requirement of a zero time average of y selects a single value of E for each F, since the time average is a monotonically decreasing function of E. This value was found numerically to be $E_0 = 0.66314F^3$. Since it is very close to the value corresponding to the homoclinic orbit, the two orbits lie very close to each other, as illustrated in Fig. E-8.

E.5.2 Finite wave amplitude A

The fact that the zero time-average trajectory lies close to the homoclinic orbit means that for $A \to \infty$ the intersection of the limit cycle in the $(y, y_\tau, y_{\tau\tau})$ space with the $y_\tau = 0$ plane (the Poincaré section) will lie close to the locus of the homoclinic intersections, which are given by $\left(2F, 0, -\frac{3}{2}F^2\right)$ according to (E.28). For a finite A, the image of the limit cycle in the Poincaré section $y_\tau = 0$ will thus lie close to the parabola $y_{\tau\tau} = -\frac{3}{8}y^2$. This property helps us to plot the Poincaré section of the stable manifold of the system with the $y_\tau = 0$ plane, as is done in Fig. E-9. Note that, had we plotted the section in normal $y - y_{\tau\tau}$ plane, the inherent thin profile of the manifold would hide any internal structure. Using instead $y_{\tau\tau} + \frac{3}{8}y^2$ for the vertical axis reveals the branching structure of the manifold for different values of A (Fig. E-9). We see that as A is decreased, the cross-sectional area of the manifold, together with the number of its branches, decreases until only two thin branches remain. When A is decreased below A_C the stable manifold disappears completely

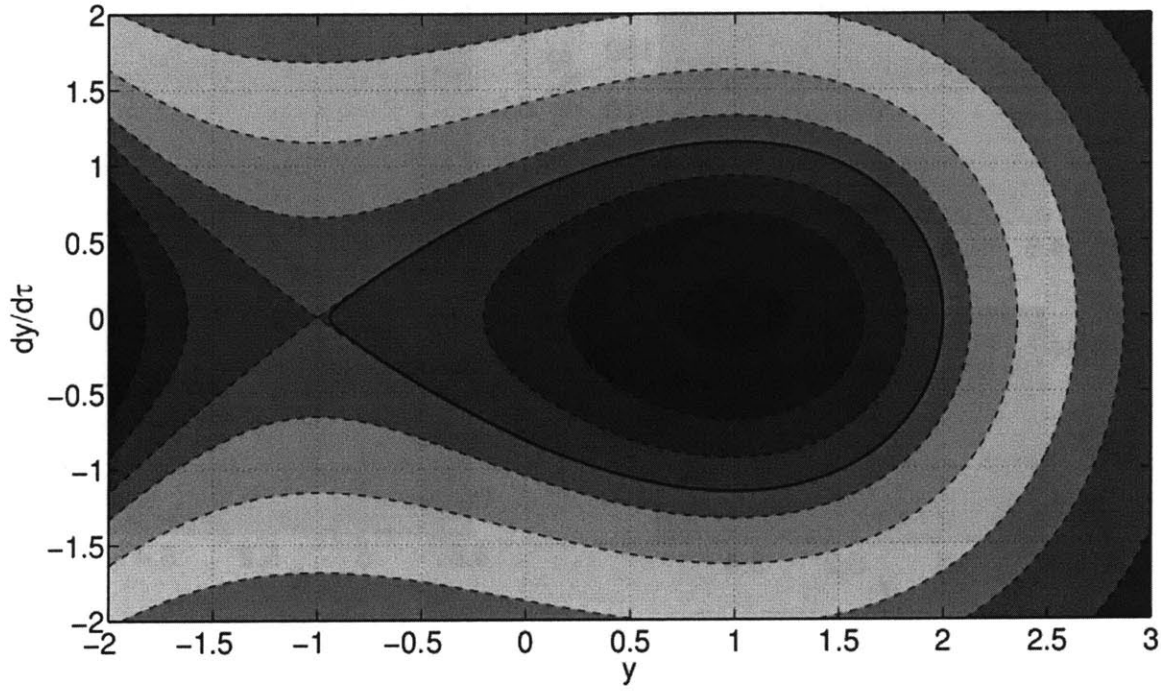

Figure E-8: The trajectories in the $y - y_\tau$ plane for the equation (E.28) with $F = 1$ are marked by dashed lines. The two critical points are a center at $(1, 0)$ and a saddle at $(-1, 0)$. The periodic solution with zero time average lies very close to the homoclinic trajectory, and is indicated by a solid line.

(Fig. E-9e). In order to determine the value of A_C with significant precision, we

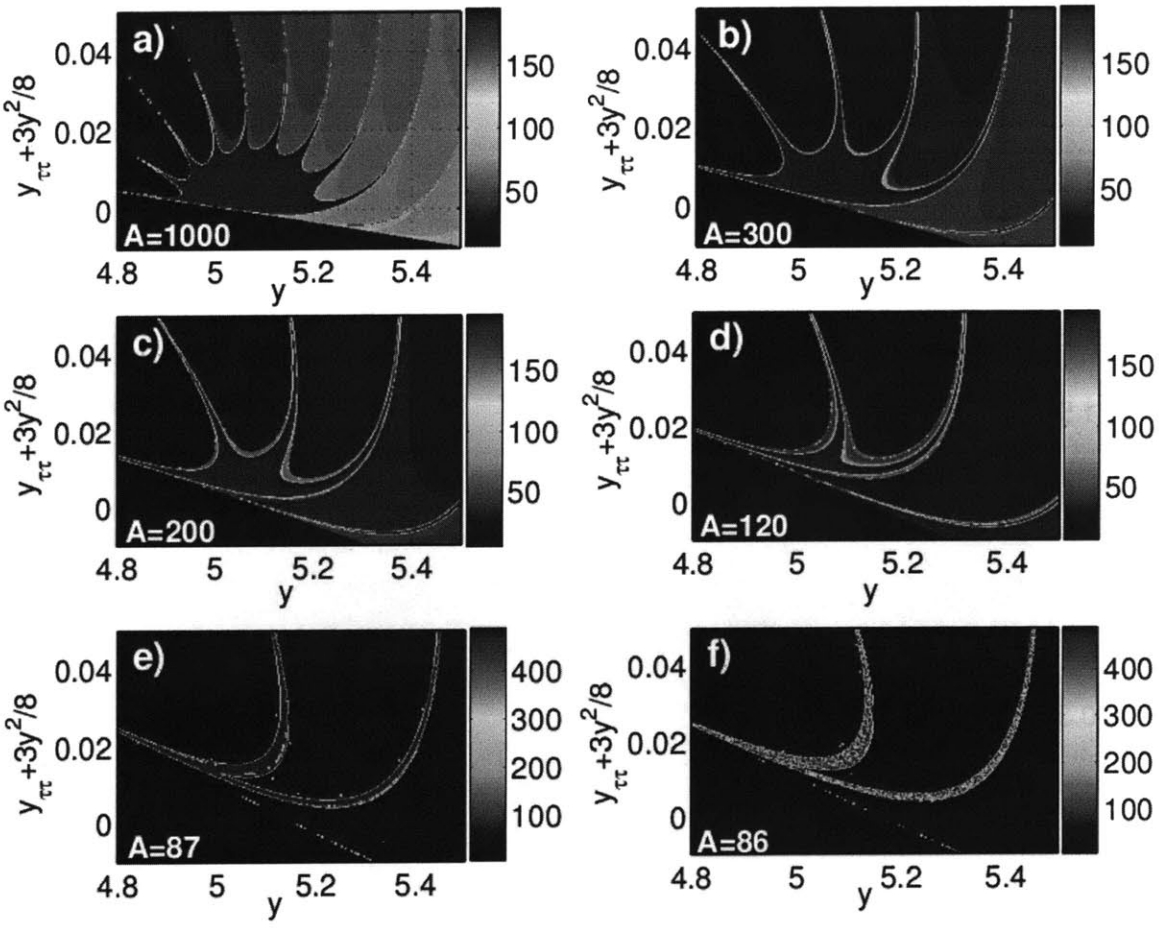

Figure E-9: The intersection of the stable manifold with the $y_\tau = 0$ plane for different values of A: **(a)** A=1000, **(b)** A=300, **(c)** A=200, **(d)** A=120, **(d)** A=87, **(e)** A=86. The number of passages through the $y_\tau = 0$, $y > 0$ half-plane before divergence to infinity is shown for points outside the stable manifold. A reduction in the volume of the manifold with decreasing A is evident, together with its disappearance at $A = 86$.

solved the equation (E.25) with A slowly decreasing in time. Every time the solution passed through the $y > 0, y_\tau = 0$ half-plane, we recorded the intersection and the current value of A. The results are shown in Fig. E-10, with each point representing one such intersection. As A is decreased, the limit cycle undergoes a period-doubling cascade and becomes a strange attractor; with further reduction of A it eventually becomes unstable, which was manifest by a sudden exponential growth in $y(t)$. We repeated this process several times with increasing precision and thus obtained the value $A_C = 86.641 \pm 0.001$.

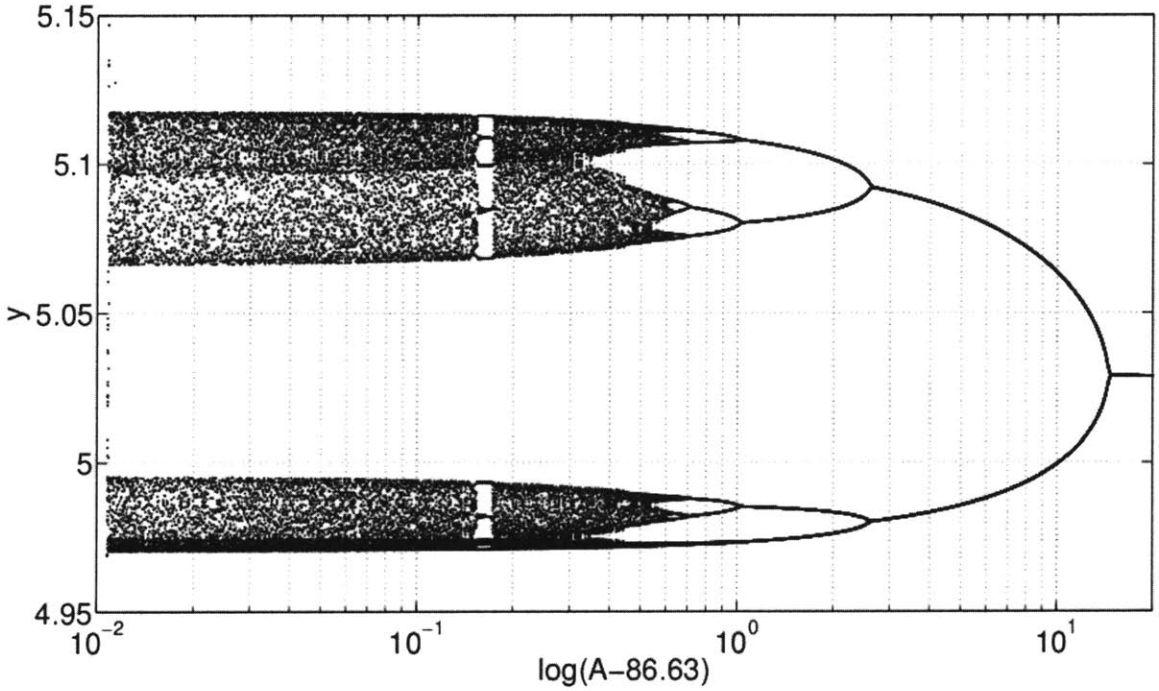

Figure E-10: The y-component of the intersection of the limit cycle with the $y_\tau = 0$ plane as a function of A. As A is decreased progressively, the limit cycle undergoes a period-doubling cascade, and below $A = 87.23$ becomes a strange attractor, with windows of periodicity. The strange attractor becomes unstable at $A = 86.641 \pm 0.001$.

E.6 The probability distribution function

We have investigated the dependence of the probability distribution $f(x)$ of $x(t)$ on the three system parameters $\mathcal{M}e, A$ and k. Firstly, the distribution was found to quickly converge to a limiting value as the memory was increased. In Fig. E-11, we plot the distribution function for $A = 0.25$ and $k = 0.1$ and several values of memory ranging from $\mathcal{M}e = 32$ to $\mathcal{M}e = 10^6$. As we see, the distribution function for $\mathcal{M}e = 256$ already lies very close to the high memory limit; thus, we expect the following statements and results for the high memory limit to be directly applicable to both the high and mid-memory regime. The profile of the distribution function is

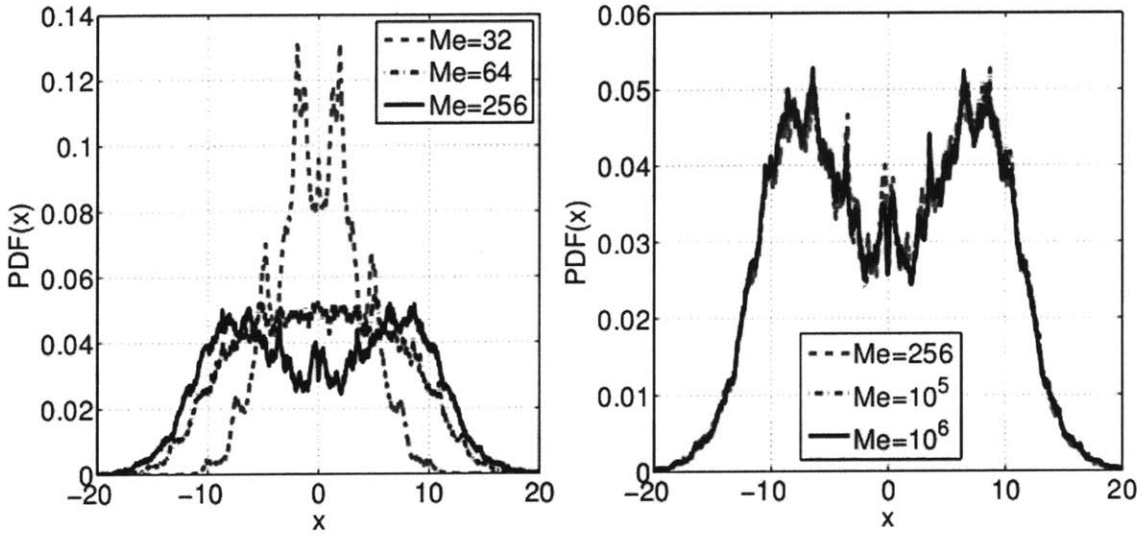

Figure E-11: The probability distribution function $f(x)$ of the drop position $x(t)$ for $A = 0.25$, $k = 0.1$ and five values of the memory. These are **(a)** $\mathcal{M}e = 32, 64, 256$ and **(b)** $\mathcal{M}e = 25, 10^5, 10^6$. A fast convergence to the high-memory limit is apparent.

closely tied to the behaviour of the solution and thus each of the 4 dynamical states identified previously has a characteristic profile of $f(x)$. For the ground state one sees two sharp peaks at $x = \pm\pi/2$, with $f(\pm\pi/2)$ being nearly 0.5. As we enter the chaotic ground state regime, the peaks get wider, with secondary peaks emerging. This trend is seen in Fig. E-12, where we plot the distribution function deduced for two values of A and a range of k between 0.001 and 100. As we cross into the region of fully chaotic motion, $f(x)$ becomes either gradually (Fig. E-12a) or abruptly (Fig. E-12b) gaussian, with most of its weight centered around the origin. Further decrease of k leads to a flattening and spreading of the distribution. For certain values of A (Fig. E-12a) this trend continued all the way down to $k = 0.001$; for others (Fig. E-12b) we observed the development of a minimum of $f(x)$ at $x = 0$, which gradually separates

the distribution function into two nearly disconnected parts. Below a certain value of k, the drop remains locked in one of the two regions, and only one of the two branches of the distribution function is then visible.

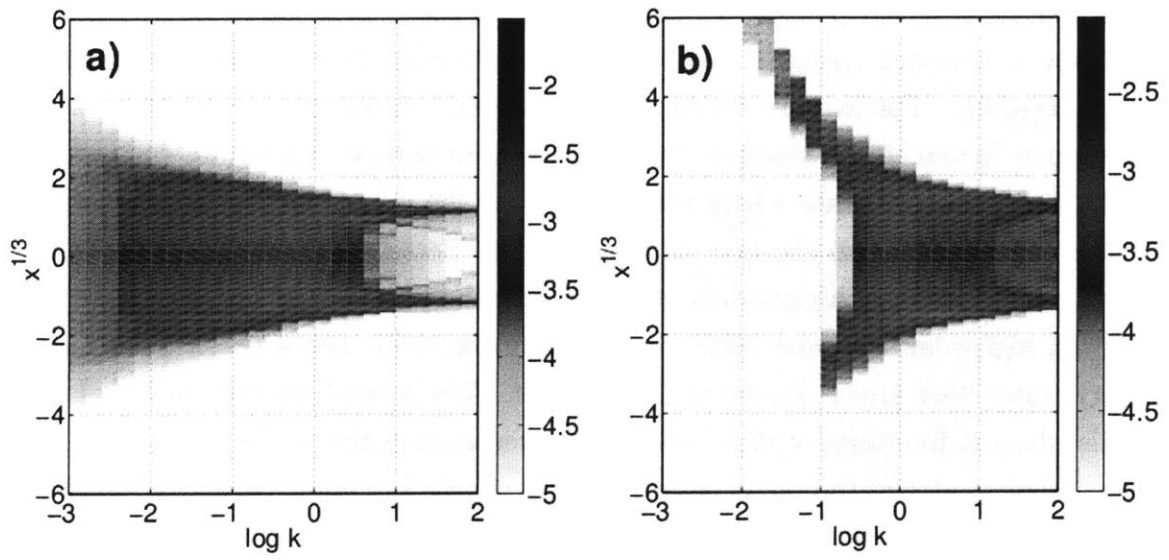

Figure E-12: The logarithm of the probability distribution function $f(x)$ as a function of x (vertical axis) and k (horizontal axis) for two values of A: **(a)** 1.58 and **(b)** 39.8. The horizontal scale is logarithmic, while the vertical scale indicates $x^{1/3}$, in order to capture the profile of the distribution function both at small and large x. In **(a)** the transition from the ground state to the chaotic ground state is clearly visible near $\log k = 1$, while the transition to a chaotic region around $\log k = 0.2$ is more gradual. In **(b)** the transition to fully chaotic motion arises at $\log k = 1.2$; at $\log k = -0.8$ the distribution function becomes asymmetric.

More work is needed to understand the nature of the transition from a symmetric to asymmetric distribution function and the mechanism behind this phenomenon. For now, our work as summarized in Fig. E-3, suggests that the asymmetric distributions appear in two separate regions. One lies near the critical value A_C and the drop's movement there is thus driven by the tendency to follow the unstable solution until eventual collapse towards the origin. The other region comprises small values of A and k, and it is there where least is known about the solution.

Several important questions are raised by this study. Is the probability distribution unique up to a mirror image around the origin? If not, what is the region of uniqueness and how can we rationalize it? Is it possible to rationalize the spatial extent of the distribution function, given A and k? And if there are multiple possible distribution functions, would they show the kind of quantization of the potential energy that has

so far eluded us? Until now, all analytic headway was made in the regions of unstable solutions and the ground states, where the drop behaviour is very regular.

Our investigation produced several results relevant to the 2-dimensional walking drop system studied experimentally. First, we showed that the mean square velocity of the drop is independent of the central force and thus equal to its value in force-free unbounded space. It would be worth checking whether this also holds in two dimensions. Further, we verified the prevalence of the ground state, in which the drop is bound to the smallest value of potential energy. This state corresponds to the 2-dimensional state where the drop orbits the origin along a circle with diameter corresponding to the first minimum of the Bessel function. Similarly to our 1-dimensional system, this ground circular orbit is the most commonly observed state, however, higher level circular orbits exist. It remains to be seen whether these higher energy states have any 1-dimensional analogues. Finally, we have observed probability distribution functions of the chaotic states resembling the profiles of the first and second eigenmodes of the quantum-mechanical simple harmonic oscillator. It seems that higher eigenmodes are not attainable in our system, which raises the question of what crucial feature is missing in our model that is required for these eigenmodes to be observed.

Bibliography

[1] G. A. Bach, D. L. Koch, and A. Gopinath. Coalescence and bouncing of small aerosol droplets. *J. Fluid Mech.*, 518:157, 2004.

[2] J. S. Bell. On the einstein podolsky rosen paradox. *Physics*, 1:195–200, 1964.

[3] J. S. Bell. On the problem of hidden variables in quantum mechanics. *Rev. Mod. Phys.*, 38:447, 1966.

[4] T. Benjamin and F. Ursell. The stability of the plane free surface of a liquid in vertical periodic motion. *Proc. R. Soc. Lond. A*, 225:505–515, 1954.

[5] F. Blanchette and T.P. Bigioni. Partial coalescence of drops at liquid interfaces. *Nat. Phys.*, 2:254–257, 2006.

[6] J. W. M. Bush. Quantum mechanics writ large. *Proc. Natl. Acad. Sci.*, 107:17455, 2010.

[7] J. W. M. Bush, D. L. Hu, and M. Prakash. The integument of water-walking arthropods: Form and function. *Adv. Insect Physiol.*, 34:117–192, 2008.

[8] M. Bussmann, S. Chandra, and J. Mostaghimi. Modeling the splash of a droplet impacting a solid surface. *Phys. Fluids*, 12:3121, 2000.

[9] M. Bussmann, J. Mostaghimi, and S. Chandra. On a three-dimensional volume tracking model of droplet impact. *Phys. Fluids*, 11:1406, 1999.

[10] Y.K. Cai. Phenomena of a liquid drop falling to a liquid surface. *Exp. Fluids*, 7:388–394, 1989.

[11] S. Chandrasekhar. *Hydrodynamic and Hydromagnetic Stability.* Clarendon Press, Oxford, 1961.

[12] E. J. Chang and M. R. Maxey. Unsteady flow about a sphere at low to moderate Reynolds number. part 1. oscillatory motion. *J. Fluid Mech.*, 277:347–379, 1994.

[13] A. K. Chesters. An analytical solution for the profile and volume of a small drop or bubble symmetrical about a vertical axis. *J. Fluid Mech.*, 81:609–624, 1977.

[14] B. K. Chi and L. G. Leal. A theoretical study of the motion of a viscous drop toward a fluid interface at low reynolds number. *J. Fluid Mech.*, 201:123–146, 1989.

[15] B. Ching, M. W. Golay, and T. J. Johnson. Droplet impacts upon liquid surfaces. *Science*, 226:535–537, 1984.

[16] Y. Couder and E. Fort. Single-particle diffraction and interference at macroscopic scale. *Phys. Rev. Lett.*, 97:154101, 2006.

[17] Y. Couder and E. Fort. Probabilities and trajectories in a classical wave-particle duality. *J Phys.*, 361:012001, 2012.

[18] Y. Couder, E. Fort, C.H. Gautier, and A. Boudaoud. From bouncing to floating: Noncoalescence of drops on a fluid bath. *Phys. Rev. Lett.*, 94:177801, 2005.

[19] Y. Couder, S. Protière, E. Fort, and A. Boudaoud. Walking and orbiting droplets. *Nature*, 437:208, 2005.

[20] S. Courty, G. Lagubeau, and T. Tixier. Oscillating droplets by decomposition on the spherical harmonics basis. *Phys. Rev. E*, 73:045301, 2006.

[21] R. B. Davis and L. N. Virgin. Non-linear behaviour in a discretely forced oscillator. *Int. J. Non-Lin. Mech.*, 42:744–753, 2007.

[22] de Broglie. *Compt. Rend. Acad. Sci. Paris*, 177:506,548,630, 1923.

[23] Louis de Broglie. Interpretation of quantum mechanics by the double solution theory. *Ann. Fond. Louis de Broglie*, 12:1–23, 1987.

[24] J. R. de Bruyn, B. C. Lewis, M. D. Shattuck, and H. L. Swinney. Spiral patterns in oscillated granular layers. *Phys. Rev. E*, 63:0413050, 1994.

[25] S. Dorbolo, D. Terwagne, N. Vandewalle, and T. Gilet. Resonant and rolling droplets. *New J. Phys.*, 10:113021, 2008.

[26] S. Dorbolo, D. Volfson, L. Tsimring, and A. Kudrolli. Dynamics of a bouncing dimer. *Phys. Rev. Lett.*, 95:044101, 2005.

[27] S. Douady. Experimental study of the Faraday instability. *J. Fluid Mech.*, 221:383–409, 1990.

[28] A. Eddi, A. Boudaoud, and Y. Couder. Oscillating instability in bouncing droplet crystals. *Europhys. Lett.*, 94:20004, 2011.

[29] A. Eddi, A. Decelle, E. Fort, and Y. Couder. Archimedean lattices in the bound states of wave interacting particles. *Europhys. Lett.*, 87:56002, 2009.

[30] A. Eddi, E. Fort, F. Moisy, and Y. Couder. Unpredictable tunneling of a classical wave-particle association. *Phys. Rev. Lett.*, 102:240401, 2009.

[31] A. Eddi, J. Moukhtar, S. Perrard, E. Fort, and Y. Couder. Level splitting at macroscopic scale. *Phys. Rev. Lett.*, 108:264503, 2012.

[32] A. Eddi, E. Sultan, J. Moukhtar, E. Fort, M. Rossi, and Y. Couder. Information stored in Faraday waves: The origin of a path memory. *J. Fluid Mech.*, 674:433, 2011.

[33] A. Eddi, D. Terwagne, E. Fort, and Y. Couder. Wave propelled ratchets and drifting rafts. *Europhys. Lett.*, 82:44001, 2008.

[34] H. E. Edgerton and Killian J. R. *Flash! Seeing the unseen by ultra-high-speed photography.* Hale, Cushman and Flint, Boston, 1939.

[35] B. Eichwald, M. Argentina, X. Noblin, and F. Celestini. Dynamics of a ball bouncing on a vibrated elastic membrane. *Phys. Rev. E*, 82:016203, 2010.

[36] L. L. English. Some properties of oil emulsions influencing insecticidal efficiency. *Bull. Illinois Nat. Hist. Surv.*, 17:233–259, 1928.

[37] R. M. Everson. Chaotic dynamics of a bouncing ball. *Physica D*, 19:355–383, 1986.

[38] M. Faraday. On a peculiar class of acoustical figures; and on certain forms assumed by groups of particles upon vibrating elastic surfaces. *Philos. Trans. R. Soc. London*, 121:299–340, 1831.

[39] Enrico Fermi. On the origin of the cosmic radiation. *Phys. Rev.*, 75:1169–1174, 1949.

[40] R. L. C. Flemmer and C. L. Banks. On the drag coefficient of a sphere. *Powder Tech.*, 48:217–221, 1986.

[41] S. Flügge. *Handbuch der Physik: Strömungsmechanik I.* Springer-Verlag, Berlin-Göttingen-Heidelberg, 1959.

[42] G.B. Foote. The water drop rebound problem: Dynamics of collision. *J. Atmos. Sci.*, 32:390–402, 1975.

[43] E. Fort, A. Eddi, A. Boudaoud, J. Moukhtar, and Y. Couder. Path-memory induced quantization of classical orbits. *Proc. Natl. Acad. Sci.*, 107:17515, 2010.

[44] P. G. Gennes, F. Brochard-Wyart, and D. Quéré. *Capillarity and Wetting Phenomena: Drops, Bubbles, Pearls, Waves.* Springer, New York, N.Y., 2003.

[45] T. Gilet and J. W. M. Bush. Chaotic bouncing of a droplet on a soap film. *Phys. Rev. Lett.*, 102:014501, 2009.

[46] T. Gilet and J. W. M. Bush. The fluid trampoline: Droplets bouncing on a soap film. *J. Fluid Mech.*, 625:167–203, 2009.

[47] T. Gilet and J. W. M. Bush. Droplets bouncing on a wet, inclined surface. *Phys. Fluids, in press*, 25, 2012.

[48] T. Gilet, D. Terwagne, N. Vandewalle, and S. Dorbolo. Dynamics of a bouncing droplet onto a vertically vibrated interface. *Phys. Rev. Lett.*, 100:167802, 2008.

[49] T. Gilet, N. Vandewalle, and S. Dorbolo. Completely inelastic ball. *Phys. Rev. E*, 79:055201, 2009.

[50] A. J. Goldman, R. G. Cox, and H. Brenner. Slow viscous motion of a sphere parallel to a plane wall - i: Motion through a quiescent fluid. *Chem. Eng. Sci.*, 22:637–651, 1967.

[51] D. I. Goldman. *Pattern formation and fluidization in vibrated granular layers, and grain dynamics and jamming in a water fluidized bed.* PhD thesis, University of Texas at Austin.

[52] A. Gopinath and D. L. Koch. Dynamics of droplet rebound from a weakly deformable gas-liquid interface. *Phys. Fluids*, 13:3526, 2001.

[53] A. Gopinath and D.L. Koch. Collision and rebound of small droplets in an incompressible continuum gas. *J. Fluid Mech.*, 454:145–201, 2002.

[54] G. Grössing, S. Fussy, J. M. Pascasio, and H. Schwabl. An explanation of interference effects in the double slit experiment: Classical trajectories plus ballistic diffusion caused by zero-point fluctuations. *Ann. Phys.*, 327:421–437, 2012.

[55] G. Grössing, S. Fussy, J. M. Pascasio, and H. Schwabl. The quantum as an emergent system. *arXiv*, page 1205.3393v1, 2012.

[56] G. Grössing, J. M. Pascasio, and H. Schwabl. A classical explanation of quantization. *Found. Phys.*, 41:1437–1453, 2011.

[57] Z. Guo and W. Liu. Biomimic from the superhydrophobic plant leaves in nature: Binary structure and unitary structure. *Plant Science*, 172:1103–1112, 2007.

[58] J. Hallett and L. Christensen. Splash and penetration of drops in water. *J. Rech. Atmos.*, 18:225–242, 1984.

[59] Daniel M. Harris, Julien Moukhtar, Emmanuel Fort, Yves Couder, and John W. M. Bush. Pilot-wave dynamics in confined geometries. *Phys. Rev. Lett.*, under review, 2013.

[60] S. Hartland. The effect of circulation patterns on the drainage of the film between a liquid drop and a deformable liquid-liquid interface. *Chem. Eng. Sci.*, 24:611–613, 1969.

[61] S. Hartland. The profile of the draining film between a rigid sphere and a deformable fluid-liquid interface. *Chem. Eng. Sci.*, 24:987–995, 1969.

[62] S. Hartland. The profile of the draining film between a fluid drop and a deformable fluid-liquid interface. *Chem. Eng. J.*, 1:67–75, 1970.

[63] S. Hartland. The pressure distribution in axisymmetric draining films. *J. Colloid Interface Sci.*, 35:227–237, 1971.

[64] S. Hartland, S. Ramakrishnan, and R. W. Hartley. The oscillations of drops and spheres at fluid-liquid interfaces. *Chem. Eng. Sci.*, 30:1141–1148, 1975.

[65] S. Hartland and J. D. Robinson. The uniform film model for the gravitational approach of fluid drops to plane and deformable interfaces. *Can. J. Chem. Eng.*, 51:647–654, 1973.

[66] S. Hartland and J. D. Robinson. A model for an axisymmetric dimpled draining film. *J. Colloid Interface Sci.*, 60:72–81, 1977.

[67] O.W. Jayaratne and B.J. Mason. The coalescence and bouncing of water drops at an air/water interface. *Proc. R. Soc. A*, 280:545–565, 1964.

[68] A. F. Jones and S. D. R. Wilson. The film drainage problem in droplet coalescence. *J. Fluid Mech.*, 87:263–288, 1978.

[69] K. Kumar. Linear theory of Faraday instability in viscous liquids. *Proc. Math. Phys. Eng. Sci.*, 452:1113–1126, 1996.

[70] B. Lafaurie, C. Nardone, R. Scardovelli, S. Zaleski, and G. Zanetti. Modelling merging and fragmentation in multiphase flows with surfer. *J. Comp. Phys.*, 113:134–147, 1994.

[71] H. Lamb. *Hydrodynamics*. Cambridge U. P., Cambridge, 1932.

[72] J.M. Luck and A. Mehta. Bouncing ball with a finite restitution: Chattering, locking, and chaos. *Phys. Rev. E*, 48:3988–3997, 1993.

[73] German A. Luna-Acosta. Regular and chaotic dynamics of the damped fermi accelerator. *Phys. Rev. A*, 42:7155–7162, 1990.

[74] Anita Mehta and J. M. Luck. Novel temporal behaviour of a nonlinear dynamical system: The completely inelastic bouncing ball. *Phys. Rev. Lett.*, 65:393–396, 1990.

[75] P. Milewski, C. Galeano-Rios, A. Nachbin, and J. W. M. Bush. A numerical model of pilot-wave hydrodynamics. *J. Fluid Mech.*, in preparation, 2013.

[76] C.A. Miller and L.E. Scriven. The oscillations of a fluid droplet immersed in another fluid. *J. Fluid Mech.*, 32:417–435, 1968.

[77] Jan Moláček and John W. M. Bush. A quasi-static model of drop impact. *Phys. Fluids*, 24, 2012.

[78] Jan Moláček and John W. M. Bush. Drops bouncing on a vibrating bath. *J. Fluid Mech.*, under review, 2013.

[79] Jan Moláček and John W. M. Bush. Drops walking on a vibrating bath: towards a hydrodynamic pilot-wave theory. *J. Fluid Mech.*, under review, 2013.

[80] W. Moore. Spreading and adherence of arsenical sprays. *Minnesota Agri. Exp. Station Tech. Bull.*, 2:1–50, 1921.

[81] D. C. Morse and T. A. Witten. Droplet elasticity in weakly compressed emulsions. *Europhys. Lett.*, 22:549–555, 1993.

[82] M. A. Naylor, P. Sanchez, and M. R. Swift. Chaotic dynamics of an air-damped bouncing ball. *Phys. Rev. E*, 66:057201, 2002.

[83] A. H. Norton. On quantum foundations and the assumption that the lorentz equation of motion defines a fully resolved electrodynamics. pages 1–10, 2012.

[84] K. Okumura, F. Chevy, D. Richard, D. Quéré, and C. Clanet. Water spring: A model for bouncing drops. *Europhys. Lett.*, 62:237–243, 2003.

[85] S. Osher and R. P. Fedkiw. Level set methods: An overview and some recent results. *J. Comp. Phys.*, 169:463–502, 2001.

[86] A. Otten and S. Herminghaus. How plants keep dry: A physicist's point of view. *Langmuir*, 20:2405–2408, 2004.

[87] A. U. Oza, D. M. Harris, R. R. Rosales, and J. W. M. Bush. Pilot-wave dynamics in a rotating frame. *J. Fluid Mech.*, in preparation, 2013.

[88] Anand U. Oza, Rodolfo R. Rosales, and John W. M. Bush. A trajectory equation for walking droplets: hydrodynamic pilot-wave theory. *J. Fluid Mech.*, under review, 2012.

[89] N. A. Patankar. Mimicking the lotus effect: Influence of double roughness structures and slender pillars. *Langmuir*, 20:8209–8213, 2004.

[90] P. Pieranski. Jumping particle model. period doubling cascade in an experimental system. *J. Phys.*, 44:573–578, 1983.

[91] P. Pieranski and R. Bartolino. Jumping particle model. modulation modes and resonant response to a periodic perturbation. *J. Phys.*, 46:687–690, 1985.

[92] J. Plateau. Experimental and theoretical researches into the figures of equilibrium of a liquid mass without weight. *Philos. Mag.*, 38:445–455, 1869.

[93] A. Prosperetti. Viscous effects on small-amplitude surface waves. *Phys. Fluids*, 19:195–203, 1976.

[94] A. Prosperetti. Viscous effects on perturbed spherical flows. *Quart. Appl. Math.*, 35:339–352, 1977.

[95] A. Prosperetti. Free oscillations of drop and bubbles: The initial-value problem. *J. Fluid Mech.*, 100:333, 1980.

[96] A. Prosperetti and H. N. Oguz. The impact of drops on liquid surfaces and the underwater noise of rain. *Ann. Rev. Fluid Mech.*, 25:577–602, 1993.

[97] S. Protière, S. Bohn, and Y. Couder. Exotic orbits of two interacting wave sources. *Phys. Rev. E*, 78:036204, 2008.

[98] S. Protière, A. Boudaoud, and Y. Couder. Particle-wave association on a fluid interface. *J. Fluid Mech.*, 554:85–108, 2006.

[99] S. Protière and Y. Couder. Orbital motion of bouncing drops. *Phys. Fluids*, 18:091114, 2006.

[100] S. Protière, Y. Couder, E. Fort, and A. Boudaoud. The self-organization of capillary wave sources. *J. Phys-condens. Mat.*, 17:S3529–S3535, 2005.

[101] D. Quéré. Wetting and roughness. *Annu. Rev. Mater. Res.*, 38:71–99, 2008.

[102] D. Quéré and M. Reyssat. Non-adhesive lotus and other hydrophobic materials. *Phil. Trans. R. Soc. A*, 366:1539–1556, 2008.

[103] Lord Rayleigh. *Proc. R. Soc. Lond. A*, 29:71, 1879.

[104] Lord Rayleigh. The influence of electricity on colliding water drops. *Proc. R. Soc. London A*, 28:406, 1879.

[105] Lord Rayleigh. On the capillary phenomena of jets. *Proc. R. Soc. London*, 29:71–97, 1879.

[106] M. Rein. Phenomena of liquid drop impact on solid and liquid surfaces. *Fluid Dyn. Res.*, 12:61–93, 1993.

[107] P. M. Reis, R. A. Ingale, and M. D. Shattuck. Forcing independent velocity distributions in an experimental granular fluid. *Phys. Rev. E*, 75:051311, 2007.

[108] D. Richard, C. Clanet, and D. Quéré. Contact time of a bouncing drop. *Nature*, 417:811, 2002.

[109] D. Richard and D. Quéré. Bouncing water drops. *Europhys. Lett.*, 50:769–775, 2000.

[110] S. W. Rienstra. The shape of a sessile drop for small and large surface tension. *J. Eng. Math.*, 24:193–202, 1990.

[111] R.M. Schotland. Experimental results relating to the coalescence of water drops with water surfaces. *Discuss. Faraday Soc.*, 30:72–77, 1960.

[112] M. E. R. Shanahan. Profile and contact angle of small sessile drops. *J. Chem. Soc., Faraday Trans. I*, 80:37–45, 1984.

[113] D. Shirokoff. Bouncing droplets on a billiard table. *Phys. Fluids*, under review, 2012.

[114] P. G. Smith and T. G. M. van De Ven. Profiles of slightly deformed axisymmetric drops. *J. Colloid Interface Sci.*, 97:1–8, 1984.

[115] M. Sussman, A. S. Almgren, J. B. Bell, P. Colella, L. H. Howell, and Welcome M. L. An adaptive level set approach for incompressible two-phase flows. *J. Comp. Phys.*, 148:81–124, 1999.

[116] D. Terwagne. *Bouncing Droplets, the Role of Deformations.* PhD thesis, Université de Liège, 2011.

[117] D. Terwagne, T. Gilet, N. Vandewalle, and S. Dorbolo. From bouncing to boxing. *Chaos*, 18:041104, 2008.

[118] D. Terwagne, F. Ludewig, N. Vandewalle, and S. Dorbolo. The role of deformations in the bouncing droplet dynamics. *Phys. Fluids*, under review:arXiv:1301.7463, 2013.

[119] S. T. Thoroddsen. The ejecta sheet generated by the impact of a drop. *J. Fluid Mech.*, 451:373–381, 2002.

[120] S. T. Thoroddsen, T. G. Etoh, and K. Takehara. High-speed imaging of drops and bubbles. *Annu. Rev. Fluid Mech.*, 40:257–285, 2008.

[121] S. T. Thoroddsen and K. Takehara. The coalescence cascade of a drop. *Phys. Fluids*, 12:1265–1267, 2000.

[122] Bruce J. Torby. *Advanced Dynamics for Engineers.* Holt, Rinehart, and Winston, New York, N.Y., 1984.

[123] J. von Neumann. *Mathematische Grundlagen der Quanten-mechanik.* Verlag Julius-Springer, Berlin, 1932.

[124] Jearl Walker. Drops of liquid can be made to float on the liquid. what enables them to do so? *The Amateur Scientist, Sci. Am.*, 238:151–158, 1978.

[125] Z. Wang, C. Lopez, A. Hirsa, and N. Koratkar. Impact dynamics and rebound of water droplets on superhydrophobic carbon nanotube arrays. *Appl. Phys. Lett.*, 91:023105, 2007.

[126] H. Wijshoff. The dynamics of the piezo inkjet printhead operation. *Phys. Rep.*, 491:77–177, 2010.

[127] F. Wilcoxon and A. Hartzell. Some factors affecting the efficiency of contact pesticides. i. surface forces as related to wetting and tracheal penetration. *Contr. Boyce. Thompson Inst.*, 3:1–12, 1931.

[128] A. M. Worthington. On the forms assumed by drops of liquids falling vertically on a horizontal plate. *Proc. R. Soc. London*, 25:261–272, 1876.

[129] A. M. Worthington. On impact with a liquid surface. *Proc. R. Soc. London*, 34:217–230, 1882.

[130] H. S. Wright, M. R. Swift, and P. J. King. The horizontal stability of a ball bouncing upon a vertically vibrated concave surface. *Eur. Phys. Lett.*, 81:14002, 2008.

[131] A.L. Yarin. Drop impact dynamics: Splashing, spreading, receding, bouncing... *Annu. Rev. Fluid. Mech.*, 38:159–192, 2006.

[132] Q. Zhou, N. Li, X. Chen, T. Xu, S. Hui, and D. Zhang. Liquid drop impact on solid surface with application to water drop erosion on turbine blades, part ii: Axisymmetric solution and erosion analysis. *Int. J. Mech. Sci.*, 50:1543–1558, 2008.

[133] J. Zou, P. F. Wang, T. R. Zhang, X. Fu, and X. Ruan. Experimental study of a drop bouncing on a liquid surface. *Phys. Fluids*, 23:044101, 2011.